Hole Dynamics in Films

Hamed Vaziri Goudarzi

Hole Dynamics in Films

Hamed Vaziri.G

Supervisor: Dr. Stéphane Popinet

L'école doctorale Sciences Mécaniques, Acoustique, Électronique, et Robotique de Paris

Sorbonne University

This dissertation is submitted for the degree of

Doctor of Philosophy

Jury members: Prof. Laurent Duchemin (reviewer and jury's president),
Prof. Emmanuelle Rio (reviewer),
Prof. Jose-Maria Lopez-Herrera (reporter),
Dr. Sébastien Tanguy (reporter).

December 2023

I dedicate this thesis to my mother, to whom I am forever in debt.

Declaration

I hereby declare that this thesis entitled "Hole Dynamics in Films and Ocean-Atmosphere Exchanges" represents my original work, conducted under the supervision of Dr. Stéphane Popinet, submitted in fulfillment for the degree of Doctor of Philosophy in mechanical engineering at Sorbonne University. I confirm that:

1. The work presented in this thesis is my own, except where indicated by appropriate citations.
2. I have not used any work, text, data, or ideas from others without proper citation and acknowledgment.
3. I have not submitted this thesis, or a substantial part of it, for any other academic qualification, and it has not been previously published.
4. I am aware of the consequences of any academic misconduct, including plagiarism and falsification, and have taken all reasonable steps to ensure the integrity of this thesis.
5. I understand that any violation of academic or ethical standards may result in the rejection of this thesis or the revocation of my Ph.D. degree.

Hamed Vaziri.G
December 2023

Acknowledgements

I would like to thank my supervisor, Dr. Stéphane Popinet, for his guidance throughout my Ph.D. and for providing me both with an opportunity to work on this project and an invaluable knowledge of the field of fluid mechanics and beyond. Furthermore, I acknowledge and appreciate the efforts of Prof. Emmanuelle Rio and Prof. Laurent Duchemin for their annual reviews of my Ph.D. progress, their scientific contribution, and their support. Lastly, I would like to thank my girlfriend Susanna for her undivided support during the final months of my Ph.D.

Abstract

Oceanic film bursting is a phenomenon in which a thin liquid film representing the cap of the bubble bursts at the surface of the ocean, producing film drops. The film bursting phenomenon is critical in ocean-atmosphere exchanges, particularly in transferring heat, mass, and momentum between the ocean and the atmosphere. The film bursting phenomenon comprises a series of complex dynamics, such as drainage, puncture, film retraction, and film disintegration into film drops. The hole healing (i.e., when a hole is too small and is closed after its nucleation) is a critical parameter that could impact the film bursting dynamics, particularly the film thickness at bursting and, thus, the liquid budget for the film drop production.

The present work investigates the dynamics of holes in free liquid films, presenting a comprehensive understanding of the hole-healing phenomenon while focusing on the film bursting in the oceanic context. This was achieved through a combination of numerical simulations and analytical approaches. The numerical simulations were carried out using Basilisk. This robust and efficient two-phase flow solver is based on a Volume-of-Fluid (VoF) method and written using the C-programming language. The underlying mechanism for the hole-healing phenomenon was studied in detail. The dichotomy simulations for the determination of the healing threshold carried out in this work have used high-resolution mesh refinement. This was possible by using an adaptive mesh scheme provided by Basilisk.

The analytical approaches were used to develop hypotheses to predict the healing threshold of a hole on a film, which were tested against numerical results. The critical dynamics of the hole are examined, and distinct power laws were identified for the tip curvature to illustrate the driving mechanism.

The variations in the hole healing threshold with other problem parameters were examined. This study was first carried out for a flat film, discovering that the healing threshold is increased by increasing the film Laplace number. This effect was pronounced for values ranging from 1 to 10000, coinciding with the customary range of film Laplace numbers observed for oceanic bursting bubbles. The observed effects were also elaborated upon, along with physical explanations.

Since the exact initial shape of the hole was shown to influence the healing threshold, an examination was carried out to study this effect on the consistency of the results from changing

the film Laplace number, taken as an example for the other. It was shown that despite variations in the threshold for different shapes, the effect of changing the film Laplace number was independent of the hole shape. Therefore, the dichotomy results were shown to be independent of the arbitrary choice of the hole shape throughout the study.

A similar study was carried out for a hole in a bubble cap after a detailed study of the bubble and gas outflow dynamics. It was discovered that the gas outflow undergoes a Venturi effect, where a stronger outflow, resulting from smaller bubble sizes or higher gas Laplace numbers, was shown to increase the healing threshold. A hypothesis was developed to predict the Venturi effect on the healing threshold, resulting in a Venturi correction term that predicted a power law dependency on the bubble diameter, which agreed with the numerical results. The Venturi effect was significant for high values of the gas Laplace number, where the healing threshold was doubled by increasing the film mean curvature from a flat film to a bubble cap with a size 20 times the bubble cap thickness.

These findings provide a comprehensive understanding of the hole-healing phenomenon, particularly in oceanic film bursting. The present work also offers a foundation for future studies on the film-bursting phenomenon involving complex dynamics, including hole healing.

Table of contents

List of figures

List of tables

Nomenclature

Greek Symbols

Δ_{min}	Minimum cell size
χ	mesh refinement error
Δ	size of a mesh cell
δ	film thickness
δ_s	surface Dirac function
γ	surface tension coefficient
κ	interface curvature
μ	viscosity
∂	partial derivative
ϕ	liquid flow between two mesh cells
ρ	density
τ	time scale
ζ	mesh refinement criterion

Superscripts

$'$	derivative
$*$	non-dimensionalized
$-$	average

$\circ$ degree Celsius

Subscripts

b bubble

g gas phase

gr gravity

h hole

ic inertia-capillary

l liquid phase

m mesh level

n time step

s curvilinear coordinate

t time

tc Taylor-Culick

vc visco-capillary

Other Symbols

Δp pressure difference inside the bubble

$\overline{\Delta p}$ average pressure difference inside the bubble

$\overline{u}$ average velocity of the gas outflow at the hole minimum cross-section

$\tau_{\Delta p}$ time scale for the evolution of the pressure inside the bubble

τ_A time scale for the evolution of the minimum cross-section area

τ_i time scale for the gas inertial acceleration

τ_u time scale for the evolution of the gas outflow velocity

FML Maximum mesh level within the initial film thickness

GML Global maximum level for mesh refinement in the quadtree grid

A_{mn} minimum cross-section area

C Venturi viscous coefficient

Q volumetric gas outflow rate

Re Reynolds number

u_{θ_b} tangential velocity within the bubble cap

u_{r_b} radial velocity within the bubble cap

V bubble volume

$\boldsymbol{D}$ deformation tensor

$\boldsymbol{f}_\gamma$ surface tension force per unit volume

$\boldsymbol{u}$ velocity vector (u, v, w)

Δp_γ capillary pressure

Δt time step size

$\kappa(r)$ total curvature of the film surface as a function of radial distance

$\kappa^+(r_0)$ positive component of the curvature at the tip of the hole as a function of the hole minimum radius

$\kappa^-(r_0)$ negative component of the curvature at the tip of the hole as a function of the hole minimum radius

κ_{r_0} total curvature at the tip of the hole

$\kappa_{r_0}^+$ positive component of the curvature at the tip of the hole

$\kappa_{r_0}^-$ negative component of the curvature at the tip of the hole

$\rho_{l/g}$ density ratio of liquid to gas

Re Reynolds number

$\tilde{F}$ either identical to F or spatially smoothed F

d hole minimum diameter

d^{*c} non-dimensional hole minimum diameter at the healing threshold

d_1 hole maximum diameter

d_b bubble maximum diameter

f discretized F on mesh cells

$F(x,t)$ volume fraction

g gravity constant

H mean curvature

h_x, h_y, h_z height functions in $x, y,$ and z direction

i, j mesh cell counters in x and y directions

L domain size

n surface unit normal

P pressure scale

p pressure

r_0 minimum radius of the hole

r_{ex} critical radial distance at which the hole tip falls into the positive feedback loop

R_f bubble cap foot radius

U velocity scale

CAM coefficient of mesh adaptation

Ga Galileo number

La Laplace number

NSA number of cells across the film thickness

Oh Ohnesorge number

Acronyms / Abbreviations

CFD computational fluid dynamics

D	dimension
MPI	message-passing interface
psu	practical salinity unit
VoF	Volume-of-Fluid

Chapter 1

Introduction

Bubbles are an integral component of numerous natural and industrial processes, playing a pivotal role in shaping the physical and chemical phenomena we observe in the world around us. Their ubiquitous presence, whether in one's daily beverages or the vast expanse of the oceans, is a testament to their significance. The mechanisms behind their creation, whether through gas injection, boiling with heat, or even external stimuli such as laser pulses and electric sparks, are as varied as their applications.

Across industries and environments, bubble bursting and subsequent droplet formation find myriad applications. From removing undesired bubbles in molten glass to aiding drug carriers in medical treatments by releasing nanoparticles, the utility of bubbles is vast and varied. In fields as critical as nuclear engineering, droplets from bursting bubbles can influence the efficiency of steam generators (Zhang and Liu, 2020), and during catastrophic events, can play a role in the dispersal of radioactive aerosols (Koch et al., 2000; Ma et al., 2022). Environmental implications of bubbles are also profound, with a staggering $10^{18} - 10^{20}$ bubbles produced in the oceans every second (Bird et al., 2010; Lewis and Schwartz, 2004), contributing to crucial climatic and biological cycles (Berny et al., 2021; Veron, 2015). Beyond these, the realm of gastronomy and beverage industries is replete with examples where the aroma-laden aerosols produced by bursting bubbles elevate the sensory experience for consumers (Gonzalez Viejo et al., 2019; Mondal and Niranjan, 2019).

Once formed in a body of liquid, the physics of the bubble ascent is driven by buoyancy, leading them to adopt specific geometries at the free surface, particularly a hemisphere or ellipsoidal shape, with a thin curved film (i.e., the "bubble cap") separating the gas inside the bubble from the surrounding liquid. A complex set of dynamics ensues as a bubble reaches the free surface. The film of the bubble drains over time, following exponential (Debrégeas et al., 1998) or algebraic (Lhuissier and Villermaux, 2012) trends, until disturbances—either internal or external—cause the nucleation of a hole. This puncture event provided the hole is sufficiently

large, marks the onset of rapid changes as the film bursts and undergoes destabilization, leading to the emergence of ligaments that fragment into film droplets. After the bursting event, capillary waves are instigated, which could, upon reaching the cavity base, give rise to an upward jet, further fragmenting to form droplets (jet drops).

Nevertheless, the film could also "heal" itself by closing the hole, a phenomenon that is the focus of this study. The healing of the hole is a direct consequence of the surface tension forces that act to minimize the surface area of the film. The hole healing process is a dynamic interplay of surface tension, viscosity, and external factors, central to many natural and industrial phenomena (Taylor and Michael, 1973). This study aims to provide a comprehensive understanding of the dynamics of holes in thin liquid films, particularly the healing threshold and its dependence on various parameters.

In short, the present work focuses on the intricacies of hole in bubble caps and flat free film dynamics with regard to the oceanic contexts, particularly emphasizing the hole-healing phenomenon as part of the overall film-bursting dynamics.

1.1 Ocean Atmosphere Exchanges Due to Bursting Films

The ocean and the atmosphere are two intertwined components of the planet's climate system. Together, they form a dynamic complex that governs Earth's weather patterns, temperature distributions, and overall climate. Many mechanisms facilitate this interplay; one intriguing example is the exchanges induced by bursting bubbles at the surface of the ocean and created by, for instance, wave breakings or rain events.

At the heart of the climate system, the ocean and atmosphere continuously exchange energy, moisture, and gases. This transfer plays a pivotal role in regulating Earth's temperature. For instance, with its vast heat capacity, the ocean acts as a buffer, absorbing excess heat from the atmosphere during warmer periods and releasing it during cooler times, thus modulating extreme temperature fluctuations (Peixoto and Oort, 1992).

Countless bubbles form due to wave breakings and burst at the ocean surface every second, a complex process illustrated in figure 1.1. As they rise through the liquid bulk, these bubbles entrain seawater gases. Upon reaching the surface and bursting, they release these gases into the atmosphere. This process is instrumental in transferring gases like carbon dioxide (CO2) and dimethyl sulfide (DMS). While CO2 plays a well-known role in the greenhouse effect and thus global warming, DMS, upon oxidation, forms cloud-condensation nuclei, influencing cloud cover and, subsequently, Earth albedo (Asher and Wanninkhof, 1998).

Studies estimate that oceans contribute nearly $10^{18} - 10^{20}$ bubbles per second. While seemingly abstract, these numbers underscore the sheer magnitude of the bubble-induced

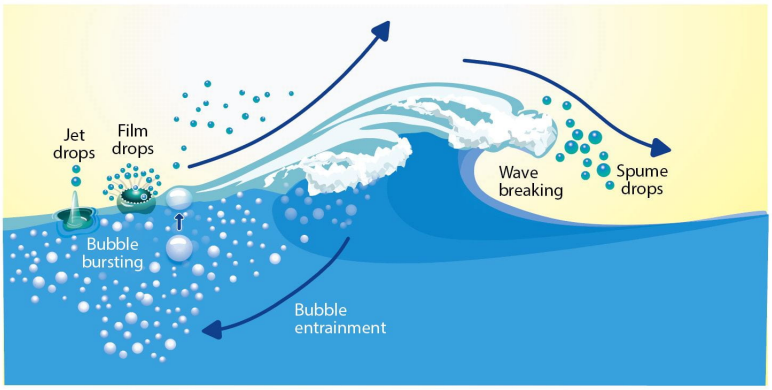

Fig. 1.1 Visualization of bubbles forming, rising, and bursting at the ocean surface. This figure has been borrowed from the work of Richter and Veron (2016).

exchange process. The bursting process of these bubbles leads to the production of sea salt aerosols, mostly through the disintegration of bubble caps into film drops and the production of jet drops (Lewis and Schwartz, 2004). These aerosols play a dual role. First, they act as cloud condensation nuclei, influencing the formation and properties of clouds, which are essential regulators of Earth's radiation balance. Second, they directly impact the climate by scattering solar radiation, thus influencing the planet's energy balance (Lewis and Schwartz, 2004).

The bubble-mediated exchange process, for instance, through the wave-breaking mechanism and the subsequent film bursting at the surface, also plays into the climate feedback loops. For instance, as global temperatures rise, increased oceanic evaporation might lead to more bubble formation by creating more extreme weather events, thus amplifying the exchange processes. While not fully understood, such a feedback loop could have profound implications for future climate scenarios (Lewis and Schwartz, 2004).

In short, the bubble bursting at the ocean surface is a linchpin in the intricate web of processes governing the climate. A comprehensive understanding of the underlying mechanisms is crucial in refining climate models and predicting future scenarios.

1.2 Bubble Bursting

The bubble-bursting process is a complex interplay of fluid dynamics, surface tension, and external factors, central to many natural and industrial phenomena (Deane and Stokes, 2002; Lhuissier and Villermaux, 2012). This section offers a holistic understanding of the bubble-bursting process from inception to its final stages.

A noteworthy component of the bubble-bursting process is the formation of film drops, a direct consequence of film bursting. As mentioned earlier, these droplets, generated from the thin liquid film of the bubble, play a crucial role in various atmospheric and oceanic processes.

To fully grasp the complexity of bubble bursting, it is essential to journey through its stages chronologically:

(i) Bubble Shape Determination: The initial shape of the bubble is dictated by a balance of forces, primarily the balance between the buoyancy force due to gravity and the surface tension force (Blanchard, 1989). The buoyancy-driven rise of the bubble, coupled with its interaction with the surrounding medium, sets the stage for subsequent processes that lead to the eventual bursting of the bubble.

(ii) Drainage: As the bubble nears the surface, the liquid film starts to drain and become thinner due to gravity. This thinning is modulated by viscosity and surfactant presence (Debrégeas et al., 1998; Lhuissier and Villermaux, 2012). The drainage process is a critical determinant of the timing of the bubble bursting, as the film must reach a critical thickness for the bursting process to initiate.

(iii) Puncture and Hole Dynamics: The puncture event, often triggered by external perturbations or film thinning, forms a hole in the bubble cap that, if sufficiently large, leads to the bursting of the film. The dynamics of this hole (mainly in the bursting condition), its growth rate, and its pattern have been the subject of numerous studies (Debrégeas et al., 1998). The hole dynamics are influenced by various factors, including the bubble size, the properties of the surrounding liquid, and the presence of surfactants (Lhuissier and Villermaux, 2012). Moreover, the underlying mechanism for hole nucleation is still not fully understood and is attributed to several possible causes, such as Marangoni effects or turbulent flow within the bubble cap. The mechanism of hole nucleation could also play a role in determining the dynamics of the hole (Debrégeas et al., 1998) by defining its initial conditions.

(iv) Film Retraction: Post-puncture, the liquid film retracts due to surface tension forces. This retraction, termed rim retraction, is pivotal in determining the size and number of resultant droplets by influencing the film disintegration process, which involves the formation of ligaments due to the Rayleigh-Plateau instability (Gilet et al., 2007).

(v) Film Disintegration into Film Drops: The retracting film eventually disintegrates, forming film drops. The size distribution and number of these drops can be influenced by various factors, including the bubble initial size and the properties of the surrounding liquid (Lhuissier and Villermaux, 2012). The size distribution of these drops is a critical

determinant of their behavior, as larger drops are more likely to be deposited back into the ocean. In comparison, smaller drops are more likely to be carried away by the wind (Lewis and Schwartz, 2004). The size distribution of these drops is also a critical factor in determining the number of cloud condensation nuclei, which influences cloud formation and properties (Lewis and Schwartz, 2004). On the other hand, the number of film drops affects the exchange rates between the ocean and the atmosphere.

Drawing connections with hole dynamics and the subsequent rim retraction or contraction could contribute to understanding the mechanisms that drive the eventual fragmentation of the film. These processes, influenced by many factors, are essential to understanding bubble and film bursting dynamics.

1.3 Hole Dynamics

1.3.1 Applications

A hole in a thin liquid film introduces an intriguing problem in fluid dynamics. A given hole, once formed, engages in a dynamic interplay that can lead to either its expansion and the eventual rupture of the film or, its closure and the healing of the film. At the heart of this phenomenon is the dominant force of surface tension, which acts as the driving mechanism orchestrating the behavior of the hole. The ability of a liquid film to autonomously heal itself by closing a hole represents not only a captivating scientific problem but also holds significance in many applications.

Thin liquid films play a pivotal role in various natural and industrial processes, from forming soap bubbles to lubricating mechanical components in nanotechnology. Understanding the dynamic behavior of these films, particularly the formation and closure of holes within them, holds profound significance in scientific research and practical applications. In the context of ocean bubbles and film bursting, gaining a comprehensive understanding of hole dynamics within thin liquid films after their nucleation plays a pivotal role in refining the modeling of the entire bursting process, ultimately influencing the production of film drops and aerosols, which in turn, impacts the rate of exchanges between the ocean and the atmosphere (Lewis and Schwartz, 2004; Smith et al., 2020).

The timing of film bursting within the lifespan of a bubble is a critical determinant of the liquid budget for drop production, as the liquid drains out of the bubble cap over time (Lhuissier and Villermaux, 2012). Although the precise mechanism governing the hole nucleation remains elusive, it is intricately linked to the subsequent development of the hole after the initial formation.

Other examples of the significance of hole dynamics include the integrity of falling films in curtain coating processes (Miyamoto and Katagiri, 1997) and the liquid-sheet-based techniques employed in spray formation (Villermaux, 2007). Moreover, from the chemical engineering and biomedical sciences point of view, the hole dynamics is essential in the study of the stability of foams and cleaning microbubbles (Laporte et al., 2016) and the fabrication of nanopores in sensors used for rapid biomolecule characterization and DNA sequencing (Storm et al., 2005).

Fabrication of nanopores for DNA sequencing is particularly intriguing, among other examples for the possible applications of studying hole dynamics, apart from the oceanic context. Storm et al. (2005) discusses a technique to fine-tune the size of nanostructures with nanometer precision where the key concept is that some holes, if small enough, contract and close. Therefore, in a controlled process in which a hole in a silicon-based sheet is slowly contracting, it is possible to stop the retraction by freezing the material at the desired size with nanometer precision.

1.3.2 Previous Works

The investigation of thin liquid films dates back to the pioneering work of Lord Rayleigh and Joseph Plateau in the late 19th century, where they explored the stability of liquid layers under various conditions and investigated the formation of liquid films. These foundational studies identified critical length scales and discussed the importance of surface tension in film stability. Subsequently, advancements in experimental techniques and theoretical models have broadened the understanding of the dynamics governing these films. Dombrowski et al. (1954) made a photographic investigation into factors such as surface tension, viscosity, and density that may impact the stability and manner of disintegration of liquid sheets produced through different apparatuses such as a nozzle source. However, these energetically charged films comprised several complex phenomena simultaneously (e.g., turbulent flow), and measurements were qualitative.

Taylor and Michael (1973) made a significant contribution by proposing an intriguing analogy between the problem of healing holes in thin liquid films and the behavior of soap films suspended between two metal rings. In this analogy, the soap film naturally assumes the shape of a catenoid. Subsequently, by analyzing the static stability of the catenoid, they presented a hole healing threshold for the geometrical ratio of the distance between the metal rings and their diameter $d_1/\delta = 1.51$, which was closely reproduced ($d_1/\delta = 1.52$) in their experiment for a soap film between two metal rings (see chapter 3, section 3.4). Accordingly, they argued that this critical ratio also determines whether a hole with maximum radius d_1 on a film of the thickness δ opens or closes. However, for the problem of holes on a free film, this healing threshold has been examined neither experimentally nor numerically.

While Taylor and Michael (1973)'s work represented a pioneering effort in understanding the dynamics of holes in thin liquid films, it is essential to acknowledge several limitations inherent to their employed approach:

- Measurement of Hole Size: One of the limitations of Taylor's model is that it derives the healing threshold based on the ring size to the ring distance ratio (δ/d_1), which corresponds to the maximum radius of the hole (d_1) in a film of thickness (δ). However, in practical experiments involving thin liquid films, measuring the maximum radius (d_1) of a hole is not feasible. Instead, the only measurable characteristic of the hole is its minimum radius (d). As a result, while valuable in the context of soap films between metal rings, Taylor's healing threshold may not directly apply to real-world thin liquid film scenarios where d is the relevant parameter.

- Assumption of Catenoid Shape: Taylor's study assumes that holes in thin liquid films naturally take on the shape of a catenoid, similar to soap films suspended between two metal rings. In reality, holes in thin films can assume various shapes depending on the specific conditions and forces at play that are linked to the nucleating mechanism. The assumption of a catenoid shape restricts the applicability of Taylor's findings to a narrow subset of possible hole geometries.

- Static Analysis: Taylor's study is primarily a static analysis of the problem, focusing on the equilibrium shape of soap films and their stability. This static approach yields a constant healing threshold value for the ratio, implying that the stability of thin liquid films is solely determined by this geometrical ratio, neglecting the dynamic aspects of hole formation, growth, and closure. In reality, the dynamics of thin liquid films are influenced by factors such as viscosity, surface tension gradients, and external perturbations. These dynamic effects can determine when and how holes form or close. Therefore, Taylor's model provides a simplified, albeit valuable, perspective on the problem by not accounting for dynamic interactions.

Since the stability of the hole is closely linked to the application for coating films, the hole dynamic on a film that lies on a substrate has been more widely studied. Taylor and Michael (1973), Sharma and Ruckenstein (1990), and Moriarty and Schwartz (1993) are some of the critical works that have been done on this problem.

In this context, while Moriarty and Schwartz (1993) only improved Taylor and Michael (1973)'s works by making a more detailed but yet static analysis, Sharma and Ruckenstein (1990) contributed to this problem by considering the dynamics of the hole. They used the finite difference method to solve a simplified version of the Navier–Stokes equation that assumes

Stokes flow as the dominant characteristic of the problem. Despite including viscosity and surface tension in their study, their work did not examine the effect of these two parameters on the healing threshold for the hole opening. Nevertheless, they observe that lowering the surface tension of the fluid may cause an otherwise closing hole to open. In this process, they also note a flickering behavior where holes could reverse their closure direction and burst. Most significantly, they discover that an increase in viscous dissipation decreases the energy budget for the hole closure, and thus, it hinders the closing of a hole.

In a more recent study by Stumpf et al. (2023), the authors conducted a static analysis focusing on the energy budget. This analysis was rooted in examining the surface area of a film with a hole, reminiscent of the approach by Taylor and Moriarty. Notably, Stumpf et al. (2023) considered a hole profile inclusive of a free rim, implying that the hole had already gathered liquid post-nucleation, ensuring volume conservation of the initial flat film. This methodology identified a critical hole size as $r/\delta \approx 2.18$, where r represents the distance from the radial axis to the center of the perceived rim rather than the smallest hole radius. When this value is adjusted based on the minimum radius, the healing threshold is determined to be $d/\delta \approx 2.74$. Moreover, they find an activation energy $\Delta\phi \approx 13.4\gamma\delta^2$ to form a spontaneously growing hole. They argue that their approach is more realistic than Taylor and Michael (1973)'s since it accounts for holes with free rims and does not insist on hole growth from an equilibrium catenoid shape that imposes zero capillary pressure.

Outside of the fluid mechanic field and from the chemical engineering and food sciences point of view, Lu and Corvalan (2015) investigated the collapse speed for holes on films with negligible viscosity and found that to be increasing. They used numerical simulations of the Navier-Stokes equations with the finite element method to explore the qualitative effects of changing the initial hole size. They also observed and pointed out the flickering behavior, as did Sharma and Ruckenstein (1990). In the same year, Lu et al. (2015) also studied viscous sheets and identified a constant collapse speed for holes, independent of the initial size and shape. They showed that viscosity effects became prominent as the hole radius approached zero. Lu et al. (2018) examined the influence of surface tension gradients on collapse speed. These gradients decreased collapsing velocity, contrary to the constant speed observed in viscous sheets. Even small amounts of surfactants were shown to alter the contraction speed significantly. Lu et al. (2019) explored the impact of shear-thinning on collapsing speed. Shear-thinning accelerated contraction due to decreasing apparent velocity near the moving front. As hole size decreased, shear-thinning effects intensified. Lu and Corvalan (2019) studied the transition between the inertial and viscous regime as the hole closes while still focusing on the speed of collapse, which followed different trends in the two regimes. They found the transitioning hole size to increase in a power-law relation with the fluid viscosity.

While Lu and Corvalan's work examined several parameters that could affect the hole dynamics, it did not investigate the effect of these parameters on the healing threshold for hole closing and opening, as the main focus of his work has been the hole collapsing speed. Moreover, despite recognizing the flickering behavior in the hole dynamic, it came short of providing a physical explanation.

1.3.3 Potentials for Contributions

The above-mentioned limitations highlight the need for a more comprehensive understanding of the hole behavior in thin free liquid films with an account for the dynamics of the problem. The present study addresses these limitations by conducting systematic investigations, accounting for dynamic factors such as viscosity and surface tension coefficient, and considering film curvature and different hole shapes, in particular, examining the possible effects of varying these parameters on the healing threshold and, if any, finding the corresponding physical explanations. By doing so, it is aimed to provide a more accurate and practical framework for understanding the behavior of holes in thin free liquid films and their response to changes in various parameters and conditions.

1.4 Thesis Outline

This thesis is organized as follows:

- Chapter 1, the present chapter, provided an introduction to the film bursting phenomenon, its significance in the ocean-atmosphere exchanges, and the role of holes in the film bursting dynamics.
- Chapter 2 first reviews the film dynamics close to the hole nucleation event to clarify the limitations of the Navier-Stokes equations employed in the present work. Subsequently, it introduces the governing equations simulated in this study. Basilisk, the numerical tool utilized in the present work, is introduced and detailed on its VoF method and adaptive meshing capabilities for enhanced accuracy and efficiency. Subsequently, the numerical configurations used in this work are introduced and described, such as flat films with holes and axisymmetric bubble caps.
- Chapter 3 studies the dynamics of hole healing on thin liquid films, highlighting the physical principles behind the hole healing phenomenon. The chapter discusses the Young-Laplace equation and its significance in determining capillary pressure due to surface tension. The chapter derives a capillary pressure profile for half-torus holes on

films using this foundation. Preliminary simulations are conducted, offering insights into the dynamics of the problem. A hypothesis is postulated with these observations and the analytical expression for the film mean curvature. This hypothesis aims to determine the hole healing threshold, primarily focusing on a static examination of the initial capillary pressure field for holes of half-torus shape. The hypothesis is tested against numerical results obtained through a dichotomy process with high precision. Furthermore, two other hole shapes are examined. Namely, the developed rim inspired by Stumpf et al. (2023), and the catenoid inspired by Taylor and Michael (1973). The chapter concludes by examining Taylor and Michael (1973)'s work.

- Chapter 4 examines the critical dynamics of the divergent outcomes of two near-identical simulations, focusing on two hole sizes immediately to the hole healing threshold. Critical moments in hole dynamics are pinpointed by analyzing the radial position of the tip, its temporal derivatives, film interface snapshots, pressure fields, and velocity vectors. Comprehensive insights are gained by studying the temporal and radial evolution of the hole tip curvature and its components. Distinct power laws are identified for the tip curvature, leading to the identification of a critical radial distance r_{ex}, upon reaching which the hole cannot retract back.

- Chapter 5 examines the variations in the hole healing threshold with other parameters of the problem in the case of a flat film using numerical simulations and a dichotomy process. These results are first presented and then discussed in detail to provide insights into the dynamics of the problem. The chapter concludes by analyzing the initial hole shape to examine whether the dichotomy results are independent of the arbitrary choice.

- Chapter 6 examines the bubble dynamics along with the associated gas outflow after the hole nucleation, identifying the factors influencing the gas outflow, such as the gas density. The shrinkage of the bubble is also examined. The chapter concludes by examining the velocity and pressure profiles of the gas outflow at the minimum cross-section area of the hole, leading to the discovery that the gas outflow undergoes a Venturi effect, predictable by Bernoulli's principle.

- Chapter 7 examines the effect of the film curvature on the hole healing threshold with a focus on the Venturi effect. The dichotomy results are first presented and then discussed in detail to provide insights into the dynamics of the problem. The chapter concludes by developing a hypothesis to predict the Venturi effect on the healing threshold, resulting in a Venturi correction term that is tested against numerical results.

- Chapter 8 summarizes and discusses the key findings of this work and provides suggestions for future works.

Chapter 2

Numerical Method

2.1 A Review on Film Rupture

The dynamics of a thin liquid film close to the puncture event (i.e., hole creation) are affected both by the fluid dynamical mechanisms and molecular physics. The fluid dynamics of the problem, governed by the Navier-Stokes equations, do not allow a thinning liquid film to rupture, even as the film thickness δ becomes infinitesimally small $\delta \to 0$. However, as the film thickness decreases, the Navier-Stokes equations are no longer able to describe the dynamics as the molecular physics of the problem becomes more critical.

The rupture of thin liquid films can be induced by several mechanisms, often influenced by the interplay of various forces at the molecular level. Here are several mechanisms that can cause thin liquid films to rupture (Lhuissier and Villermaux, 2012; Yu et al., 2023):

- **Van der Waals Forces:** These forces can induce attractive forces between molecules across the film, leading to instability and rupture in very thin films, typically in the nanometer range.
- **Capillary Pressure:** Differences in capillary pressure, arising from variations in curvature, can lead to the thinning and eventual rupture of the film.
- **Marangoni Effect:** Gradients in surface tension due to temperature or concentration differences can result in fluid flow within the film, leading to thinning and rupture in certain regions.
- **Gravity-Driven Drainage:** The action of gravity can lead to the liquid draining from the upper parts of the film, causing the thinning and rupture of elevated regions of the film.
- **Electrostatic Forces:** Repulsive electrostatic forces between like-charged regions within the film can lead to instabilities and the rupturing of the film.

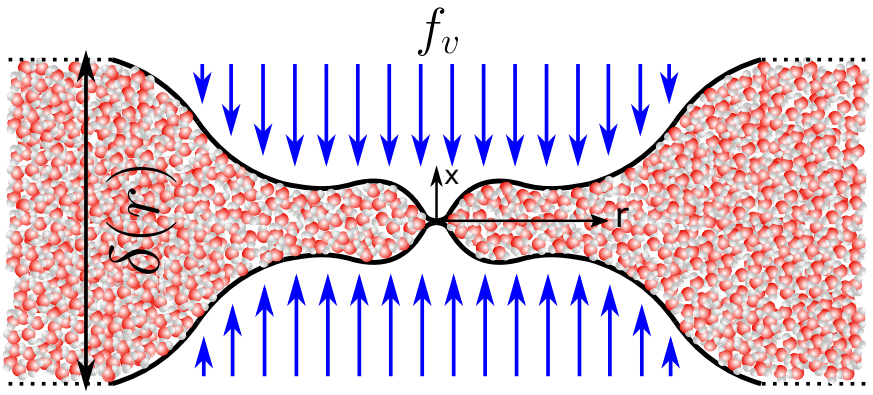

Fig. 2.1 A descriptive scenario of the normal stresses acting on the opposing surfaces of a thin liquid film with thickness inhomogeneities that could engage van der Waals forces (f_v) in the rupture process. $\delta(r)$ represents the film thickness as a function of radial distance for a hypothetical and axisymmetric hole.

- **Thermal Fluctuations:** These can cause variations in film thickness, leading to the formation of thin spots that can rupture under the influence of disruptive forces.
- **Evaporation:** The removal of the liquid phase through evaporation can also result in the thinning and eventual rupture of the film, especially in volatile solvents exposed to ambient conditions.
- **External Stress or Impact:** Physical stress, such as shear or impact from an external object, can cause the rupture of the film.
- **Osmotic Pressure:** Differences in solute concentration can generate osmotic pressure differences, leading to fluid flow and thinning of the film, potentially causing rupture.
- **Surfactant Depletion:** The depletion or uneven distribution of surfactants can cause instability and rupture of the film due to differences in surface tension.

Nonetheless, a majority of these mechanisms can only cause thickness inhomogeneities and thinning of the liquid film in such a way that it would create a shear stress within the liquid film. On the other hand, in order for the two opposing surfaces of the film to meet and break, the presence of normal stress is necessary to act on the two liquid surfaces, as illustrated in figure 2.1.

While gravity-driven drainage and evaporation can continuously decrease the overall thickness in the film, several mechanisms are known to introduce thickness inhomogeneities on the bubble cap as it is draining, including the Marangoni effect, impurities within the film, and marginal regeneration flow. Therefore, one possibility is that the actual film puncture, that is, the breakage of the two interfaces, occurs through the engagement of the molecular forces.

For a liquid film of thickness δ between parallel surfaces, the intermolecular attractive van der Waals force between the two surfaces is generally effective only up to several hundred angstroms or becomes especially relevant when the thickness of a liquid film reaches below 10 nanometers. In thin films of such dimensions, molecules of the opposing surfaces are close enough to experience significant intermolecular interactions that could rupture the film in an interplay with the opposing forces that become relevant at such scales.

Van der Waals attraction forces, noted by f_v in figure 2.1, can puncture the film not only for film thicknesses of an average below $10nm$, but also in thicker films and within areas where the local microscopic patches of inhomogeneities in the film thickness allows the intermolecular forces to be relevant. Such a hypothesis cannot be experimentally verified due to the spatial scales of the hole puncture and time scales involved in a bursting event. Therefore, to further understand the intricacies of film rupture, there is a pressing need for advancement in high-resolution experimental devices capable of capturing the fine-scale dynamics at the moment of puncture with higher frame rates.

Nevertheless, it is often reported through experimental studies that, for instance, surface bubbles supposedly rupture at thicknesses much higher than the effective thickness of van der Waals forces. Therefore, the rupture of thin liquid films is a complex phenomenon that is not fully understood. At the same time, several mechanisms are recognized that can induce the rupture of thin liquid films, either as a result of the interplay of different forces at the molecular scale or the fluid dynamics at a larger scale.

2.2 Governing Equations

This work examines various two-phase flow configurations, with a central emphasis on understanding the hole dynamics on a liquid film after the hole puncture. The main configurations studied include:

- holes on flat films, with several possibilities for the hole shapes
- axisymmetric spherical bubble cap with a hole

The equations that govern these configurations are detailed as follows.

The dynamics of a thin liquid film near the puncture event and hole creation are influenced both by fluid dynamical mechanisms and molecular physics, as discussed in the previous section. While in the Navier-Stokes equations, van der Waals forces could potentially be incorporated into the momentum equation as a potential akin to gravity, in smoothed particle hydrodynamics, a more natural representation includes applying a surface force $\mathbf{f}_v$ to the outermost layer of fluid

particles, directing them towards the opposite interface. For instance, Xu et al. (2020) employed a van der Waals force model to simulate the rupture of a thin liquid film on a substrate.

However, in the present work, the focus is on the dynamics of the hole after its nucleation and the subsequent healing or bursting process. Therefore, the molecular physics of the problem is not considered in the governing equations. Consequently, the dynamics of the film are studied by simulating the incompressible and variable-density Navier-Stokes equations that include surface tension. The equations presented here are recognized as the momentum equation, continuity or mass conservation equation, and volume conservation equation. They are expressed as follows:

$$\rho\left(\partial_t \boldsymbol{u} + \boldsymbol{u}\cdot\boldsymbol{\nabla}\boldsymbol{u}\right) = -\boldsymbol{\nabla}p + \boldsymbol{\nabla}\cdot(2\mu\boldsymbol{D}) + \boldsymbol{f}_\gamma + \rho\boldsymbol{g} \tag{2.1}$$

$$\partial_t \rho + \boldsymbol{\nabla}\cdot(\rho\boldsymbol{u}) = 0 \tag{2.2}$$

$$\boldsymbol{\nabla}\cdot\boldsymbol{u} = 0 \tag{2.3}$$

In these equations, $\boldsymbol{u} = (u,v,w)$ represents the fluid velocity; $\rho \equiv \rho(\boldsymbol{x},t)$ denotes the fluid density; $\mu \equiv \mu(\boldsymbol{x},t)$ symbolizes the dynamic viscosity; $\boldsymbol{D}$ signifies the deformation tensor, defined as $D_{\mathrm{ij}} \equiv \left(\partial_i u_j + \partial_j u_i\right)/2$; $\boldsymbol{f}_\gamma$ is the surface tension force per unit volume; and $\boldsymbol{g}$ the acceleration of gravity vector (Popinet, 2009).

Since surface tension acts only at the free surface of the fluid, $\boldsymbol{f}_\gamma$ is found based on the Young-Laplace equation (see equation 3.5) by

$$\boldsymbol{f}_\gamma = \gamma\kappa\delta_s\boldsymbol{n} \tag{2.4}$$

where κ is the interface curvature, n the unit normal, s the curvilinear coordinate, and δ_s a surface Dirac δ-function, which is zero everywhere except on the interface (Popinet, 2018).

In the context of two-phase flows, the introduction of the volume fraction $F(x,t)$ for the liquid phase is followed by the definition of density and viscosity using the arithmetic mean as such:

$$\rho(\tilde{F}) \equiv \tilde{F}\rho_l + (1-\tilde{F})\rho_g \tag{2.5}$$

$$\mu(\tilde{F}) \equiv \tilde{F}\mu_1 + (1-\tilde{F})\mu_2 \tag{2.6}$$

Here, ρ_l and ρ_g represent the densities of the liquid and gas phase, respectively [1], and μ_l and μ_g represent their respective viscosities. The field $\tilde{F}$ can either be identical to F or can be constructed by applying a spatial smoothing filter to F. Subsequently, the advection equation governing density can be substituted with an analogous advection equation governing the

[1] Or alternatively, fluid one and two.

volume fraction F.

$$\partial_t F + \nabla \cdot (F\boldsymbol{u}) = 0 \tag{2.7}$$

Alternatively, one may consider employing the harmonic mean instead of the arithmetic mean in equations 2.27 and 2.28. If this approach is chosen, the density and viscosity can be expressed as follows:

$$\rho(\tilde{F}) \equiv \frac{\rho_l \rho_g}{\rho_g \tilde{F} + (1-\tilde{F})\rho_l} \tag{2.8}$$

$$\mu(\tilde{F}) \equiv \frac{\mu_1 \mu_2}{\mu_2 \tilde{F} + (1-\tilde{F})\mu_1} \tag{2.9}$$

2.2.1 Additional Remarks

The choice between using the arithmetic and harmonic means in simulations holds significant implications for the accuracy of the results. Neither of these methods can be universally deemed superior, as the optimal choice depends on various parameters specific to the simulations. Of paramount importance are the ratios of specific properties, namely ρ_l/ρ_g and μ_l/μ_g, as well as the mesh cell size containing the interface, as detailed in Quan and Schmidt (2007). In cases where the less viscous fluid is expected to have minimal impact, Tryggvason et al. (1998) employed the arithmetic average for interface viscosity but opted for the harmonic mean when this was not the case. It should be underscored that the method selection for calculating the mean of these properties, $\rho(\tilde{F})$ and $\mu(\tilde{F})$, are determined independently. In the present work, the harmonic mean is used for both density and viscosity, as it was found to be more stable in the simulations carried out.

Lastly, one could note the possibility of using lubrication equations, resulting in a much simpler set of partial differential equations than the full Navier-Stokes. Many studies have used the lubrication assumption to study thin liquid films on a substrate theoretically and numerically (see Moriarty and Schwartz, 1993; Witelski and Bernoff, 2000). Nonetheless, owing to inherent constraints within the lubrication approximation, the lubrication model cannot simulate the dynamics of closing holes. For instance, the primary assumption of this model, which is that film thickness is much smaller than its length and width, breaks down close to the hole. Therefore, to study the hole dynamics on thin films accurately enough to examine the hole healing threshold, it is necessary to simulate the full Navier-Stokes equations described in this section.

2.2.2 Non-dimensionalisation

There are nine physical variables involved in the problem of a hole on a bubble cap, namely, $\boldsymbol{g}, \rho_l, \rho_g, \mu_l, \mu_g, \gamma, \delta, d, d_b$, where the subscript l and g refer to the film and gas, respectively. This number is reduced to seven for a hole on a flat film as $d_b \to \infty$. Applying the Buckingham theorem, one could find that there are $9-3=6$ dimensionless parameters governing the problem independently, where there are three physical dimensions: length, mass, and time.

In the present work, the governing dimensionless parameters are selected to be the hole size d/δ, film Laplace number

$$\mathrm{La}_l = \rho_l \delta \gamma / \mu_l^2, \tag{2.10}$$

gas Laplace number

$$\mathrm{La}_g = \rho_g \delta \gamma / \mu_g^2 \tag{2.11}$$

The Bond number using the hole size

$$\mathrm{Bo}_h = \frac{\rho_l g d^2}{\gamma}, \tag{2.12}$$

density ratio $\rho_{l/g} = \rho_l/\rho_g$, and bubble size (or cap curvature) d_b/δ. Therefore, the healing threshold d^{*c}, or the critical value for d/δ below which holes would close instead of opening, must be a function of the other five parameters. In other words,

$$d^{*c} = f(\mathrm{La}_l, \mathrm{La}_g, \mathrm{Bo}_h, \rho_{l/g}, d_b/\delta) \tag{2.13}$$

The Laplace number, La, compares surface tension effects with viscosity in a given fluid phase. The Laplace number is similar to the Reynolds number except that the velocity scale U in

$$\mathrm{Re} = \rho \delta U / \mu \tag{2.14}$$

is replaced with the visco-capillary velocity

$$U_{vc} = \gamma/\mu \tag{2.15}$$

resulting in $\mathrm{La} = \rho\delta\gamma/\mu^2$. Alternatively, in the literature, Ohnesorge Oh is used as well to describe the same comparison of effects with

$$\mathrm{Oh} = 1/\sqrt{\mathrm{La}} \tag{2.16}$$

Employing this selection of governing parameters, the viscosity ratio $\mu_{l/g}$ while not selected as a governing parameter, is accessible by

$$\mu_{l/g} = \sqrt{\frac{\rho_{l/g}\mathrm{La}_g}{\mathrm{La}_l}} \tag{2.17}$$

By considering a characteristic length equal to the thickness of the film δ, the inertia-capillary velocity, also known as Taylor-Culick velocity, and the inertia-capillary time scale of the problem, is found to be

$$U_{ic} = U_{tc} = \sqrt{\gamma/\rho\delta} \tag{2.18}$$

and

$$\tau_{ic} = \sqrt{\rho\delta^3/\gamma} \tag{2.19}$$

respectively. Considering the visco-capillary time scale

$$\tau_{vc} = \mu\delta/\gamma, \tag{2.20}$$

the Ohnesorge Number can, therefore, be understood as the ratio of visco-capillary to inertia-capillary time scales

$$\mathrm{Oh} = \tau_{vc}/\tau_{ic}. \tag{2.21}$$

Similarly, for the Laplace number it can be expressed using these time scales that

$$\mathrm{La} = (\tau_{ic}/\tau_{vc})^2 \tag{2.22}$$

Employing these scales, in addition to

$$P = 2\gamma/\delta \tag{2.23}$$

for the characteristic value of pressure, one can form

$$\boldsymbol{u}^* = \boldsymbol{u}/U_{ic},\ p^* = p/P,\ t^* = t/\tau_{ic},\ \boldsymbol{\nabla}^* = \delta\boldsymbol{\nabla},\ \kappa^* = \delta\kappa,\ \delta_s^* n = \delta\delta_s n,\ \partial_t^* = \tau_{ic}\partial_t$$

based on which the governing equations 2.1, 2.2, and 2.3 can be non-dimensionalized and written in a general form that includes gravity as

$$\partial_{t^*}\boldsymbol{u}^* + \boldsymbol{u}^*.\boldsymbol{\nabla}^*\boldsymbol{u}^* = -\boldsymbol{\nabla}^* p^* + \frac{1}{\sqrt{\mathrm{La}}}\boldsymbol{\nabla}^{*2}\boldsymbol{u}^* + \kappa^*\delta_s^* n + \mathrm{Bo}\frac{\boldsymbol{g}}{g} \tag{2.24}$$

$$\partial_{t^*}\rho + \boldsymbol{u}^*.\boldsymbol{\nabla}^*\rho = 0 \tag{2.25}$$

$$\nabla^* . \boldsymbol{u}^* = 0 \tag{2.26}$$

along with the arithmetic means for density and viscosity values

$$\rho(\tilde{F}) \equiv \tilde{F} + (1-\tilde{F})\rho_{l/g} \tag{2.27}$$

$$\mu(\tilde{F}) \equiv \tilde{F} + (1-\tilde{F})\sqrt{\frac{\rho_{l/g}\mathrm{La}_g}{\mathrm{La}_l}} \tag{2.28}$$

Additionally, it is essential to mention that gravity, effects of which are presented by the Bond number based on the characteristic length of the hole Bo_h, could be omitted from the momentum equation 2.1 when studying the hole dynamics. This exclusion is attributed to the disparate time scales on which gravity operates

$$\tau_{gr} = \sqrt{\frac{c}{g}} \tag{2.29}$$

compared to the time scales of the dynamics of hole opening and closing, τ_{ic}, regulated by surface tension and inertia (or τ_{vc} if more influenced by surface tension and viscosity and resulting in Galilei number $Ga^2 = g\delta^3/\gamma^2$ instead of the Bond number). In other words, for $\mathrm{Bo}_h = \tau_{ic}/\tau_g \ll 1$ the gravity term could be safely omitted from the momentum equation 2.1 and the set governing parameters given by 2.13 reduces to

$$d^{*c} = f(\mathrm{La}_l, \mathrm{La}_g, \rho_{l/g}, d_b/\delta) \tag{2.30}$$

The above equations will be incorporated into our numerical tool, Basilisk, to simulate varying configurations. Basilisk and its associated processes are outlined in the subsequent sections, with details related to the numerical configuration following after that. These elaborations aim to clarify the application and implications of these equations in our numerical experiments and simulations, the results of which are discussed in the subsequent chapters.

2.3 Numerical Tool

2.3.1 Basilisk

To simulate the problem numerically, Basilisk (see Popinet, 2009) that has been improved upon its predecessor, Gerris (see Popinet, 2003), is used to solve the two-phase incompressible Navier-Stokes equations of 2.25, 2.24, and 2.26. Basilisk is an open-source software program written as a variant of C programming language for the solution of partial differential equations.

Basilisk employs the volume-of-fluid (VoF) method to track the interface on a Quad/Octree structured grid, allowing adaptive mesh refinement based on a criterion of wavelet-estimated discretization error, which is pivotal for capturing the evolution of complex fluid interfaces with high precision. This refinement/coarsening ensures optimal allocation of computational resources, leading to high-fidelity simulations of fluid interfaces and surface tension-driven flows with relatively low computational costs. This solver ensures the conservation of mass and momentum even amidst topological transformations such as merging and pinching. Basilisk code has been validated through numerous studies, demonstrating its ability to resolve intricate fluid mechanics problems (see basilisk.fr).

The corresponding finite-volume spatial discretization in Basilisk is a partitioning where all variables are collocated at the center of squared cells in 2D or cubes in 3D settings. For each cell, a calculation is made of the elements entering and leaving the cell while the cell remains stationary. In this approach, F, introduced to distinguish between the liquid and gas phases during the formulation of the Navier-Stokes equations, is discretized on each cell in the mesh and is represented by f. The scalar field conveys the volume fraction of the liquid phase present in each cell. Here, a value of $f = 0$ is indicative of a pure gas cell, $f = 1$ denotes a pure liquid cell, and an intermediate value of f corresponds to a cell that is intersected by an interface, with the value specifying the percentage of liquid in the cell. Each cell in the mesh is analyzed for the quantities entering and leaving, ensuring precise representation and analysis of fluid dynamics and interactions within the system.

Basilisk utilizes a piecewise-linear geometrical VoF method for solving equation 2.26 and employs an implicit scheme for the time advancement of the viscous term in the momentum equation 2.24. The advection equation 2.7 is resolved using the Bell-Colella-Glaz algorithm, and incompressibility is maintained through a projection technique at the end of each time step. A multigrid solver, with an adjustable relative tolerance (set to 10^{-4} in this work, unless specified otherwise), is used to solve the heat equation and the Poisson equation arising from the implicit treatment of viscous terms and from the projection technique, ensuring the satisfaction of the incompressibility condition (Popinet, 2009, 2018).

2.3.2 Interface Reconstruction and Transport

To numerically solve the two-phase Navier-Stokes equations, the position of the interface must be determined. Basilisk achieves this by reconstructing the interface position from the volume fraction, f. This process involves using the volume concentration in neighboring cells to create a piecewise continuous interface. This method is advantageous as it quickly resolves the position of the interface using only the eight cells surrounding the working cell. The interface reconstruction method applied by Basilisk is based on an algorithm developed

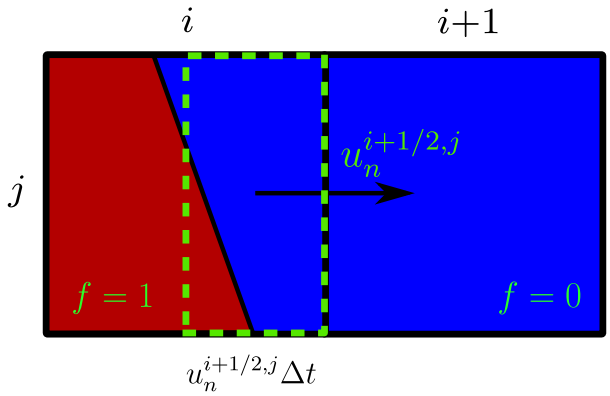

Fig. 2.2 Illustration of the interface transport method in Basilisk, showing the geometric flux estimation from one cell to another. The figure depicts a cell (i, j) with a known volume fraction $0 < f < 1$ and interface position, showing the calculation of outgoing liquid flow to the neighboring cell $(i+1)$ based on the velocity between them $u_n^{i+1/2,j}\Delta t$.

by Scardovelli and Zaleski (1999), which enables the determination of the orientation of the interface normal from the volume concentration in the surrounding cells. Once the interface normal is obtained, the line segment defining this interface is positioned such that the resulting fluid volume fraction matches the value of f in the cell.

To trace the evolution of the interface position between the two fluids, estimating the quantity of fluid transferring from one cell to another is necessary. Using a material balance involving the initial quantity, the volume fraction in a given cell (i, j), the inputs, and the outputs at time step n, the volume fraction at step $n+1$ can be calculated by

$$f_{n+1}^{i,j} V_{n+1}^{i,j} = f_n^{i,j} V_n^{i,j} + \phi_n^{i-1/2,j} - \phi_n^{i+1/2,j} + \phi_n^{i,j-1/2} - \phi_n^{i,j+1/2} \tag{2.31}$$

where V corresponds to the volume of a cell, $V = \Delta^2$ in 2D, and ϕ to the liquid flow between two cells.

Once interfaces are reconstructed, the flow between the cells at step $n+1$ can be estimated. Figure 2.2 illustrates the sketch for the liquid transport from one cell to another. The volume fraction f in cell i, j and the position of the interface are known parameters. From the relative velocity between cell i and cell $i+1$ (denoted here as $u^{i+1/2,j}$), the outgoing liquid flow from the cell is estimated. This is represented by defining a rectangle with length Δ, corresponding to the length of the cell, and width $u_n^{i+1/2,j}\Delta t$. Everything within this rectangle is transported to cell $i+1$.

2.3.3 Surface Tension Calculations

The interface reconstruction method utilized for fluid transport cannot be employed for evaluating surface tension due to its lack of precision. As discussed by Popinet (2009), a second derivative of the interface position is essential to determine the radii of curvature accurately. To enhance accuracy and obtain the best possible approximation of curvature, height functions are introduced in each spatial direction, denoted as h_x and h_y (and h_z in 3D). For a cell i, their values are determined by the volume fraction field as follows:

$$\Delta\bar{h}_i = \int_{x_{i-1/2}}^{x_{i+1/2}} h_i(x)dx = \sum_{j=-\infty}^{j=\infty} f_{i,j} + \text{ constant} \tag{2.32}$$

where $\bar{h}_i$ represents the average height function value in cell i, and the sum is performed over an entire column of cells ($j = \infty$). Using the calculated values for $\bar{h}_i$, the interface curvature can be determined by

$$\kappa = \frac{h_y''}{\left(1 + h_y'^2\right)^{3/2}} \tag{2.33}$$

Using the centered spatial discretization, the expression 2.33 becomes

$$\kappa_i = \frac{\frac{h_{i-1}^- - 2\bar{h}_i + h_{i+1}^-}{\Delta^2}}{\left(1 + \left(\frac{h_{i+1}^- - h_{i-1}^-}{2\Delta}\right)^2\right)^{3/2}} \tag{2.34}$$

However, interface reconstruction accuracy also depends on the mesh resolution. This relationship is illustrated in Figure 2.3, where it is qualitatively evident that an increase in cell size leads to a corresponding increase in error.

2.3.4 Mesh Adaptation

One of the standout features of Basilisk is its adaptive meshing capability, enabling it to yield highly precise results while optimizing computational resources. In Basilisk, every mesh cell can be broken down into four smaller cells in 2D, or eight in a 3D setting at each time step. Figure 2.3 illustrates the mesh adaptation in Basilisk, where level one in the mesh refinement corresponds to a cell as large as the entire numerical domain, and level three is the highest level of the mesh resolution. In the example shown in figure 2.3, there are ten cells in total, while without the Basilisk mesh adaptation, this number would increase to 64. Therefore, the mesh adaptivity is particularly advantageous for multi-scale simulation processes, such as the bubble

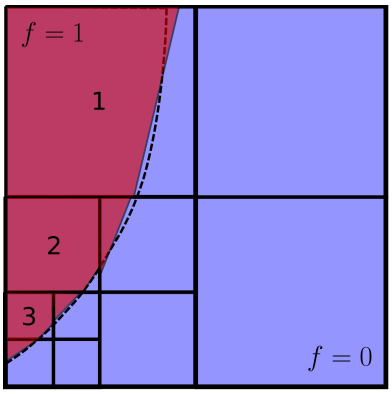

Fig. 2.3 Illustration of Basilisk adaptive meshing, for a hypothetical example with level one as the entire domain and level three as the highest resolution, reducing cell count from 64 to 10, emphasizing its utility in multi-scale simulations. It also underscores the surface reconstruction error for larger mesh cells, stressing the need for optimal mesh resolution for accurate interface reconstruction.

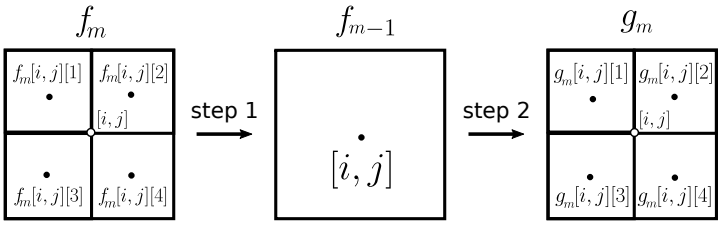

Fig. 2.4 Depicting the mesh refinement and coarsening process in Basilisk, revealing how a coarsened field f_{m-1} is derived from the scalar field f_m by averaging values at the mesh level m, and converting it back to a refined filed g_m using linear extrapolation to estimate the refinement error $\chi = |f_m - g_m|$.

burst scenario discussed in our study, where the film thickness is much smaller than the bubble size at bursting.

The refinement or coarsening of the mesh is influenced by various physical criteria set by the user and was introduced by Popinet (2003). Moreover, a detailed review was later done by van Hooft et al. (2018) on the basilisk mesh adaptivity. Nevertheless, only a summary of this method in a 2D setting will be discussed in the following.

Given the scalar field f_m, where m indicates the maximum level of mesh refinement in the grid that constructs the scalar field f, the mesh adaptation method begins by constructing a coarsened field f_{m-1} based on f_m. This process, which is depicted by figure 2.4, is done by averaging each of four values of f_m at the mesh level m and assigning the result to the parenting cell (one level lower in mesh resolution) at the center of f_{m-1} simply by using

$$f_{m-1}[i,j] = \sum_{k=1}^{4} \frac{f_m[i,j][k]}{4} \tag{2.35}$$

In expression 2.35, k indicates the number of the four children cells of the resolution m in the parent mesh cell with resolution $m-1$, which is also illustrated in figure 2.4. From this coarsened field f_{m-1}, a refined field g_m is constructed. These refined values are found through a linear interpolation.

Having calculated g_m, which has the same mesh resolution as the initial field f_m, a deciding parameter χ that measures the absolute error between the original field and the reconstructed one is calculated through

$$\chi_m = |f_m - g_m| \tag{2.36}$$

This error is then compared with the refinement criterion ζ to determine whether the mesh is good, too fine, or too coarse. Given the value of $\chi_m[i,j]$, the mesh at $[i,j]$ is too coarse if $\chi_m[i,j] > \zeta$, too refined if $\chi_m[i,j] < 2/3\zeta$, and good provided that $2/3\zeta \leq \chi_m[i,j] \leq \zeta$.

The refinement criterion ζ is user-defined and based on arbitrary scalar fields set by the user. In simulations of the present work, four scalar fields, $f, u, v,$ and$p$, are examined in the mesh adaptation process with the corresponding refinement criterion $\zeta_f = 10^{-12}$, and $\zeta_u = \zeta_v = \zeta_p = 10^{-4}$, unless mentioned otherwise. This means that, for instance, the mesh is refined or coarsened until the error $2/3\zeta_f \leq \chi_m[i,j] \leq \zeta_f$. Therefore, the mesh is adapted as described above, using the `adapt_wavelet()` function, and according to the error in interface, velocity, and pressure field. The entire process ensures there is never more than one level of difference between two neighboring cells.

While highly effective, the method of mesh adaptation in Basilisk requires prudent constraint to prevent initialization failures due to excessive cell production and maintain interface integrity by avoiding excessive coarsening of the grid in critical areas. For example, virtually singular points on the interface slope or curvature or in the velocity field could prompt the method to refine the mesh persistently, never fulfilling the error criterion.

To avoid excessive mesh refinement, which can lead to a initialization failure and an increase in computational cost, it is crucial to judiciously set a global maximum and a minimum level for mesh adaptation, ensuring optimal balance between precision and computational efficiency, particularly in instances where such singular points might provoke incessant refinement.

Figure 2.5 shows two simulations. Sub-figure a) and b) correspond to a simulation of a doughnut shape[2] with the maximum mesh level of 16. In contrast, sub-figure c) and d) correspond to the same simulation but with a maximum mesh level of 5.

In both these simulations, the refinement criterion is set to $\zeta = 10^{-2}$ for scalar fields $f, u, v,$ and p to ensure having the same refinement criterion while avoiding crashing the simulation due to the high number of cells in the case with the high maximum level. Considering the color maps of the mesh refinement level for these two simulations given in sub-figure b) and d),

[2]The axisymmetrical condition is applied to the numerical configuration.

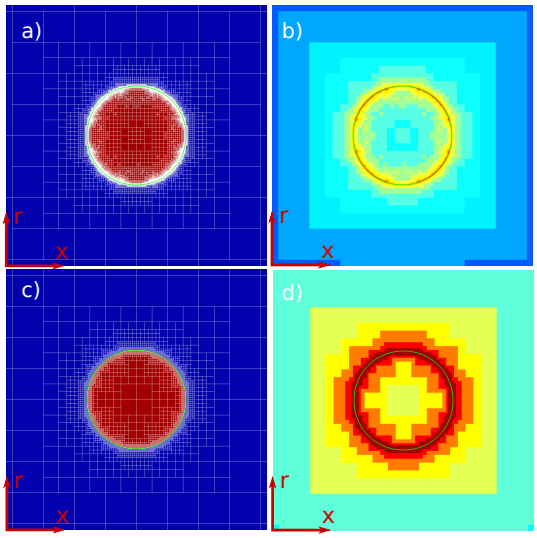

Fig. 2.5 Comparison of simulations of a doughnut shape under axisymmetrical conditions applied around the x-axis with varying mesh levels. Sub-figures a) and b) feature a detailed representation with a mesh level of 16, while c) and d) illustrate the same scenario at a coarser mesh level of 5, highlighting the saturation problem. The doughnut shape is represented by a circle with a radius of $0.1L$ where $L = 8.55$ is the domain size, under axisymmetrical conditions applied around the x-axis.

it can be observed that the mesh is saturated at its highest level when the maximum mesh level is set too low. This saturation indicates that the problem might not be numerically converged, provided the refinement criterion ζ is set properly and not too low. On the other hand, a high maximum level, even though relieving this problem, exponentially increases the computational cost. This issue is shown in figure 2.6, where the exponential expression $\text{cells} = 1.05 \times 2^{\text{level}^{1.13}}$ closely fits the increase in the number of mesh cells.

Therefore, depending on the specific case study, the maximum level of mesh refinement should be determined based on its incremental impact on simulation results, ensuring any increase beyond this point yields minimal effect on the outcomes while minimizing the computational cost. On the other hand, the size of the smallest cell in the domain must be set to so that the smallest cell size could capture the features of the problem accurately. This value is found using

$$\Delta_{\text{min}} = \frac{L}{2^{\text{GML}}} \tag{2.37}$$

where GML is the global maximum level for mesh refinement in the quadtree grid or the maximum number of divisions that the solver is allowed to make on the domain of size L. Specific values and the rationale behind their selection will be discussed further in the numerical convergence section in appendix A.

Nevertheless, the general value for GML when studying the hole dynamics on films has been set so that for each case, the maximum mesh level within the initial film thickness (FML)

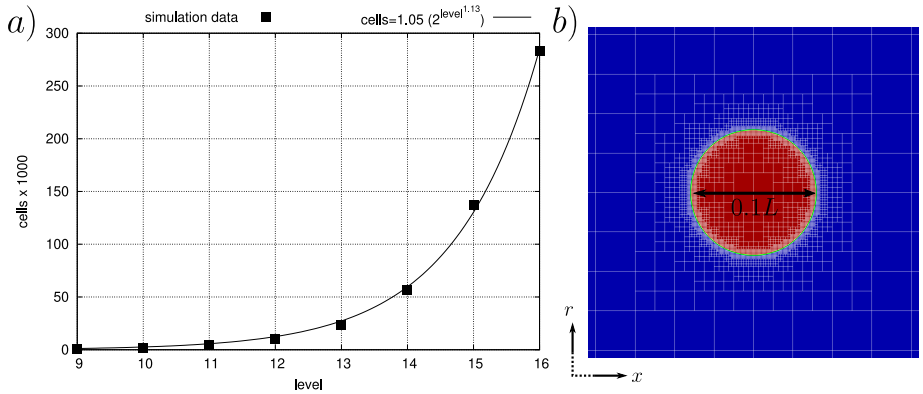

Fig. 2.6 Depiction of the exponential relation between mesh refinement level and cell count in Basilisk, illustrating the compromise between avoiding mesh saturation and managing computational costs. The figure underscores the precision of the exponential expression cells $= 1.05 \times 2^{\text{level}^{1.13}}$ in estimating the increase in the number of mesh cells with refinement levels. (b) The numerical configuration used to generate the data points in (a) is presented using the fraction field color map. The doughnut shape is modeled using a circle with a radius of $0.1L$ where $L = 8.55$ is the domain size, under axisymmetrical conditions applied around the x-axis.

is *seven* levels, unless mentioned otherwise. In the simulations, FML is used instead of GML to ensure the same resolution (i.e., the same value for Δ_{min}) between different cases where the size of the domain L could be different.[3] Appendix B provides more information on the determination of the domain size for the simulations and its possible effects on the hole dynamics.

The plot in figure 2.6 also illustrates how the Basilisk mesh adaptation application significantly reduces computational time. For example, taking the maximum refinement level of 12 results in 10360 cells for this particular configuration, while a uniform mesh grid requires 2^{12^2} or 17 million cells. As the requirement for the smallest mesh cell becomes more strict (i.e., higher mesh refinement), the mesh adaptivity feature becomes more beneficial. Even more important is the number of dimensions involved in the problem since the number of mesh cells in a uniform grid is given by

$$2^{\text{level}^{\text{dimensions}}} \tag{2.38}$$

Comparing expression 2.38 with the exponential fit found in figure 2.6, one can deduce that the mesh adaptivity lowers the effective dimension of the problem. In contrast, the dimension reduction has a maximum. Therefore, the number of mesh cells in an adaptive grid can be found by using

$$2^{\text{level}^{(\text{dimensions}-\text{CAM})}} \tag{2.39}$$

[3]The domain size is different between different cases, particularly when studying the hole dynamics on a bubble cap.

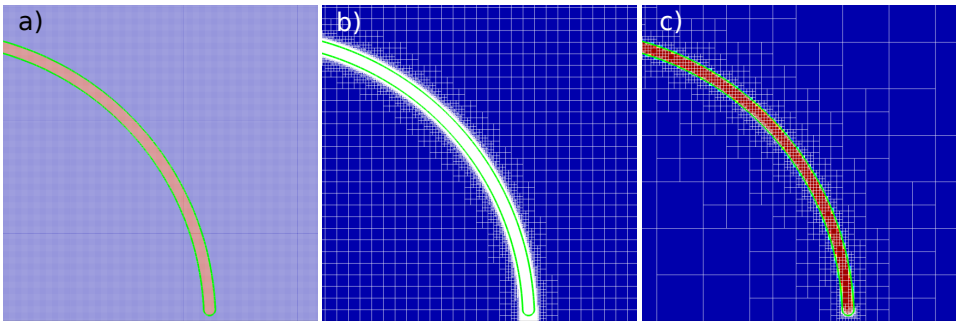

Fig. 2.7 Comparison of three fraction initialization approaches. Case a) utilizes a fine uniform grid resulting in approximately 4.2 million mesh cells; case b) employs selective refinement area near the interface, reducing the count to 67,000 cells; and case c) leverages the `adapt_wavelet()` function for optimal accuracy with about 2500 cells. In case a) the line width of the mesh cells has been decreased substantially due to the much higher number of cells that would otherwise render the figure completely white

where CAM is the coefficient of mesh adaptation that depends on the numerical configuration of the problem. In the test example above, CAM was found to be 0.87.

2.3.5 Fractions Initialization

To initialize a simulation in Basilisk, the fractions of the two fluids must be created using the `fraction()` function in Basilisk. This function requires to be provided with the geometrical definition of the liquid phase fraction (i.e., $f = 1$), which is as accurate as the mesh grid on which the geometry is defined at $i = 0$. A crude approach is to initialize the problem with a fine uniform grid or, more efficiently, a grid that is only refined near the interface geometry of the fractions. However, this approach could lead to the simulation crashing at the initialization if the maximum mesh level in the program is set to high.

To avoid this problem while maintaining the desired maximum mesh level, one could use the `adapt_wavelet()` function in a loop, starting from the coarse grid and measuring the error difference of the given geometry between each iteration so that the loop stops when further refinement does not make a noticeable difference in the fractions accuracy. Figure 2.7 shows the differences in these three approaches. In the initialization of cases a, b, and c with the same maximum level of five for all cases, there are about 4.2 million, 67000, and 2500 mesh cells, respectively. Using this approach, though a numerical detail, is the difference between a successful and crashed run when employing a high maximum level for mesh refinement, which is the case for most of the results given in the following chapters to yield high-accuracy results, particularly on the hole healing threshold.

2.4 Numerical Configurations and Conditions

The main numerical configurations utilized in this study are outlined in this section. These configurations represent holes in flat films, with different hole shapes and a circular hole shape in a bubble cap (i.e., curved film). Each configuration offers unique insights and is detailed in the subsequent chapters.

Appendix A and B provide information on the numerical convergence with respect to the mesh resolution and confinement studies examining the effect of the domain effective size on the hole dynamics, respectively. These studies are conducted to ensure the numerical results are converged, and the domain size is large enough to avoid any confinement effects.

Appendix F provides information on other numerical configurations that were tested but not included in the main body of the thesis. These configurations include retracting flat film with a straight rim, hemispherical bubble, and bubble rising and drainage. The results of these configurations are not discussed in the main body of the thesis because these configurations served as qualitative and qualitative inspection of the numerical tool and the bubble dynamics.

2.4.1 Hole in a Flat Film

For the case of the hole on a flat film, several hole shapes have been studied. Of these configurations, there are only two distinctly defined geometries that are discussed in the following sections. However, the profile shape in the configuration defined in section 2.4.1.1 can be changed from circle to catenoid or rectangle without a substantial change in the numerical configuration.

2.4.1.1 Half-Torus

Using the cylindrical coordinate system, the numerical configuration to simulate a hole on a flat film is illustrated in figure 2.8(a). In comparison with the definition of the cylindrical system, the longitudinal coordinate z axis, and the radial coordinate, the r axis of this system, corresponds to the x and r axis in figure 2.8(a)[4], respectively. Like a straight rim, here the film is assembled by combining part A, represented by a rectangle, and part B, represented by a quarter circle. The former models the flat portion of the film, while the latter denotes the hole shape, which in this case is a half-torus. In this figure, P.C shows the point of this conjunction, where the curvature of the interface κ is singular.

The hole is considered to have symmetry of revolution around the longitudinal coordinate and reflectional symmetry around the radial coordinate. Therefore, applying the axisymmetric

[4] Same definition applies to other numerical configurations defined using the cylindrical system.

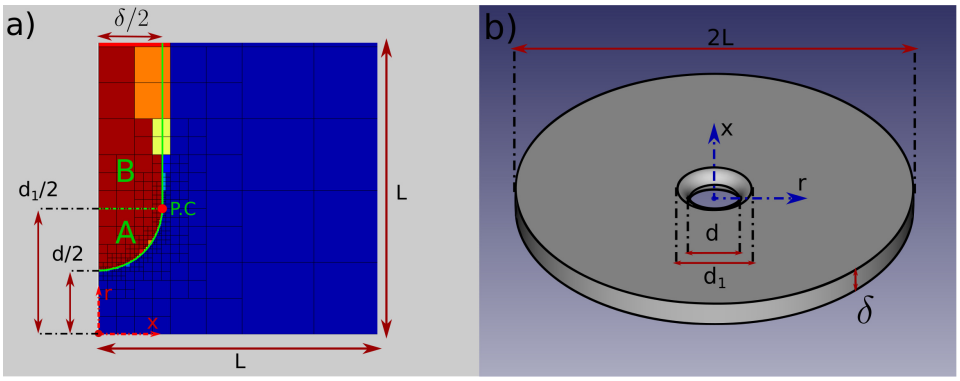

Fig. 2.8 Numerical setup for simulating a hole in a flat film, illustrated using a cylindrical coordinate system. The setup combines a rectangle (part A) representing the flat portion of the film and a quarter circle (part B) representing the hole, with a singular curvature at the point of conjunction (P.C). The cylindrical system longitudinal (z) and radial (r) coordinates correspond to the x and r axis, respectively.

condition to the numerical configuration given in figure 2.8(a) with x as the axis of revolution and r as the reflectional one, the numerical configuration models what is shown in figure 2.8(b) (i.e., the simulation domain is a thin cylinder of height δ). The simulation begins with uniformly initializing pressure[5] and velocity fields to zero values.

This configuration will be employed to conduct three distinct case studies, each illuminating different aspects of the subject. Firstly, it will examine the velocity of rim retraction, alongside the preceding section, a study which will henceforth be denominated as toroidal rim retraction. Secondly, the contraction velocity will be analyzed and compared to the findings from Lu and Corvalan (2015) and Lu et al. (2015). Lastly, the study will delve into the dynamics of the hole and explore the hole healing threshold.

2.4.1.2 Developed Rim

Here is a similar but numerical configuration with the difference in the hole shape. In this case, the hole shape is a portion of a torus and not necessarily its half, representing an already developed rim compared to the previous case with the half-torus hole shape. This is done by making a fraction field with a specific portion of a circular profile for the hole shape, joined by the flat part of the film, as illustrated in figure 2.9. In this configuration, two new parameters have been used: a the radial distance to the center of the developed rim or torus, b the radius of this rim, and v_1 which identifies the portion of the torus that is connected to the flat part of the film. These definitions are also depicted in the figure 2.9.

The work of Stumpf et al. (2023) inspires this numerical configuration, which proposed such a shape for the spontaneously growing holes after their nucleation on a flat film. While

[5]The zero pressure field is not "correct". However, it does not present a problem for the simulation.

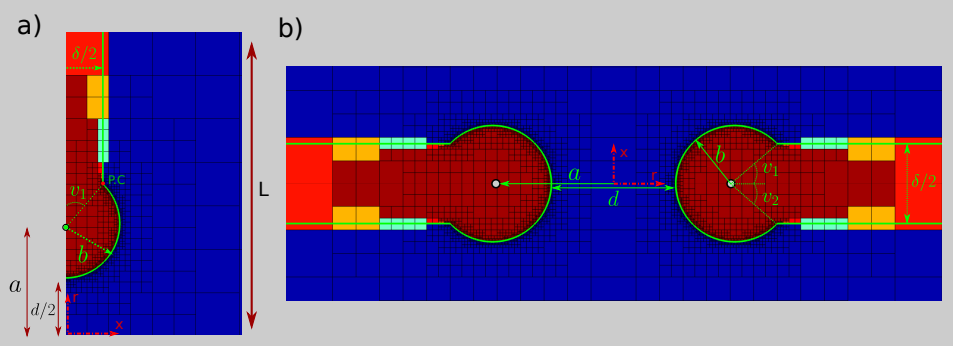

Fig. 2.9 Numerical setup for simulating a hole in a flat film with a developed rim for the hole shape, illustrated using a cylindrical coordinate system. The setup combines a rectangle (part A) representing the flat portion of the film and a developed rim for the hole shape, with a singular curvature at the point of conjunction (P.C). The cylindrical system longitudinal (z) and radial (r) coordinates correspond to the x and r axes, respectively.

studying the problem statically using the energetic arguments, Stumpf et al. (2023) based their main idea on the conservation of mass after the hole nucleation, thus resulting in a developed rim instead of a half-torus hole shape that accounts for the displaced liquid mass in place of the hole gap in the film. In subsequent chapters, where the hole dynamics are examined theoretically and numerically, the details of this numerical configuration will be discussed in more depth.

This configuration will be first employed to examine the proposed healing threshold by Stumpf et al. (2023) for such a film and hole shape. Moreover, it will be used for testing a healing threshold that will be hypothesized later in the present work.

2.4.2 Hole in a Bubble Cap

To simulate a hole on a bubble cap, one must first determine the static shape of the bubble. The accurate shape of a bubble is provided by the full Young-Laplace equation, which is a nonlinear partial differential equation that describes the shape of an interface, such as a bubble, in a fluid, taking into account surface tension and pressure differences. In a simplified notion of this equation, the bubble Bond number

$$\mathrm{Bo}_b = \frac{\rho_l g d_b^2}{\gamma}, \tag{2.40}$$

comparing the gravitational to capillary forces ratio could provide a qualitative estimation of the bubble shape. Taking the size of the bubble d_b as the characteristic length, a larger bubble is assigned with a higher Bo_b for the same values of surface tension and gravitational constant.

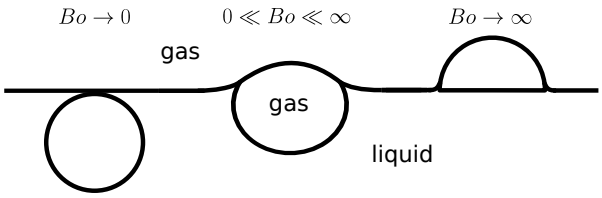

Fig. 2.10 Simplified sketch of three bubble shapes representing varying Bond numbers: Spherical for Bo $\to 0$ (submerged, small bubbles), half-spherical for Bo $\to \infty$ (large bubbles floating on the liquid surface), and intermediate shapes for $0 <$ Bo $< \infty$.

Figure 2.10 illustrates three bubble shapes corresponding to three categories of Bond numbers and thus bubble shapes and sizes: Bo $\to 0$ where the very small bubbles take a spherical shape and are submerged under the flat surface of the liquid, Bo $\to \infty$ where the very large bubbles take a half-spherical shape and float on the liquid surface, and $0 <$ Bo $< \infty$ for which bubbles take an intermediate shape between the two extremes.

Bubbles with Bo $\to \infty$ are numerically the least costly. That is because the numerical domain comprising the problem with the axisymmetric condition has a minor area for the same bubble size, resulting in the least number of mesh cells. Therefore, this half-spherical shape has been taken for simulations in the present work to narrow the focus on a selected set of physical parameters and make the computations more efficient. The shape of the bubble cap might have potential effects on the hole dynamics and could be subjected to examination.

Figure 2.11(a) illustrates the numerical configuration to simulate a symmetrical hole on a symmetrical bubble cap with a half-spherical shape that corresponds to a very high Bo_b using the cylindrical coordinate system similar to the configuration of the hole on a flat film. In this configuration, a hole with a circular shape of size d is located on top of the bubble cap with diameter d_b and on the center of the radial axis to enable 2D axisymmetric simulations, which is an essential key to avoid the necessity for a 3D simulations.

Although the aim is to simulate a half-spherical cap with a single hole at its pole by imposing the axisymmetric condition using x as the axis of revolution and r as the reflective one, the numerical configuration models instead of a complete sphere with two holes on its poles. The upper part of the modeled sphere is illustrated in 2.11(b), while the entire model depicted in $2D$ is given in figure 2.12.

Surface tension drives the behavior of both the hole and the bubble cap. As a result, the hole dynamics (whether it heals or bursts) are decided much more quickly than the time it takes for capillary waves to travel across the bubble cap from one end to the other. Consequently, the existence of the second hole is not suspected of having any effects on the hole dynamic except potentially through changing the intensity of the gas outflow through the hole opening. In fact,

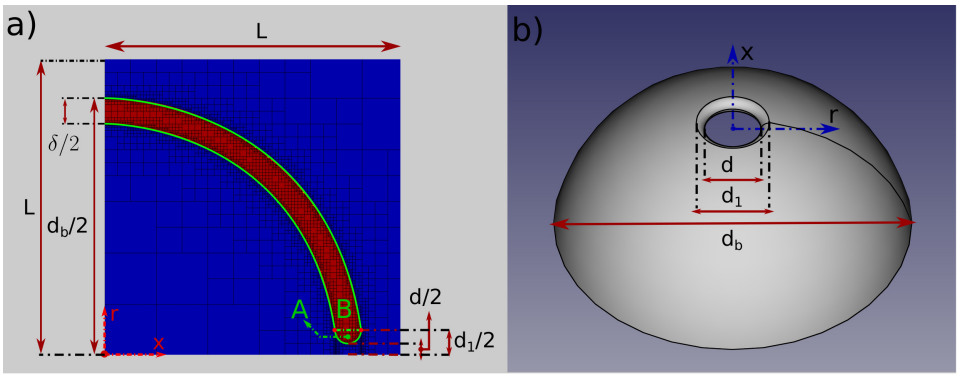

Fig. 2.11 Illustration of the numerical setup for simulating a symmetrical hole on a half-spherical bubble cap shown in sub-figure b, corresponding to a high Bond number, and utilizing a cylindrical coordinate system. A circular hole of size d is centrally located on the bubble cap with diameter d_b, enabling 2D axisymmetric simulations.

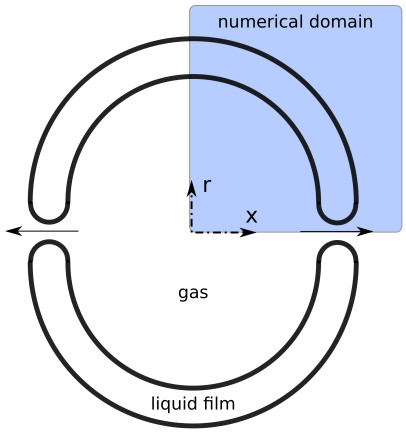

Fig. 2.12 Depiction of the effective 2D axisymmetric model representing a full sphere with two polar holes instead of a hemispherical one with one hole.

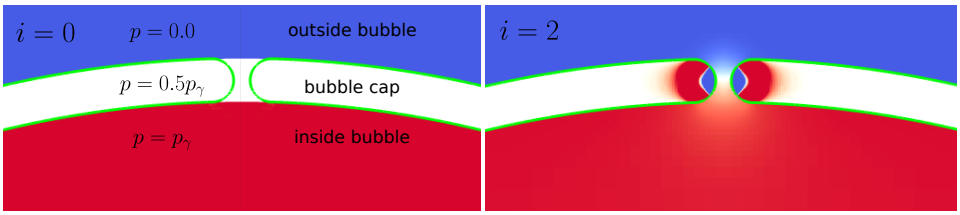

Fig. 2.13 Pressure color maps displaying, on the right, the initial pressure configuration within the bubble cap and surrounding film, with distinct pressure jumps due to surface tension. While the area near the hole might initially exhibit non-uniform pressure, it is swiftly rectified by the pressure solver, ensuring the pressure field accuracy throughout the simulation, as shown on the left.

when studying the bubble shrinkage dynamics, the effect of the second hole on the bubble cap must be considered, as shown in chapter 6, section 6.1.2.

The velocity field is set to zero values to initialize this numerical configuration. However, for the pressure field, there are two pressure jumps in the domain due to surface tension, occurring once by traversing the interface from inside the bubble cap

$$\Delta p_1 = 2\gamma/(d_b/2 - \delta) \tag{2.41}$$

to within the liquid film, and once more when traversing from within the liquid film to the outside of the bubble cap

$$\Delta p_2 = 2\gamma/d_b. \tag{2.42}$$

Therefore, the initial pressure field inside the cap and the film is set to capillary pressure $\Delta p_\gamma = \Delta p_1 + \Delta p_2$ and Δp_2, respectively, while it is set to zero for the outside of the cap. Figure 2.13 shows this initial configuration for the pressure field.

Undeniably, the hole area right after its nucleation (i.e., the gap between the two hole edges at the initial step) and the film area near the hole have a more complicated pressure field than a uniform one. Nevertheless, it has been examined that the initial pressure value set for this region does not affect the simulation as the pressure solver quickly corrects the initial pressure field, often in less than two simulation steps, as illustrated in figure 2.13.

The numerical configuration presented in this section will be employed to study the hole healing or bursting dynamics.

2.4.3 Dichotomy on Hole Healing Threshold

The critical or healing threshold defined as d^{*c} is the critical value of d/δ below which holes would close instead of opening. To determine d^{*c} for a specified set of dimensionless parameters, which is the main focus of the present work, the dichotomy method is adopted in

this study. This method is a classic root-finding technique that hones in on the d^{*c} by iteratively narrowing down an interval until the desired precision is achieved.

In the implementation of the dichotomy method for this investigation:

1. An interval (a,b) is initially selected based on trial simulations that ensure for $d/\delta = a$, the hole in the film closes, while for $d/\delta = b$, it opens.

2. The method begins by examining the midpoint of this interval, computed as $(a+b)/2$. A simulation is run for this midpoint value.

3. Based on the result of this simulation, one-half of the interval is discarded. Specifically, if the hole behavior at the midpoint resembles the behavior at a, then the interval is narrowed to $((a+b)/2,b)$. Conversely, if it resembles the behavior at b, then the interval becomes $(a,(a+b)/2)$.

4. This process is repeated, with each iteration halving the interval, and converging toward the exact value of the healing threshold.

5. The precision of the dichotomy, signifying the accuracy with which we are approaching the true threshold, is represented as $(b-a)/2^N$, where N is the number of iterations in the dichotomy process.

By employing this iterative approach, the dichotomy method ensures a systematic and precise determination of the hole healing threshold.

2.5 Dimensionless Parameters

As discussed earlier, and given that there are four dimensionless parameters governing the problem of the hole on the bubble cap when discarding gravity effects. Thus, the main objective in studying the hole dynamics is to investigate whether the critical healing threshold d^{*c} varies with the other four parameters, along with the other factors in the problem that will be examined, such as the hole shape.

Since the general context of the present study is the bubble bursting in the ocean, the typical values for the physical parameters of the problem in this specific context will be used as the basis for the simulations of the present work. Table 2.1a gathers a set of values for the physical parameters in the case of a typical ocean bubble. In table 2.1a, density, viscosity, and surface tension values have been set according to the work of Nayar et al. (2016) and by choosing a sea surface temperature of $20°C$ and a sea surface salinity of 30 *psu*, which corresponds to most typical values for the ocean surface bubbles (see Ernie R. Lewis, 2004).

(a)	$\rho_l (kg\, m^{-3})$	$\rho_g (kg\, m^{-3})$	$\mu_l (N.s\, m^{-2})$	$\mu_g (N.s\, m^{-2})$	$\gamma (N\, m^{-1})$
	1021	1.225	1.065×10^{-3}	1.48×10^{-5}	73.66×10^{-3}

(b)	ρ_l/ρ_g	La_l	La_g	d_b/δ
	833	663	3446	50

Table 2.1 (a) Typical values for physical parameters in the study of ocean bubbles, grounded in conditions with a sea surface temperature of $20°C$ and a sea surface salinity of 30 psu. The density, viscosity, and surface tension values are adapted from the work of Nayar et al. (2016), providing a representative basis for simulations in the current study. (b) The corresponding dimensionless parameters with a liquid film thickness δ of $10\mu m$ and a bubble diameter d_b of $0.5mm$.

In order to define the four parameters governing the problem beside d/δ, that is, $\mathrm{La}_l = \rho_l \delta\gamma/\mu_l^2$, $\mathrm{La}_g = \rho_g \delta\gamma/\mu_g^2$, and ρ_l/ρ_g, one needs to determine the values for δ and d_b corresponding to the time of bubble bursting, along with the values given in table 2.1a. The film thickness and bubble size range of typical values are more complex to determine than the other physical parameters.

Firstly, many studies observe cap film thicknesses at bursting up to several micrometers, particularly for larger bubbles (Lhuissier and Villermaux, 2012; Spiel, 1998). This thickness is influenced by the physical properties of the liquid, such as viscosity and surface tension, as well as by environmental conditions like temperature and pressure. Moreover, surfactants, which lower the surface tension of a liquid, play a crucial role in determining the bubble cap film thickness. Natural seawater surfactants originating from biological sources and other organic matter can alter the bubble film properties, making them more stable and affecting their thickness (Blanchard, 1989). In conclusion, while the typical range for bubble cap film thickness is often a few micrometers, the precise thickness at the moment of bursting depends on various factors and can be difficult to measure directly in the natural environment of the ocean.

Second and more importantly, the thickness of the bubble cap film can also vary with the size of the bubble, meaning that δ and d_b are not independent parameters, with smaller bubbles generally having thinner cap films compared to larger bubbles. Spiel (1998) concluded, based on experimental results, that there is a maximum for the film thickness. He argued that the film thickness increases with cap diameter up to $\delta \approx 3\mu m$ for $d_b \approx 11mm$, where after the

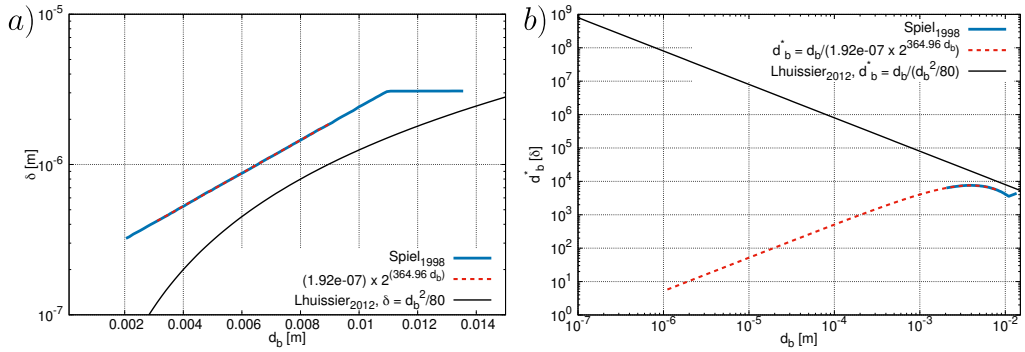

Fig. 2.14 (a) Film thickness as a function of bubble size, according to the findings of Spiel (1998) and Lhuissier and Villermaux (2012). The data points in this figure are extracted from the original figure in Spiel (1998) using the WebPlotDigitizer software (Rohatgi, 2022). (b) The ratio of bubble size to film thickness as a function of bubble size, according to panel (a).

film thickness remains constant despite increasing d_b. Moreover, Lhuissier and Villermaux (2012) emphasized the existence of a power law between these two variables, suggesting the expression

$$\delta = d_b^2/80 \tag{2.43}$$

Figure 2.14 illustrates the film thickness as a function of the bubble size, according to the findings of Spiel (1998)[6] and Lhuissier and Villermaux (2012). Subsequently, one can note that these two studies offer two different trends for the film thickness as a function of the bubble size. While Spiel (1998) suggests an exponential increase in the film thickness with the bubble size, with a saturation point at $\delta \approx 11\mu m$, Lhuissier and Villermaux (2012) proposes a power law relation between these two variables as given in expression 2.43.

Additionally, Lhuissier and Villermaux (2012) suggested that bubbles with sizes ranging from $100\mu m$ up to $1cm$ are more likely to produce film drops due to the film bursting. Using expression 2.43 and the upper bound of the bubble size $d_b = 1cm$, one finds a ratio of $d_b/\delta = d_b^* = 8000$, whereas if d_b and δ were to be chosen separately from their corresponding observable range, this ratio could be as low as ten. Such a ratio will result in a much costlier numerical simulation since d_b determines the necessary size of the numerical domain and δ the order of the smallest cells.

For instance, to have only one cell across the film for $d_b^* = 8000$, 13 levels of mesh refinement would be required while requiring 2^5 number of cells across (NSA) the film thickness to guarantee a minimum accuracy of the dynamics within the film, adding another five mesh levels, making a sum of 18 levels, which is exceptionally high.

[6]The data points in this figure are extracted from the original figure in Spiel (1998) using the WebPlotDigitizer software (Rohatgi, 2022).

The following expression finds GML depending on the film thickness ratio to bubble size and the required number of cells across the film:

$$\mathrm{GML} = \log_2^{(d_b^* + \mathrm{NSA})}. \tag{2.44}$$

Using expression 2.44, a value of $d_b^* = 1000$ with 2^5 cells across the film results in a feasible GML of 15. Nevertheless, simulating such a ratio is feasible only for a handful of showcasing simulations and not viable for several tens of thousands of simulations, which has been the case in the present work to study the hole healing threshold.

The high number of required simulations for this study results from the fact that the main objective is to examine the variation of the healing threshold with the other four parameters of the problem, requiring the dichotomy process as discussed in section 2.4.3. For example, to study only the effect of liquid, viscous effects vs. surface tension on the healing threshold with 20 data points for La_l and healing threshold accuracy of $10^{-3}[\delta]$, about 250 simulations are required in a single trial.

On the other hand, the value of d_b^*, even though suggested by Lhuissier and Villermaux (2012) to be of the order of 10^3 and increasing with decreasing bubble size, is contradicted by the findings of Spiel (1998), who suggests an opposite trend with d_b^* decreasing with decreasing bubble size. Therefore, d_b^* values of orders of 10^2 are also plausible. Subsequently, a value of $d_b^* = 50$ has been optimally selected as the standard ratio for the simulations of the present work. With this choice, and using the values given in 2.1a, the set of governing dimensionless parameters as a basis for the simulations is gathered in table 2.1b.

It is worth noting that the relation between the physical and non-dimensional parameters is not unique. For instance, for a single value of non-dimensionalized time in the simulations, there are infinite corresponding times in a physical case depending on the choice of dimensional parameters that would result in the same dimensionless parameters. Consequently, the set of dimensional parameters given in table 2.1 is not a unique set of parameters that results in the same set of dimensionless parameters provided in this table.

2.6 Remarks on the Possibilities of a 3D Simulations

This section investigates the possibility of a 3D simulation for bubble film bursting. As discussed earlier, in a 2D axisymmetric setting in Basilisk and by using 15 levels for GML (an extremely high value), the bubble size to thickness ratio can reach $d_b^* = 1000$ while simulating up to 2^5 cells across the film. However, in a 3D setting and using expression 2.38, a staggering total of 2^{45} or $10^{13.5}$ cells would be required in a uniform grid. Implementing an adaptive

mesh strategy and using equation 2.39 with assuming a very high efficiency in mesh adaptivity $CAM = 0.8$, around 2^{33} or 10 billion mesh cell would have to be simulated at each time step. This could be found using a single expression

$$\text{cells} = 2^{\left(\log_2^{(d_b^*+\text{NSA})}\right)^{(\text{dimensions}-\text{CAM})}} \tag{2.45}$$

Moore's Law, initially posited by Gordon Moore in 1965, predicts that the number of transistors on a microchip will double approximately every two years, leading to an exponential increase in computing power and efficiency, while the cost of computers will be halved. It Slotnick et al. (2014), a study by NASA on the state of the world capacity for computational fluid dynamics (CFD) simulations predicted that CFD problems will have sizes of 10 billion points by 2020, 100 billion points by 2025, and 1 trillion cells by 2030. So far, the 2020 milestone has been well reached as simulations have been recently performed, with a total number of mesh cells of around 10s of billions (Lehmann, 2023). While this number is expected to reach an order of one trillion cells by 2030 for the most extensive and resourceful CFD simulations, the current best computational resources are barely able to simulate a simplified bubble as described above (with a larger film thickness than usual surface bubbles) and with the help of a very effective mesh adaptation method. Nevertheless, given the expected capacities yet to be reached, an accurate and realistic 3D bubble-bursting simulation could be feasible in the next one or two decades.

Using multiple cores simultaneously, parallelization is done by dividing the mesh grid into sub-divisions, each processed by a single core in its local memory. At the same time, its data must be explicitly shared by passing messages between processes. This is done by the message-passing interface (MPI). For instance, for calculating the global maximum value in the pressure field, the data from different local memories have to be compared. Basilisk conveniently provides options called reduction functions for enabling the code to be used in a parallel computation setting. Nevertheless, except for simple measurements of the simulation (i.e., finding the maximum or minimum value of a parameter), parallel computation dictates the need for writing unique MPI functions to find global measurement values of the simulation.

Increasing the number of cores employed in parallel computation does not always decrease the computation time because, for each added core, MPI requires more time to reconstruct the entire domain from the local results of each core at each step of the simulation, which means that depending on the numerical setup, there is an optimal range for the number of cores in MPI. Common knowledge in this field suggests an optimal number of 30,000 grid points per second and core.

The computational resources on a Navier cluster belonging to the laboratory d'Alembert and available for the present work comprise 288 cores. Considering this number, along with the optimal number of grid points per second and core, one finds a maximum of 9 million grid points to be efficiently simulated using all the cores on the Navier cluster, which means that the potentially available resources are off at least by three orders of magnitude for a simplified 3D bubble showcasing simulation that would require 300,000 cores instead. This is while Jean Zay, France's most powerful supercomputer, has only 90000 cores, and Adastra, a new French supercomputer newly inaugurated in 2023, has 300,000 cores. Therefore, making such an endeavor – a single 3D bubble simulation and not the study of the hole healing threshold – a possible yet impractical notion.

2.7 Summary

The dynamics of liquid films and bubbles are dictated by the incompressible and variable-density Navier-Stokes equations, encompassing surface tension. This chapter explored these governing equations for various two-phase flow configurations. The configurations introduced included liquid films with straight retracting rims, flat films with a hole, an axisymmetric bubble cap with a hole, axisymmetric bubble bursting, and axisymmetric bubble rising and drainage; each could provide unique insights into the behavior and interactions of liquid and gas phases at different interfaces, particularly, the hole healing threshold and rim retraction and contraction speed.

This chapter also introduces Basilisk, a powerful tool for numerical simulations of such fluid dynamics problems, illustrating its VoF method along with adaptive meshing capabilities and how it optimizes precision and computational resources.

The chapter serves as a precursor to the detailed analysis and results of simulations of the introduced problems in later sections, providing the necessary numerical framework and tools to comprehend and investigate the results of dynamics of holes in liquid films and bubbles along with their rupture.

Chapter 3

Analytical and Numerical Study of the Hole Healing Threshold

Free liquid films, existing as two-dimensional entities, do not possess an inherent inclination to rupture or disintegrate. Unlike one-dimensional counterparts such as jets, liquid films only develop holes when triggered by nucleation events. As discussed in the previous chapter, these nucleation events could stem from many different mechanisms, including turbulent induced flows inside the film, thermal fluctuations, van der Waal forces, and impurities in the flow (Lhuissier and Villermaux, 2012).

Regardless of the exact mechanism of hole nucleation in ocean bubbles bursting, the fate of a nucleated hole of a given size and shape (i.e., whether it closes and heals or opens and bursts) can be an independent subject of study. As will be shown, depending on the hole initial configuration and physical parameters of the problem, there exists a certain healing threshold d^{*c} below which the hole eventually closes. Hence, the central focus of this chapter is first to investigate the hole dynamics and the mechanism enabling the healing event and second to study the healing threshold analytically and numerically. The hole is considered right after the nucleation event, and assuming that the created hole is axisymmetric with several different types of hole profiles, including the torus shape as shown in figure 3.1, the developed rim inspired by Stumpf et al. (2023), and the catenoid shape based on the work of Taylor and Michael (1973).

3.1 Problem Description of a Hole on a Flat Film

Figure 3.2 presents the two-dimensional axisymmetric sequences of the hole dynamics, having two distinct behaviors: closing or healing and opening or bursting. As observed, the only

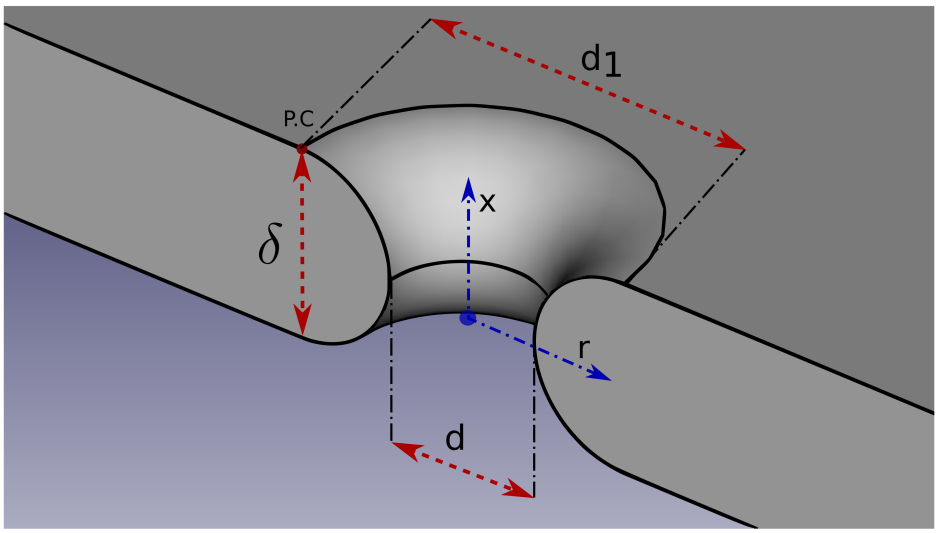

Fig. 3.1 Geometrical description of an axisymmetric hole on a flat thin liquid film, where δ, d, and d_1 are the film thickness, hole minimum size, and maximum size, respectively. *P.c* indicates the point where the flat part of the geometry meets the hole shape, in this case, a circular profile in 2D axisymmetric, which results in a torus shape when revolved around the x-axis.

difference in the initial conditions of the simulations is the initial hole size, yet as illustrated, it drastically alters the initial pressure field inside the film and in the hole vicinity. The smaller hole tends to close while the larger one expands. One can begin with the Young–Laplace equation that relates the pressure difference to the shape of the interface to delve into the mechanisms driving these contrasting behaviors.

3.1.1 Young-Laplace Equation

The Young–Laplace equation articulates the capillary pressure difference sustained across the interface of two static fluids (e.g., water and air) resulting from surface tension. This equation encapsulates the equilibrium balance of forces acting on a fluid surface. Specifically, in equilibrium, the normal force of pressure exerted on a fluid surface element is counteracted by the surface tension forces operating along the boundaries of that element (Behroozi, 2022).

For two static fluids meeting at an interface, treated as a surface (i.e., zero thickness), the balance of normal stress yields:

$$\Delta p_\gamma = \gamma \nabla \cdot \hat{n} \tag{3.1}$$

Here, $\Delta p_\gamma = p_1 - p_2$ denotes the Laplace pressure: the pressure difference experienced when transitioning from fluid 2 (gas) to fluid 1 (liquid). The coefficient γ signifies the surface tension coefficient between the film and gas, and $\hat{n}$ is the unit normal directed outward from the surface.

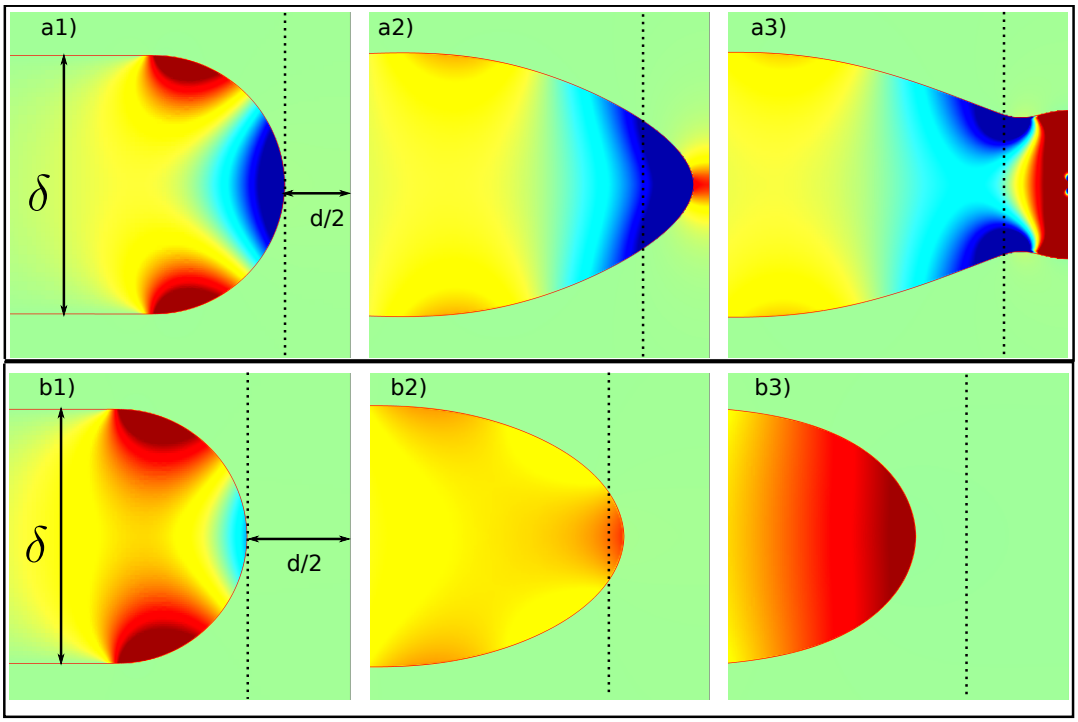

Fig. 3.2 The figure depicts the hole healing phenomenon on a flat free film through sequences of closing and opening axisymmetric holes. This is illustrated by a pressure color map and the film interface evolution (represented by the red line separating the two phases) in the top and bottom rows, respectively. While specific parameters were not necessary to be detailed, the primary difference between the two cases is the initial hole size d, marked by the black dashed line. Snapshots were taken at three points: a1 and b1 for the initial stage, a2 and b2 at an intermediate stage, and a3 and b3 for the final record of the simulations.

For a surface defined in 3D space, the relation between the mean curvature and the surface unit normal is:

$$\gamma \nabla \cdot \hat{n} = 2\gamma H \tag{3.2}$$

where H represents the mean curvature. At any point p on surface S in $\mathbf{R}^3$, planes that intersect p and contain the normal to S generate a curve with a signed curvature. This curvature varies with the plane rotation angle θ. The extreme curvatures, κ_1 and κ_2, are the surface principal curvatures. Thus, the mean curvature at point p on S can be calculated as:

$$H = \frac{1}{2}(\kappa_1 + \kappa_2) \tag{3.3}$$

The principal curvatures of the interface at p is calculated by the inverse of the diameter of the two curves on two perpendicular planes passing through p

$$\kappa_1 = 2D_1^{-1}, \ \kappa_2 = 2D_2^{-1} \tag{3.4}$$

The sign of the curvature depends on the choice of normal: the curvature is positive if the surface curves "towards" the normal (center of curvature is inside the traversed fluid) and negative otherwise (see de Gennes et al., 2004, p. 8).

Employing these definitions, equation 3.1 can be reframed as:

$$\Delta p_\gamma = \gamma(\kappa_1 + \kappa_2) = 2\gamma\left(\frac{1}{D_1} + \frac{1}{D_2}\right) \tag{3.5}$$

Figure 3.1 illustrates a flat liquid film hole, presenting two opposing principal curvatures. At the hole edge, where the diameter is minimum and equivalent to d, determining both principal curvatures is straightforward: one, given by d, is negative, while the other, defined by the film thickness δ, is positive. Using Laplace's relation, one can compute the capillary pressure both within the film and at the edge of the hole as:

$$\Delta p_\gamma = 2\gamma\left(\frac{1}{\delta} - \frac{1}{d}\right) \tag{3.6}$$

Due to their inverse signs, the surface tensions from each curvature oppose each other, as implied by equation 3.6, resulting in contrasting capillary pressures at the hole edge. Moreover, the capillary pressure on any point of the flat portion of the film equates to zero or the same as the surrounding gas pressure. Given a pressure field around the hole that consistently surpasses the rest of the film pressure ($\Delta p_\gamma > 0$), it can be expected that the fluid in this region would recede towards lower pressure zones in the film. Thus, to a first-order approximation, one could

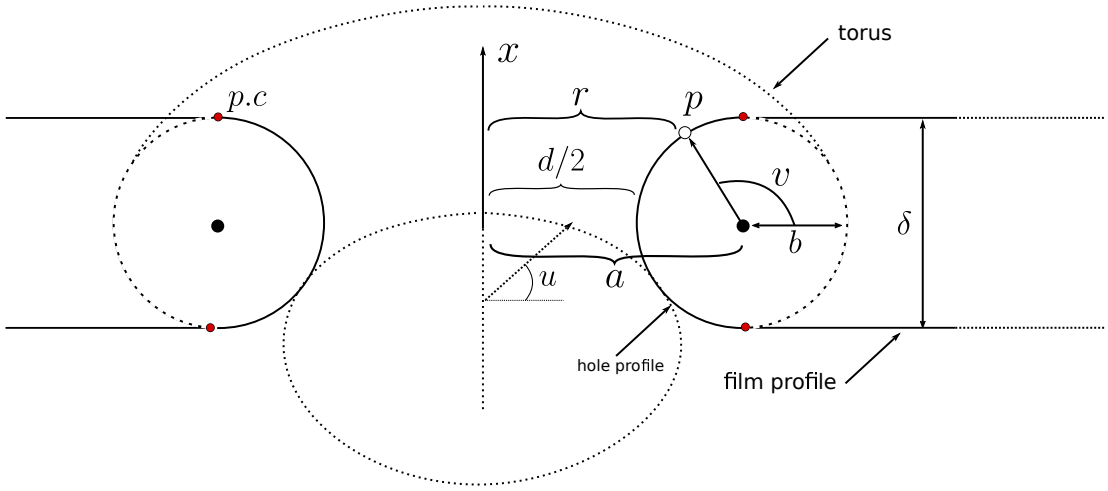

Fig. 3.3 Illustration of a torus shape attached to a rectangle at $v = \pi/2$ (i.e., at point P.c) and $v = 3\pi/2$, representing the geometry of an axisymmetric hole on a flat film. The axis of revolution is denoted by x. The torus is defined using the $u - v$ coordinate system as illustrated, while a and b are geometric parameters related to the torus structure. Here, a represents the distance from the x-axis to the torus center, b indicates the radius of the torus, and p an arbitrary point on the hole profile with distance r from the x-axis.

describe the hole dynamics predominantly based on the capillary pressure at the hole tip. The hole would expand if d exceeds δ, leading to a pronounced positive pressure in the hole vicinity. Conversely, it would close if d is less than δ, resulting in a pronounced negative pressure.

3.1.2 Torus Holes - Capillary Pressure

As depicted in figure 3.2, while the pressure difference adjacent to the hole edge aligns with the relation given by equation 3.6, the entire pressure field subsequent to the static shape of both the hole and the film exhibits greater complexity. Stemming from this observation, the primary goal of this section is to formulate an analytical expression that captures the initial film curvature, specifically around the hole vicinity. For an axisymmetric hole exhibiting a circular profile—whether on a flat or curved film—the hole geometry mirrors that of a half torus as shown in Figure 3.3. The mean curvature H of this shape at any given point p is expressed by

$$H(v) = -\frac{a + 2b\cos v}{2b(a + b\cos v)} \tag{3.7}$$

where u and v denote the angular deviations defined in figure 3.3. Meanwhile, a and b represent the distance from the hole center to the torus tube center and the tube radius, respectively (see Abbena et al., 2017, p. 406-407). The u, v coordinate system is conventionally used to articulate the torus shape in mathematical contexts, such as in Abbena et al. (2017).

Given our numerical framework, which leverages radial distance r, the hole minimum size d, and film thickness δ—which also denotes the diameter of the hole circular profile—equation 3.7 can be transformed to

$$H(r) = 1/2\left(\frac{1}{\delta/2} + \frac{\left(r - \frac{d}{2} - \delta/2\right)}{r(\delta/2)}\right) \tag{3.8}$$

Combining equation 3.8 with equation 3.3 yields the two principal curvatures:

$$\kappa^{+} = 1/D_1 = \frac{1}{\delta/2} \tag{3.9}$$

$$\kappa^{-}(r) = 1/D_2(r) = \frac{\left(r - \frac{d}{2} - \delta/2\right)}{r(\delta/2)} \tag{3.10}$$

These equations show that the first principal curvature, κ_1, remains positive and constant across the entire hole profile. In contrast, the second curvature varies with r and is consistently negative, denoted by $\kappa_2 = \kappa^{-}$. The Laplace pressure as a function of radial distance over the hole profile is determined using equation 3.5:

$$\Delta p_\gamma(r) = \gamma\left(\frac{1}{\delta/2} + \frac{(r - \frac{d}{2} - \delta/2)}{r(\delta/2)}\right) \tag{3.11}$$

The comprehensive pressure field for the entire film interface is captured by:

$$\Delta p_\gamma(r) = \begin{cases} \gamma\left(\frac{1}{\delta/2} + \frac{(r-\frac{d}{2}-\delta/2)}{r(\delta/2)}\right), & r < (d+\delta)/2 \\ 0, & r \geq (d+\delta)/2 \end{cases} \tag{3.12}$$

The resultant pressure field from the static hole shape exhibits a discontinuity at $r = (d+\delta)/2$, which arises due to the interface curvature discontinuity as it transitions from a circular half-torus to a flat surface. Moreover, analyzing equation 3.12 reveals that the initial pressure field across the film and within the hole region is not consistently positive when the hole size matches the film thickness. This observation complicates identifying the hole healing threshold, which is substantially influenced by its initial shape and pressure field.

Utilizing the analytical expression 3.12 for the capillary pressure derived from the film curvature profile, it becomes feasible to plot $\Delta p_\gamma(r)$ and juxtapose it with values obtained from numerical simulations of films with varying hole sizes. When the surface tension coefficient is set to $\gamma = 1$, figure 3.4 effectively evaluates $H(r)$—the mean curvature of film surfaces with distinct hole sizes along the r-axis. The considered hole sizes are $d = \{0.5, 0.75, 1.00, 1.25\}$. Such results vouch for the precision of the numerical method when assessing the surface mean

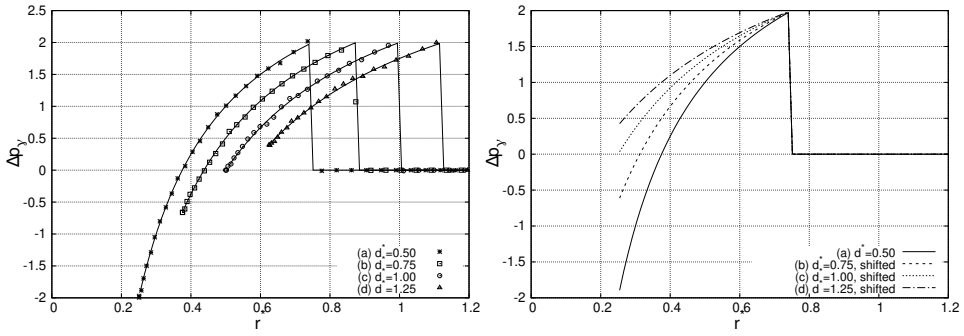

Fig. 3.4 On the left, the film capillary pressure $\Delta p_\gamma(r)$ is shown for $\gamma = 1$, depicting the radial variation of mean curvature $H(r)$ for hole sizes $d^* = \{0.5, 0.75, 1.00, 1.25\}$. Numerical results (symbols) and analytical results (solid lines) from equation 3.12 are contrasted, emphasizing the numerical method accuracy. On the right, curvature profiles for $d^* = \{0.75, 1.00, 1.25\}$ are shifted to align with $d^* = 0.5$ profile, facilitating shape comparisons and dispelling notions of identical profiles.

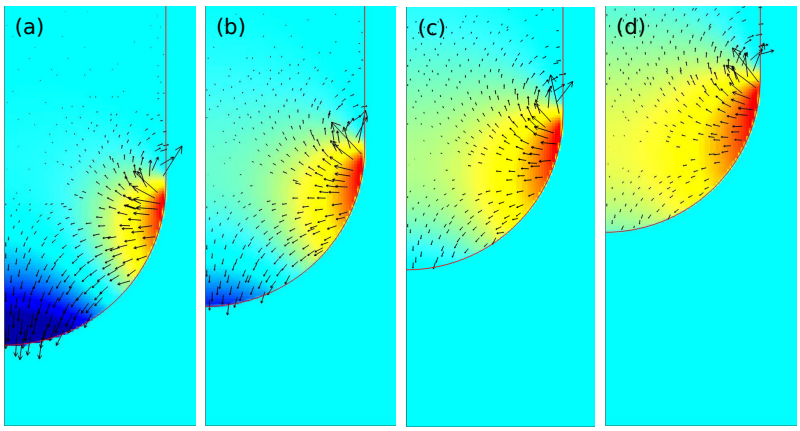

Fig. 3.5 Visualization of the initial pressure field using color maps and overlaid velocity vectors for films with hole diameters: (a) $d = 0.50$, (b) $d = 0.75$, (c) $d = 1.00$, and (d) $d = 1.25$, 20 steps after the start of the simulation in all cases. The color scale ranges from -1 to $+2$. The difference in the distinct pressure patterns and the subsequent dynamics of the hole region due to different hole sizes are demonstrated.

curvature against the analytical expression 3.12. One might initially perceive that these profiles share a similar shape, only offset along the r-axis. However, as evidenced in figure 3.4, each profile is distinct for every d.

Figure 3.5 vividly depicts the initial pressure fields within four cases, especially proximal to the hole. This visualization uses a consistent color scale for the four films of different sizes explored in figure 3.4. The data presented was captured 20 steps into the simulation (i.e., $i = 20$), allowing the initial pressure field to be adjusted to more accurate values. Additionally, the velocity vector field overlays the pressure color map, granting a more nuanced perspective into the initial motion of the hole and the dynamic interactions around the hole region.

Observing the interface hole edge in figure 3.5, one notes that for $\delta > d$, the capillary pressure is negative $\Delta p_\gamma < 0$. This suggests that the region surrounding the hole edge within the film maintains a lower pressure than the broader film area. In contrast, when $\delta < d$, $\Delta p_\gamma > 0$ manifests, giving rise to a high-pressure zone. However, as previously mentioned and evidenced by the four initial states for pressure and velocity fields in figure 3.5, the film dynamics extend beyond mere representation by the capillary pressure value at the hole edge—a value which, in isolation, is comparatively simpler to ascertain.

In figure 3.5, one can observe a distinct, singular-like point in the initial pressure fields. This is attributable to the discontinuity in the curvature of the interfaces, which is further evident from the curvature profiles presented in figure 3.4. This singular point generates a vorticity source and capillary wave, which subsequently induces ripples propagating through the film interface and could affect the healing threshold.

To avoid the impact of the curvature discontinuity of the interface on the healing threshold, one might consider employing a catenoid shape, as proposed by Taylor and Michael (1973). Such a shape offers a uniform interface with a mean curvature value of zero. Nonetheless, this shape introduces another challenge: it creates a discontinuity in the interface geometry, specifically where the flat region intersects with the hole profile. The influence of the hole shape will be delved into more comprehensively in the subsequent sections.

3.1.3 Torus Holes – Preliminary Numerical Simulations

The tendency for simplification has often led to basing the estimation of hole bursting or healing predominantly on the capillary pressure at the hole edge, as characterized by expression 3.6. This has often been due to neglecting to consider the complete initial capillary pressure at the film interface, provided by expression 3.12 for the circular hole profile. Such an approach typically posits $d^{*c} = 1$ as the threshold for hole healing. Nevertheless, as the preliminary numerical simulations will demonstrate, this assertion is invalid.

Here, three hole sizes $d/\delta = \{0.5, 1.00, 1.5\}$ have been selected to investigate the evolution of the film interface near the hole area and the subsequent changes in the pressure fields in figure 3.6 and figure 3.7, respectively. For this purpose, five snapshots have been taken at five simulation steps $i = \{0, 1000, 2000, 4000, 8000\}$, resulting in almost the same time steps between the simulations $t^* \approx \{0.0, 0.11, 0.22, 0.45, 0.9\}$.[1]

[1]The non-dimensional time unit and the time step of each simulation varies for each set of parameters and between simulations. However, the purpose of these results, such as in figure 3.6 and figure 3.7, either interface evolutions or pressure fields, is to provide qualitative insights into the problem dynamics as the simulations run, and for qualitative comparisons between hole shapes. Therefore, it is not unnecessary to precisely match the recorded times between simulations, which would introduce additional complications. Hence, for these and similar results, the measurements were taken using equal simulation steps rather than equal times.

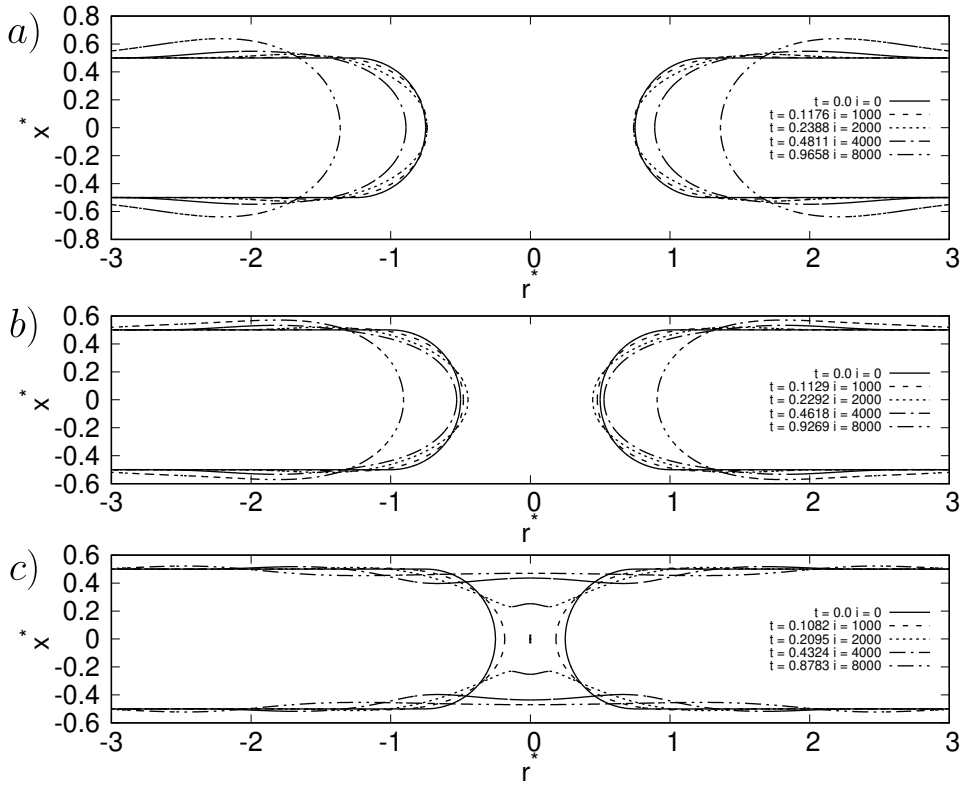

Fig. 3.6 Evolution of the film interface near the hole area with the circular profile for three hole sizes across five simulation steps $i = \{0, 1000, 2000, 4000, 8000\}$. Case a) with $d^* = 1.5$, b) with $d^* = 1.0$, and c) with $d^* = 0.5$. These simulation steps correspond to $t^* \approx \{0.0, 0.11, 0.22, 0.45, 0.9\}$. The progression of the interface highlights varying behaviors, from healing in $d^* = 0.5$ to "flickering" in the $d^* = 1.0$ case to direct bursting for the larger $d^* = 1.5$ hole. The set of parameters used for these simulations is listed in table 2.1.

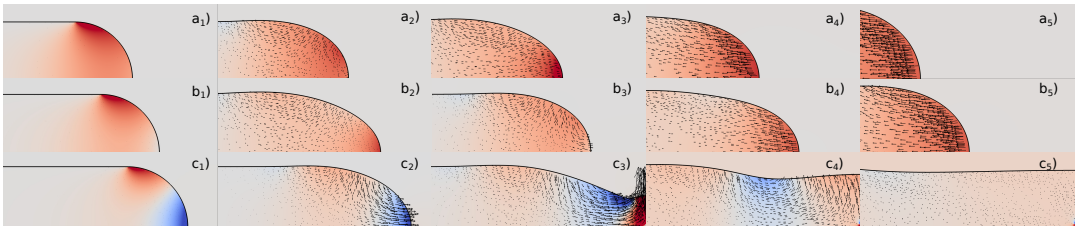

Fig. 3.7 Evolution of pressure fields for holes with a half-torus shape and sizes across five simulation steps $i = \{0, 1000, 2000, 4000, 8000\}$ corresponding to $t^* \approx \{0.0, 0.11, 0.22, 0.45, 0.9\}$. Case a) with $d^* = 1.5$, b) with $d^* = 1.0$, and c) with $d^* = 0.5$. Color map values range from -1.5 to 1.5 consistently within and across cases. The transition from singular-like regions in the pressure field to more continuous ones over time is evident. These snapshots demonstrate the intricacy of the pressure fields and their influence on the simulation outcome. The set of parameters used for these simulations is listed in table 2.1.

From these observations, the hole in the $d^{*c} = 1.0$ case initially contracts before reversing its trajectory to burst. This pattern can be described as "flickering." Such a flickering behavior has already been documented in works by Lu and Corvalan (2015) and Sharma and Ruckenstein (1990). In contrast, the larger $d^{*c} = 1.5$ hole progresses directly to bursting, with no preceding flickering. Notably, if a hole commences its movement by retracting, it definitively continues to burst. Conversely, when a hole begins by contracting, its fate—either healing or bursting—remains complex.

A pivotal insight drawn from figure 3.6 reveals that when the hole size matches the film thickness, the film eventually bursts, contradicting the commonly assumed $d = \delta$ for the healing threshold. Conversely, a hole half the size of the film thickness leads to the film healing. This suggests that the exact bursting threshold resides between $0.5 < d^{*c} < 1.0$, which is a testament to the complex pressure dynamics within the film. Consequently, the cases $d^* = \{0.5, 1.00\}$ were subjected to investigations using both the pressure and velocity vector fields. Figure 3.7 offers a detailed exploration of these two scenarios, showing how the initial pressure field—originating from the static configuration—and the ensuing flow, induced by the internal pressure differentials, evolve as the simulation advances.

3.2 Torus Holes – Healing Threshold Hypothesis

Upon analyzing the hole dynamics depicted in figure 3.7, it is apparent that the outcome of a hole nucleation event is closely tied to the initial interface curvature and the consequent capillary pressure within the hole region. Thus, this section posits a hypothesis to predict the healing threshold analytically, focusing solely on the static and initial conditions of the problem. This hypothesis draws inspiration from the observations made in figures 3.5 and 3.7.

Several works have done the analytical study of the hole healing threshold on a free film. Taylor and Michael (1973) utilized the catenoid soap film model to analyze hole dynamics in a free film. More recently, Stumpf et al. (2023) presented a model that factored in a film with an already developed circular rim (i.e., rim diameter larger than film thickness or $2b > \delta$), ensuring mass conservation following hole nucleation, as illustrated in figure 2.9. Conversely, much research has been devoted to hole dynamics in films situated on substrates, including notable contributions by Moriarty and Schwartz (1993). A commonality amongst these studies is the usage of energy-based arguments to calculate a healing threshold. They typically juxtapose the energy state of an intact film against that of a film marred by a hole. In what follows, we propose a different approach.

The first key idea is to imagine the initial static film surface as a connected string of small balls or alternatively as a stack of sliding layers with infinitesimal width, to which different

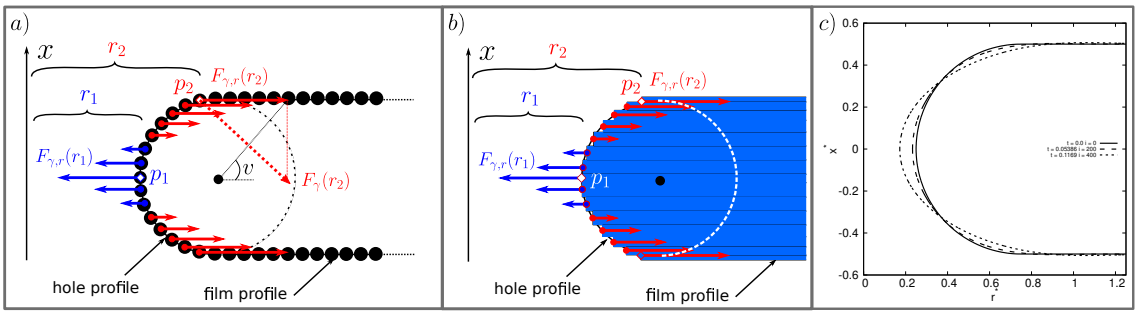

Fig. 3.8 (a) Conceptual illustration of the film surface imagined as a connected string of small balls. (b) An alternative conceptualization of the film as a stack of sliding layers with infinitesimal width, affected by varying forces due to capillary pressure. (c) The interface evolution in a numerical simulation of a film with a circular interface with the initial $d/\delta = 0.5$ evolving 400 steps or for 0.1 time unit confirms the alignment of the conceptual illustration with the actual dynamics of the problem. These representations serve as a visual aid for the presented hypothesis on the healing threshold and are not meant to be proposed as physically accurate.

forces are exerted due to the capillary pressure at the film surface and the hole area. This conceptualization, illustrated in figures 3.8a and 3.8b, and substantiated by the numerical simulations presented in figure 3.8c, provides the foundation to hypothesize an estimation of the healing threshold. This estimation derives from the cumulative radial forces exerted—essentially, the surface integral of the capillary pressure multiplied by the corresponding surface element or the total applied forces.

In mathematical terms, the surface area of a torus is described as:

$$S(u_1,u_2,v_1,v_2) = \int_{u_1}^{u_2}\int_{v_1}^{v_2} \left(ab + b^2 cos\,(v)\right) dvdu \tag{3.13}$$

Leveraging equations 3.1 and 3.2, the integral of the capillary pressure over this defined surface is:

$$\sum \Delta p_\gamma(u_1,u_2,v_1,v_2) = 2\gamma \int_{u_1}^{u_2}\int_{v_1}^{v_2} H(v)dvdu \tag{3.14}$$

with $H(v)$ defined by equation 3.7.

To calculate the integral of forces on a film with a half torus hole shape (circular profile in axisymmetric) as given in figure 3.3, one can multiply the pressure and surface integral, both of which have identical differential elements $dvdu$ in this formulation. For this calculation, one finds

$$\sum F_\gamma = 2\gamma \int_0^{2\pi}\int_{\frac{\pi}{2}}^{3\pi/2} S(u_1,u_2,v_1,v_2).H(v)dvdu \tag{3.15}$$

In this equation, the first integral multiplies the capillary pressure by the surface area and sums over the range $v \in [\pi/2, 3\pi/2]$ for the standard torus shape, emphasizing solely the

hole interface or the left half of the torus. Meanwhile, the second integral accounts for the axisymmetric revolution around the x-axis with $u \in [0, 2\pi]$.

For determining the radial component of this integral (i.e., the cumulative radial forces), the innermost integral in equation 3.15 can be adjusted to:

$$\sum F_{\gamma,r} = 2\gamma \int_0^{2\pi} \int_{\frac{\pi}{2}}^{3\pi/2} \left(ab + b^2 \cos(v)\right) H(v).cos(\pi - v)\, dvdu \tag{3.16}$$

An initial approach posits the healing threshold as the specific a/b ratio where $\sum F_{\gamma,r} = 0$. This implies that if the sum of all radial forces exerted on the interconnected balls or layers is zero, the hole might not retract sufficiently to reach the radial axis and mend. By employing this methodology and setting expression 3.16 to zero, the integral equation can be solved after substituting for $H(v)$ to obtain:

$$\begin{aligned} -2\gamma \int_0^{2\pi} \int_{\frac{\pi}{2}}^{3\pi/2} \cos(v)(a + 2b\cos(v))dvdu = 0 \\ -8\gamma\pi[b \cdot \left(\frac{\sin(2v)}{2} + v\right) + a\sin(v)]_{\frac{\pi}{2}}^{\pi} = 0 \\ \rightarrow \qquad a - \frac{\pi b}{2} = 0 \end{aligned}$$

where the integral constant has been taken equal to zero. By referring to figure 3.3 and using

$$a = \frac{d+\delta}{2}, b = \frac{\delta}{2} \tag{3.17}$$

one could find, a healing threshold of

$$d^{*c} = 0.57 \tag{3.18}$$

Nevertheless, this preliminary method overlooks the varying initial radial positions of the small balls. One could imagine two competitive runners where one possesses superior strength and represents the hole-bursting team, while the other, with inferior strength, represents the hole-healing team. If the inferior runner starts closer to the finish line, predicting the race outcome becomes more intricate than merely contrasting their strengths, which is the same as integrating the radial forces.

Therefore, a second key idea is introduced in this hypothesis: *the radial force applied to each ball or film surface element must be examined alongside the radial distance that each element must traverse towards the x-axis for the hole to heal*. For instance, the second ball labeled as point p_2 with radial distance $r = r_2$ in figure 3.8 requires $b(1 + \cos(v))$ more

movement than the first ball represented by p_1 with $r = r_1$. Thus, even if two counteracting forces are applied to these balls such that $F_r(r1) = -F_r(r2)$, the hole minimum radius would be likely to decrease, contrary to the preliminary expectation of it remaining static when the cumulative radial force equals zero.

To incorporate this secondary notion in the initial hypothesis, one could express the force unit in terms of distance using $F_{\gamma,r}(v)/\gamma$, which signifies the distance covered in a time unit due to the initial capillary pressure $\Delta p_\gamma(v)$ acting on the film surface element. Subsequently, one could account for the difference in the initial radial positions by writing

$$-F_{\gamma,r}(v)/\gamma + b\cos(\pi - v) \tag{3.19}$$

where the first term represents the distance covered by the exerted force in a time unit, and the second term is the radial distance advantage of the ball to which the force is applied, a concept depicted in figure 3.8. Here, forces are given a negative sign to ensure the distance from the torus center $b\cos(v)$ is seen as a benefit for a given point when a positive integral suggests an overall hole size reduction, favoring the healing process. By applying equation 3.19 with 3.16, the result is:

$$2\int_{\frac{\pi}{2}}^{3\pi/2}\left(\int_0^{2\pi}(a+2b\cos(v))\cos(v)du - b\cos(v)\right)dv \tag{3.20}$$

which, when equated to zero for finding the healing threshold, could be solved analytically:

$$2\pi\cdot\left(b\cdot\left(\frac{\sin(2v)}{2}+v\right)+a\sin(v)\right)-b\sin(v)=0$$
$$\rightarrow \qquad \left(\pi^2+1\right)b-2\pi a=0$$

$$\frac{a}{b}=\frac{\pi^2+1}{2\pi} \tag{3.21}$$

where the integral constant has been taken equal to zero. Using expression 3.17, the healing threshold based on the proposed hypothesis (equating equation 3.20 to zero) is found

$$d^{*c} = 0.73 \tag{3.22}$$

Equation 3.22 suggests that for a film with a circular profile (in 2D axisymmetric) connected to a flat segment at points $v = \pi/2$ and π as depicted in figure 3.3, any hole smaller than $d = 0.73\delta$ would eventually close and heal – a hypothesis based on analyzing the exerted initial radial force on the film surface and the radial position of each surface element.

Although this hypothesis is restricted to films with circular hole profiles, it is conceivable to have different hole configurations while retaining the circular profile and simply adjusting

the angular segment of the torus linked to the flat one. In the above case, this angular segment is defined by $v \in [\pi/2, 3\pi/2]$. Conversely, studies like Stumpf et al. (2023) examine a rim with $v \in [0.21\pi, 1.79\pi]$, discontinuously linked to the flat portion resembling a developed rim, to account for the mass conservation after the hole nucleation in a flat film. The presented hypothesis will be applied to the developed rim hole configuration in the subsequent sections.

3.2.1 Numerical Examination of the Healing Threshold Hypothesis

The proposed hypothesis was evaluated using numerical simulations to determine the healing threshold. This evaluation utilized the dichotomy process, a root-finding method elaborated in section 2.4.3. The simulations were based on the numerical configuration specified in section 2.4.1.2. Additionally, seven levels of mesh refinement within the film thickness were used in conjunction with the default values for the mesh adaptation criterion, as highlighted in section 2.3.4. For a standard oceanic scenario, characterized by the dimensionless parameters in table 2.1, the healing threshold was computed to be:

$$d^{*c} = 0.750 \tag{3.23}$$

This value was determined with an accuracy of ± 0.005 in the dichotomy process. Given that the dynamics of the problem were not incorporated when establishing the healing threshold hypothesis, it may be more accurate to carry out the dichotomy simulations for inviscid scenarios with very high Laplace numbers for both fluid phases. Meaning the surface tension effects sharply dominate the viscous ones in the problem. Accordingly, the previously established liquid and gas Laplace numbers for the standard oceanic case, $\mathrm{La}_l = 663$ and $\mathrm{La}_g = 3446$, were increased to $\mathrm{La}_l = 1e^6$ and $\mathrm{La}_g = 1e^6$ respectively. In this inviscid context, the healing threshold was found to be:

$$d^{*c} = 0.771 \tag{3.24}$$

This value was derived with a similar level of precision in the dichotomy process. A juxtaposition of the numerically found healing threshold 3.24 with the prediction 3.22 reveals a mere 5% difference between the two. This close agreement underscores the validity of the hypothesis in its capacity to predict the healing threshold for a torus-shaped hole.

3.3 Mass Conserving Holes - Stumpf et al. (2023)

Stumpf et al. (2023) examined the minimum size of a hole necessary for its nucleation to be energetically favorable compared to a flat film, considering the conservation of mass between

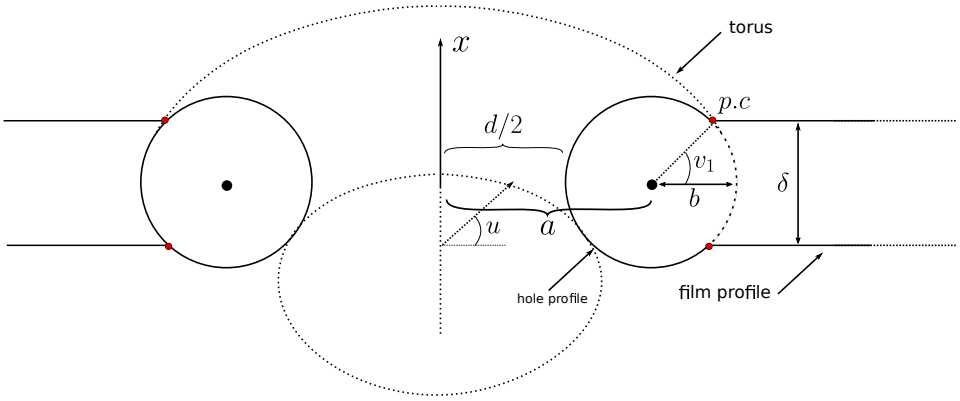

Fig. 3.9 Illustration of the developed rim with circular profile employed by Stumpf et al. (2023) to represent a hole shape in a thin liquid film that accounts for mass conservation after hole nucleation in a flat film. The segment of the torus is characterized by parameters a, b, and v_1 with the same definitions as in figure 3.3. Angle $v_1 < \pi/2$ demarcate the portion of the torus corresponding to the hole shape attached to the flat part at point P.c profile and based on equation 3.25. In this configuration $\delta \neq 2b$.

the two states. Although Stumpf et al. (2023) does not specifically investigate the healing threshold of holes, assuming they spontaneously grow if their size surpasses a critical value, this critical value aligns conceptually with the hole healing (or bursting) threshold. This section reviews the methodology outlined by Stumpf et al. (2023), and the healing threshold proposed in the preceding section is applied to Stumpf et al. (2023)'s suggested mass conserving hole configuration.

Stumpf et al. (2023) employs a circular profile for the hole shape, representing a developed rim or a segment of a torus with a diameter larger than the thickness of the flat part of the film. This configuration is depicted in figure 3.9. For mass conservation to hold valid after the hole nucleation in a flat film with thickness δ, the ratio of the rim radius to the film thickness, or b/δ, must adhere to the relation

$$\frac{b}{\delta} = \frac{\frac{a}{\delta}}{\sqrt{2\pi\frac{a}{\delta} - 1}} \tag{3.25}$$

which also defines what portion of a torus corresponds to this mass-conserving shape. Based on equation 3.25, the values for v_1 and v_2 can be determined as:

$$v_1 = \arcsin\left(\frac{\delta}{2b}\right), v_2 = 2\pi - v_1 \tag{3.26}$$

From expressions 3.25 and 3.26, it becomes apparent that an additional equation is necessary to determine $\frac{a}{\delta}$. Utilizing energetic considerations, Stumpf et al. (2023) deduced:

$$a^{*c} = \frac{a}{\delta} = 2.18 \tag{3.27}$$

At this value and above, the nucleation of a spontaneously growing hole is energetically preferred to the flat film. This critical ratio can also be translated into:

$$d^{*c} = \frac{d}{\delta} = 2.74 \tag{3.28}$$

which relates the hole minimum size to the film thickness using the relation $d = 2(a-b)$. Furthermore, using this critical ratio in conjunction with equations 3.26 and 3.27, the portion of the torus that constitutes the developed rim is determined as:

$$v_1 = 0.21\pi, v_2 = 1.79\pi \tag{3.29}$$

3.3.1 Numerical Investigation of Stumpf et al. (2023)

Based on the numerical configuration introduced in section 2.4.1.2 and the hole shape proposed by Stumpf et al. (2023), the present section presents the numerical results of the dichotomy process on the healing threshold for this specific case. In these simulations, six levels of mesh refinement within the film thickness were used, and a value of $\zeta = 1e^{-3}$ was chosen for the volume fraction, velocity, and pressure field during the mesh refinement process. With the values from table 2.1, which represent a standard case with seawater properties as elaborated in section 2.5, the healing threshold is determined as

$$a^{*c} = 1.288 \tag{3.30}$$

with an accuracy of ± 0.01 in the dichotomy process. Given this healing threshold, the corresponding mass conserving v_1 and v_2 were derived using equations 3.25 and 3.26 as

$$v_1 = \frac{\pi}{4} + 0.004\pi, \quad v_2 = 2\pi - v_1 \tag{3.31}$$

In a manner analogous to section 3.1.2, three hole sizes, represented as $d/\delta = \{0.5, 1.00, 1.5\}$ or equivalently $a/\delta = \{0.90, 1.18, 1.47\}$, were analyzed. The primary objectives were to comprehend and compare the variations in the film interface near the hole and the associated pressure field modifications relative to the half-torus case. The findings are depicted in figures 3.10 and 3.11, with five snapshots taken at intervals consistent with section 3.1.2, approxi-

mately corresponding to time steps $t^* = \{0.0, 0.11, 0.22, 0.45, 0.9\}$. For a direct comparison, identical parameters were utilized to generate the pressure color map and velocity vectors while maintaining the same seven mesh levels. It is worth noting that the mesh level used in the simulations to produce these figures differed from the dichotomy process in this case, which is six levels.

The flickering behavior was once again observed in figure 3.10, but in this instance, the flickering occurs for the $d^* = 1.5$ scenario instead of $d^* = 1.0$. This stems from the fact that the healing threshold is altered and increased in this configuration compared to the previous one with a half-torus hole shape. The progression of hole shape from an initially discontinuously defined geometry is also observable. Additionally, figure 3.11 provides insights into the pressure field progression and how the flow was affected by variances in internal pressures throughout the simulations. The effect of the singular point is also notable through the pressure color maps, where a strong capillary wave travels in both directions from the discontinuity location in the initial configuration.

By comparing equations 3.30 and 3.27, it is evident that the numerical simulations yield a notably different value for the healing threshold of the theoretically suggested hole configuration with mass conservation, as posited by Stumpf et al. (2023). Given that the dynamics of the problem were not considered in the healing threshold derivation via equation 3.27, it might be beneficial to conduct the dichotomy simulations for a high Laplace number scenario. This approach would align the simulated problem more consistent with the theoretical context. Consequently, the liquid and gas Laplace numbers, previously defined as $\mathrm{La}_l = 663$ and $\mathrm{La}_g = 3446$, were increased to $\mathrm{La}_l = 1e^6$ and $\mathrm{La}_g = 1e^6$, respectively. Adopting these revised values, which renders the problem almost inviscid, led to the determination of the healing threshold as

$$a^{*c} = 1.375 \tag{3.32}$$

with an accuracy of ± 0.005 in the dichotomy process. This result is somewhat closer to the value proposed by Stumpf et al. (2023), which is $a^{*c} = 2.18$. However, the theoretical prediction significantly diverges from the numerical outcomes. Given the numerical insights through observing how the initial state evolves, via figure 3.10 and 3.11, this difference in the healing threshold could be attributed to the presence of a sharp discontinuity in the proposed hole geometry as discussed above.

Based on the new healing threshold, one could find the new torus angles as

$$v_1 = \frac{\pi}{4} - 0.0008\pi, \quad v_2 = 2\pi - v_1 \tag{3.33}$$

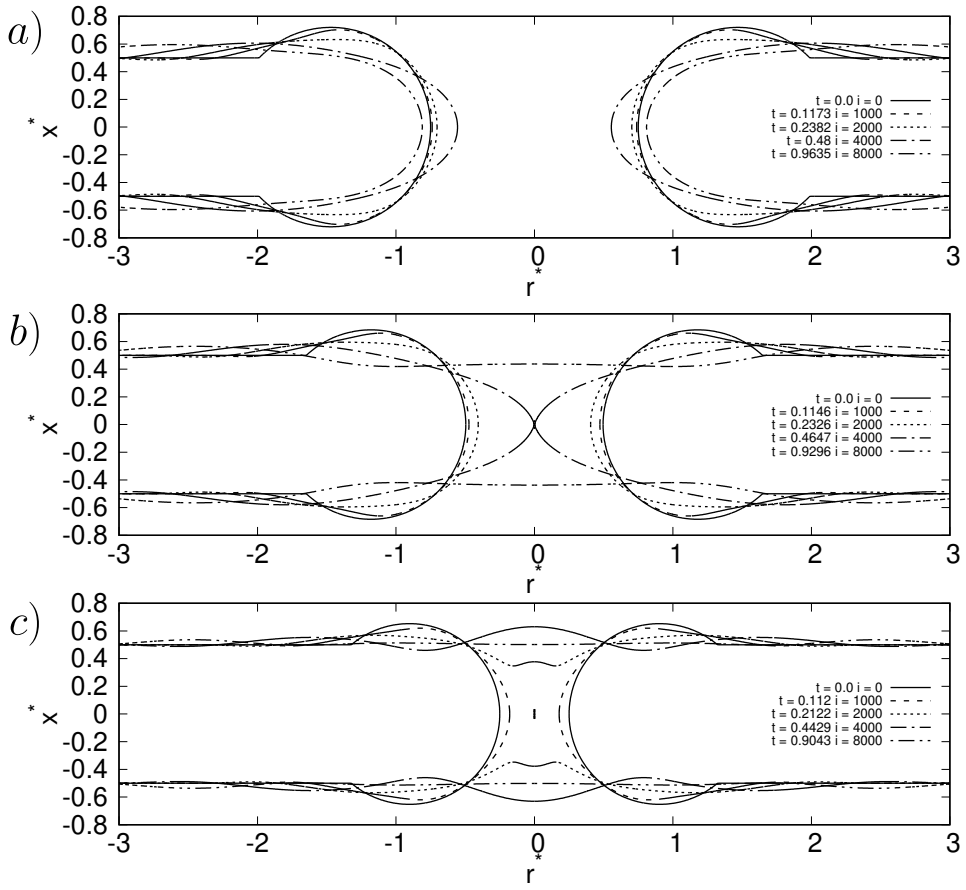

Fig. 3.10 Evolution of the film interface near the hole area with the developed rim profile for three hole sizes across five simulation steps $i = \{0, 1000, 2000, 4000, 8000\}$. Case a) with $d^* = 1.5$, b) with $d^* = 1.0$, and c) with $d^* = 0.5$. These simulation steps correspond to $t^* \approx \{0.0, 0.11, 0.22, 0.45, 0.9\}$. The progression of the interface shows the different dynamics, from healing in $d^* = \{0.5, 1.0\}$ to "flickering" and eventual bursting in the $d^* = 1.5$. The set of parameters used for these simulations is listed in table 2.1.

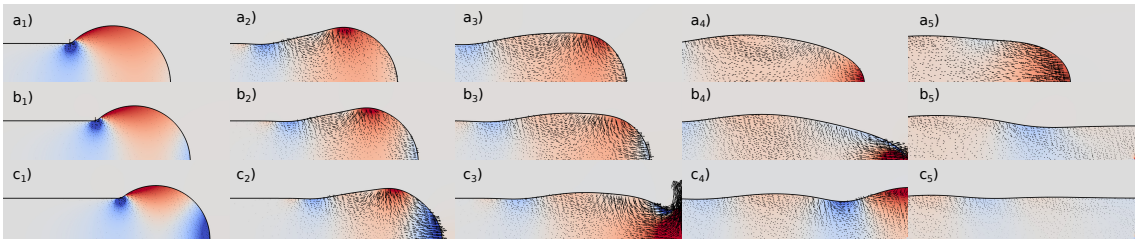

Fig. 3.11 Evolution of pressure fields for holes with developed rim profiles and sizes across five simulation steps $i = \{0, 1000, 2000, 4000, 8000\}$ corresponding to $t^* \approx \{0.0, 0.11, 0.22, 0.45, 0.9\}$. Case a) with $d^* = 1.5$, b) with $d^* = 1.0$, and c) with $d^* = 0.5$. Color map values range from -1.5 to 1.5 consistently within and across cases. The existence of a strong discontinuation in the pressure field is evident in a1, b2, and b3 at the point where the flat part meets the hole profile. The set of parameters used for these simulations is listed in table 2.1.

Analyzing the changes in the angle v_1 when increasing the Laplace number (comparing equation 3.31 and 3.33) suggests that this value converges to $v_1 = \pi/4$ in a purely inviscid scenario.

It should be noted that the hypothesis proposed by Stumpf et al. (2023) had never been previously explored, either theoretically or numerically. This makes the expression 3.30 the first numerical investigation of this recent work.

3.3.2 Applying the Analytical Hypothesis

Given that the shape of the hole retains its torus geometry despite variations in the angle of attachment to the flat portion of the film, the hypothesis proposed in section 3.2 can be applied to this configuration. Consequently, one would expect to find $a^{*c} = 1.375$ using the proposed hypothesis, a value found above through numerical simulations for this configuration.

To derive this, one can utilize equation 3.21, which yields the critical ratio $a/b = 1.73$. This can be combined with equation 3.26, setting $v_1 = \pi/4$, to deduce the following:

$$\begin{aligned} \frac{b}{\delta} &= \frac{1}{2\sin(\pi/4)} \\ \frac{a}{\delta} &= \frac{a}{b}\frac{b}{\delta} \\ \rightarrow \qquad a^{*c} &= \frac{1.73}{2\sin(\pi/4)} \\ a^{*c} &\approx 1.22 \end{aligned} \tag{3.34}$$

This result deviates from the numerical result of the inviscid case, where $a^{*c} = 1.375$, by 10%. It is worth noting that in deploying the hypothesis from section 3.2, which was derived considering a half-torus hole shape, the additional torus segments $v \in [\pi/4, \pi]$ and $v \in [3\pi/2, 7\pi/4]$ were not incorporated into the equation 3.20. Hence, relative to section 3.2, the healing threshold has been altered even when using the same critical ratio $a/b = (\pi^2+1)/(2\pi)$ provided by equation 3.21. This alteration, thus, is only due to the adjustment of the relation $b/\delta = 1/2$ to $b/\delta = 1/2\sin(\pi/4)$ to accommodate the geometric modification.

Furthermore, since in this configuration, there exist two variables, the angle of attachment to the torus or equivalently b/δ, and the hole size given by a/δ, the proposed hypothesis is not capable of predicting the hole healing threshold of its radius without being provided by the value for b/δ that defines the other constraint on the hole geometry rendering the hypothesis impractical in its presented form while leaving the possibility of modifications to account for the second geometrical constraint.

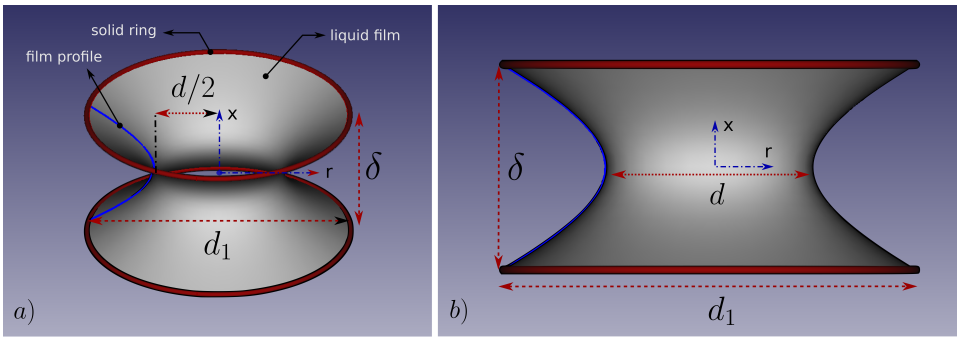

Fig. 3.12 Geometrical representation of a soap film between two metal rings juxtaposed with a description of an axisymmetric hole on a liquid film, illustrating the analogy invoked by Taylor and Michael (1973). In this configuration, d indicates the minimum radial distance, d_1 the size of the metal rings, and δ is the distance between the rings in the soap film problem, corresponding to the minimum and maximum diameter of the hole and film thickness in the film with a hole problem, respectively. The soap film has the catenoid profile described by equation 3.35 and is highlighted with the blue line in this figure.

3.4 Zero Mean Curvature Holes – Taylor and Michael (1973)

In their study, Taylor and Michael (1973) posited that the challenge of healing holes can be analogized with the behavior of a soap film suspended between two metal rings, as depicted in figure 3.12. Based on this analogy, Taylor introduced a prediction for the hole healing threshold. Below is a detailed summary of the methodology for determining this threshold.

It is well-established that a soap film adopts the shape of a catenoid, a minimal surface with zero mean curvature at all points. Utilizing the formulation by Lamb (1916), Taylor and Michael (1973) initiated their analysis with the equation

$$\frac{r}{d/2} = \cosh \frac{x}{d/2} \tag{3.35}$$

to define the catenoid profile. The boundary condition for the catenoid soap film between the two metal rings is given by

$$\cosh \delta/d = d_1/d \tag{3.36}$$

Here, d_1 represents the ring diameter, equivalent to the hole maximum radius or the gap between the hole two inner edges. At the same time, δ signifies the distance between the rings, mirroring the film thickness as shown in figure 3.1. Recasting this boundary condition using $\zeta = \delta/d$ yields

$$\cosh \zeta/\zeta = d_1/\delta \tag{3.37}$$

Within expression 3.37, the function $\cosh \zeta/\zeta$ has its smallest value at the critical juncture where $\zeta = \coth \zeta = 1.200$. As a result, the maximal value of δ/d_1 where the soap film remains

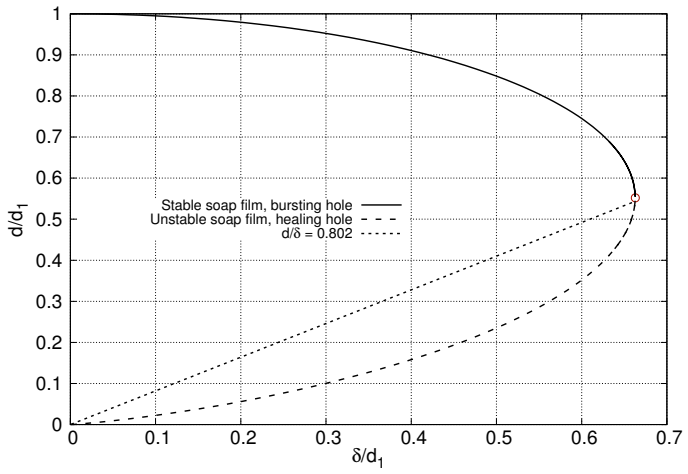

Fig. 3.13 Graph illustrating the relationship between the minimum and maximum radial distance d/d_1 in the catenoid soap film and the ratio of rings distance to their size δ/d_1. The dashed sloped line shows the hole healing threshold predicted by Taylor and Michael (1973), intersecting the profile at the point where $\delta/d_1 = 0.663$ shown by a red circle. Points on the curve upper half correspond to stable catenoid configurations, while those on the lower half indicate unstable films prone to rupturing or a bursting and healing hole, respectively

in equilibrium is $\delta/d_1 = 0.663$. Beyond this value, no catenoid shape can satisfy the boundary condition. For values below this threshold, Taylor and Michael (1973) identified two potential configurations emerging for the soap film that can fulfill the boundary conditions by analyzing the surface energy variations, the same basis employed by Stumpf et al. (2023). Accordingly, there exists two distinct ζ values for each δ/d_1 smaller than 0.663. Among them, one is stable, while the other is inherently unstable. On the other hand, only a single configuration exists at $\delta/d_1 = 0.663$ that was defined as an unstable equilibrium.

Hence, in the context of a soap film, where the relevant parameters are δ and d_1, the threshold for soap film stability, as calculated by Taylor and Michael (1973), stands at $\delta/d_1 = 0.663$. Consequently, when the two rings immersed in a soapy liquid are pulled apart, if this value is exceeded, the soap film will rupture as there exists no catenoid shape satisfying the $\delta/d_1 > 0.663$ ratios. In contrast, the film will spontaneously adopt the stable configuration at lower values out of the two possibilities.

Figure 3.13 charts the relationship between d/d_1 and δ/d_1. This graph reveals that any vertical line with $\delta/d_1 < 0.663$ intersects the curve at two locations, denoting two possible hole sizes $d/\delta = 1/\zeta$ configurations for the soap film. The upper half of the curve corresponds to stable soap film configurations, whereas points on the lower half indicate unstable configurations. On the other hand, only a single configuration is possible for every slope line representing a unique d/δ value as the slope line intersects the curve only once to define the value of δ/d_1.

It is important to note that in the study by Taylor and Michael (1973), an unstable configuration for the soap film corresponds to the case where the hole in the liquid film closes or heals (i.e., the hole collapses). In contrast, the stable catenoid shape in the soap film implies the retraction and expansion of the hole, leading to the bursting of the film.

Based on their analysis, Taylor and Michael (1973) proposed the healing threshold as

$$d_1^{*c} = 0.663 \tag{3.38}$$

By incorporating the boundary condition in equation 3.37 and employing a numerical script for the Newton root-finding method, this can be transformed into

$$d^{*c} = 0.802 \tag{3.39}$$

Taylor and Michael (1973) verified this theoretical conclusion by experimenting with catenoid soap films. They gradually separated two metal rings immersed in soapy liquid and determined the furthest possible distance between $\delta = 1.99cm$ for rings of diameter $d_1 = 3cm$. They observed that soap films would collapse for values surpassing $d_1/\delta = 0.660$, identifying this as the critical threshold for maintaining the soap film in the catenoid shape. This critical value corresponds to $d^{*c} = 0.773$, closely reproducing the value predicted in equation 3.39.

Moreover, this value is also in close agreement with the value numerically found in equation 3.23 for the half-torus hole shape. However, one must note that near the critical value for d_1^{*c}, a slight variation in d_1^{*c} can lead to more significant changes in d^{*c}, as shown in figure 3.13. This is due to the fact that the curve is almost vertical near the critical value. Hence, the conversion from d_1^{*c} to d^{*c} may minimize the error in the healing threshold (d^{*c}) prediction.

3.4.1 Numerical Investigation of Taylor and Michael (1973)

Numerical simulations have been utilized to determine the healing threshold for the hole configuration proposed by Taylor and Michael (1973) through the dichotomy process. In these simulations, the numerical configuration detailed in section 2.4.1.2 was modified to include the catenoid profile for the hole shape. All other numerical parameters remained consistent with those described in section 3.2.1. As a result, the healing threshold for a typical oceanic film, as outlined in section 2.5, was determined as:

$$d^{*c} = 0.687 \tag{3.40}$$

with an accuracy of ± 0.005 in the dichotomy process.

For the inviscid case, where high Laplace numbers, $\mathrm{La}_l = 1e^6$ and $\mathrm{La}_g = 1e^6$, are considered, the healing threshold was determined to be:

$$d^{*c} = 0.732 \tag{3.41}$$

To analyze the healing threshold predicted by Taylor and Michael (1973), one should contrast the numerical result for the inviscid case in equation 3.41 with that in equation 3.39. This comparison is relevant since the dynamics of the problem were not considered when Taylor and Michael (1973) determined the healing threshold by statically studying the soap film problem. This comparison indicates a 10% difference in the predicted value compared to the numerical simulation results. This difference can be attributed to the presence of a sharp discontinuity in the film geometry at the point where the flat part meets the hole catenoid profile.

Similar to sections 3.1.2 and 3.3.1, the evolution of the film interface and snapshots of the pressure color maps for three hole sizes are presented in figures 3.14 and 3.11, respectively. The same set of both numerical and dimensionless parameters was employed to ensure a direct comparison across all three sections[2]. Using equation 3.37, the three hole sizes $d/\delta = \{0.5, 1.00, 1.5\}$ correspond to $\delta/d_1 = \{0.53, 0.65, 0.54\}$. This indicates that the ratio for d/d_1 in the catenoid shape increases as d does as well. This phenomenon is evident when observing the initial configurations for the three scenarios: the discontinuity becomes more pronounced in cases with larger d values because of the elevated d/d_1 ratio. The flickering behavior near the healing threshold, observed in the previous cases, is also present and noticeable in both $d/\delta = 1.0, 1.5$ cases.

3.5 Summary

In this chapter, the intricacies of the hole dynamics on a thin liquid film were presented in detail, exploring the underlying physics of the problem and the mechanisms that enable hole healing on a film. Specifically, it was elaborated on how smaller holes possess the potential to close and heal while larger ones tend to burst. The Young-Laplace equation, which determines the capillary pressure due to surface tension, was detailed along with the mathematical method to compute the mean curvature of a given surface.

Building upon this knowledge, the capillary pressure profile over the interface for half-torus-shaped holes on flat films was derived. Preliminary simulations were conducted, offering

[2]However, for case a) with $d/\delta = 1.5$, the final snapshot was taken at $i = 7620$ instead of $i = 8000$ due to an unintended early termination of the simulation.

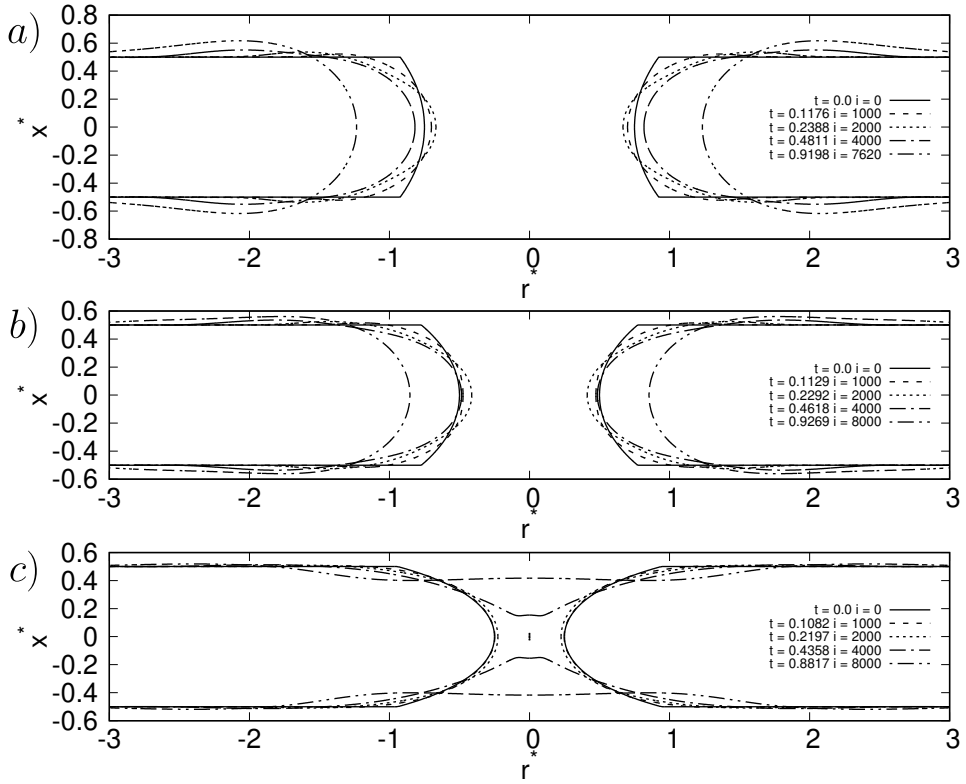

Fig. 3.14 Evolution of the film interface near the hole area with the catenoid profile for three hole sizes across five simulation steps $i = \{0, 1000, 2000, 4000, 8000\}$. Case a) with $d^* = 1.5$, b) with $d^* = 1.0$, and c) with $d^* = 0.5$. These simulation steps correspond to $t^* \approx \{0.0, 0.11, 0.22, 0.45, 0.9\}$. The interface evolution shows the healing behavior for $d^* = \{0.5\}$ to "flickering" in $d = 1.0$ and a direct bursting in the $d^* = 1.5$ case. The set of parameters used for these simulations is listed in table 2.1.

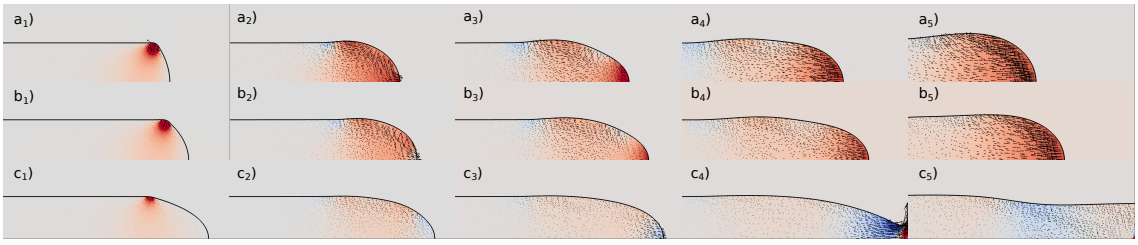

Fig. 3.15 Evolution of pressure fields for holes with catenoid profiles and sizes across five simulation steps $i = \{0, 1000, 2000, 4000, 8000\}$ corresponding to $t^* \approx \{0.0, 0.11, 0.22, 0.45, 0.9\}$. Case a) with $d^* = 1.5$, b) with $d^* = 1.0$, and c) with $d^* = 0.5$. Color map values range from -1.5 to 1.5 consistently within and across cases. A pronounced discontinuity in the pressure field is clearly observed in a1, b2, and b3, where the hole profile joins the flat section even though the initial film curvature profile is uniformly zero in this configuration. The set of parameters used for these simulations is listed in table 2.1.

insights into the dynamics of the problem, evident through the interface evolution, pressure color maps, and overlaid velocity vector fields. The dynamics were observed to be profoundly influenced by the film initial configuration, leading to a differential in capillary pressure values. This, in turn, orchestrates the flow within the film and around the hole region.

A hypothesis was postulated with these observations and the analytical expression for the film mean curvature. It aimed to determine the hole healing threshold, primarily focusing on a static examination of the initial capillary pressure field for holes of half-torus shape. This hypothesis was tested against numerical results obtained through a dichotomy process with high precision. The outcome validated the hypothesis capability to calculate the healing threshold with an error margin of less than 5%.

The same hypothesis was subsequently applied to another hole configuration, as suggested by Stumpf et al. (2023), related to spontaneously growing holes in thin liquid films. The results indicated the hypothesis remained valid, though with a slightly higher margin of error (10%) when juxtaposed with simulation results for the healing threshold of this particular hole configuration, referred to as the developed rim.

The developed rim configuration posited by Stumpf et al. (2023), derived from mass conservation principles, was discussed and examined numerically. The healing threshold proposed by Stumpf et al. (2023) for such a configuration, grounded in energetic arguments, was contrasted with numerical simulation dichotomy findings. As a result, the analytical predictions for this configuration $a^{*c} = 2.180$ deviated significantly from the numerical simulation finding $a^{*c} = 1.375$. Given the numerical insights through observing how the initial state evolves, this difference could be attributed to a sharp discontinuity in the proposed hole geometry. The effect of this discontinuity on the pressure field was also examined, revealing a strong capillary wave propagating in both directions from the discontinuity location in the initial configuration.

Furthermore, the primary work by Taylor and Michael (1973) received a comprehensive examination. A central proposition from this research—that the problem of the hole on a thin liquid film can be analogized with soap films between two metal rings—was elaborated upon in detail. The healing threshold postulated by Taylor and Michael (1973) was examined against the numerical outcomes, resulting in close parallels, with $d^{*c} = 0.732$ from the simulations compared to $d^{*c} = 0.802$ from the analytical prediction by Taylor and Michael (1973). This difference can be attributed to the presence of a strong discontinuity in the pressure field at the point where the flat part meets the hole catenoid profile despite the initial film curvature profile being uniformly zero over the entire film.

The comprehensive examination in this chapter bridged analytical theories with numerical simulations, providing a robust understanding of the factors determining the hole healing threshold.

Chapter 4

Critical Hole Dynamics

The intricate dynamics of holes in thin liquid films were detailed in the previous chapter, especially how smaller holes tend to close in contrast with larger holes due to the overall exerted capillary pressure in the film that depends on the hole shape. Subsequently, the hole healing threshold was introduced and numerically measured for different hole configurations. The bursting and healing concept was delved into using numerical measurements. However, a primary question remains intriguing: In the proximity of the hole healing threshold, what mechanism causes the two almost identical holes differing only marginally in initial size to result in dramatically different end-states, with one bursting and the other healing? This chapter aims to answer this question.

4.1 Near Threshold Simulations

An in-depth study is conducted on two cases to investigate the hole dynamics near the healing threshold and elaborate on the mechanism responsible for the radical change caused by a minimal difference in the initial state of a hole. The two test cases are defined similarly based on the standard film bursting in the oceanic context noted in table 2.1. The numerical configuration used in these cases is the semi-spherical bubble cap described in section 2.4.2 and 2.3.4 using seven mesh levels and high accuracy for the solvers and mesh adaptation to capture the details necessary for this study.

These simulations are distinguished solely by the initial size of the holes. These sizes are selected to be as near as possible to the healing threshold while ensuring they are discernible from one another based on the accuracy of the mesh levels and the dichotomy process used.

The results of the dichotomy process indicate a value of $d^{*c} = 0.749 \pm 0.005$ for the present numerical configuration. Consequently, the two cases lie closest to this critical value. For the healing and bursting cases, the sizes selected are $d^*_{\mathrm{h}} = 0.744$ and $d^*_{\mathrm{b}} = 0.754$, respectively,

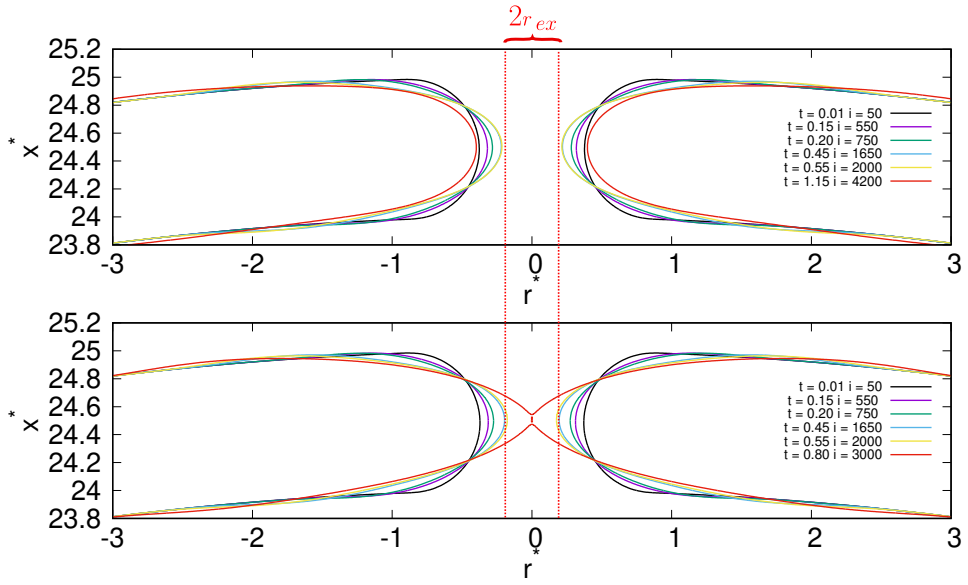

Fig. 4.1 Film interface near the hole region for the bursting ($d_{\mathrm{b}}^{*} = 0.754$ on the top) and healing ($d_{\mathrm{h}}^{*} = 0.744$ on the bottom) case, selected to lie closest to the critical value $d^{*c} = 0.749 \pm 0.005$ determined by the dichotomy process. The snapshots are given at the recognized pivotal moments of the hole dynamics $t_a^{*} = 0.15$, $t_b^{*} = 0.2$, $t_c^{*} = 0.45$, $t_d^{*} = 0.55$. Additionally, the initial state of the simulations and the final record before the termination are included. The final record for the healing case occurs earlier than the bursting case and as soon as the healing is detected. On the other hand, the final record in the bursting case has been taken when the hole size has become larger than the initial hole size. r_{ex} denotes the critical radial distance upon reaching which the hole could not retract back.

where the subscripts h and b refer to the healing and bursting case, respectively. The initial hole shapes and film interfaces for these two cases are shown in figure 4.1.

One could track the location of the hole tip in the simulation and plot the evolution of the hole minimum radius with time $r_0^{*}(t)$ as presented in figure 4.2a. The plot for $r_0^{*}(t)$ shows how the two cases start from virtually the same initial positions and follow the same trend where the film tip extends towards the center until $t^{*} \approx 0.45$ when they depart to radically different directions.

4.2 Tip Position, Velocity, and Acceleration

Using a simple backward finite difference discretization on the time derivative function ∂_t, one could estimate the velocity of the hole tip $\partial_t r_0^{*}(t)$ by

$$\partial_t r_0(t + \Delta t/2) = \frac{r_0(t) - r_0(t - \Delta t)}{\Delta t} \tag{4.1}$$

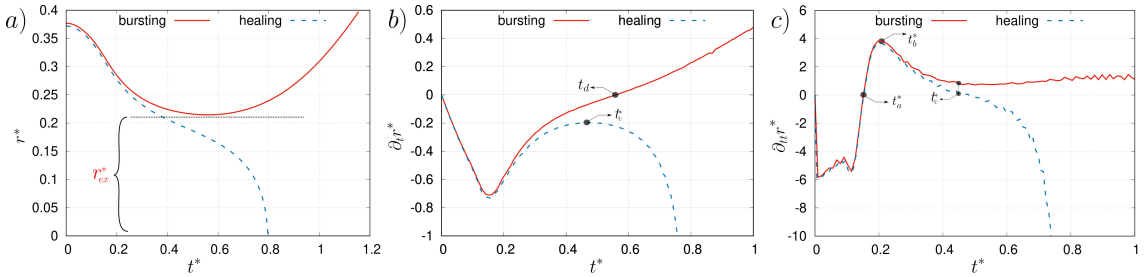

Fig. 4.2 Evolution of the hole minimum radius $r_0^*(t)$ and its first and second temporal derivatives with time for the bursting and healing case. Sub-figure a) compares the hole tip minimum radius over time for the two cases, illustrating their similar starting points and initial trends before diverging at $t^* \approx 0.45$. Sub-figure b) provides the hole tip velocity and its acceleration in sub-figure c) emphasizes their distinct behaviors post-divergence. Pivotal moments of the hole dynamics are recognized and marked through these plots $t_a^* = 0.15$, $t_b^* = 0.2$, $t_c^* = 0.45$, $t_d^* = 0.55$, while r_{ex} denotes the critical radial distance.

and for its acceleration $\partial_{tt} r_0^*(t)$ using

$$\partial_{tt} r_0(t + \Delta t/2) = \frac{r_0(t) - 2r_0(t - \Delta t) + r_0(t - 2\Delta t)}{\Delta t^2} \tag{4.2}$$

Applying this formulation to the numerical measurements of $r_0^*(t)$ inevitably increases the noise in the measured data. Therefore, a smoothing filter could filter out the derivative noise. Here, the natural cubic splines method was employed to plot the hole tip velocity and acceleration, given in figure 4.2b and c.

Examining the plot for the tip velocity $\partial_t r_0^*(t)$ and acceleration $\partial_{tt} r_0^*(t)$, one can find four critical points in these two simulations:

- $t_a^* \approx 0.15$ when $\partial_{tt} r_0^*(t) = 0$ for both cases, meaning that the acceleration of the tip changes from inward to outward direction.
- $t_b^* \approx 0.2$ when the tip experiences the maximum outward acceleration with $\partial_{ttt} r_0^*(t) = 0$.
- $t_c^* \approx 0.45$ when for the healing case $\partial_{tt} r_0^*(t) = 0$. Hence, the tip restarts the inward acceleration before its velocity can be reversed. In contrast, the bursting case continues to accelerate outwardly until, as a result, its velocity eventually changes sign from the inward to outward direction.
- $t_d^* \approx 0.55$ when the tip reverses direction, from contraction to retraction, in the bursting case with $\partial_{tt} r_0^*(t) = 0$.

Figure 4.3 provides pressure color maps overlaid with velocity vectors and film interface for the two cases and recorded at these critical moments during the simulation. Initial inward acceleration is observable for both scenarios when $t^* < t_a^*$. This acceleration is influenced by

the initial interface curvature and the ensuing pressure field within the film, as presented in sub-figures h1 and b1 of figure 4.3. A low-pressure zone at the tip of the film (or hole) prompts the fluid to accelerate inward towards this area. This activity attenuates curvature gradients at the interface by altering the surface of the film at its tip. By the time $t^* = t_a^*$ is reached, the tip has a near-uniform pressure distribution, resulting in negligible accelerations. This condition can be observed in sub-figures h2 and b2 of figure 4.3.

However, as an inward momentum has already been established due to the initial imbalances, the fluid continues its inward trajectory beyond the acceleration-free state. This alters the shape of the interface past its near-uniform state, leading to an elevated pressure region at the tip. Simultaneously, this new shape induces an outward acceleration, counteracting the inward momentum and movement of the hole tip. Nonetheless, this outward acceleration and the high-pressure region at the tip do not increase monotonically. Instead, it peaks at $t^* = t_b^*$. The corresponding dynamic is visualized in sub-figures h3 and b3 of figure 4.3. In order to go beyond mere observations, this phenomenon can be further comprehended by analyzing the curvature temporal and radial progression.

4.3 Tip Curvature Temporal and Radial Evolution

At the tip of the hole, where $x = 0$ and $r = r_0$, the total curvature of the surface (some of the two principal curvatures) $\kappa_{r_0} = 2H(r_0)$ is plotted against time in figure 4.4a where the critical moments of the holes dynamic are marked accordingly. Even though the radical shift in the hole dynamics is evident in different trajectories taken for the total curvature in the two cases, the cause for such behavior remains hidden. Therefore, one could investigate further by examining the two curvature components separately.

The total curvature κ_{r_0} at the tip has two components, with one always negative and the other positive (see section 3.1.2)

$$\kappa_{r_0} = \kappa_{r_0}^- + \kappa_{r_0}^+ \tag{4.3}$$

For the negative component of the curvature at the tip, $\kappa_{r_0}^-$ the value is directly linked to the hole size and can be found analytically by using

$$\kappa_{r_0}^- = -1/r_0 \tag{4.4}$$

On the other hand, no analytical expression exists for $\kappa_{r_0}^+$ beyond the initial state of the film, where a half circle defines the hole profile. Nevertheless, having the measurement for κ_{r_0} directly from the simulations along with the knowledge of equation 4.4, one could calculate

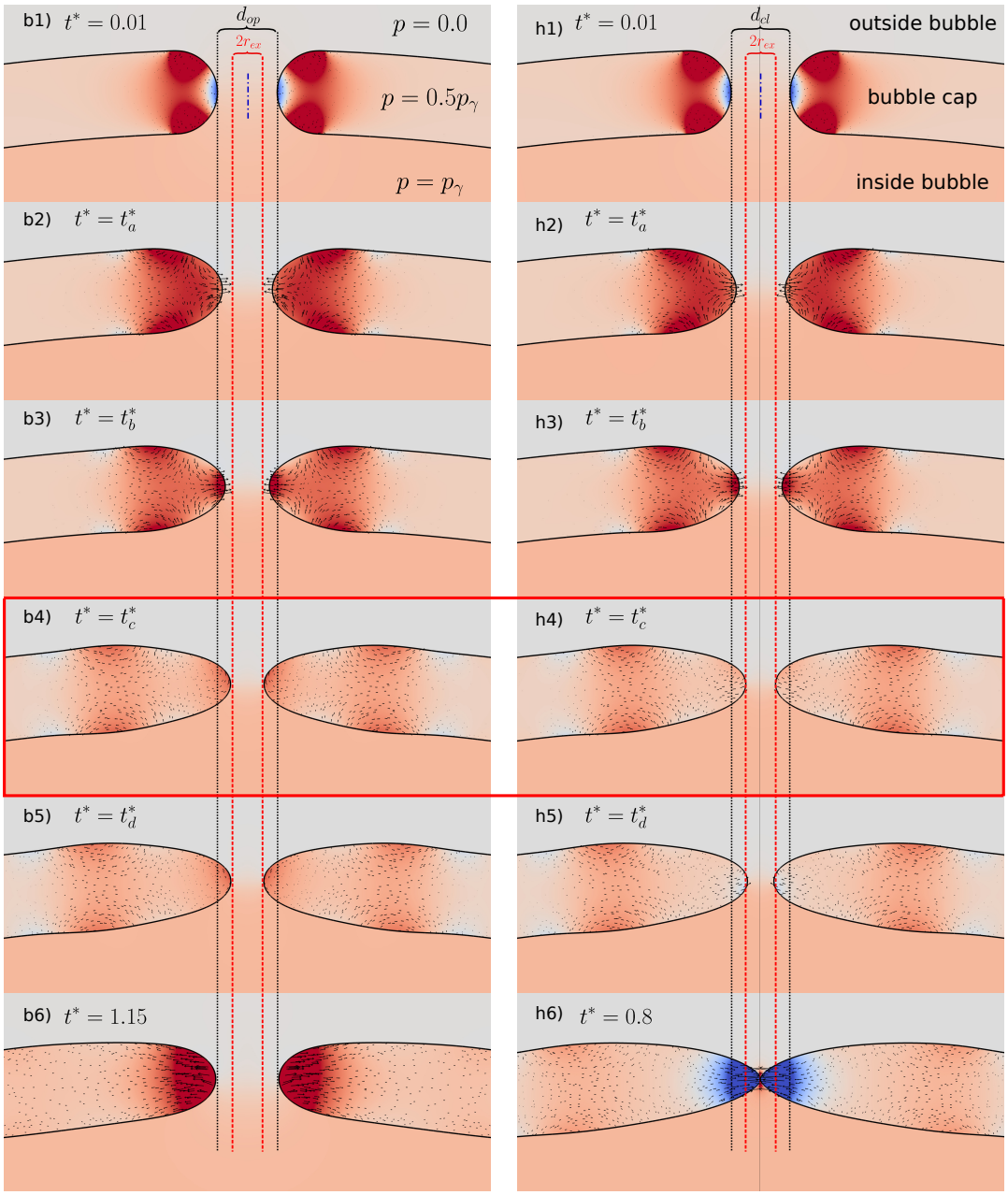

Fig. 4.3 Pressure color maps overlaid with velocity vectors and film interface at various time stamps. The top and bottom rows represent the bursting and healing cases, respectively. Sub-figures h1) and b1) illustrate the initial inward acceleration due to surface tension-induced pressure differences. By sub-figures h2) and b2), a near-uniform pressure distribution at the tip emerges, resulting in minimal accelerations. Sub-figures h3) and b3) capture the outward acceleration peak due to the interface reshaping and the resultant pressure build-up. Sub-figures h4) and b4) illustrate the critical moment that differentiates the two cases, where the healing case reaches the critical radial distance r_{ex} while the bursting case falls short. Sub-figures h5) and b5) correspond to when the acceleration changes sign for the healing case from positive to negative. Lastly, h6) and b6) show the final record of these simulations (at different times). The time stamps are shown in each of the sub-figures.

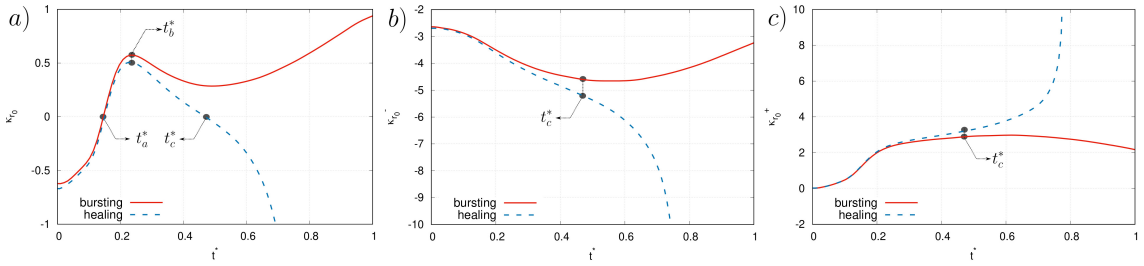

Fig. 4.4 (a) Evolution of the total curvature κ_{r_0} at the tip of the hole over time, marked with the important moments in the hole dynamic. (b) Time evolution of the negative component of curvature at the tip, $\kappa^-_{r_0}$, calculated using equation 4.4. (c) Time evolution of the positive component of curvature at the tip, $\kappa^+_{r_0}$, derived using equations 4.4 and 4.5. The radical shift in hole dynamics between the two cases is apparent through differences in curvature trajectories, but underlying causes necessitate further exploration.

$\kappa^+_{r_0}$ as

$$\kappa^+_{r_0} = \kappa_{r_0} - \kappa^-_{r_0} \tag{4.5}$$

Employing equation 4.4 and 4.5, the two components of surface curvature at the tip, $\kappa^-_{r_0}$ and $\kappa^+_{r_0}$, are plotted against time in figure 4.4b and c separately. Nonetheless, the exact cause or mechanism behind the observed radical difference in the hole dynamics remains evasive. Therefore, one could plot these parameters against the radial distance instead of time to open another window on the underlying mechanism.

4.3.1 Power Law for Tip Curvature

The total curvature and its components at the tip of the hole are plotted against the radial distance in figure 4.5a and b for both cases, respectively. Given the expression 4.4, one could calculate the rate of change for $\kappa^-_{r_0}$ with the radial distance by

$$\partial_r \kappa^-_{r_0} = 1/r_0^2 \tag{4.6}$$

Accordingly, $\kappa^-_{r_0}$ monotonically increases as the hole contracts (i.e., its minimum size r_0 decreases). On the other hand, since there is no analytical expression for $\kappa^+_{r_0}$, for one to examine its rate of change r_0, the only possibility would be to study the slope of the numerically calculated values.

It is worth mentioning that the curvature measurements from the numerical simulations commonly contain a certain level of noise, as shown in figure 4.6. The numerical method used for calculating κ has been discussed in section 2.3.3 where equation 2.34 summarized how the curvature value is calculated using the height functions and finite difference discretization applied to the differential equation 2.33. From the formulation in equation 2.34, it is evident

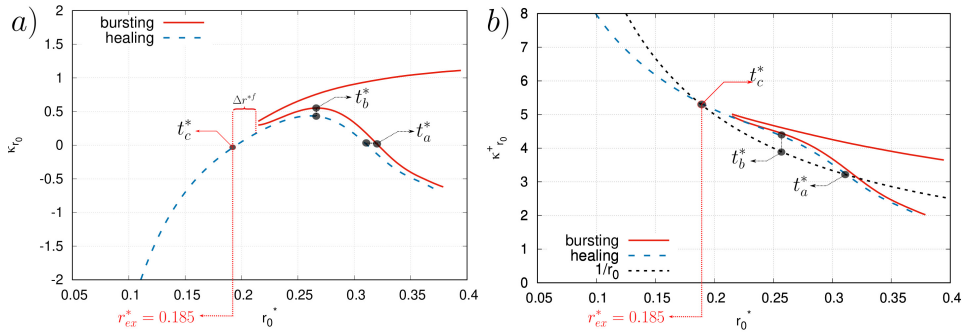

Fig. 4.5 (a) Plot of the total curvature κ_{r_0} and its components as functions of the radial distance for both the healing and bursting case. (b) Comparative rate of change in the curvature components κ^+ and κ^- for r_0, illustrating the crucial radial distance r_{ex} where the dynamics shift, leading to contrasting outcomes in the two scenarios. In sub-figure b), since for both cases $\kappa^- = 1/r_0$, κ^- has been drawn once and labeled by $1/r_0$ instead. To apply the Bezier smoothing filter, the curve for the $\kappa^+(r_0)$ in the bursting case (red solid line) is divided into an increasing and a decreasing part separating at the point where the hole movement reverses direction, to render the data monotonic.

that the finite difference discretization of the equation 2.33 inevitably introduces some noise in the measurements, in addition to the possible noise contained in the calculation of the height functions.

Here, the Bezier curve smoothing filter was used to remove the noise in the curvature measurements presented in figure 4.4 and 4.5. To apply the Bezier algorithm, one must first render the data monotonically, which is the curve corresponding to the $\kappa^+(r_0)$ of the bursting case is divided into two parts in the figures mentioned above, one corresponding to the monotonic increase of the $\kappa^+(r_0)$, which ends at $r_0 = r_0^{*f}$, and the other to its decrease, starting at $r_0 = r_0^{*f}$. One could compare the smoothed curves with the original data via the results in figure 4.6 to confirm the validity of the smoothed curves.

Examining the variation of the curvature components in the logarithmic scale, one could identify three distinct regions for the $\kappa^+(r_0)$, illustrated via figure 4.7:

- $0.3 < r_0$: where $\kappa^+(r_0)$ has a distinct power law with r_0 such that $\kappa^+(r_0) \propto r_0^{-5/2}$. Therefore, one finds for the total curvature at the hole tip in this regime

$$\kappa_{r_0} \propto r_0^{-5/2} - r_0^{-1} \tag{4.7}$$

- $r_0 < 0.2$: where $\kappa^+(r_0)$ has a distinct power law with r_0 such that $\kappa^+(r_0) \propto r_0^{-3/5}$.
- $0.2 < r_0 < 0.3$: where the relation between $\kappa^+(r_0)$ transitions from $\kappa^+(r_0) \propto r_0^{-5/2}$ as $\kappa^+(r_0) \propto r_0^{-3/5}$ as r_0 decreases. This transition occurs approximately at $t^* = t_b^*$.

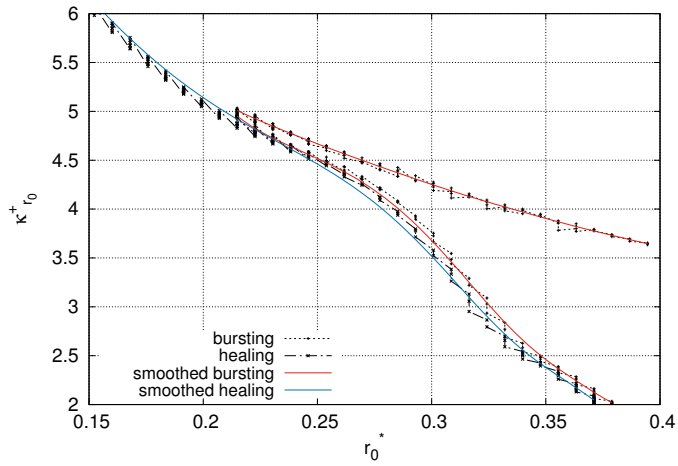

Fig. 4.6 Comparison of the raw (noisy) curvature measurements from numerical simulations with smoothed curves using the Bezier curve filter. The inherent noise due to finite difference discretization in equation 2.33 is evident. The validity of the Bezier smoothing is demonstrated by juxtaposing the original and filtered data, labeled by the smoothed "name of the case."

Consequently, one finds

$$\kappa_{r_0} \propto r_0^{-3/5} - r_0^{-1} \tag{4.8}$$

Notably, the curve corresponding to the retraction trajectory in the positive component of the tip curvature $\kappa^+(r_0)$ for the bursting hole falls on the same slope line as in the further contraction of the healing case. This is observable in 4.7, where the red solid curve and dashed blue line align on the $n = -0.6$ even though they belong to the two opposite behavior for the hole. Based on this observation, one could deduce that $\kappa^+(r_0) \propto r_0^{-3/5}$ represents the natural mode for the $\kappa^+(r_0)$ while the $\kappa^+(r_0) \propto r_0^{-5/2}$ is rooted in the initial configuration of the hole.

4.3.2 Effect of Capillary Wave on Tip Curvature

As discussed in section 3.1.2 and evident from equation 3.12, the initial circular hole profile, as is the case in the current simulations, includes a discontinuity in the surface curvature of the film. Figure 4.8 plots the total curvature $\kappa(r)$ of the film surface as a function of radial distance for both healing and bursting cases[1]. Unlike the curvature at the hole tip, the curvature components cannot be plotted over the film surface since neither component is known analytically, except at $r = r_0$.

Besides the initial state, several records are provided in figure 4.8 corresponding to the pivotal times during the healing and bursting simulation. The wave propagation in both cases

[1]The curves were smoothed using the natural cubic splines method.

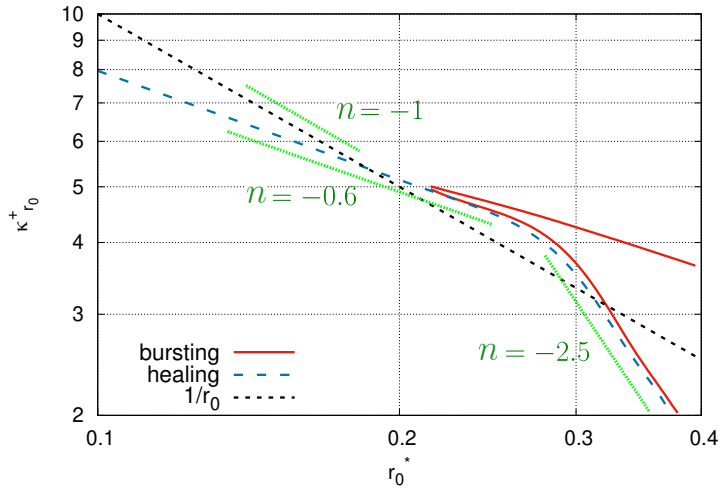

Fig. 4.7 Log-log plot illustrating the variation of the curvature component $\kappa^+(r_0)$ with r_0, highlighting three distinct regions with their respective power law behaviors: $\kappa^+(r_0) \propto r_0^{-5/2}$, $\kappa^+(r_0) \propto r_0^{-3/5}$, and the transition between them. The alignment of the retraction trajectory curve of the bursting case after reaching its minimum r_0 value (solid red, upper part) and further contraction of the healing case curve (dashed blue) on the $n = -0.6$ line suggests that natural mode of $\kappa^+(r_0)$ is governed by $\kappa^+(r_0) \propto r_0^{-3/5}$, while $\kappa^+(r_0) \propto r_0^{-5/2}$ governs the initial adaptation of the film surface that includes a discontinuity in its curvature.

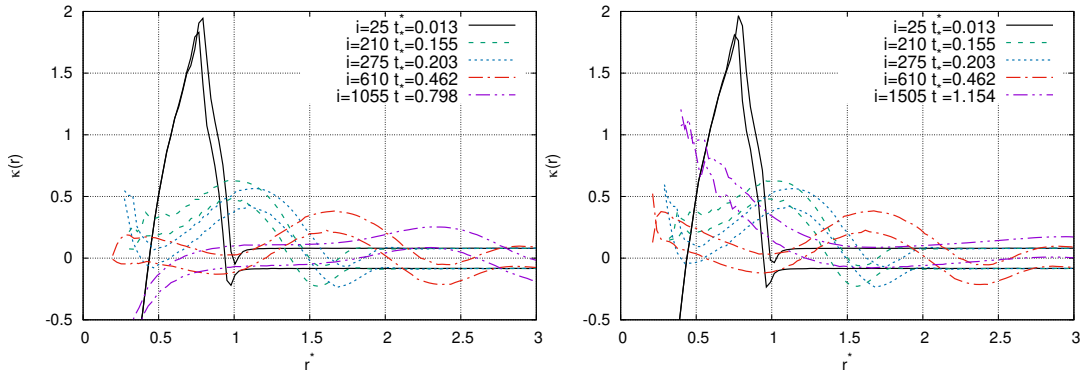

Fig. 4.8 Total curvature, $\kappa(r)$, of the film surface as a function of radial distance for both healing (left sub-figure) and bursting (right sub-figure) cases. The displayed curves, smoothed using the natural cubic splines method, represent the curvature at pivotal times during each simulation. For each record, two curves represent the inner and outer interface curvatures, with the outer interface (larger radial extent) showing slightly lower values. The propagation of the capillary wave initiated by the discontinuity in the initial total curvature can be observed, illustrating its impact on the temporal variation in $\kappa(r)$, particularly at the tip, and subsequently on the hole dynamics.

has the same characteristic since the Laplace number and other parameters of the problem are set equally in both cases. Nevertheless, the two curves eventually follow two radically different trajectories.

As mentioned earlier, the studied cases in this chapter are based on the semi-spherical bubble cap configuration discussed in section 2.4.2. Therefore, as opposed to a flat film, the curvature on the inner interface (inside the bubble) differs from the outside interface by a relatively small amount that depends on the bubble curvature (bubble diameter). Consequently, at each instance, the curvature values in figure 4.8 are given using two curves representing the two interfaces. At any given record, the lower curve with slightly lower curvature values corresponds to the outer interface with $x > (d_1/2 - \delta/2)$.

The discontinuity in the initial total curvature over the film surface is illustrated for both cases. Consequently, a capillary wave is seeded and propagates on the interface, driving the temporal variation in $\kappa(r)$ at a given radial distance. One could notice that the transition from $\kappa^+(r_0) \propto r_0^{-5/2}$ to $\kappa^+(r_0) \propto r_0^{-3/5}$ illustrated in figure 4.7 occurs at the same time when the effect of the initial capillary wave is almost damped at the tip of the hole where $r = r_0$, verifiable through figure 4.8. Therefore, it becomes clear that the initial regime for the positive component of the curvature with $\kappa^+(r_0) \propto r_0^{-5/2}$ is a consequence of the wave propagation caused by the discontinuity in the surface curvature.

4.4 The Critical Mechanism

Figure 4.5b offers invaluable insights into the mechanism behind the radical difference of outcomes with a minimal change in the initial conditions. Through this plot, one could compare the rate of change of the two curvature components with r_0. Starting from the initial condition, the simulations begin with $\kappa^- > \kappa^+$, while the hole is accelerated in the contracting direction. Initially, the rate of change with r_0 for κ^+ is higher than for κ^- in both cases due to the initial hole configuration. This leads to the equalization of the two curvature components and zero total curvature at $t^* = t_a$. As the hole continues contracting because of the existing inward momentum, the balance rates of changes for κ^+ and κ^- shifts.

Having recognized the distinct regions for $\kappa^+(r_0)$ with the two unique power laws in figure 4.7, one could observe via figure 4.5b that as the hole contracts and r_0 reduces, the two rates of changes eventually equalize at $t = t_b$. This results in zero rate of change for the total curvature $\partial_t \kappa(r_0) = 0$ and thus, zero rate of change in acceleration $\partial_{ttt} r^*(t) = 0$ at the tip of the hole. This denotes that the outward acceleration at the tip reaches its maximum at this juncture instead of monotonically increasing due to the shift in dominance from κ^+ to κ^- as the hole size decrease

beyond this point. For $t_b^* < t^* < t_c^*$, Since the tip still has inward momentum, r^* is further reduced, while the outward acceleration which is opposing this movement is decreased.

As illustrated in 4.5b, there exists a critical radial distance r_{ex}, beyond which not only the κ^- increases faster than κ^+ by decreasing r_0, but also the value of κ^- is already higher than κ^+ which causes r_0 to further reduce, creating a positive feedback loop. Meaning upon reaching this point, $\partial_{tt} r^*(t), \partial_{ttt} r^*(t) < 0$ always remain true. Therefore, the mechanism behind the critical dynamics of the hole near its healing threshold is understood by examining the critical radial distance r_{ex} and whether or not the tip of the hole could reach this position. For the circular hole configuration studied here, this critical value was found

$$r_{ex} = 0.185 \tag{4.9}$$

Therefore, the essential difference between the two cases studied here is that the healing case reaches r_{ex}^* and thus falls over and into the positive feedback loop. In contrast, the bursting case could not do so because of having a minimally larger initial radial distance to traverse to reach r_{ex}^*. This means the inward momentum for the bursting case reaches zero and reverses direction before the hole tip can reach r_{ex}^*.

The different stages of the hole dynamic at its tip could be summarized as

$$\text{Tip Hole Dynamics} = \begin{cases} 1)\ \text{decreasing acceleration} & 0 < t^* < t_a, & \kappa^- > \kappa^+, & \partial_r \kappa^- > \partial_r \kappa^+ \\ 2)\ \text{increasing deceleration} & t_a < t^* < t_b, & \kappa^- < \kappa^+, & \partial_r \kappa^- > \partial_r \kappa^+ \\ 3)\ \text{decreasing deceleration} & t_b < t^* < t_c, & \kappa^- < \kappa^+, & \partial_r \kappa^- < \partial_r \kappa^+ \\ 4)\ \text{increasing acceleration} & r_0 < r_{ex} & \kappa^- > \kappa^+, & \partial_r \kappa^- < \partial_r \kappa^+ \end{cases} \tag{4.10}$$

with the increasing acceleration stage defining the positive feedback loop, within which the hole size could only decrease further. These stages are accordingly marked in figures 4.2, 4.4, and 4.5. Observing the snapshots of the hole dynamics given in figures 4.1, one could identify the moment at which the two films depart to opposite trajectories along with a detailed view of the pressure field and velocity vectors at that moment, provided in figure 4.3 with the sub-figures h4 and b4. At this critical moment, the healing hole reaches, even though barely, the $r_0 = r_{ex}$, indicated by the red dashed line, while the bursting hole comes just short of this critical distance and starts retracting.

The initial difference in the hole sizes studied is 0.05, making the starting radial distances of the holes differ by $\Delta d/2 = 0.025$. As noted from figure 4.2a or 4.5, the bursting case reverses direction at

$$r^{*f} = r_{ex}^* - \Delta r_0^{*f} = 0.155, \tag{4.11}$$

where r^{*f} notes the radial position of where this reversal occurs and $\Delta r_0^{*f} = 0.03$ denotes the amount by which the bursting case falls short of reaching r_{ex}^*. Consequently, one could confirm the explanation above on how the minimal difference in the initial positions of the hole tips causes the two radically different outcomes.

When compared with the initial distance, one finds that for the bursting case

$$r_0^{*f} - r_{ex}^* - \Delta d/2 = 0.005, \tag{4.12}$$

indicating that the initial difference in the starting position does not completely justify the final radial distance difference between the two cases when the bursting case stops contracting. This difference could be understood in the light of the fact that the initial inward momentum of the two holes is also dependent on their initial starting position: the larger the hole size, the less inward momentum generated according to the change in the capillary pressure of the hole area discussed in section 3.1.2. However, given the expression 4.11 and 4.12, one could estimate that the difference in the initial inward momentum of the holes is only responsible for 15% of the difference in radial positions at the time of reversing direction for the bursting case. At the same time, 85% is contributed to the difference in the starting positions. Hence, the initial momentum could be assumed to be almost the same.

The critical dynamics of the hole near its healing threshold discussed above resemble a well-known mechanical problem where a ball is pushed up on a hill. This analogy is depicted using figure 4.9. In this analogy, the top of the hill would be the critical point r_{ex}^* where any further move for the ball would result in its continuous and accelerating fall. Therefore, one could imagine the two healing and bursting holes as the blue and red balls, respectively, as illustrated in figure 4.9. The force that pushes the two balls is analogous to the inward momentum of the hole caused by the film curvature in its initial state. As shown above, one could imagine the exerted force on the two balls virtually having the same intensity. On the other hand, the starting point for the blue ball is slightly closer to the top of the hill, enabling it to fall over.

4.5 Summary

This chapter closely examined and identified the underlying mechanism responsible for two virtually identical simulations resulting in radically different outcomes. For this purpose, two high-precision simulations were done for two holes of sizes $d_{\mathrm{cl}}^* = 0.744$ and $d_{\mathrm{op}}^* = 0.754$.

Investigating the radial position of the tip and its first and second temporal derivatives made it possible to recognize the pivotal moments in the evolution of the hole dynamics. These

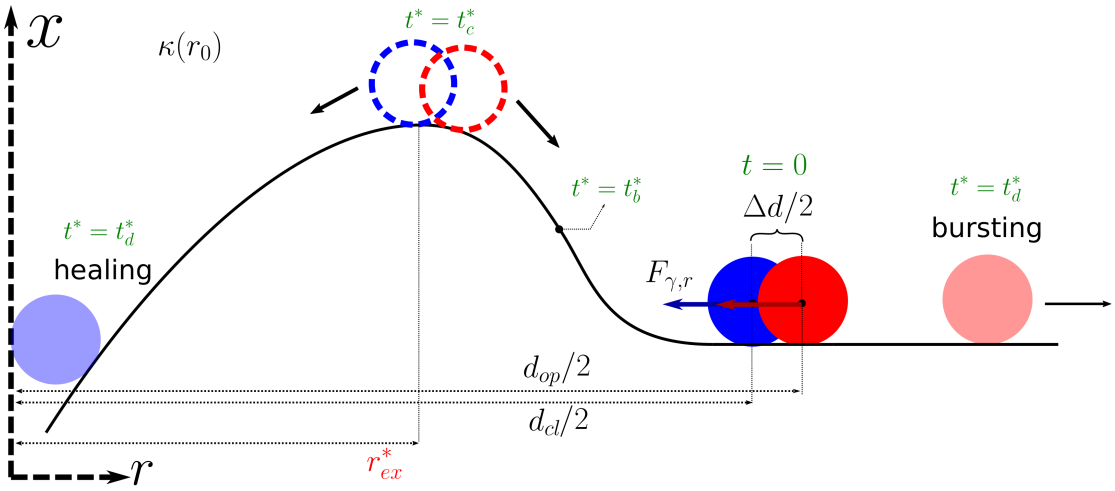

Fig. 4.9 Analogy between the critical dynamics of a hole near its healing threshold and a ball pushed on a hill. The blue and red balls represent the healing and bursting holes, respectively. The top of the hill represents the critical point r_{ex}^*. Despite the exerted force on both balls being assumed identical, the blue ball falls over the hill because of a closer starting position to the top of the hill, which is equivalent to the healing scenario.

pivotal moments were also investigated through the snapshots of the film interface and pressure field, along with the velocity vectors near the tip area.

Nonetheless, a complete understanding of the hole critical dynamics remained elusive until a thorough examination focused on the temporal and radial evolution of the tip curvature with its dual components was carried out. This study identified distinct power laws to govern the tip curvature positive component, while the negative one was given analytically, resulting in a power law for the total curvature at the tip. Using these results on the radial evolution of the curvature components in figure 4.5b and 4.7 along with the pivotal moments recognized previously in section 4.2, the underlying mechanism was discussed and detailed. For a further understanding of the problem, this examination of the critical hole dynamics was concluded by suggesting an analogy that describes the problem of pushing a ball up on a hill.

Chapter 5

Hole Healing Threshold Variations – Flat Film

This chapter investigates the relationship between the hole healing threshold and the various parameters associated with the problem. We employ a numerical dichotomy process to study a hole on a flat film, as detailed in section 2.4.1.1.

Considering a hole on a film and referencing section 2.2.2, the non-dimensional parameters independently governing the dynamics are chosen as follows:

$$d^{*c} = f(\mathrm{La}_l, \mathrm{La}_g, \rho_{l/g}, d_b/\delta) \tag{2.30}$$

Given that this chapter is focused on a flat film, the term d_b/δ can be excluded from expression 2.30, leading to:

$$d^{*c} = f(\mathrm{La}_l, \mathrm{La}_g, \rho_{l/g}) \tag{5.1}$$

It is apparent from expression 5.1 that while the density ratio has been chosen as an independent parameter, the viscosity ratio is determined indirectly using:

$$\mu_{l/g} = \sqrt{\frac{\rho_{l/g}\mathrm{La}_g}{\mathrm{La}_l}} \tag{2.17}$$

Hence, the primary objectives of this chapter are twofold: 1. Examine how d^{*c} varies with the three non-dimensional parameters presented in expression 5.1. 2. Offer a physical rationale for the observed variations, wherever feasible.

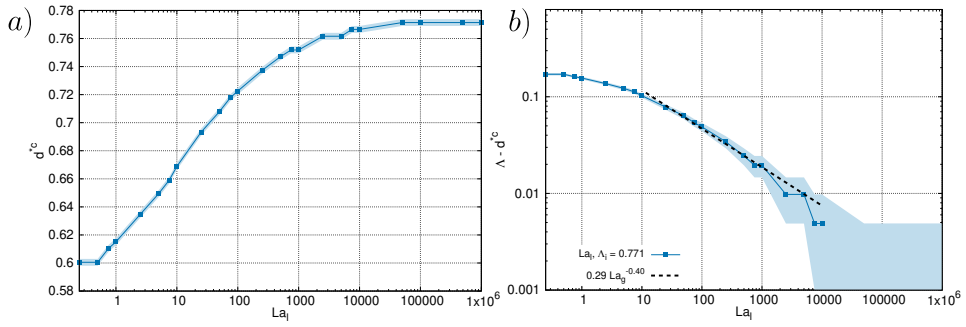

Fig. 5.1 (a) Relationship between the healing threshold d^{*c} and the film Laplace number La_l. (b) The logarithmic plot of the same values highlights the transitional zone for La_l between 1 and 10,000 and shows the distinct power law relationship, with flanking regions of minimal variations. The filled curve around the solid lines represents the accuracy of the dichotomy process equal to ± 0.005 with seven mesh levels within the film thickness. The filled curve is enlarged as the $\Lambda - d^{*c}$ decreases in panel (b) due to the logarithmic scaling. The saturation at the end of

5.1 Liquid Viscosity vs Surface Tension – La_l

5.1.1 Dichotomy Results

An essential physical parameter influencing the film healing threshold is the film Laplace number, La_l, which represents the ratio of viscosity effects to surface tension in the film. To investigate its effect, La_l is varied over a wide range, keeping all other parameters constant based on the standard oceanic case provided in table 2.1.

The result of the numerical dichotomy process is shown in figure 5.1a and b, where it becomes evident that the viscous effects in the liquid phase are an influential factor in studying holes on liquid films. It is observed in figure 5.1 that firstly, increasing the film Laplace number increases the healing threshold d^{*c}. In other words, a film more dominated by surface tension than viscous effects can heal larger holes.

Moreover, there exists a transitional zone for La_l values between 1 and 10,000, where the healing threshold exhibits a distinct power law relationship with the Laplace number. A fitting process yields this relationship as:

$$d^{*c} = \Lambda - 0.29 La_l^{-0.40} \tag{5.2}$$

Here, $\Lambda = 0.771$ denotes the healing threshold in the inviscid scenario (high Laplace number), a value inferred from figure 5.1a. Figure 5.1b further illustrates that this transitional phase is flanked by regions with minimal variation across the $La_l = [1, 10000]$ span. Notably, viscous effects become pronounced as La_l approaches unity and continue to be significant for $La_l <$ 10000.

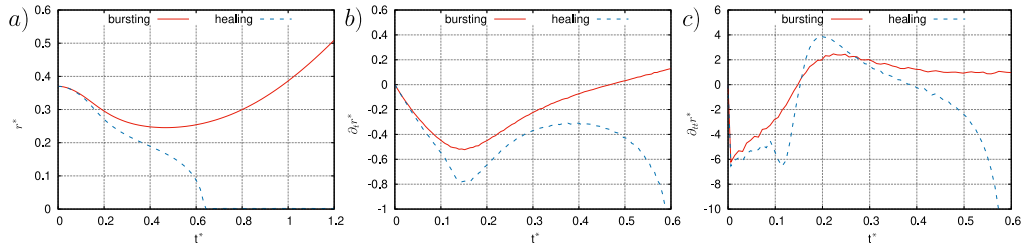

Fig. 5.2 (a) Position of the hole tip highlighting the healing behavior of the bursting case with $La_l = 100$ in contrast to the healing case with $La_l = 1000$. (b) Velocity of the hole tip showing the impact of changing La_l on viscous dissipation. (c) Acceleration of the hole tip influenced by the La_l, where the case with higher La_l shows a stronger overshoot at $t^* \approx 0.2$.

In the context of bursting films in the ocean, one can find the typical range of Laplace number in which these bursting events typically occur. Among the parameters involved in the Laplace number, only the film thickness varies considerably for the ocean bubbles compared to the film density, viscosity, or surface tension coefficient. Using the prevalent δ values from table 2.1, the Laplace number mainly spans between 10 and 10,000—a spread across three orders of magnitude. Comparing this with the observations from figure 5.1b, it becomes evident that considering viscous effects within the fluid is crucial in oceanic film burst studies, given the significant variation in the healing threshold d^{*c} within this range.

5.1.2 Physical Rationale – Examining Energy Dissipation

In order to find the physical explanation for the effect of viscosity, two cases were studied similarly to chapter 4 by keeping all parameters alike while simulating two different film Laplace numbers, 100 and 1000. A hole size of $d^* = 0.74$ was chosen based on the dichotomy results from figure 5.1, which induces bursting for $La_l = 100$ and healing for $La_l = 1000$.

The position of the film tip, its velocity, and acceleration are plotted in figure 5.2a, b, and c. According to figure 5.2a, one can first confirm that the more viscous case with $La_l = 100$ heals while the other bursts. Moreover, as shown in figure 5.2b and c, the reduced Laplace number amplifies viscous dissipation, altering the film velocity and acceleration.

To pinpoint how enhanced viscous effects within the film cause a hole to burst rather than heal, the temporal and radial evolutions of the tip curvature and its components—κ_{r_0}, $\kappa_{r_0}^+$, and $\kappa_{r_0}^-$—were scrutinized, as shown in figures 5.3 and 5.4.

In subsection 4.4, it was discovered that a critical radial distance r_{ex} exists for the tip of the film upon reaching which the film will close. Furthermore, the underlying mechanism was described in an analogy to the top of a hill for a ball that is pushed upward from the foot of the hill. This critical distance coincides with the first instance where both $\kappa^- > \kappa^+$ and $\partial_r \kappa^- < \partial_r \kappa^+$ are valid, illustrated in figure 5.4b. In chapter 4, the differentiating parameter

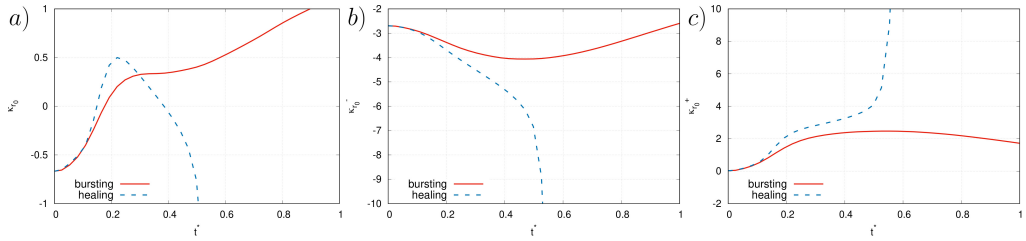

Fig. 5.3 Temporal evolution of the tip curvature and its components κ_{r_0}, $\kappa^+_{r_0}$, and $\kappa^-_{r_0}$ provided in panels (a), (b), and (c), respectively, and for the scenarios of hole healing with $La_l = 1000$ and bursting with $La_l = 100$.

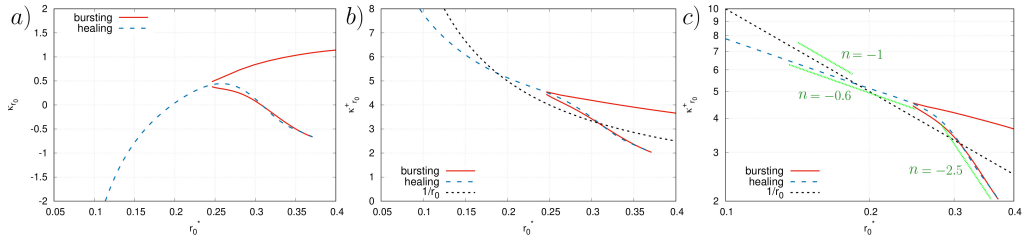

Fig. 5.4 Radial evolution of the tip curvature and its components κ_{r_0}, $\kappa^+_{r_0}$, and $\kappa^-_{r_0}$ provided in panels (a), (b), and (c), respectively, and for the scenarios of hole healing with $La_l = 1000$ and bursting with $La_l = 100$. The logarithmic plot in panel (c) illustrates the power laws for $\kappa^+_{r_0}$ found by fitting functions applied to different regions for r^*_0. To apply the Bezier smoothing filter, the curve for the $\kappa^+(r_0)$ in the bursting case (red solid line) is divided into an increasing and a decreasing part separating at the point where the hole movement reverses direction, to render the data monotonic.

was the difference in the initial radial position of the film tip (i.e., hole size); hence, the case with the further distance to r_{ex} could not reach r_{ex}, causing the hole to burst after the initial contraction eventually.

Here, on the other hand, while having identical hole sizes, the case with more viscosity does not reach the critical point r_{ex} as evident in figure 5.4b because of losing more of its momentum via viscous dissipation. One could examine the total, kinetic, and potential energy to confirm this hypothesis.

The total energy is calculated by adding the potential and kinetic energy

$$E = E_p + E_k \tag{5.3}$$

The kinetic energy is provided by

$$E_k = \frac{1}{2}\int \rho \boldsymbol{u}^{*2} dV \tag{5.4}$$

where dV represents the volume differential element. For a discretized spatial domain, the equation 5.4 becomes

$$E_k = \sum_{i=1,j=1}^{i=\infty,j=\infty} \frac{1}{2}\rho[i,j] f[i,j] \left(2\pi r[i,j]\Delta[i,j]\right) \left(u[i,j]^2 + v[i,j]^2\right) \tag{5.5}$$

where $2\pi r[i,j]\Delta[i,j]$ represents the volume of a given mesh cell in the axisymmetric coordinates. On the other hand, the potential is given by

$$E_p = A\gamma \tag{5.6}$$

where A represents the total surface area of the film. However, calculating the surface area of the discretized domain is problematic when using the VoF method. Three methods of various accuracies for surface area measurements are detailed and examined in appendix C. Nevertheless, the problem in surface area calculation persists despite using the most accurate of the three methods discussed. This is evident by examining figure 5.5a, where the calculated total energy initially increases– a nonphysical result due to the inaccuracy of measurements for the total surface area.

Despite this discussed inaccuracy in calculating the system potential energy, the proposed hypothesis is nonetheless supported by the plot of total energy and its two components provided in figure 5.5. Examining the kinetic energy temporal evolution presented in figure 5.5c, it is evident that a lower film Laplace number results in more viscous dissipation. For instance, at

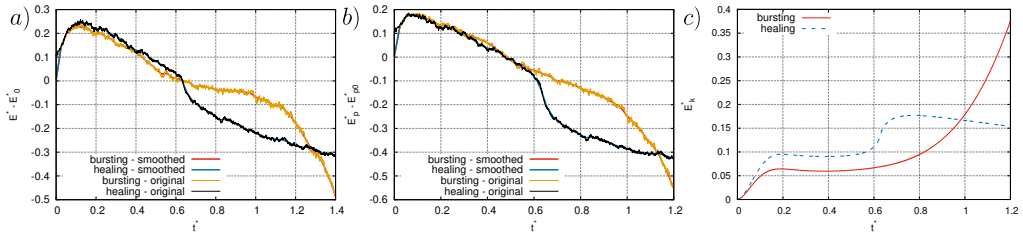

Fig. 5.5 For the scenarios of hole healing with $La_l = 1000$ and bursting with $La_l = 100$: Panel (a) provides the temporal evolution of the total energy subtracted by its initial value. The initial increase in total energy is due to inaccuracies in surface area measurement. Panel (b) plots the potential energy subtracted by its initial value over time. Panel (c) shows the temporal evolution of the kinetic energy, highlighting the effect of the Laplace number on viscous dissipation.

$t^* = 0.4$, the kinetic energy is 50% higher for the case with a higher Laplace number, even though both systems had the same potential energy budget.

Using a similar analogy discussed in section 4.4, therefore, one may conclude that a lower film Laplace number (i.e., higher viscous effects) for a hole on a liquid film is similar to having more friction for a ball that is pushed upward on a hill.

5.2 Gas Viscosity vs Surface Tension – La_g

5.2.1 Dichotomy Results

When the liquid film starts contracting at the hole area after initialization of the problem, the air must be pushed out of the way. The possibility that this phenomenon could affect the healing threshold has been briefly discussed by Lu and Corvalan (2015) while suggesting aspects of the problem that could be studied in future works. Taking upon this suggestion, this section examines the effect of variations in the gas Laplace number La_g on the hole healing thresholds on a flat film.

Figure 5.6 provides the dichotomy results for a wide range of gas Laplace numbers and several density ratios. Accordingly, it is observed that for a given density ratio $\rho_{l/g}$, a higher value for La_g results in the increase of the healing threshold, regardless of the value for $\rho_{l/g}$. However, the amount of impact from varying La_g is influenced by the $\rho_{l/g}$ value. Accordingly, it is observed that a higher density ratio $\rho_{l/g}$ results in a lower impact from the La_g variation.

5.2.2 Physical Rationale – Viscosity Ratio

These dynamics could be better understood by considering the equation 2.17. Accordingly, the viscosity ratio is influenced both by $\rho_{l/g}$ and La_g. Therefore, keeping the density ratio constant

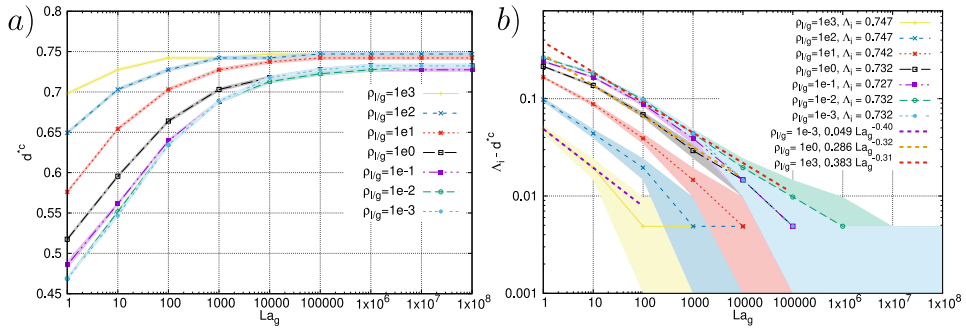

Fig. 5.6 Sub-figure (a) shows the dichotomy results presenting the effect of the gas Laplace number La_g on the healing threshold across varying density ratios $\rho_{l/g}$. The plot indicates an increase in the healing threshold with a rise in La_g, with the magnitude of this effect being moderated by the density ratio. Sub-figure (b) plots the results using the logarithmic scale and introduces a power law found by a fitting function. The filled curve around the solid lines represents the accuracy of the dichotomy process equal to ± 0.005 with seven mesh levels within the film thickness. The filled curve is enlarged as the $\Lambda_i - d^{*c}$ decreases in sub-figure (b) due to the logarithmic scaling. The liquid Laplace number $La_l = 633$ has been kept constant for all cases.

and varying the gas Laplace number also results in variations in the viscosity ratio. According to the equation, higher La_g means a higher $\mu_{l/g}$ or a gas with lower viscosity compared to the liquid film. Using the relation 2.17, the results given in figure 5.6 are alternatively presented in figure 5.7

One might suppose that since there is no gas flowing out through the hole in the case of a flat film, the viscosity of the gas should not have any effects on the healing threshold. However, the contrary is shown to be the case as provided in figure 5.7, where a less viscous gas phase (i.e., higher $\mu_{l/g}$ ratio) augments the healing process, increasing the hole healing threshold.

This effect can be understood by considering that a more viscous fluid requires more energy to move. As illustrated in the previous section, when examining the effect of film Laplace variation, the film tip sets out moving inward, and whether it could close the gap or not depends on whether it reaches the critical radial distance r_{ex}. Considering that the hole tip has to push the gas out of the gap while moving inward, it can be understood that a more viscous gas consumes more of the film total energy, making it energetically costlier for the hole tip to reach r_{0c}.

Given the results in the logarithmic scale plotted in figure 5.6b for La_g, one can write

$$d^{*c} = \Lambda_i - 0.38 La_g^{-0.31} \tag{5.7}$$

with $\rho_{l/g} = 1000$ and $\Lambda_i = 0.747$. Similarly, and according to the results in figure 5.7b, one finds

$$d^{*c} = \Lambda_i - 0.058 \mu_{l/g}^{-0.80} \tag{5.8}$$

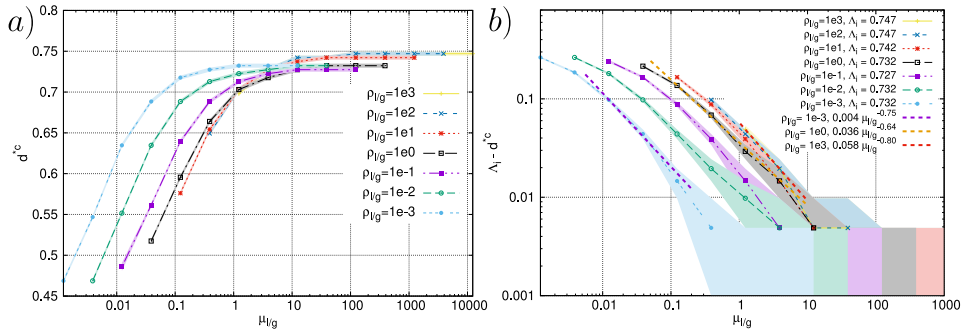

Fig. 5.7 Sub-figure (a) shows the influence of the viscosity ratio $\mu_{l/g}$ on the healing threshold, derived from variations in the gas Laplace number La_g and density ratio $\rho_{l/g}$. A heightened $\mu_{l/g}$ ratio, indicating a relatively less viscous gas phase, correlates with an augmented healing threshold. Sub-figure (b) plots the results using the logarithmic scale and introduces a power law found by a fitting function. The filled curve around the solid lines represents the accuracy of the dichotomy process equal to ± 0.005 with seven mesh levels within the film thickness. The filled curve is enlarged as the $\Lambda_i - d^{*c}$ decreases in sub-figure (b) due to the logarithmic scaling. The liquid Laplace number $\mathrm{La}_l = 633$ has been kept constant for all cases.

with $\rho_{l/g} = 1000$ and $\Lambda_i = 0.747$. Moreover, the same fitting power functions have been applied to cases with $\rho_{l/g} = 1,$ and 0.001, included in 5.6b and 5.7b. These power functions indicate that by increasing $\rho_{l/g}$, the value of $|n|$ decreases and converges to $|n| = 0.31$ in equation 5.7, while it increases to $|n| = 0.80$ in equation 5.8. These extracted power laws summarize the findings for the healing hole variation with the La_g, or $\mu_{l/g}$.

5.3 Liquid and Gas Density Ratio – $\rho_{l/g}$

5.3.1 Dichotomy Results

As observed in the previous section, changing the density ratio of the two phases can alter the hole dynamics and affect the hole healing threshold. Consequently, this section examines the variation of d^{*c} with $\rho_{l/g}$ while keeping the other parameters of the problem the same.

For this purpose, firstly, the dichotomy results previously given in figure 5.6 are re-arranged for the variation in the $\rho_{l/g}$ and presented in figure 5.8. This figure shows that while maintaining the same value for La_g, a higher density ratio $\rho_{l/g}$ results in a higher healing threshold. However, the viscosity ratio also varies in this condition (i.e., constant La_g).

Alternatively, one could study the effects of density ratio variations while keeping the viscosity ratio constant by varying the La_g so that according to the expression 2.17, $\mu_{l/g}$ would remain constant. This result is presented in figure 5.8 by the black curve that is labeled

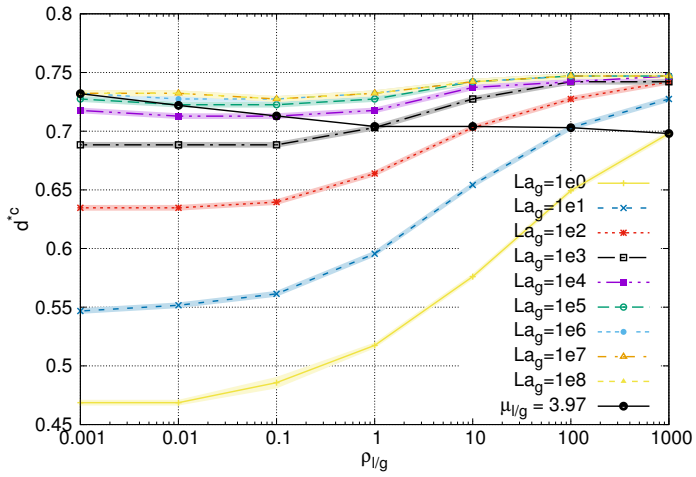

Fig. 5.8 Variation of healing threshold d^{*c} with the density ratio $\rho_{l/g}$ for different gas Laplace numbers La_g. The influence of a constant viscosity ratio $\mu_{l/g}$ is also shown by the black curve labeled $\mu_{l/g} = 3.97$, highlighting the minimal decrease in the healing threshold with an increase in $\rho_{l/g}$ under this condition. The filled curve around the solid lines represents the accuracy of the dichotomy process equal to ± 0.005 with seven mesh levels within the film thickness. The liquid Laplace number $\mathrm{La}_l = 633$ has been kept constant for all cases.

$\mu_{l/g} = 3.97$. Accordingly, the increase in the density ratio minimally decreases the healing threshold while keeping the viscosity ratio constant.

5.3.2 Physical Rationale – Capillary Wave Attenuation

One possible explanation for the observed effect is found by examining the evolution of the capillary wave due to the singularity in the film surface curvature discussed in the section. Given a denser surrounding, it would be expected that the capillary wave would be attenuated faster. This idea is supported by the results provided in figure 5.9, where the evolution of surface curvature is plotted at different time stamps. The comparison is made for two cases with different density ratios while keeping the same viscosity ratio. The radical change in the propagation of the capillary wave is observed between these two cases, where the case with a higher gas density quickly attenuates the wave and hinders its propagation.

As discussed in section 4.3.1, the capillary wave propagation strongly affects the positive component of the hole tip curvature. This effect was illustrated by comparing the two distinct power laws describing the variation of $k^+_{r_0}$ with r_0. According to the discussion in section 4.3.1, a faster transition from the initial regime $\kappa_{r_0} \propto r_0^{-5/2} - r_0^{-1}$ to $\kappa_{r_0} \propto r_0^{-3/5} - r_0^{-1}$, results in increasing the critical radial distance r_{ex}, which would consequently increase the healing threshold.

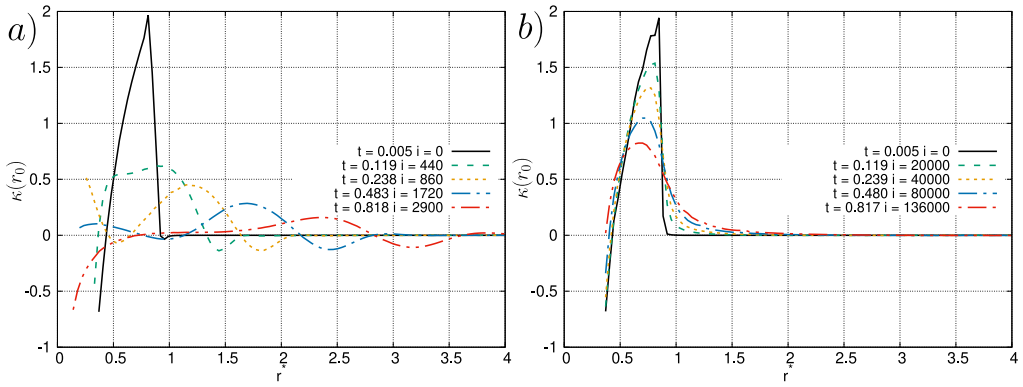

Fig. 5.9 Evolution of surface curvature at different time stamps for two cases with varying density ratios while maintaining constant viscosity ratios. The graph depicts a more rapid attenuation of the capillary wave in (b), the case with higher gas density, showing its influence on the propagation dynamics of the capillary wave.

A faster attenuation of the capillary wave is equivalent to a faster transition in $k^{+}_{r_0}$ phases. Therefore, a higher gas density that results in a faster attenuation causes the observed increase in the hole healing threshold discussed above.

5.4 Hole Shape Effects

5.4.1 Dichotomy Results

As discussed previously, the exact shape of the hole after its nucleation on a bursting film is directly linked to the nucleating mechanism. Since the exact hole shape immediately to its natural nucleation remains an open topic for examination, an arbitrary choice has been made in the present work to use the circular profile for the hole shape.

Discussed in section 2.4.1.1 and illustrated in figure 2.8a, the numerical geometry of the flat film is constructed using a circular profile as the shape profile of the hole (part A) joined by a rectangular shape representing the flat part of the film (part B). While this configuration allows the avoidance of singularity in the first derivative of the film interface, it introduces a singular point in the second derivative, which is the curvature of the interface, at the point of conjunction with the flat part of the film. The circular profile is the only shape that can ensure an interface with a continuous first derivative for a flat film with a hole. On the other hand, the prominent work of Taylor and Michael (1973) assumes a catenoid shape given by the expression 3.35 ensuring a continuous and zero curvature everywhere on the interface of the hole, whereas introducing a singular point in the first derivative of the interface at the point of conjunction with the flat part. Therefore, this section examines the effect of the hole shape

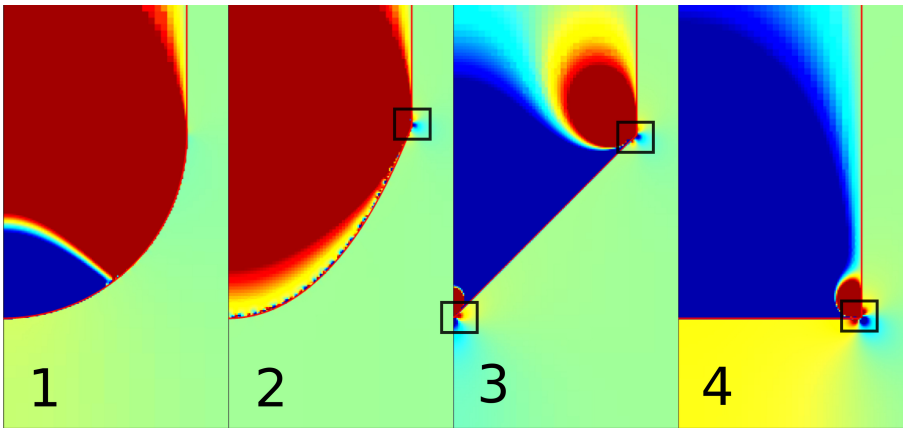

Fig. 5.10 Numerical configurations illustrating the influence of hole shapes on the initial pressure field. From left to right: 1) circular, 2) catenoidal, 3) rectangular, and 4) triangular shapes. Snapshots, taken ten steps post-initialization, display the film interface alongside a pressure field color map. Noteworthy are the black rectangles highlighting singular points in the first derivative of the interface.

to verify that the nature of the presented results in this work is not dependent on the arbitrary choice of the hole shape.

For this purpose, four different shapes, circular, catenoid, square, and triangle, have been selected for the geometry of part A in figure 2.8a to examine the effect of the hole shape. For these simulations, all physical parameters have been set according to the values in table 2.1 corresponding to a standard case of bubble bursting in the ocean. Figure 5.10 shows the numerical configuration of these four cases along with the color map of the initial pressure field, recorded ten steps after the initialization of each case. This figure illustrates the effect caused by utilizing different hole shapes on the initial pressure field due to having a different surface curvature profile. One can also note the singular points on the first derivative of the interfaces marked by small black squares in figure 5.10.

In order to verify that the studied effects of other parameters of the problem are independent of the choice for the hole shape, it is decided here to investigate the effect of film Laplace number as an example instead of redoing all previous simulations for the effect of the hole shape.

Figure 5.11 shows the dichotomy results for the variation of the critical healing threshold with La_l for different hole shapes. At any given value for La_l, the healing threshold is affected by the choice of the shape. For instance, it is slightly decreased for the catenoid compared to the circular shape, confirming that the hole shape is an important parameter of the problem when determining the exact value of a given hole healing threshold. However, the effect of varying La_l on the healing threshold remains consistent with the previous observations for the

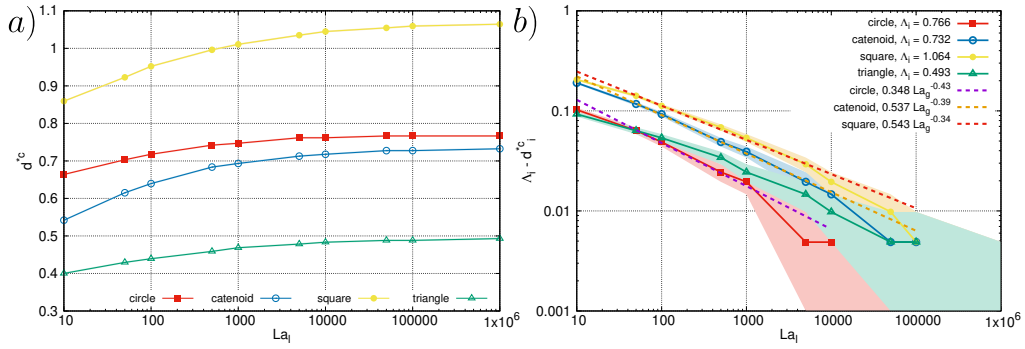

Fig. 5.11 (a) Hole healing threshold variation with La_l across four hole shapes: circular, catenoidal, rectangular, and triangular. Despite the pronounced influence of hole shape on the healing threshold for a given La_l, the effect of La_l variation on d^{*c} remains consistent with previous observations for a circular profile, as highlighted by the power law in the logarithmic view on the right. Sub-figure (b) plots the results using the logarithmic scale and introduces a power law found by a fitting function. The filled curve around the solid lines represents the accuracy of the dichotomy process equal to ± 0.005 with seven mesh levels within the film thickness. The filled curve is enlarged as the $\Lambda_i - d^{*c}$ decreases in sub-figure (b) due to the logarithmic scaling.

circular profile, as highlighted by the power law in the logarithmic view on the right. An effect that is held true regardless of the arbitrary choice for the hole shape.

Furthermore, the square profile hole shape in 2D axisymmetric creates a cylindrical hole with sharp edges. As observed from the dichotomy results of the inviscid case in figure 5.11, the healing threshold for a cylindrical hole is $d^{*c} \approx 1$. This result is consistent with the static study of the healing threshold discussed in section 3.1.1.

5.4.2 Interpretation

The power law for healing threshold variation with La_l is found by a fitting function applied to the results of the circular profile, given by the expression 5.2. The power law is also applied to the results of the other shapes, and the results are plotted in the logarithmic view in figure 5.11b. The results show that the power law is valid for all shapes, with little variation in the power law coefficient n.

Therefore, the dichotomy results provided in figure 5.11, along with the comparison of the power law coefficients, confirm that the observed effect of varying La_l on the healing threshold is independent of the arbitrary choice of the hole shape. Consequently, the results presented in this work on the effect of varying different parameters of the problem on the hole healing threshold are valid regardless of the choice of the hole shape. While the exact value of d^{*c} for a given set of parameters can vary depending on the hole shape, the key focus of studying the hole dynamics in this work is to investigate the effect of varying the governing parameters of

the problem on the hole healing threshold, rather than determining the exact value of d^{*c} for a given initial configuration of the hole, which as discussed in section , is not well-defined for a physical example of a hole nucleation event.

5.5 Summary

In this chapter, numerical simulations were exploited through a dichotomy process to investigate the effects of varying the governing parameters of the problem on the hole healing threshold.

It was found that the increase in the film Laplace number La_l results in the increase of the healing threshold. Mainly, it was found that a transitional zone is joined by two invariable regions where the healing threshold varies according to the power law given in expression 5.2. Moreover, it was discovered that this transitional zone coincides with the typical range of values for the film Laplace number in the oceanic context.

To explain the observed effects from varying La_l, the temporal evolution of the total, potential, and kinetic energy of the system was investigated. Subsequently, it was suggested that the increase in La_l results in the decrease of the energy dissipation, providing the film with a higher energy budget to reach the critical radial distance r_{eq} during the initial contacting phase.

The other parameter examined was the gas Laplace number. This study showed that a higher La_g also increases the healing threshold. Additionally, it was observed that for higher density ratio values $\rho_{l/g}$, the observed effect from varying La_g is amplified.

Since it became evident that the density ratio of the two fluids also plays a vital role in determining the healing threshold, this parameter was examined exclusively. As a result, it was found that while keeping the La_g constant, the increase in $\rho_{l/g}$ causes the healing threshold to increase as well. However, the opposite effect was observed by keeping the viscosity ratio $\mu_{l/g}$ constant instead of La_g, where a higher gas density resulted in a slight decrease in the healing threshold. The latter effect was then investigated by examining the temporal evolution of the capillary wave, illustrated in the plot of the surface curvature at different times. Consequently, it was found that a higher gas density results in a faster attenuation of the initial capillary wave, leading to the increase of the r_{ex} and, thus, the increase in the healing threshold.

Lastly, the effect of the hole shape was studied to clarify whether or not the observed effects in the previous sections could depend on the arbitrary choice of hole shape. For this purpose, the effect of the film Laplace number, taken as an example of such parameters, was re-studied for four shapes: circular, catenoid, square, and triangle. Consequently, while the healing threshold varied for different shapes for a given La_l, it was found that the observed

effect from varying La_l remains valid and following the power law found for the circular profile given by the expression 5.2.

Chapter 6

Hole and Bubble Dynamics

This chapter studies the dynamics of a hole in a bubble cap (i.e., a curved film). Since, in this case, a high-pressure gas outflow exits through the hole opening, the problem of the hole on the curved film is affected and is not the same as the flat film. The purpose of this chapter is to study the gas outflow and bubble dynamics to lay the groundwork for studying the effect of film curvature and gas outflow on the hole healing threshold discussed in the subsequent chapter.

In this process, firstly, the dynamics of the outflowing gas and its effect on the bubble form and size are detailed, which here is referred to as the study of the bubble shrinkage. Secondly, the coupled dynamics of the gas outflow, bubble cap, and hole opening are examined in detail for different stages during the simulation and various gas densities. Thirdly, the velocity and pressure profiles of the gas outflow at the hole opening are examined, hinting that the gas may undergo a Venturi effect when exiting through the hole. Finally, the hypothesis of the Venturi effect is studied in detail, first formulating the concept along with a qualitative examination and then a quantitative analysis of the effect on a given streamline velocity of the gas outflow, confirming the hypothesis.

The basis of the studies in this chapter is the bursting and healing case described in section 4.1. Nevertheless, the bursting case is the primary focus since the purpose of this chapter is to study the gas outflow dynamics. Moreover, the density ratio for this bursting case has been varied in section 6.2.1 and 6.2.1 to examine the effect of the gas inertia on the dynamics of the gas outflow.

6.1 Bubble Shrinkage and Gas Outflow

As discussed previously, in the case of a bubble cap described in section 2.4.2 and illustrated in figure 2.11, there exists an excess of pressure Δp inside the film caused by surface tension. Starting from the outside of the bubble with the ambient pressure and crossing through the film,

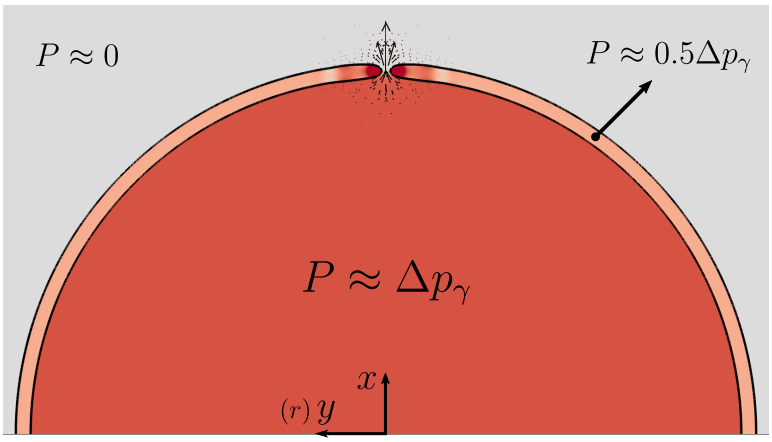

Fig. 6.1 Visualization of the gas outflow dynamics from a bubble. The excess pressure within the bubble drives the gas out through the hole, with the overlaid pressure field and velocity vectors captured at $t^* \approx 1$. The simulation is based on parameters from table 2.1 with $d_b^* = 50$ and $d^* = 0.754$ first described in section 4.1 as a critical bursting case.

two jumps occur in the pressure field. First

$$\Delta p_1 = \frac{2\gamma}{(d_b/2 - \delta)} \tag{2.41}$$

and second

$$\Delta p_2 = \frac{2\gamma}{(d_b/2)}, \tag{2.42}$$

corresponding to the crossing of the two interfaces of the film. Consequently, the total pressure difference is approximately

$$\Delta p = \Delta p_\gamma \approx \frac{8\gamma}{d_b} \tag{6.1}$$

provided $\delta \ll d_b$, a reasonable assumption for the bubble cap problem.

The excess pressure accelerates the fluid out of the bubble through the hole opening, as illustrated in figure 6.1. The pressure field overlaid with velocity vectors for the gas phase is recorded at $t^* \approx 1$ for a simulation set up according to table 2.1 with $d_b^* = 50$ and $d^* = 0.754$ (i.e., a bursting case).

6.1.1 Bubble Cap Radial Contraction

As a direct consequence of the gas outflow, as shown in figure 6.1, the bubble size shrinks due to the volume conservation principle. To demonstrate this effect, two simulations with hole sizes near the healing threshold and physical parameters set according to table 2.1 have been

carried out with one case healing and the other bursting[1]. To illustrate the bubble shrinkage in these two simulations, one must first find the velocity components in the polar coordinate system since the bubble cap moves radially inward when shrinking. The r axis of the numerical domain with $x-r$ coordinates has been relabeled as the y axis to avoid confusion with the radial axis in the polar coordinate $r-\theta$.

At any given point with x and y coordinates in the 2D axisymmetric numerical domain, one can find the corresponding polar coordinates using

$$r = \sqrt{x^2+y^2} \tag{6.2}$$

and

$$\theta = \arctan(y/x). \tag{6.3}$$

Similarly, the velocity components in the polar coordinates are found using

$$u_r = u\cos(\theta) + v\sin(\theta) \tag{6.4}$$

and

$$u_\theta = u\sin(\theta) + v\cos(\theta) \tag{6.5}$$

where u and v represent the velocity in the x and y directions, respectively. Using these conversions, figure 6.2 provides the radial and tangential velocity color maps uniquely for the bubble cap by excluding the gas phase. Given the size of the bubble cap compared to the film thickness, for each case, the segment containing the film has been cropped and tilted for better visualization while minimizing the figure size. Nevertheless, the actual configurations of the bubble are the same as in figure 6.1.

Sub-figures (a) and (b) of figure 6.2 provide the radial velocity field u_r^* at $t^* \approx 1$ in both cases– a qualitative representation of how the bubble cap shrinks due to the gas outflow. The u_r^* color map with maximum and minimum values set to 0 and -0.0005, respectively, illustrates how the film is contracted inwardly in the radial direction, causing the bubble volume to decrease, and how the bubble shrinkage effect creates a complex radial velocity field near the hole region. The bubble cap in the bursting case has a higher u_r^* value on average since the hole opening increases over time, causing the bubble to shrink further as more gas escapes the bubble. In contrast, u_r^* eventually reaches zero in the healing case when the hole closes.

Figure 6.2 also provides the color map of the tangential velocity u_θ^* for bursting and healing cases in sub-figures (c) and (d), respectively. Using the u_θ^* color map with maximum and

[1]These two simulations are, in fact, the same as in section 4.1.

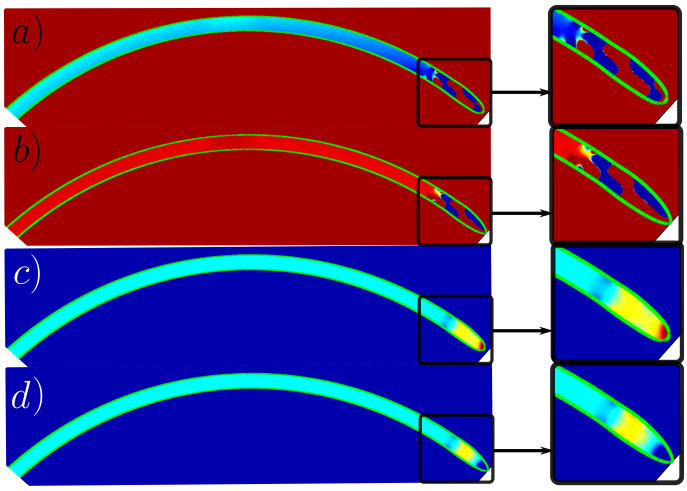

Fig. 6.2 Illustration of radial and tangential velocities color maps during the shrinkage of the bubble for the healing and bursting cases described in section 4.1 captured at $t^* \approx 1$. Sub-figures (a) and (b) show the radial velocity u_r^*, highlighting the bubble volume shrinkage for the bursting and healing case, respectively, with maximum and minimum values set to 0 and -0.0005. Sub-figures (c) and (d) depict the tangential velocity u_θ^*, emphasizing the hole tip retraction for the bursting and healing case, respectively, with maximum and minimum values set to 0.2 and -0.1.

minimum values set to 0.2 and -0.1, respectively, one could qualitatively examine the velocity of the hole tip, which is retracting in the bursting case and contracting in the healing case.

6.1.2 Shrinkage Rate Estimation

One can calculate the volumetric gas outflow rate using

$$Q(t) = 2A_{mn}(t)\overline{u_{\text{th}}(t)} \tag{6.6}$$

where $\overline{u_{th}(t)}$ is the average speed of the gas outflow at the hole throat where $x^* \approx 24.5$, and

$$A_{mn}(t) = \pi r_0^2(t) \tag{6.7}$$

the corresponding cross-section area. The prefactor 2 in equation 6.6 is included to account for the fact that there are two exiting holes in the numerical domain as detailed in section 2.4.2 and depicted in figure 2.12. Given the order of magnitude of the outflow speed, one can confirm that the Mach number is always far below one, validating the incompressible assumption made in section 2.2. Therefore, the gas outflow must be compensated by the shrinkage of the bubble (i.e., decrease of bubble volume).

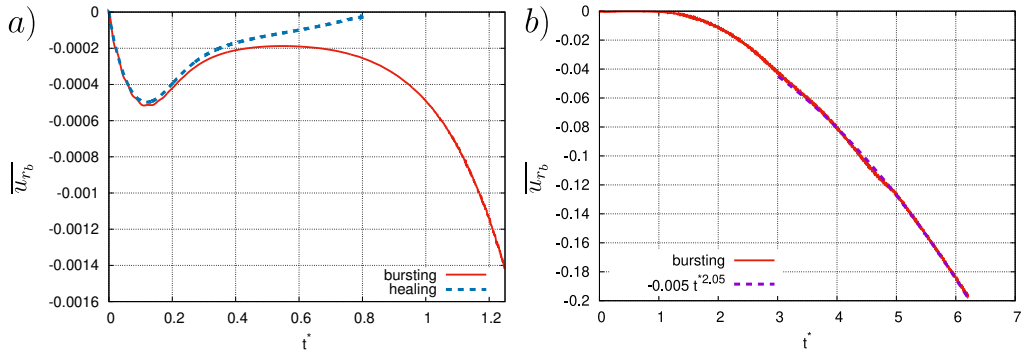

Fig. 6.3 (a) Temporal variation of the average radial velocity, $\overline{u_{r_b}}^*$, within the bubble cap for the healing and bursting cases described in section 4.1, with negative values indicating bubble shrinkage. (b) Temporal variation of $\overline{u_{r_b}}^*$ for the bursting case over an extended period, showing its behavior in the quasi-steady state. The power function fit for the bursting case, $\overline{u_{r_b}}(t) = -0.005t^{*2.05}$, is represented for the time range $t^* = [3, 6.25]$.

To measure the shrinkage rate of the bubble dV/dt, one can approximate the bubble shape to remain spherical with a volume

$$V = \frac{4}{3}\pi \overline{r_b}^3 \tag{6.8}$$

during the emptying process to find the rate of change in the bubble volume

$$dV/dt = 4\pi \overline{r_b}^2 \overline{u_{r_b}} \tag{6.9}$$

where $\overline{r_b}$ is the average bubble radius and $\overline{u_{r_b}} = dr_b/dt$ is the average radial velocity within the bubble cap when considering a polar coordinate as described in section 6.1.1 and depicted in figure 6.2. To measure $\overline{u_{r_b}}$, the film tip area is excluded to ensure the measurement is not affected by the capillary waves and its subsequent vortices within the film and near the tip area. Figure 6.3a shows the temporal variation of the $\overline{u_{r_b}}$ for the healing and bursting cases described in section 4.1, with $\overline{u_{r_b}} < 0$ indicating the shrinkage of the bubble. Additionally, sub-figure (b) shows the same plot for the bursting case but in a longer period to focus on how $\overline{u_{r_b}}$ varies with time in the quasi-steady state. For that purpose, a power function fit is employed to find $\overline{u_{r_b}}(t) = -0.005t^{2.05}$ for the period $t^* = [3, 6.25]$.

Employing the measured data for $\overline{u_{r_b}}$ directly from the simulations with equation 6.9, figure 6.4 with sub-figures (a) and (b) shows the temporal evolution of the approximated shrinkage rate dV/dt alongside the volumetric outflow rate of gas Q calculated using equation 6.6 for both of the healing and bursting cases described in section 4.1, respectively. It is observed that for both cases, the shrinkage rate approximation given by equation 6.9 closely matches with the volumetric outflow rate of the gas for $t^* < 1$ and after the inertial acceleration phase.

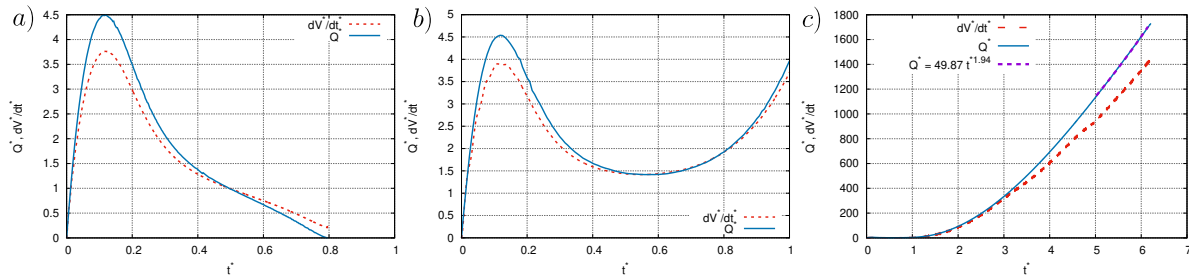

Fig. 6.4 Sub-figure (a) and (b) show the temporal evolution of the shrinkage rate with comparison of the approximated value dV/dt using equation 6.9 and the volumetric outflow rate of gas Q calculated via equation 6.6 for both the healing and bursting cases as described in section 4.1, respectively. This comparison illustrates a close match between the two rates for $t^* < 1$ and post the inertial acceleration phase. Sub-figure (c) demonstrates the divergence between the approximated shrinkage rate dV/dt and the outflow rate Q for $t^* > 4$ due to the deviation of the bubble cap shape from spherical. A fitting power function $Q = 49.87t^{1.94}$ is shown, closely tracking the measured data in the quasi-steady state for $t^* = [5, 6.25]$.

However, the shrinkage rate approximation dV/dt starts to diverge from Q for $4 < t^*$ as the bubble cap contracting shape gradually deviates from the spherical shape and the assumption in finding equation 6.9 is no longer valid. Figure 6.4c shows the fitting power function $Q = 49.87t^{1.94}$ closely following the measure data in the quasi-steady state for $t^* = [5, 6.25]$.

6.2 Bubble and Gas Coupled Dynamics

The gas outflow speed depends not only on the inertial acceleration and the viscous dissipation rate but also on the hole size, or in other words, on the minimum cross-section area[2] (A_{mn}) in the gas outflow and its temporal evolution. Furthermore, the pressure difference generating this flow decreases as the high-pressure gas exits through the hole. These features are detailed in the following sections.

Figure 6.5 provides the temporal evolution of the minimum cross-section area A_{mn} and its rate of change dA_{mn}/dt, which is following the r_0 and dr_0/dt evolution of the bursting case given in figure 4.2. The flickering motion affects the gas flow by varying A_{mn}, particularly when the simulation begins. It is worth noting that due to the gas inertia, a certain amount of time is required for the gas flow to reach a quasi-steady state for a given A_{mn} value and Δp; an

[2]The minimum cross-section is a circular disk of radius r_0 where r_0 is the distance from the hole tip to the x-axis.

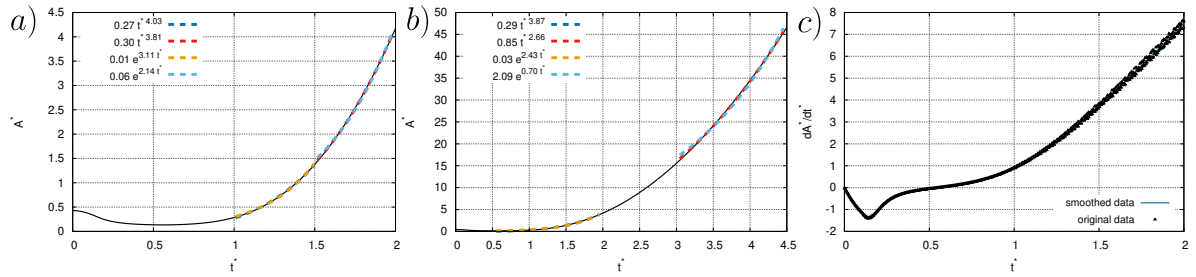

Fig. 6.5 Temporal evolution of the minimum cross-section area A_{mn} in panels (a) and (b), and its rate of change dA_{mn}/dt in panel (c), corresponding to the development of r_0 and dr_0/dt in the bursting bubble case described in section 4.1 (see figure 4.2). Panels (a) and (b) depict the fitted exponential decay of $A_{mn}(t) = me^{-nt}$ and its comparison with power function fits for different periods, illustrating the changing dynamics of the gas flow within the bubble and the impact of flickering motion in the early stages of the simulation.

amount of time that is proportional to the gas inertia by

$$\tau_i = \sqrt{\frac{V}{\rho_{l/g}}\Delta p} \tag{6.10}$$

with V as the volume of the bubble

$$V = \frac{\pi}{6} d_b^3 \tag{6.11}$$

However, in the current problem, τ_i, A_{mn}, Δp, and V vary notably in time, rendering a coupled complex dynamic for the gas outflow.

Figure 6.5a and b show several exponential fits in different periods and of the format

$$A_{mn}(t) = me^{-nt} \tag{6.12}$$

where $e = 2.718$. Accordingly, a time scale for the $A_{mn}(t)$ can be suggested as

$$\tau_A = 1/n \tag{6.13}$$

Subsequently, the time scale for the evolution of the minimum cross-section area in the period $t^* = [1, 1.5]$ is $\tau_A^* \approx 1/3$, which increases to $\tau_A^* \approx 7/5$ for the period $t^* = [3, 4.5]$ corresponding to a quasi-steady state hole tip retraction. On the other hand, according to equation 6.10, the initial inertial time scale of the gas is

$$\tau_i^* \approx 5/2 \tag{6.14}$$

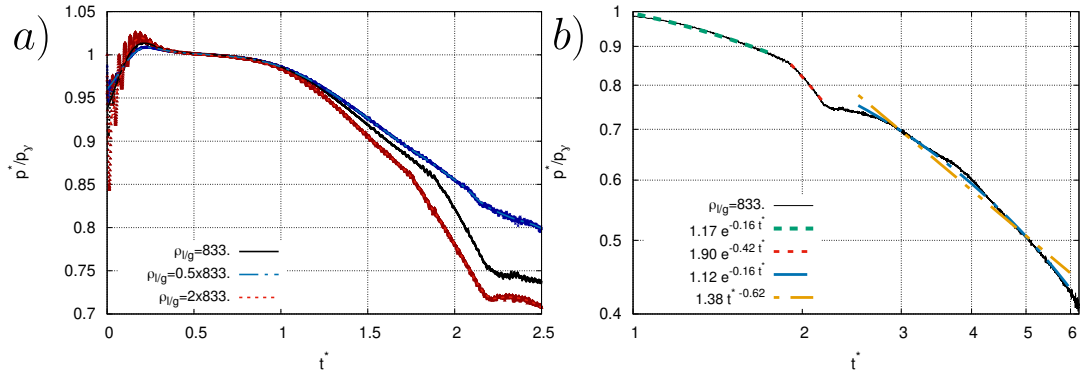

Fig. 6.6 Evolution of the average pressure difference $\overline{\Delta p}(t)$ inside a bursting bubble described in section 4.1, but for various gas densities. In sub-figure (a), the response of gas outflow for gas densities $\rho_g^* = \{1/833, 2/833, 0.5/833\}$ is compared, highlighting the faster bubble evacuation in less dense gases within $t^* < 2.5$. Sub-figure (b) analyses $\overline{\Delta p}(t)$ using exponential and power fit functions for the case with ($\rho_g^* = 1/833$), showing a better accuracy with the exponential functions.

where $\Delta p/P = 4/d_b$ (see equation 2.23 or the footnote below[3]) with $d_b^* = 50$ and $\rho_{l/g} = 833$. As a result, it becomes evident that $\tau_A < \tau_i$ is always true for at least $t^* < 4.5$, meaning that the gas never has sufficient time to adapt to the changes in A_{mn} and reach a constant speed.

Although the exponential fit is used here to discuss the time scale τ_A, it is noted from figure 6.5a and b shows that power functions work better, particularly for larger t^*.

6.2.1 Bubble Pressure

The average pressure difference within the bubble $\overline{\Delta p}(t)$, which drives the gas outflow, decreases as the gas exits through the hole. Figure 6.6 presents the values for $\overline{\Delta p}(t)$ for three cases of different gas densities $\rho_g^* = \{1/833, 2/833, 0.5/833\}$. Sub-figure (a) compares the inertial response of these cases for $t^* < 2.5$ while sub-figure (b) examines more precisely the evolution of $\overline{\Delta p}(t)$ for the standard case with $\rho_g^* = 1/833$ using the logarithmic scale with a longer period and fitting functions. Sub-figure (a) shows that the less dense gas expectedly empties quicker. However, it is also notable that the average pressure slightly increased after the initialization of the simulation. This effect is attributed to the hole contraction motion that initially occurs and creates a high-pressure area near the hole opening, increasing the calculated average pressure of the bubble.

Sub-figure (b) illustrates that the average pressure inside the bubble substantially decreases and is halved in five time units of the simulation. Utilizing two different types of fit functions, it is evident that $\overline{\Delta p}(t)$ is more accurately approximated by an exponential than a power function.

[3] $P = 2\gamma/\delta$ is the pressure scale used in the nondimensionalization of the governing equation. Hence, $\Delta p = 4/d_b^*[P]$.

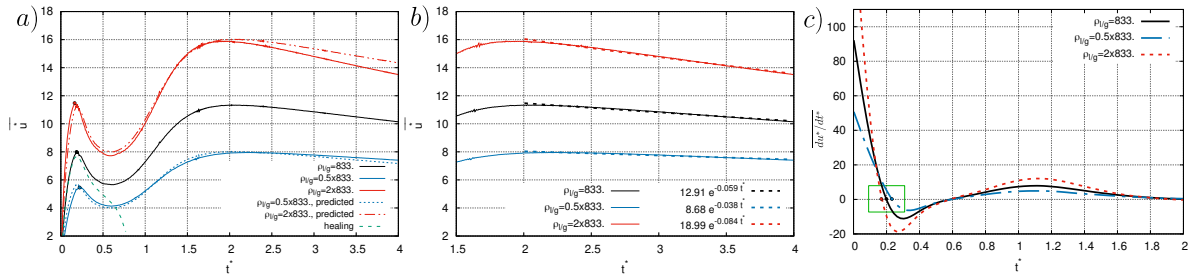

Fig. 6.7 Analysis of average exiting gas velocity $\overline{u^*}$ and acceleration $\overline{du^*/dt^*}$ for different gas densities in the bursting bubble described in section 4.1. Sub-figure (a) displays three curves representing the evolution of $\overline{u^*}$ for densities $\rho_g^* = \{0.5/833, 1/833, 2/833\}$ over the period $0 < t^* < 4$, including a comparative healing case ($\rho_g^* = 1/833$ and $d^* = 0.744$). This graph highlights the initial acceleration phase ($0 < t^* \lessapprox 0.2$) and validates the theoretical velocity-density relationship (6.19) through superimposed dashed lines for adjusted densities based on the case with $\rho_g^* = 1/833$. Sub-figure (b) illustrates exponential fits for the gas velocity $u^*(t)$ in the quasi-steady state. Sub-figure (c) focuses on comparing the duration of inertial acceleration for different gas densities by marking the first instance of $\overline{du^*/dt^*} = 0$.

For $1 < t^*$ and using the exponential fits, one can recognize two distinct regions

$$\overline{\Delta p}(t) \propto \begin{cases} e^{\frac{-t^*}{6.25}} & 1 < t^* < 1.8 \text{ or } 2.5 < t^* < 6 \\ e^{\frac{-t^*}{2.38}} & 1.9 < t^* < 2.25. \end{cases} \tag{6.15}$$

According to equation 6.15, there are two time scales for the temporal evolution of the pressure inside the bubble (with e as the exponential base). According to equation 6.14 and using $\tau_{\Delta p}^* = 6.25$ that is valid except when $1.9 < t^* < 2.25$, the pressure time scale is larger than the gas inertial time scale $\tau_{\Delta p} > \tau_i$. This effect is expected because $\overline{\Delta p}(t)$ is derived by the amount of gas exiting the hole and, thus, by the gas inertia.

6.2.2 Gas Outflow Velocity

Similarly, for the three cases discussed above, the average exiting velocity $\overline{u^*}$ and acceleration $\overline{du^*/dt^*}$ of the gas through the hole opening is examined in figure 6.7. Sub-figure (a) shows the three curves representing the evolution of $\overline{u^*}$ for $t^* = [0,4]$ in addition to a healing case with $\rho_g^* = 1/833$ and $d^* = 0.744$ for comparison with the bursting case. For a given density ratio, one can note the initial acceleration of the gas when $0 < t^* \lessapprox 0.2$ and where the gas inertia determines how quickly the gas gains momentum to match the pressure difference $\overline{\Delta p}(t)$. The inertial acceleration of the gas takes different durations according to the density of the gas by comparing the time when $\overline{du^*/dt^*} = 0$ for the first time in each curve using sub-figure (c). This time is delayed as the gas density increases and is found to be $t^* \approx 0.17, 0.19,$ and 0.22 for the cases with $\rho_g^* = 0.5/833, 1/833,$ and $2/833$, respectively.

For $t^* \lessapprox 0.6$, the cross-section area is continuously decreasing as the hole initially contracts (see figure 6.5), hence hindering the gas outflow and affecting $\overline{u^*}$. However, the effect on $\overline{u^*}$ becomes evident only after the gas has gained the corresponding momentum to the initial pressure difference $\overline{\Delta p}(t)$ inside the bubble $0.2 \lessapprox t^*$. Consequently, the average gas velocity decreases after reaching a local maximum value at $t^* \approx 0.2$. This effect continues until $t^* \approx 0.6$ when the hole starts to retract, increasing A^*_{mn}, which in return facilitates the outflow of the gas and increases $\overline{u^*}$. Nevertheless, the acceleration of the gas is eventually stopped at $t^* \approx 2$ due to, firstly, the substantial decrease of $\overline{\Delta p}(t)$ as the gas escapes the bubble over time (see figure 6.6). Secondly, the film retraction speed reaches a constant value after a period of $\Delta t^* \approx 1$ from the onset of its retraction at $t^* \lessapprox 0.6$. Therefore, the gas outflow could be considered to have reached a quasi-steady state at $t^* \approx 2$ where $\overline{u^*}$ is no longer increased due to the acceleration in the hole retraction.

Considering the momentum equation 2.1, one can assume that the gas velocity of the flow induced by the initial pressure difference results from a balance between the pressure gradient (∇p) and viscous stresses ($\mu_g \nabla^2 u$) within the gas flowing through the opening such that

$$\frac{\Delta p}{L} \propto \mu_g \frac{u}{L^2} \tag{6.16}$$

with L as a length scale. Setting $L = d$ together with equation 6.1 results in a gas characteristic velocity

$$u \propto \frac{d}{d_b} \frac{\gamma}{\mu_g} \tag{6.17}$$

Using the equation 2.17, one can re-write the equation 6.17

$$u \propto \gamma \frac{d}{d_b} \sqrt{\frac{\rho_{l/g} \mathrm{La}_g}{\mathrm{La}_l}} \tag{6.18}$$

to involve the gas density instead of viscosity, which is not considered an independent parameter in this examination, as discussed previously.

According to the equation 6.18 one finds

$$\overline{u^*} \propto \sqrt{\frac{1}{\rho^*_g}} \tag{6.19}$$

as a hypothesis defining the relation between the average velocity of the outflowing gas and its viscosity, here varied by the density ratio according to equation 2.17. To test this hypothesis, the curve corresponding to the case with $\rho^*_g = 833$ is multiplied by the corresponding density ratio using the relation 6.19. The results are provided in figure 6.7a where the dashed red and blue

lines represent the result of the hypothesis above for the cases with $\rho_g^* = 2 \times 833$, and 0.5×833 based on the values of the case with $\rho_g^* = 833$ given by the solid black curve. These results show a good accuracy between the predicted values and the measured data from the simulations, validating the relation 6.19 for the gas flow.

Furthermore, 6.7b shows the results of exponential fits for $u(t)$ of the form

$$u(t) = me^{-nt} \tag{6.20}$$

after the gas outflow has reached a quasi-steady state ($2 \lessapprox t^*$). Accordingly, the exponential fits yield velocity time scales of $\tau_u^* = 26, 17,$ and $, 12$ for cases with $\rho_g^* = 2/833, 1/833,$ and $0.5/833$, respectively.

6.3 Gas Outflow Velocity and Pressure at the Hole Throat

Figure 6.8 shows the gas exiting velocity u and pressure p profiles for the bursting case in sub-figures (a) and (b), respectively. The velocity and pressure profiles have been recorded at the hole minimum cross-section A_{mn} (i.e., $x^* \approx 24.5$) and identically at various times starting from the initialization until the final record at $t^* = 4.68$.

Similar to what was discussed in relation with 6.7, one can examine the gas velocity in more detail using figure 6.8a, which presents individual velocity profiles at the hole and at pivotal times rather than the averaged value $\overline{u(t)}$. From figure 6.8a, it is observed that the flow first accelerates and that the maximum velocity in the vertical profile (u_{mx}) reaches a local maximum value at $t^* \approx 0.2$. Subsequently, the gas flow decelerates since the hole tip moves inwardly and A_{mn} decreases. At $t^* \approx 0.6$, when the cross-section area is at its minimum, u_{mx} reaches a local minimum value. Upon reaching this point, the gas outflow speed increases again as the hole tip movement reverses its direction, and A_{mn} monotonically increases from this point onward. However, at $t^* = 1.98$, u_{mx} reaches a global maximum value corresponding to the onset of the quasi-steady state.

Most importantly, 6.8a illustrates the formation of a growing saddle shape in the gas velocity profile from the onset of reaching the quasi-steady state at $t^* \approx 2$. Furthermore, the gas velocity profiles illustrate the formation of a boundary layer on the film surface, the length of which grows in time. Therefore, in a given profile for $t^* \approx 2$, starting from the boundary of the gas and liquid, the gas velocity reaches its maximum value u_{mx} at a distance equal to one film thickness from the film boundary. Beyond this distance from the boundary and further closer to the radial axis, the gas velocity is decreased to reach a local minimum value u_{mn} at the center line with $y^* = 0$. Examining the pressure profiles provided in figure 6.8b along with the corresponding

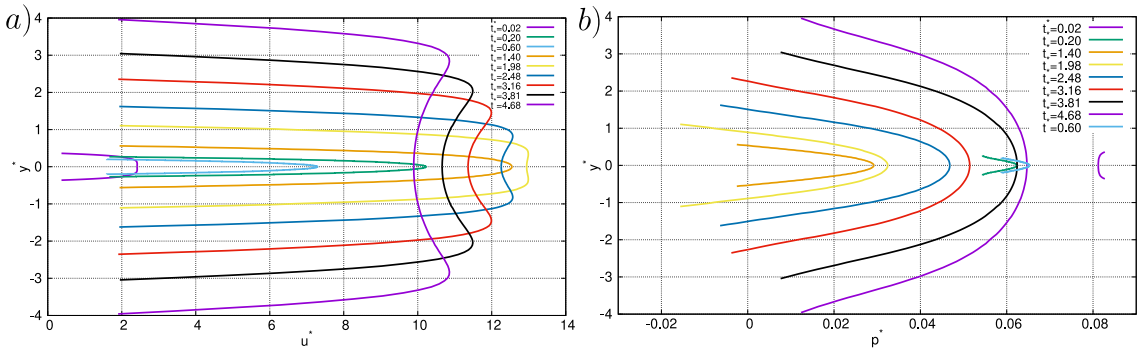

Fig. 6.8 Detailed temporal evolution of gas velocity profiles, u^*, at $x^* \approx 24.5$ with $A^* = A^*_{mn}$ during a bubble bursting event. (a) The figure depicts key moments in the velocity profile development, with the flow initially accelerating as the gas gains inertia, with u^*_{mx} peaking at $t^* \approx 0.2$, followed by a deceleration as the hole tip retracts. u^*_{mx} attains a local minimum at $t^* \approx 0.6$, and then increases again, reaching a global maximum at $t^* = 1.98$, indicating the onset of quasi-steady state. This panel illustrates the formation of a saddle-shaped velocity profile and a boundary layer on the film surface, which expands over time. (b) This section presents the corresponding pressure profiles, revealing that the maximum pressure of a given profile resides at the center line with the minimum velocity, indicative of a Venturi-like effect.

velocity profiles, it is noted that this local minimum value of the velocity at the center line is accompanied by the maximum pressure value, reminding of a Venturi effect, which will be discussed subsequently.

6.4 Venturi Effect on the Gas Outflow

Given the strong gas flow exiting through the hole opening, it is intriguing to investigate the possible effects of such a flow on the hole dynamics. Figure 6.9 illustrates an example of such an effect for a nearly inviscid gas (i.e., $\mathrm{La}_g = 10^7$) flowing through the hole opening using the pressure color map overlaid with the velocity vectors.[4] The tip of the hole is strongly affected and deformed. One can note that the gas outflow, if strong enough, could drag and elongate the hole tip along with the outflow. Moreover, Figure 6.9 also shows the formation of strong vortices in the gas phase near the hole exiting area.

6.4.1 Concept and Formulation

For an incompressible flow, a spatial increase in the cross-section area increases fluid velocity by mass conservation while its pressure drops to conserve mechanical energy. Figure 6.10a

[4]The high values $\mathrm{La}_l = \mathrm{La}_g = 10^7$ were chosen so that the gas flow effect on the bubble cap would be pronounced for visualization purposes.

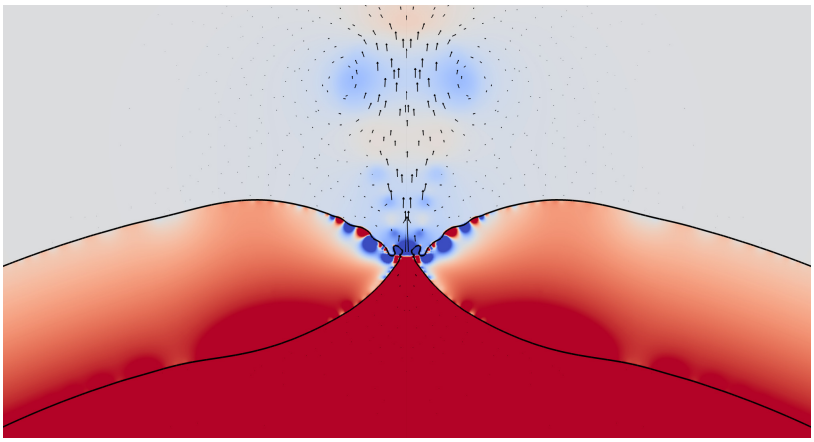

Fig. 6.9 Visualization of the dynamics induced by a nearly inviscid gas flow with $\mathrm{La}_l = \mathrm{La}_g = 10^7$ through the hole opening with $d_b^* = 15$, $d^* = 0.6$. The pressure color map with maximum and minimum set to 1.5 and -1.5, respectively, and overlaid with velocity vectors, clearly shows the pronounced deformation at the hole tip due to the strong gas outflow. Additionally, robust vortical structures in the gas phase near the hole exit area are evident.

presents the velocity vector field and color map near the hole for the bursting case described in section 6.1 and recorded at $t^* \approx 1$, while sub-figure (b) provides the streamline for the same case and recording time. Figure 6.10 indicates that the gas flowing out of the bubble and passing through a Venturi shape created by the film interface undergoes a similar effect as the Venturi effect governed by Bernoulli's principle where the velocity of the gas changes following the change in the cross-section area at the hole opening. For an inviscid flow, the Bernoulli equation along a streamline (the Venturi equation) states

$$p_1 - p_2 = \frac{\rho}{2}(u_2^2 - u_1^2). \tag{6.21}$$

with subscripts 1 and 2 indicating the upstream and downstream values, respectively.

Solving for the downstream velocity u_2 and considering a viscous flow, the Venturi equation 6.21 can be modified into

$$u_2 = C\sqrt{\frac{2}{\rho}(p_1 - p_2) + u_1^2}. \tag{6.22}$$

to take into account the viscous dissipation by involving an empirical coefficient C that primarily depends on the Reynolds number of the flow and the shape of the Venturi (Karthik Ms et al., 2015).

Given the discussion in the previous section and the velocity and pressure profiles of the gas outflow from the bubble presented in 6.8, it becomes intriguing to examine whether the gas outflow undergoes a similar effect to that of a flow in Venturi device as described in equation

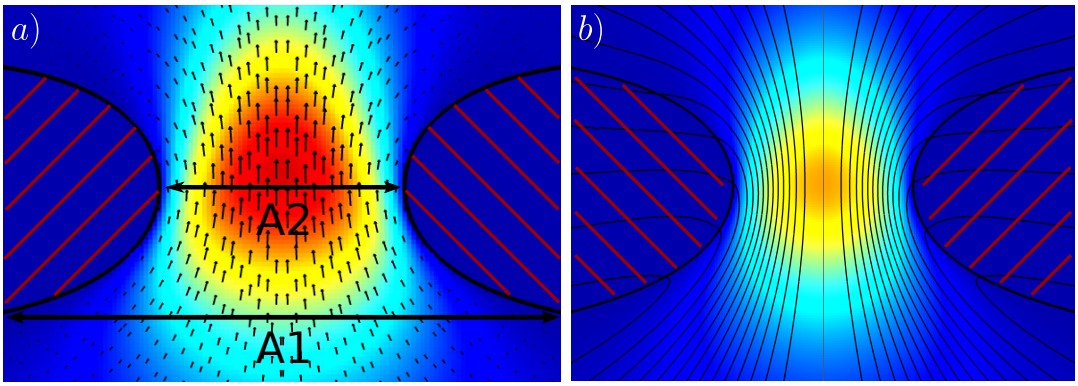

Fig. 6.10 (a) Color-map representation of the gas velocity in the x-direction near the hole opening at $t^* = 1$. The overlay of the velocity vector field qualitatively illustrates the Venturi effect following Bernoulli's principle, where A_1 and A_2 show the maximum and minimum cross-section areas. (b) Streamlines of the gas outflow through the hole captured at $t^* = 1$ overlaid with the velocity color map in the x-direction.

6.22. Figure 6.10b shows the gas outflow streamlines passing through the hole at $t^* = 0.25$ for the bursting case described in section 6.1. When the gas outflow approaches the hole, and the cross-section area decreases, the distance between the streamlines is reduced, indicating a higher exiting velocity.

The data points of velocity and pressure values are plotted against the x-axis near the hole area in figure 6.11 for the same bursting case at $t^* = 0.1$ and $t^* = 1$ in sub-figures (a) and (b), respectively. At any given point on the x-axis, there are multiple data points corresponding to the different locations on the y-axis (i.e., distance from the center line). Figure 6.11 makes it possible to distinguish different streamlines of the gas flow. The velocity and pressure values corresponding to the center streamline are distinguished using the solid black lines, showing the spatial evolution in the x-axis as the gas exits the hole.

6.4.2 Validation

To examine the Venturi effect according to the equation 6.22, one needs two data points on the same streamline. For that purpose, two points with $x_1^* = 24$ and $x_2^* = 24.5$ (the hole throat) are selected on the center-line ($r^* = 0$) as it is the only streamline known in advance throughout the simulation. Should the flow undergo a Venturi effect, using the upstream values u_1 and p_1 from the data point at $x_1^* = 24$ in the equation 6.22, one can predict the values for u_2 and p_2. Figure 6.12a shows the comparison between the measured value of u_2 with the Venturi predicted value found using equation 6.22 while assuming an inviscid condition (i.e., $C = 1$). The comparison of the two curves shows that the downstream gas velocity closely follows the Venturi effect

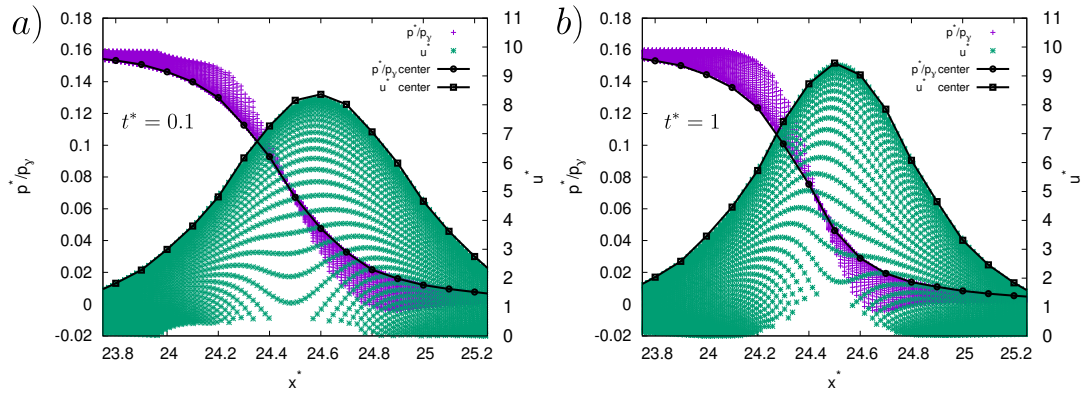

Fig. 6.11 Visualization of the pressure and gas velocity variations along the x-axis near the hole at $t^* = 0.1$ and $t^* = 1$ provided in panels (a) and (b), respectively. In each plot, the left axis corresponds to pressure, while the right axis represents the gas velocity in the x-direction. The center streamline values for pressure and velocity are distinguished using solid black lines with circle and square markers, respectively.

prediction after gas outflow reaches a quasi-steady state (i.e., $t^* \lessapprox 2$). That is when the gas has completed the inertial acceleration phase, and the film retraction has reached a constant speed.

To better examine the discrepancy between the measured value of u_2 and the value predicted by the inviscid Venturi effect, figure 6.12b plots the Venturi coefficient C using

$$C = \frac{u_2^{\text{measured}}}{u_2^{\text{venturi}}}. \tag{6.23}$$

As observed from these results, for $2 \gtrapprox t^*$ the center streamline in the gas flow has $C \approx 1$, indicating both a good agreement with the Venturi prediction and that the vicious effect on the Venturi prediction becomes less important as the gas flow gains velocity.

As discussed by Karthik Ms et al. (2015), C varies with the Reynold number of the flow inside a given Venturi device, meaning that the same concept could apply here for the observed variation in C given by figure 6.12b. To verify this effect, one could plot the Reynolds number of the gas flow at the hole throat using

$$Re = \frac{\rho_g u_g r}{\mu_g} \tag{6.24}$$

where the hole minimum radius r has been selected as a length scale of the flow. Employing equation 2.17, one can re-write equation 6.24 into

$$Re = u_g r \sqrt{\frac{\text{La}_g}{\rho_{l/g}\text{La}_l}}. \tag{6.25}$$

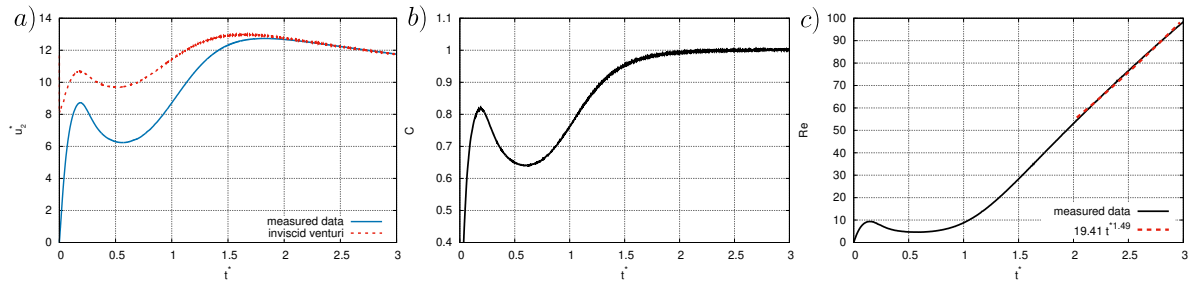

Fig. 6.12 (a) Comparison of the downstream gas velocity u_2^* measured at $x_2^* = 24.5$ with the velocity predicted by the Venturi effect using an inviscid flow assumption (i.e., $C = 1$) according to equation 6.22. The plot illustrates the close alignment with Venturi prediction in the quasi-steady state post $t^* \approx 2$. (b) Plot of the Venturi coefficient C, calculated as the ratio of measured to Venturi-predicted gas downstream velocity u_2^*, showing its convergence to 1 for $t^* \approx 2$ and corroborating the reduced viscous effects on the Venturi prediction with increasing Re. (c) Temporal evolution of Re at x_2^*, calculated using equation 6.25 with fitted power function for $t^* = [2,3]$. Additionally, for $t^* \lessapprox 1$, one finds $Re < 10$ for the gas flow at the hole throat.

Figure 6.12c presents the temporal evolution of Re at the hole throat using equation 6.25. One can see that as Re increases, C approaches 1, and the viscous effect on the Venturi flow decreases. It is worth noting that even though gas velocity at the hole throat begins to decrease for $2 \gtrapprox t^*$, the Reynolds number continues to increase since the hole minimum radius, the length scale of the flow increases faster than the velocity is decreased. Fitting a power function, the relation

$$19.41 t^{1.49} \tag{6.26}$$

is found to closely estimate the increase of Re with time for $t^* = [2,3]$. Moreover, 6.22c shows that for the gas flow at the hole throat $Re < 10$ for $t^* \lessapprox 1$.

Given the examination of the gas outflow using figure 6.12 for the center streamline values and comparison with the downstream velocity predicted by Bernoulli's principle, the exiting gas flow is found to undergo a Venturi effect, predictable by the equation 6.22, and confirming the speculated notion at the beginning of this section.

6.5 Summary

This chapter has examined the gas outflow from the bubble through the hole opening and the subsequent shrinkage of the bubble as a result of volume conservation. The bubble shrinkage rate was approximated using equation 6.9 and was compared to the simulation results, yielding a good agreement.

The gas outflow was found to be a coupled function of the gas density and viscosity, the hole size, and the pressure difference between the inside and outside of the bubble. This complex dynamic was investigated in detail, and the following conclusions were drawn:

- The inertial acceleration of the gas outflow was found to be a function of the gas density, with less dense gases accelerating faster.
- The time scale of the cross-section area evolution is smaller than the inertial time scale of the gas outflow for the bursting case studied here.
- The pressure difference was found to decrease substantially (halved in five time units of the simulation) as the gas escapes the bubble according to an exponential function rather than a power function.
- The gas outflow was identified to reach a quasi-steady state at $t^* = 2$ after the hole retraction speed is stabilized.
- A hypothesis was proposed to relate the gas outflow velocity to the gas viscosity using equation 6.16 and 6.19, which was confirmed to be accurate using the numerical results.

The velocity and pressure profiles of the gas outflow at the minimum cross-section area of the hole were examined in detail for the same bursting case. After reaching the quasi-steady state, the gas velocity was found to be maximum near the film boundary and minimum at the center line, while the pressure profile was found to be the opposite. This observation led to the speculation that the gas outflow undergoes a Venturi effect, predictable by Bernoulli's principle.

Consequently, the gas outflow was examined qualitatively and quantitatively using Bernoulli's principle for the center streamline values, and the results were compared with the measured values to draw the following conclusions:

- The center streamline values of the gas outflow were found to undergo a Venturi effect with good agreement after the flow reaches a quasi-steady state.
- The viscous effect on the Venturi prediction was shown to decrease as the gas flow gains more velocity and the Reynolds number of the flow increases.

Apart from the viscous dissipation of the flow that makes the gas outflow initially deviate from Bernoulli's principle, the more complex condition of the problem at hand comes from the fact that firstly, the cross-section area sharply varies from $\approx \infty$ to A_{mn}. Secondly, the cross-section area is not only changing in space but also in time as the film tip moves and its shape changes. Therefore, the gas outflow near the hole opening is more complex than a pipe or nozzle flow.

Nevertheless, it is plausible that the pressure drop associated with the Venturi effect at the hole proximity, if strong enough, could cause an otherwise bursting case to heal. The following chapter will examine this counter-intuitive idea that the high-pressure gas exiting the bubble could help the healing of an otherwise bursting bubble.

Chapter 7

Hole Healing Threshold Variations–Bubble Cap

In chapter 5, the hole healing threshold variations with different parameters of the problem for the case of a flat film were studied. However, as detailed in chapter 6, the problem of a hole on a bubble cap introduces a new parameter, the film curvature, which could affect the healing threshold, such that

$$d^{*c} = f(\mathrm{La}_l, \mathrm{La}_g, \rho_{l/g}, d_b/\delta). \tag{2.30}$$

Therefore, this chapter investigates the hole healing threshold variations with different parameters of the problem explicitly for the case of a bubble cap in similar manners as chapter 5.

It is worth noting that the dichotomy results for the liquid Laplace number La_l effects on the hole healing threshold in the case of a bubble cap are not discussed in the present chapter as the effect was found to be identical to that of the flat film presented in chapter 5. This is because the liquid Laplace number mainly affects the flow with the bubble cap in a similar manner as in the case of the flat film.

As discussed in chapter 6, the film curvature creates an initial pressure difference given by

$$\Delta p = \Delta p_\gamma \approx \frac{8\gamma}{d_b} \tag{6.1}$$

in the bubble and a subsequent gas outflow. As detailed in section 6.4, the hole opening creates a Venturi effect on the gas outflow that causes a local pressure drop at the hole minimum cross-section, which could augment the hole closure and, therefore, increase the healing threshold. Hence, in this chapter, the somewhat counter-intuitive idea that the high-pressure gas exiting the bubble could augment the hole healing is investigated by simulating for different bubble

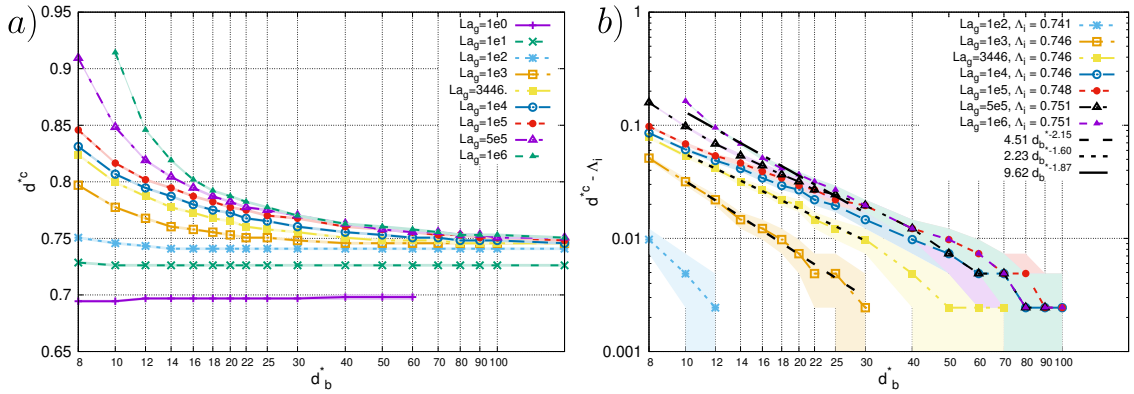

Fig. 7.1 (a) Healing threshold d^{*c} versus bubble size d_b^* for varying gas Laplace numbers La_g while keeping constant $\mathrm{La}_l = 633$ and $\rho_{l/g} = 833$, highlighting the Venturi effect on the healing process. (b) $d^{*c} - \Lambda_i$ is plotted on a logarithmic scale against d_b^*, where Λ_i is the corresponding healing threshold for the flat film with a given La_g. The power fitting functions for several values of La_g are provided with a trend that indicates a convergence towards $n \approx -2$ for increasing values of La_g. The filled curve around the solid lines represents the accuracy of the dichotomy process equal to ± 0.005 with seven mesh levels within the film thickness. The filled curve is enlarged as the $d^{*c} - \Lambda_i$ decreases in panel (b) due to the logarithmic scaling.

sizes d_b^* and gas characteristics while taking a standard film bursting case in the oceanic context described in table 2.1 as a basis for other parameters.

7.1 Bubble Size and Film Curvature – d_b^*

7.1.1 Dichotomy Results

In figure 7.1a, the result of the dichotomy simulations for a wide range of bubble sizes from $d_b^* = 8$ to $d_b^* = 150$ and gas Laplace numbers from $\mathrm{La}_g = 1$ to $\mathrm{La}_g = 10^6$ are provided while $\mathrm{La}_l = 633$ and $\rho_{l/g} = 833$ are kept constant for all cases. One can see the effect of film curvature in figure 7.1, where it is observed that the healing threshold d^{*c} is increased by increasing the film curvature (i.e., the intensity of the gas outflow).

Figure 7.1b represents the same data in a different form, where the healing threshold d^{*c} is first subtracted by Λ_i, the healing threshold for the flat film ($d_b^* \to \infty$), and then is plotted using the logarithmic scale against the bubble diameter d_b^* for the same set of simulations. The logarithmic scale is used to show the power law dependency of the Venturi effect on the bubble diameter d_b^*. Fitting a power function to the simulations results for the typical case with $\mathrm{La}_g = 3446$, one can find

$$d^{*c} - \Lambda_i = 4.51 d_b^{*-1.6} \tag{7.1}$$

where $\Lambda_i = 0.746$ is the healing threshold for the flat film with $\mathrm{La}_g = 3446$. The result of the power law fitting for other La_g values are marked in figure 7.1b with a slightly decreasing trend by increasing La_g that appears to either converge to or fluctuate around $n = -2$. The power function fitting process in figure 7.1b becomes more difficult as the variations in $d^{*c} - \Lambda_i$ become smaller and of the same order as the dichotomy accuracy and smallest mesh cell size of the simulations. Consequently, figure 7.1b does not include curves corresponding to $\mathrm{La}_g < 100$.

7.1.2 Physical Rationale

Since the intensity of the gas outflow is proportional to the bubble size d_b^* by equation 6.1, one can expect that by decreasing the bubble size, the healing threshold will increase. This is because a smaller bubble generates a more substantial gas outflow and, thus, a more noticeable pressure drop at the hole cross-section according to the Venturi equation 6.21. This effect is confirmed by figure 7.1a.

Moreover, figure 7.1a shows the fact that the film curvature effect is pronounced for higher values of gas Laplace number, whereas for lower values, the healing threshold is almost independent of the bubble size. The curve with $\mathrm{La}_g = 1$ in figure 7.1a marks the transition between the two regimes. This is because, for lower values of La_g, the gas outflow is dominated by viscosity; hence, C in equation 6.22 is expected to decrease substantially. On the other hand, for an inviscid gas flow, for instance the case with $10^6 \leq \mathrm{La}_g$ in figure 7.1a, the Venturi effect is responsible for a 20% increase in the healing threshold when decreasing the bubble size from $d_b^* = 50$ to $d_b^* = 10$.

7.1.2.1 Venturi Correction

As observed in figure 7.1b, there is a power law dependency of the Venturi effect on the bubble diameter $\propto d_b^{*-n}$ with $n \approx -2$. In this section, an attempt is made to find an analytic expression to predict the Venturi effect on the healing threshold that examines the relation between this effect and d_b^* to compare with the numerical results.

As discussed in section 3.1.1, for a flat film, and to a first-order approximation, a hole bursts if the pressure jump (due to surface tension) associated with the film thickness δ is larger than the pressure jump associated with the hole diameter d. In other words,

$$\frac{\gamma}{\delta} > \mathscr{A}\frac{\gamma}{d}, \tag{7.2}$$

with $\mathscr{A}$ a (dimensionless) constant of order one, which is the same as the healing threshold d^{*c}.

The Venturi pressure drop through the opening, as discussed in section 6.4, is of the order

$$\Delta p_{\text{venturi}} \propto C(\mu_g)\rho_g u^2 \tag{7.3}$$

where $C(\mu_g)$ is a coefficient accounting for the viscous effects, the value of which would be proportional to the intensity of the viscous effects in the gas outflow. The Venturi pressure drop contributes to the hole healing force, similar to the pressure change linked to the diameter of the hole (d) in expression 7.2. Therefore, the correction to the expression 7.2 as a result of the Venturi effect (i.e., Venturi correction) is

$$\frac{\gamma}{\delta} > \mathscr{A}\frac{\gamma}{d} + \mathscr{B}C(\mu_g)\rho_g u^2 \tag{7.4}$$

with $\mathscr{B}$ another dimensionless constant of order one. Using the hypothesis on the gas outflow velocity discussed in section 6.2.2 and employing the equation

$$u \propto \frac{d}{d_b}\frac{\gamma}{\mu_g} \tag{6.17}$$

for the characteristic velocity u replaced in expression 7.4, one finds

$$\frac{\gamma}{\delta} > \mathscr{A}\frac{\gamma}{d} + \mathscr{B}C(\mu_g)\rho_g\left(\frac{d}{d_b}\frac{\gamma}{\mu_g}\right)^2. \tag{7.5}$$

Since the length scale d is of the same order as the film thickness δ, one can replace d wiht δ in expression 7.5 so that

$$\frac{d}{\delta} > \mathscr{A} + \mathscr{B}C(\mu_g)\left(\frac{\delta}{d_b}\right)^2 \text{La}_g. \tag{7.6}$$

Consequently, by changing the bursting inequality 7.6 into an equality of the two opposing pressure terms, the healing threshold d^{*c} is found:

$$d^{*c} - \mathscr{A} = \mathscr{B}C(\mu_g)d_b^{*-2}\text{La}_g. \tag{7.7}$$

It is worth noting that an implicit assumption in finding equation 7.7 is that the gas outflow is dominated by viscosity rather than inertia. This assumption provides the velocity characteristic given by equation 6.17.

7.1.2.2 Venturi Correction Power Law Dependency on d_b^*

The Venturi correction provided by expression 7.7 states that a smaller bubble can heal larger holes than a bigger bubble with the same set of parameters, a primary result aligned with

the dichotomy results provided in figure 7.1. Most importantly, however, is the fact that the expression 7.7 predicts a power law dependency of the Venturi correction on the bubble diameter $\propto d_b^{*-2}$, which is in rough agreement with the numerical results in figure 7.1b for the typical case with $La_g = 3446$ with $n = 1.6$. The value of n is observed to increase and converge to (or fluctuate around) $n \approx 2$ by decreasing La_g, an effect that agrees with the implicit assumption in finding the Venturi correction, as discussed in the previous section. That is because the Venturi correction in equation 7.7 is derived for a gas outflow dominated by viscosity.

Additionally, the expression 7.7 states that the Venturi effect is amplified for a less viscous gas (i.e., a higher La_g). That is also expected since having a higher La_g leads to less viscous dissipation in the gas and, therefore, a more substantial outflow velocity at the hole cross-section, resulting in a higher pressure drop. Figure 7.1 confirms this effect. However, the predicted power law for La_g in the expression 7.7 has to be examined against numerical results, a topic discussed in the following section.

7.2 Gas Viscosity vs Surface Tension – La_g

7.2.1 Dichotomy Results

7.2.1.1 Short Range La_g – 10^6

Figure 7.2a shows the result of the dichotomy simulations for hole healing variation with La_g in the case of a hole on a bubble cap for a range of gas Laplace numbers from $La_g = 1$ to $La_g = 10^6$ and bubble sizes from $d_b^* = 8$ to $d_b^* = 150$. In fact, figure 7.2a represents the same results as figure 7.1a but with an x-axis of La_g instead of d_b^* to highlight the effect of gas Laplace number on the healing threshold. Similar to the case of a flat film, d^{*c} is found to increase with increasing La_g. However, contrary to the case of a flat film, the healing threshold does not reach a plateau for higher values of La_g, but it continues to increase. Figure 5.6 shows that in the flat film case, d^{*c} reaches a plateau for the inviscid gas with $La_g = 10^6$, while d^{*c} is rapidly increasing in the case of a bubble cap at $La_g = 10^6$ as observed from figure 7.2a. This is because, as discussed earlier in the previous chapter, the gas dynamic is essentially different in the two cases.

7.2.1.2 Short Range La_g – 10^{12}

Figure 7.3a presents the result of the dichotomy simulations for hole healing variation with La_g in the case of a hole on a bubble cap for a broader range of gas Laplace numbers from $La_g = 1$ to $La_g = 10^{10}$, but fewer bubble sizes $d_b^* = \{20, 50, 80\}$. These results show that in the case of

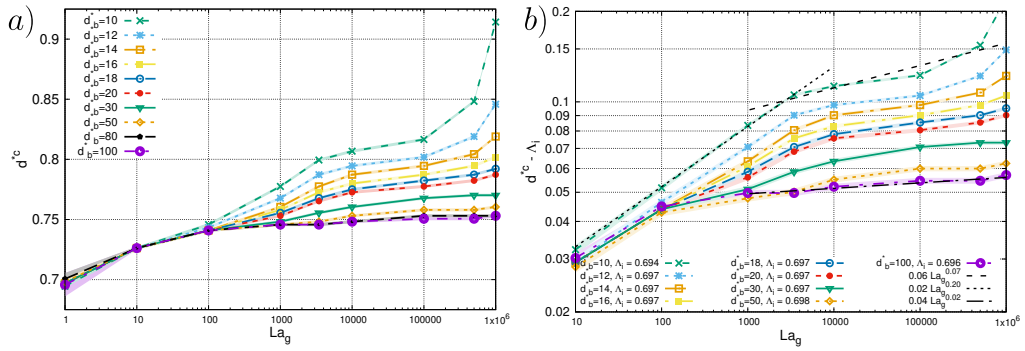

Fig. 7.2 Comparative analysis of the healing dynamics for holes on bubble caps under varying gas Laplace numbers La_g while keeping constant $La_l = 633$ and $\rho_{l/g} = 833$: (a) depicts the threshold variation with La_g for different bubble sizes, and (b) examines the power law dependency of the Venturi correction on La_g for different d_b^* by plotting $d^{*c} - \Lambda_i$ on a logarithmic scale against La_g. Here, Λ_i is the corresponding healing threshold for the lower end of the La_g range with a given d_b^*. Using fit functions, the power law is found to be $n = 0.2$ for $10 \leq La_g \lessapprox 10^4$ and $n = 0.07$ for $10^4 \lessapprox La_g \leq 10^6$ in the case with $d_b^* = 10$. The filled curve around the solid lines represents the accuracy of the dichotomy process equal to ± 0.005 with seven mesh levels within the film thickness. The filled curve is enlarged as the $d^{*c} - \Lambda_i$ decreases in panel (b) due to the logarithmic scaling.

a bubble cap, d^{*c} eventually reaches a plateau, but for values much higher than $La_g = 10^6$, as opposed to the case for a flat film. Moreover, figure 7.3a shows that La_g at which the plateau occurs is dependent on the bubble size d_b^*, where the larger the bubble size, the higher the La_g at which the plateau occurs, which means that the Venturi effect delays the healing threshold reaching a plateau when increasing La_g.

Moreover, figure 7.3a shows that the substantial variation of d^{*c} with La_g is observed for very high values of La_g that were not included in the first examination given in figure 7.2. These results show that the Venturi effect could cause a significant increase in the healing threshold for very high values of La_g and small bubble sizes. For instance, for $La_g = 10^8$ the healing threshold is increased by 115% by increasing the film mean curvature from 0 for a flat film to $2/d_b^* = 1/10$ for a bubble cap with $d_b^* = 20$.

In the dichotomy process for the results given in figure 7.3, some data points were not included in the presented figure as the dichotomy process for these points was not completed to reach the maximum accuracy allowed by the mesh refinement level. The complete results of the dichotomy process for the case of $d_b^* = 20$ are provided in the appendix in figure D.1. Considering the full plot with incomplete dichotomies, the trend of the results is found to be clear, and the missing data points do not appear to affect the overall conclusion, and thus, they were removed from figure 7.3 for clarity. However, it is worth noting that Λ_i for the cases with $d_b^* = 20$ and 80 were estimated from figure D.1.

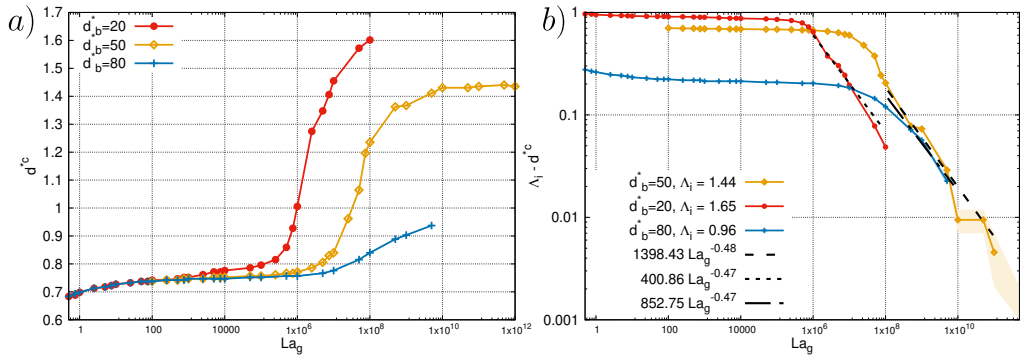

Fig. 7.3 (a) Healing threshold d^{*c} variation with gas Laplace number La_g over an extended range for holes on bubble caps, for bubble sizes $d_b^* = \{20, 50, 80\}$ while keeping constant $La_l = 633$ and $\rho_{l/g} = 833$. The d^{*c} reaches a plateau for La_g values much higher than $La_g \approx 10^6$, as opposed to the case for a flat film. (b) Logarithmic representation of the healing threshold deviation $\Lambda_i - d^{*c}$ against the gas Laplace number La_g, where Λ_i is the corresponding healing threshold for the plateau value of d^{*c} for a given La_g. The fit functions indicate $\Lambda_i - d^{*c} \propto La_g^{-0.5}$ regardless of the bubble size d_b^*, while the onset of the power law dependency is dependent on d_b^*. The filled curve around the solid lines represents the accuracy of the dichotomy process equal to ± 0.005 with seven mesh levels within the film thickness. The filled curve is enlarged as the $\Lambda_i - d^{*c}$ decreases in panel (b) due to the logarithmic scaling.

7.2.2 Venturi Correction Power Law Dependency on La_g

7.2.2.1 Short Range La_g – 10^6

Figure 7.2b represents the same data as in figure 7.2a, but with a logarithmic scale for both axes in order to examine the power law dependency of the Venturi effect on La_g. The y-axis of this plot represents the healing threshold d^{*c} subtracted by the healing threshold Λ_i corresponding to the lower end of the La_g range. This value, $d^{*c} - \Lambda_i$, is then plotted using the logarithmic scale against the same range of La_g as in figure 7.2a. Fitting a power function to the simulations result for the case with $d_b^* = 10$, one can find

$$d^{*c} - \Lambda_i = \begin{cases} 0.02 La_g^{0.2} & 10 \leq La_g \lessapprox 10^4 \\ 0.06 La_g^{0.07} & 10^4 \lessapprox La_g \leq 10^6 \end{cases} \tag{7.8}$$

where $\Lambda_i = 0.694$ is the healing threshold for the flat film with $d_b^* = 10$ and $La_g = 1$.

Equation 7.8 shows that the Venturi correction power law dependency on La_g is not constant. For relatively lower values of La_g, with $La_g \lessapprox 10^4$, the power law is found $n \approx 0.2$, with a slight decrease by the increase in d_b^*. However, for higher values of La_g with $10^4 \lessapprox La_g \leq 10^6$, the power law is reduced to $n \approx 0.07$. Comparing the highest value, $n \approx 0.2$, with the predicted value $n = 1$ from the Venturi correction given by equation 7.7, one can see that the power law dependency of the Venturi correction on La_g is lower than the predicted value, at least for the

range of La_g values examined in figure 7.2, and certainly not constant for different ranges of La_g values.

It is worth noting that as discussed in section 7.1.2.1, equation 7.7 implicitly assumes that the gas outflow is dominated by viscosity rather than inertia. Therefore, the power law dependency of the Venturi correction on La_g in the range of values studied in figure 7.2 is not necessarily expected to match the prediction by equation 7.7. Moreover, the variation in La_g also causes a change in the value of the Venturi coefficient $C(\mu_g)$, making the prediction of the power law dependency of the Venturi correction on La_g more complicated. Nevertheless, figure 7.2b shows that by decreasing La_g, the power law dependency on La_g is increased to get closer to $n = 1$, the value predicted for a gas outflow dominated by viscosity.

The dichotomy process for a lower range of La_g is not provided because these simulations were unsuccessful and found to be computationally too time-consuming due to having too low viscosity ratios $\mu_{l/g}$ (see equation 2.17). The dichotomy simulations become lengthier as La_g is decreased and approaches 1, to the point where the simulations are not computationally feasible without changing other variables of the problem, which would diminish the integrity of the examination for d^{*c} variation against only La_g. The trend of the results for the lower range of La_g could not be deduced with certainty from the results of figure 7.2, as d^{*c} does not reach a plateau for the lowest examined value $La_g = 1$.

7.2.2.2 Long Range La_g – 10^{12}

Figure 7.3b represents the same data as in figure 7.3a, but with a logarithmic scale for both axes. The y-axis of this plot represents $\Lambda_i - d^{*c}$, where Λ_i is the healing threshold corresponding to the plateau value of d^{*c} for a given d_b^* and in the high limit of the La_g values, since in this case, as opposed to the short-range results in 7.2, the healing threshold reaches a plateau. This value, $\Lambda_i - d^{*c}$, is then plotted using the logarithmic scale against the same range of La_g as in figure 7.3a.

Fitting a power function of the form $m(La_g)^n$ to the simulations results with $d_b^* = 20, 50,$ and 80 in the high range of La_g, one can find $n = -0.47, -0.48,$ and -0.47 respectively. These values show little variations with d_b^*, close to $n = -0.5$. Therefore, regardless of the bubble size d_b^*, one can deduce

$$\Lambda_i - d^{*c} \propto La_g^{-0.5} \tag{7.9}$$

with the onset of the power law dependency depending on d_b^*. As observed from figure 7.3b, the larger the bubble size, the higher the La_g at which the power law given by relation 7.9 starts to be valid.

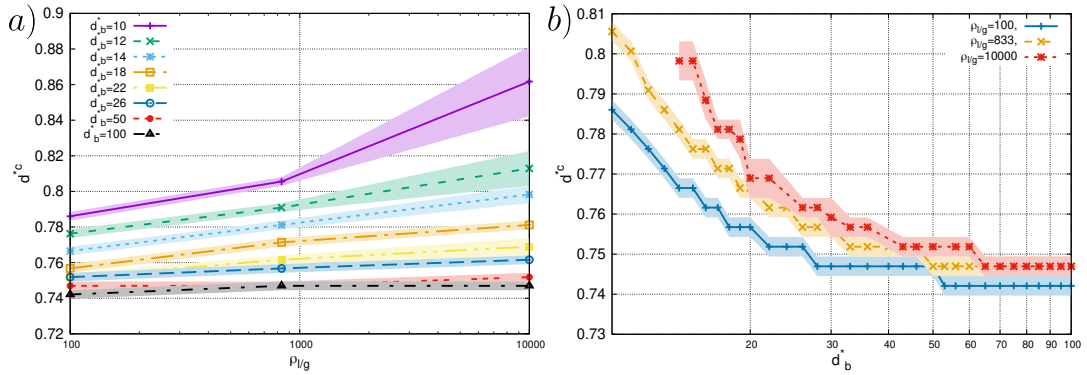

Fig. 7.4 (a) Healing threshold d^{*c} versus density ratio $\rho_{l/g}$ for varying bubble sizes d_b^* while keeping constant $\mathrm{La}_g = 3446$ and $\mathrm{La}_l = 633$. (b) Re-arranging the data in sub-figure (a) to show the effect of varying d_b^* on d^{*c} for different $\rho_{l/g}$ values. The Venturi effect is slightly more pronounced for less dense gasses. The filled curve around the solid lines represents the accuracy of the dichotomy process equal to ± 0.01 with six mesh levels within the film thickness, with the exception of a few simulations terminating before the completion of the dichotomy process. These data points, with $\rho_{l/g} = 10000$ and low d_b^* values, were omitted from panel (b) but included in panel (a).

It is worth emphasizing that relation 7.9 is not equivalent to the relation 7.8, and thus not a power law dependency of the Venturi correction on La_g as presented in the form of equation 7.7, instead it is a power law for $\Lambda_i - d^{*c}$ variations with La_g, where Λ_i is not the same as in section 7.2.2.1.

7.3 Liquid and Gas Density Ratio – $\rho_{l/g}$

7.3.1 Dichotomy Results

Figure 7.4a shows the result of the dichotomy simulations for hole healing variation with $\rho_{l/g}$ for a range of ratios from $\rho_{l/g} = 100$ to $\rho_{l/g} = 10000$ and bubble sizes from $d_b^* = 10$ to $d_b^* = 100$, while $\mathrm{La}_g = 3446$ and $\mathrm{La}_l = 633$ are kept constant for all cases. However, the dichotomy process includes only three data points in the studied range with $\rho_{l/g} = \{100, 833, 10000\}$. This is because, as observed from the results in figure 7.4a, d^{*c} is almost independent of $\rho_{l/g}$, therefore, the dichotomy process with more data points for $\rho_{l/g}$ is not essential. An effect similar to the case of a flat film, discussed in section 5.3, where it was illustrated in figure 5.8 that d^{*c} varies minimally with $\rho_{l/g}$ for $\mathrm{La}_g \approx 1000$ as is the case in the present section.

Nonetheless, it is observed that by decreasing the bubble cap curvature (i.e., increasing the bubble size d_b^*), d^{*c} becomes completely independent of $\rho_{l/g}$, as shown in figure 7.4a, which is in contrast with the case of a flat film. Therefore, the effect of the $\rho_{l/g}$ in the case of a bubble

cap must follow a different mechanism than the case of a flat film, even though the effect seems to be similar in the two cases for the higher values of d_b^*.

Additionally, figure D.2 in the appendix provides further results on the hole healing threshold variation with $\rho_{l/g}$ with varying La_l and La_g, while keeping $d_b^* = 50$ for all cases. The three panels of this figure correspond to three different values for La_g, within each of which La_l is varied.

7.3.2 Physical Rationale

Figure 7.4b, represents the same data as in figure 7.4a, but with the x-axis representing the change in d_b^*, showing that the Venturi effect is slightly more pronounced for less dense gasses. This effect could be attributed to the fact that after initialization of the problem, the gas outflow is accelerated faster for less dense gasses as illustrated in section 6.2.2, and therefore, the Venturi effect becomes relevant at earlier stages of the gas outflow.

7.4 Summary

In this chapter, the hole healing threshold variations with different parameters of the problem for the case of a bubble cap were studied with an emphasis on studying the effect of the film curvature and the subsequent Venturi effect, initially discussed in chapter 6.

The results of the dichotomy simulations for a wide range of bubble size from $d_b^* = 8$ to $d_b^* = 150$ and gas Laplace numbers from $La_g = 1$ to $La_g = 10^6$ were provided while $La_l = 633$ and $\rho_{l/g} = 833$ were kept constant for all cases. The results showed that the healing threshold d^{*c} is increased by increasing the film curvature (i.e., the intensity of the gas outflow), confirming the Venturi effect hypothesis discussed in chapter 6. Moreover, the results showed that the film curvature effect also varies with the gas Laplace number, where the effect is pronounced for higher values of La_g.

In an attempt to find an analytical expression to predict the Venturi effect on the healing threshold, a hypothesis was developed in section 7.1.2.1 with an implicit assumption that the gas outflow is dominated by viscosity rather than inertia (to formulate an expression for the velocity characteristic value used in the derivation). This hypothesis resulted in a Venturi correction term presented in equation 7.7, which states that a smaller bubble can heal larger holes than a larger one for the same set of parameters. The Venturi correction predicted a power law dependency on the bubble diameter $\propto d_b^{*-2}$, which was found to be in agreement with the numerical results provided in figure 7.1b.

Moreover, the expression 7.7 states that the Venturi effect is amplified for a less viscous gas (i.e., a higher La_g) with a dependency of $\propto La_g$. However, the predicted relation for La_g was shown to be more complicated to examine against the numerical results as the variations in La_g also cause changes in the value of the Venturi coefficient $C(\mu_g)$. Additionally, the dichotomy simulations for a lower range of La_g were not provided due to the fact that these simulations are computationally too time-consuming. Nevertheless, the results in figure 7.2b show that by decreasing La_g, the power law dependency on La_g is increased to get closer to $n = 1$, a value predicted for a viscosity dominated gas outflow by expression 7.7.

The dichotomy simulations in figure 7.2 and in figure 7.3 for the variation of d^{*c} against La_g, illustrated that d^{*c} reaches a plateau for La_g values much higher than $La_g \approx 10^6$, as opposed to the case for a flat film. The examination using a wider range of La_g values given in figure 7.3a showed that the Venturi effect could cause a significant increase in the healing threshold for high values of La_g. For instance, with $La_g = 10^8$ the healing threshold is more than doubled by increasing the film mean curvature from 0 for a flat film to $2/d_b^* = 1/10$ for a bubble cap with $d_b^* = 20$. Before reaching the plateau, the dichotomy simulations in figure 7.3b showed that $\Lambda_i - d^{*c}$ varies with La_g with a power law of $\propto La_g^{-0.5}$ where the onset of the power law depends on the bubble size studied.

Lastly, the dichotomy simulations in figure 7.4 showed that the Venturi effect is slightly more pronounced for less dense gasses, which could be attributed to the fact that after initialization of the problem, the gas outflow is accelerated faster for less dense gasses. Therefore, the Venturi effect becomes relevant at earlier stages of the gas outflow.

Chapter 8

Conclusions and Discussions

8.1 Summary of the Thesis

The dynamics of holes in free liquid films have long been subjects of intrigue and importance, not only in fluid mechanics but also in chemical engineering and biological applications. While focused on the problem of hole dynamics, the present work via chapter 1 introduced a general context for the role of a film bursting in the ocean-atmosphere exchanges, drawing the links between the hole dynamics and the bigger picture.

Before stating the governing equations, a review was offered in chapter 2 on the film dynamics close to the hole nucleation event to clarify the limitations of the Navier-Stokes equations employed in the present work. Subsequently, the governing equations simulated in this study were introduced. Basilisk, the numerical tool utilized in the present work, was introduced and detailed on its VoF method and adaptive meshing capabilities for enhanced accuracy and efficiency. Subsequently, the numerical configurations used in this work were introduced and described, such as flat films with holes and axisymmetric bubble caps. This foundation equips readers for subsequent detailed analyses and results, setting the stage for exploring the hole dynamics in the subsequent chapters.

Chapter 3 studied the dynamics of hole healing on thin liquid films, highlighting the physical principles behind the hole healing phenomenon. The chapter discussed the Young-Laplace equation and its significance in determining capillary pressure due to surface tension. The chapter derived a capillary pressure profile for half-torus holes on films using this foundation, as illustrated in figure 8.1a. Preliminary simulations were conducted, offering insights into the dynamics of the problem, evident through the interface evolution, pressure color maps, and overlaid velocity vector fields. The dynamics were observed to be influenced by the film initial configuration, leading to a differential in capillary pressure values. This, in turn, orchestrates the flow within the film and around the hole region.

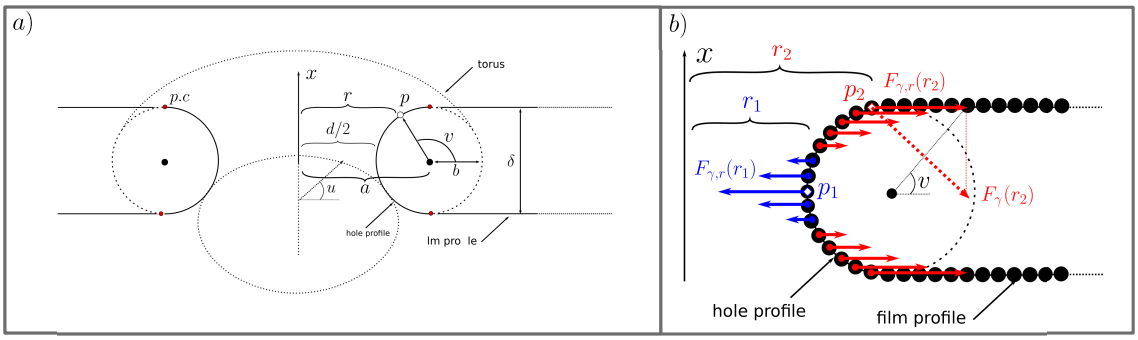

Fig. 8.1 (a) Description of a half-torus hole on a thin liquid film (b) Schematic representation of the key idea behind the hypothesis proposed in chapter 3.

Accordingly, a hypothesis was postulated with these observations and the analytical expression for the film mean curvature. It aimed to determine the hole healing threshold, primarily focusing on a static examination of the initial capillary pressure field for holes of half-torus shape. The key idea for this hypothesis was that the hole healing threshold is influenced not only by the initial capillary pressure field but also by the initial hole configuration, particularly the radial distance of each interface element from the x-axis as illustrated in figure 8.1b.

This hypothesis, formulated in expression 3.20, was tested against numerical results obtained through a dichotomy process with high precision. The outcome validated the capability of the hypothesis to calculate the healing threshold with an error margin of less than 5%.

$$2\int_{\frac{\pi}{2}}^{3\pi/2}\left(\int_{0}^{2\pi}(a+2b\cos(v))\cos(v)du-b\cos(v)\right)dv \tag{3.20}$$

Subsequently, the hypothesis application was extended to the hole configuration with a developed rim, as suggested by Stumpf et al. (2023). Despite a marginally higher error for these configurations, the hypothesis still held validity. Discrepancies between analytical predictions and numerical results, particularly for the developed rim configuration, highlighted the complexities involved, especially when considering the sharp discontinuities in hole geometry. Additionally, the chapter critically evaluated Taylor and Michael (1973)'s work, drawing parallels between holes in thin films and soap films between rings. Overall, this chapter synthesized theoretical insights with numerical analyses, offering a comprehensive understanding of the determinants of the hole healing threshold.

Chapter 4 examined the critical dynamics of the divergent outcomes of two near-identical simulations, focusing on two hole sizes immediate to the hole healing threshold. Critical moments in hole dynamics were pinpointed by analyzing the radial position of the tip, its temporal derivatives, film interface snapshots, pressure fields, and velocity vectors. Comprehensive insights were gained by studying the temporal and radial evolution of the hole tip curvature and

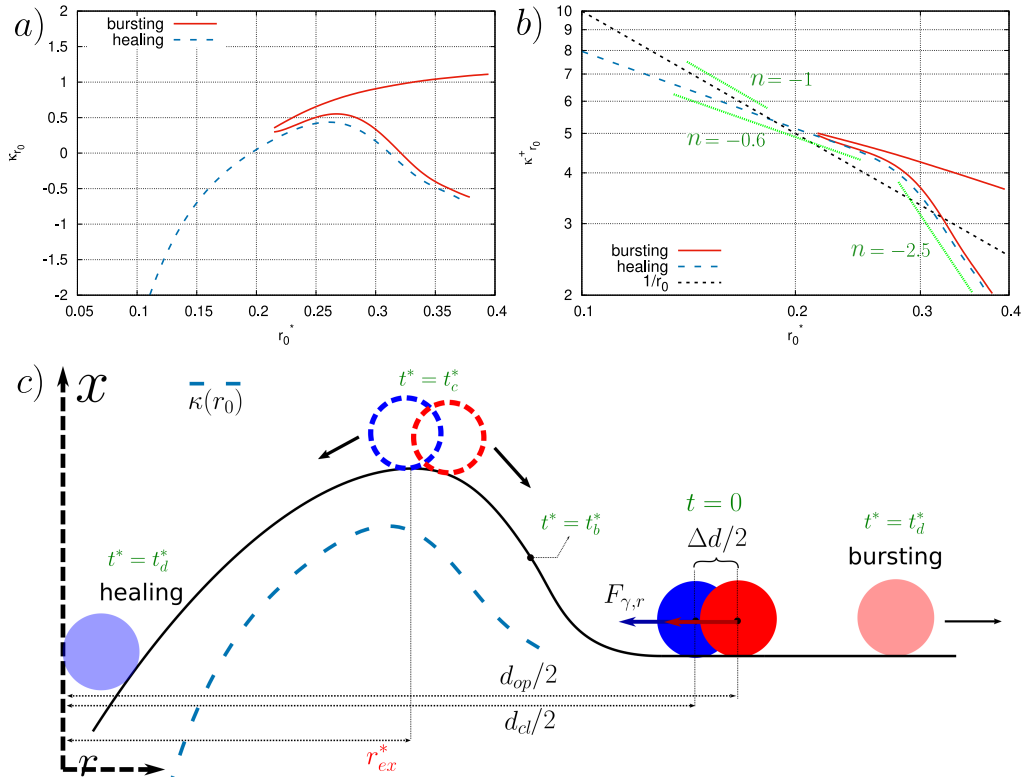

Fig. 8.2 (a) The hole tip curvature evolution with respect to the radial distance for the two healing and bursting simulations with $d_{\mathrm{cl}}^* = 0.744$ and $d_{\mathrm{op}}^* = 0.754$, respectively. (b) The hole tip positive component of the curvature evolution with respect to the radial distance for the two healing and bursting simulations shows the power law dependency on the radial distance. (c) Schematic representation of the analogy between the hole dynamics and pushing a ball up a hill.

its components, as provided in figure 8.2a and b. Distinct power laws were identified for the tip curvature as given in figure 8.2b.

These findings were contextualized with earlier observations to yield an understanding of the driving mechanism based on identifying a critical radial distance r_{ex}, upon reaching which the hole cannot retract back. The chapter concluded by drawing an analogy between the flickering hole dynamics and pushing a ball up a hill, as illustrated in figure 8.2c. In this analogy, the ball is the hole tip, the hill is the tip curvature evolution with respect to the radial distance, the push is the initial capillary pressure difference at the hole region, and the ball position is the radial distance of the hole tip with r_{ex} being the top of the hill. This analogy was used to explain the divergent outcomes of the two healing and bursting simulations.

In Chapter 5, the variations in the hole healing threshold with other parameters of the problem in the case of a flat film were examined using numerical simulations and a dichotomy process. Consequently, it was found that increasing the film Laplace number, La_l, raised the healing threshold, as evident by the plot provided in figure 8.3a. By studying the system energy

evolution, it was inferred that higher La_l values reduced energy dissipation, providing the film with a higher energy budget in the initial contact phase to reach the critical radial distance.

The healing threshold increase was about 35% when the Laplace number was raised from 1 to 10^4 where the threshold shifted as per expression 5.2. Minimal variations were noted outside this range, resulting in three distinct zones with a transitional zone between the other two. Upon examining the typical physical parameters associated with bursting bubbles in the ocean, it was found that the variation in the healing threshold for film Laplace numbers ranging from 1 to 10^4 aligns with the customary range of film Laplace numbers observed in oceanic bursting bubbles. This underscored the importance of accounting for viscosity versus surface tension effects in studies focused on oceanic film bursting.

A higher gas Laplace number, La_g, also elevated the healing threshold, more so with a higher density ratio $\rho_{l/g}$. This effect is illustrated in figure 8.3b. Moreover, examining the density ratio revealed that a higher gas density increased the healing threshold when La_g was constant, as shown in figure 8.3c. Nevertheless, the threshold slightly decreased when the viscosity ratio $\mu_{l/g}$ was constant instead of La_g, and the density ratio $\rho_{l/g}$ was increased. This effect was attributed to a faster attenuation of the initial capillary wave with higher gas density.

The chapter concluded by analyzing the hole shape. As a result, it was found that despite variations in the threshold for different shapes at a given La_l, the effects from changing La_l were consistent with the power law of the circular profile in expression 5.2, confirming the independence of the dichotomy results mentioned above from the arbitrary choice of the hole shape. The support for this conclusion is provided in figure 8.3d.

In chapter 6, the dynamics of gas outflow from a bubble through an opening, as illustrated in figure 8.4a and b, were explored, alongside the associated shrinkage of the bubble following the volume conservation law. The shrinkage rate was approximated using equation 6.9, which showed good agreement with simulation results as illustrated in figure 8.4f.

The gas outflow was determined to be influenced by a combination of factors, including gas density, viscosity, hole size, and the pressure differential between the inside and outside of the bubble. Detailed investigations yielded several insights. It was found that the inertial acceleration of the gas outflow depended on the gas density, with less dense gases accelerating more quickly as depicted in figure 8.4e. The timescale of the holes cross-sectional area change was shorter than the inertial timescale of the gas outflow for the studied bursting scenario.

The pressure difference decreased significantly as the gas escaped the bubble, halving in five time units of the simulation, and followed an exponential decay rather than a power-law relationship. The gas outflow reached a quasi-steady state after the hole retraction speed stabilized. A hypothesis was proposed linking the gas outflow velocity to the gas viscosity,

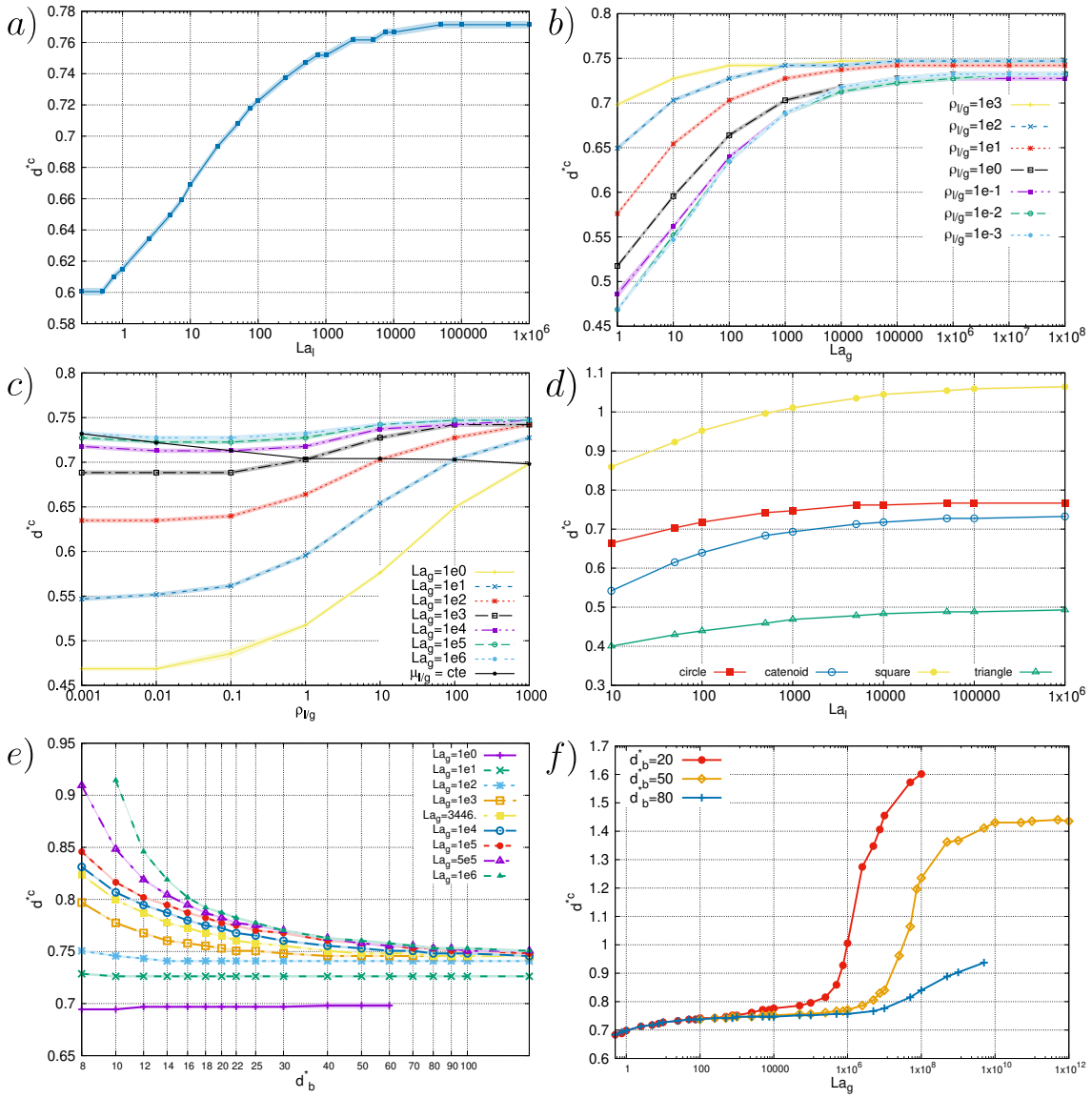

Fig. 8.3 (a) The healing threshold variations with the film Laplace number La_l for a flat film. (b) The healing threshold variations with the gas Laplace number La_g for a flat film. (c) The healing threshold variations with the gas density ratio $\rho_{l/g}$ for a flat film. (d) The healing threshold variations with the hole shape for different film Laplace numbers La_l. (e) The healing threshold variations with the film Laplace number La_l for a hole on a bubble cap. (f) The healing threshold variations with the gas Laplace number La_g for a hole on bubble cap.

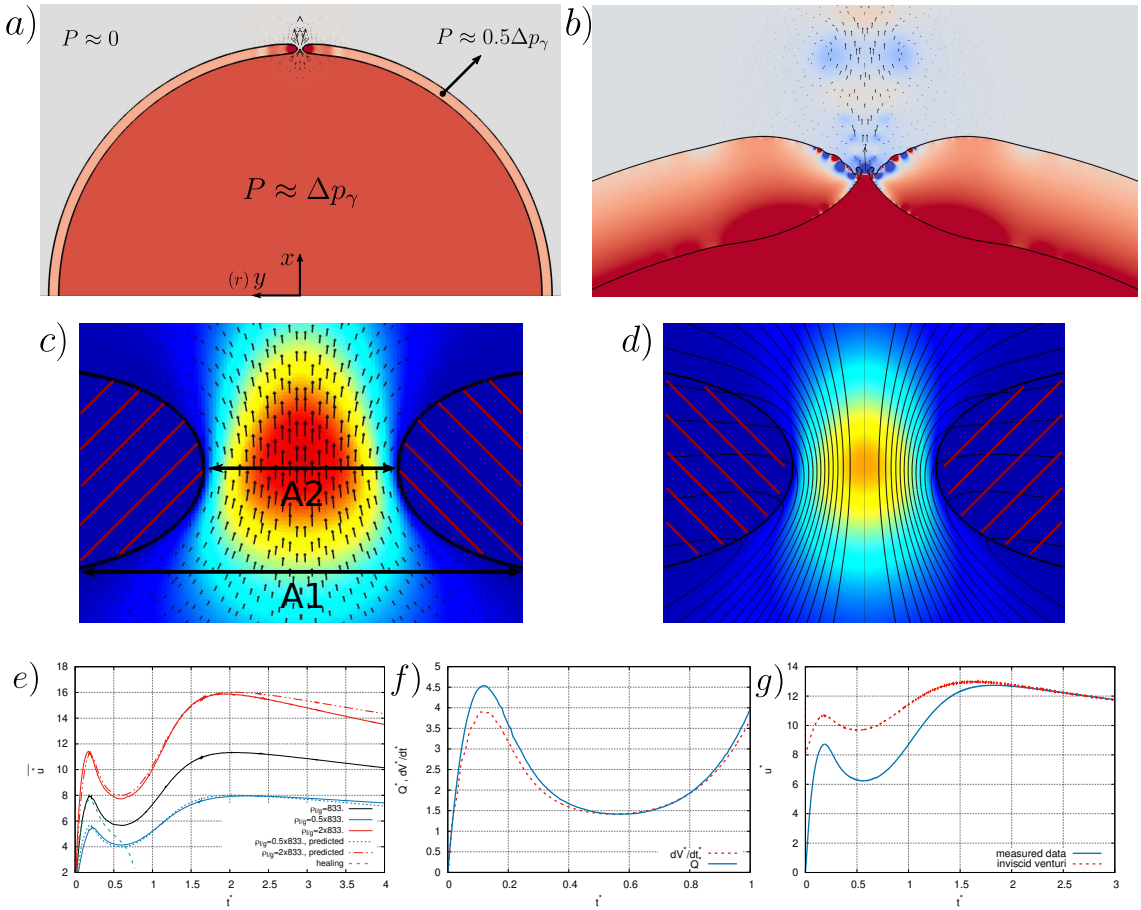

Fig. 8.4 (a) Illustration of the gas outflow from a bubble through a hole opening. (b) An example showcasing how the gas outflow could substantially affect the hole dynamics. (c) The gas velocity color map near the hole region exhibits the Venturi effect. (d) The gas outflow streamlines near the hole region. (e) The average gas outflow velocity at the minimum cross-section area of the hole for different gas densities. (f) The bubble shrinkage rate, comparing the numerical results with the theoretical prediction for a bursting case (g) Validation of the Venturi effect on the gas outflow where Bernoulli's principle well predicts the downstream velocity at the minimum cross-section area of the hole after the flow reaches a quasi-steady state.

which was later confirmed through numerical results, as indicated by equations 6.16 and 6.19, and illustrated in figure 8.4e.

The velocity and pressure profiles of the gas outflow at the minimum cross-section area of the hole were examined in detail for the same bursting case. This study led to the speculation that the gas outflow undergoes a Venturi effect, predictable by Bernoulli's principle. Consequently, the gas outflow was first examined qualitatively, as shown in figure 8.4c and d, then quantitatively using Bernoulli's principle for the center streamline values. The central streamline values of the gas outflow indeed underwent a Venturi effect once the flow reached a quasi-steady state, as evident in figure 8.4g. Moreover, the impact of viscosity on the Venturi effect prediction diminished when gas flow velocity and Reynolds number were increased.

In chapter 7, the effect of the film curvature on the hole healing threshold was studied in detail. The results showed that the healing threshold d^{*c} is increased by increasing the film curvature (i.e., the intensity of the gas outflow), confirming the Venturi effect hypothesis discussed in chapter 6. This effect is shown in figure 8.3e.

Moreover, as illustrated in figure 8.3e and f, the results showed that the film curvature effect also varies with the gas Laplace number, where the effect is pronounced for higher values of La_g. To find an analytic expression to predict the Venturi effect on the healing threshold, a hypothesis was developed with an implicit assumption that the gas outflow is viscous-dominated rather than inertia-dominated (to formulate an expression for the velocity characteristic value used in the derivation). This hypothesis resulted in a Venturi correction term presented in equation 7.7, which states that a smaller bubble can heal larger holes than a larger one for the same set of parameters. The Venturi correction predicted a power law dependency on the bubble diameter $\propto d_b^{*-2}$, which was found to agree with the numerical results provided in figure 7.1b.

Furthermore, the expression 7.7 states that the Venturi effect is amplified for a less viscous gas (i.e., a higher La_g) with a dependency of $\propto \mathrm{La}_g$. However, the predicted relation for La_g was shown to be more complicated to examine against the numerical results as the variations in La_g also cause changes in the value of the Venturi coefficient $C(\mu_g)$. Additionally, the dichotomy simulations for a lower range of La_g were not provided since these simulations are computationally too time-consuming. Nevertheless, the results in figure 7.2b show that by decreasing La_g, the power law dependency on La_g is increased to get closer to $n = 1$, the value predicted for a viscous-dominated gas outflow by expression 7.7.

The dichotomy simulations in figure 8.3f for a more extensive range of La_g values showed that d^{*c} reaches a plateau for La_g values much higher than $\mathrm{La}_g \approx 10^6$, as opposed to the case for a flat film. This examination also showed that the Venturi effect could cause a significant increase in the healing threshold for high values of La_g. For instance, with $\mathrm{La}_g = 10^8$ the

healing threshold is more than doubled by increasing the film mean curvature from 0 for a flat film to $2/d_b^* = 1/10$ for a bubble cap with $d_b^* = 20$.

8.2 Suggestions for Future Work

8.2.1 Potential for Experimental Validations

The present work studied the hole-healing phenomenon through numerical and analytical approaches, offering a comprehensive understanding of the dynamics of the problem. Nevertheless, a direct comparison between the numerical findings and experimental results is still missing. That is because the experimental results on hole healing in free films are not available in the literature in a manner compatible with the detailed study presented in this work. For instance, as indicated, the initial condition of the hole on a film and the nucleating mechanism can have a significant effect on the healing threshold. Without an exact control over the initial condition of the hole, it is not possible to compare the numerical results with experimental ones, when examining the value of the hole healing threshold (as opposed to its variation with the governing parameters of the problem).The lack of such experimental results is partly due to the difficulty of controlling the initial condition of the hole on a film, which is linked with the nucleating mechanism, and partly due to the spatial and temporal scales involved in the problem.

Similarly, there exists also a lack of experimental results on the hole healing threshold variation with the governing parameters of the problem, which could be more feasible and practical to examine experimentally for comparison with the numerical results.

The primary work by Taylor and Michael (1973) is often regarded as an analytical study, confirmed by experimental results. However, as discussed in chapter 3, the analytical predictions by Taylor and Michael (1973) for the healing threshold of a hole, other than not including the dynamics of the problem, is based on a significant assumption that the hole on a free film can be analogized with a soap film between two metal rings. This configuration was extensively reviewed in chapter 3, where it was pointed out that the experimental support for the proposed static healing threshold by Taylor and Michael (1973) was, in fact, based on experimenting with a soap film between two metal rings and not actual holes on a free film. Furthermore, numerous studies have examined the creation and healing of dry patches in a film on a substrate involving the contact angle problem–a different dynamics than in the hole healing on a free film, particularly when considering the film bursting in the oceanic context.

To tackle this limitation, an experimental setup could be designed to study the hole healing threshold variation with different problem parameters. In the case of the flat film, one can

choose two liquids of different viscosities so that the liquid Laplace number can be varied between the two for several orders of magnitude. Subsequently, a hole could be artificially nucleated using a reproducible mechanism, for instance, a laser beam or a needle. The healing threshold could be measured by observing the film dynamics using a high-speed camera. To enable such an experiment, the liquid viscosities must be chosen high enough such that the film dynamics are not too fast to be captured by the camera. At the same time, this choice does not impact the examination for the variation of the healing threshold with the liquid Laplace number. The goal of such experiments is to examine whether a higher liquid Laplace number results in a higher healing threshold as suggested by the numerical results in chapter 5.

For example, pure glycerin has a viscosity of about $1,412\,\mathrm{cP}$ at $20^{\circ}\mathrm{C}$. However, by mixing glycerin with water, one can create a solution that has a similar density to water but a much higher viscosity. For instance, a 90% glycerin-water solution can have a viscosity roughly ten times that of water, yielding two orders of magnitude variation for the liquid Laplace number. In this case, the key is to adjust the concentration of glycerin in the solution to achieve the desired viscosity while keeping the density close to that of water to keep the density ratio constant. Additionally, the temperature of the two liquids has to be noted since it can significantly affect both viscosity and density.

To examine the effect of the gas Laplace number, one can use two different gases with different viscosities, for instance, air and Sulfur Hexafluoride (SF6), which is about six times more viscous than air while having a similar density, resulting in gas Laplace numbers ratio of 36. This ratio could be increased by varying the gas temperatures. However, SF6 is a greenhouse gas, which is not ideal for the environment and must be used cautiously. On the other hand, to study the effect of the density ratio in the case of a flat film as discussed in chapter 5, one can use two different gases with different densities, for instance, air and Helium, which is about seven times less dense than air while having a similar viscosity.

To experimentally verify the Venturi effect on the healing threshold, one can use a bubble configuration with a high value of Ga to resemble the bubble cap configuration studied in chapter 6. However, this would require a larger bubble size to have a higher value of Ga, which is not ideal for studying the Venturi effect as the gas outflow intensity is decreased for larger bubbles. Alternatively, smaller bubbles could be examined while assuming that the bubble shape does not significantly affect the hole healing dynamics. In either cases, the fluid inside the bubble could be varied in density and viscosity to examine the effect of the gas Laplace number on the healing threshold. The bubble size could also be varied to examine the effect of the film curvature on the healing threshold. It would be interesting to physically examine whether a smaller bubble can heal larger holes than a larger one for the same set of parameters as predicted by the Venturi correction in equation 7.7.

Most importantly, it would be essential to examine the effect of, for instance, the film Laplace number on the film drop production as a result of the film bursting. One could speculate on how the variation in the hole healing threshold could affect the film thickness at bursting, changing the liquid budget for the film drop production. This could be examined by measuring the film thickness at bursting for different values of the film Laplace number or, alternatively, by examining the total volume of the film drop produced for different values of the film Laplace number. A similar study could be conducted for the variations in the gas Laplace number and the density ratio of the two fluids.

8.2.2 Potential for Further Numerical Studies

In order to make the numerical results more relevant to the case of film bursting in the oceanic context, one can develop the present work to simulate more realistic bubble shapes and cap initial conditions. This could be achieved by employing the numerical configuration detailed in appendix F, section F.3, that can examine the rising and cap drainage of an axisymmetric bubble as illustrated in figure F.4. Consequently, one can use the quasi-steady state bubble solution of this numerical configuration and numerically introduce an axisymmetric hole on the top of the bubble cap to study the hole dynamics more realistically. This configuration benefits from a more accurate initial condition for the bubble cap thickness and pressure field within the bubble and the film.

The speed of hole contraction, referred to as the speed of collapse by Lu and Corvalan (2015), could be studied in more detail against the results provided by Lu and Corvalan (2015), suggesting a power law dependency on the minimum radius of the hole. Appendix E provides numerical measurements for the hole tip movement and its temporal derivatives, which could be used to examine the hole collapse speed in more detail. Additionally, the collapse speed could be examined against changes in the governing parameters of the problem, such as the film Laplace number, the gas Laplace number, and the density ratio of the two fluids, as provided in the appendix. Nevertheless, the provided numerical results in the appendix were not extensively examined, a point that could be addressed in future works.

Molecular dynamics could be incorporated into the governing equations and Basilisk solver in an attempt to study a naturally induced film rupture. This could be done in parallel with employing the realistic bubble configuration described above. However, such a study would require a significant amount of computational resources and, thus, unsuitable for dichotomy studies with numerous simulations. Nevertheless, it could be used to configure the hole immediately after its rupture.

The surface tension gradient are currently not possible to account for when using the Basilisk solver. However, the solver could be modified to incorporate the surface tension

gradient, which could be used to study the effect of the surface tension gradient on the hole dynamics, as it is one of the key parameters in the context of oceanic film bursting.

8.2.3 Possible Applications for Studying the Hole Nucleation

Identifying the actual shape of the hole in a bursting film through physical experiments is problematic for several reasons. For instance, the relevant size of holes can be as small as $1nm$ while the time that the nucleation event, along with the following bursting or healing of the hole, could be as short as 0.1 nanosecond. Such spatial and time scales together are extremely difficult to capture simultaneously. For instance, in an experimental study by Thoroddsen et al. (2007) on the bubble pinch-off, the spatial resolution of the system for the fastest frame rates of 10^6 fps was limited to $10\mu m$.

Other techniques, such as Interferometry, Atomic Force Microscopy (AFM), or Scanning Electron Microscopy (SEM), could be employed to resolve these experimental limitations. For instance, AFM can provide spatial resolution of atomic scales. Nevertheless, the temporal resolution of AFM is limited. Similarly, SEM can provide a resolution of a few nanometers while lacking the temporal resolution. Interferometer techniques can measure distances and changes with precision down to the wavelength of light used, often resulting in nanometer-scale spatial resolution or, measured at very high frequencies. Therefore, it could be possible to use interferometry techniques to study the hole nucleation in a bursting film directly.

On the other hand, the numerical results presented in section 5.4 may provide an opening to indirectly study the actual shape of the hole and even the nucleating mechanism creating the hole. Since the critical healing threshold at any given value of La number is different between different hole shapes, one can investigate the actual shape of the hole that occurs in a typical bursting case by comparing a set of experimental results with the results given in figure 8.3. For instance, if the experimentally found threshold were the closest to the result for the triangular shape, it would hint that the shape of the hole is more likely to be similar to a triangular shape. Hypothetically, if different mechanisms of hole nucleation could each be linked to a unique hole shape, then by studying the shape described above, one can speculate on the nucleating mechanism behind the hole creation. This is one of the potential applications for the numerical results presented in this work.

8.3 Concluding Remarks

The present work studied the dynamics of holes in free liquid films, presenting a comprehensive understanding of the hole-healing phenomenon while focusing on the film bursting in the oceanic context. As a result, the following key conclusions were drawn:

- The initial condition of the hole on a film and the nucleating mechanism can have a significant effect on the healing threshold. Nevertheless, the variation in the healing threshold with the problem parameters, such as the film Laplace number, is independent of the initial condition of the hole.
- When assuming a circular axisymmetric hole on a flat film, a new static hypothesis was proposed to predict the healing threshold. The hypothesis was tested against numerical results, yielding good agreement. While searching for similar hypotheses in the literature, there were no other studies that proposed a static hypothesis to predict the healing threshold for such a problem. The closet study was carried out by Taylor and Michael (1973), yielding a static healing threshold for a catenoid hole based on an analogy with a soap film between two metal rings. This healing threshold was in rough agreement with the numerical results.
- The hole healing threshold is increased by increasing the film Laplace number. The effect of the film Laplace number is pronounced for values ranging from 1 to 10^4, coinciding with the customary range of film Laplace numbers observed in oceanic bursting bubbles.
- The hole healing threshold is increased by increasing the gas Laplace number. The effect of the gas Laplace number is more significant for higher values of the density ratio of the two fluids.
- The hole healing threshold is increased by increasing the density ratio of the two fluids in the case of a flat film.
- For a hole on a bubble cap, the gas outflow was found to undergo a Venturi effect with good agreement after the flow reached a quasi-steady state.
- The healing threshold is increased by increasing the film curvature (i.e., the intensity of the gas outflow), confirming the Venturi effect hypothesis. The film curvature effect also varies with the gas Laplace number, where the effect is pronounced for higher values of La_g.
- A hypothesis was developed to predict the Venturi effect on the healing threshold, resulting in a Venturi correction term presented in equation 7.7, which states that a

smaller bubble can heal larger holes than a larger one for the same set of parameters. The Venturi correction predicted a power law dependency on the bubble diameter $\propto d_b^{*-2}$, which agreed with the numerical results.

The above insights were obtained through a combination of numerical simulations and analytical approaches and can be used to improve the understanding of the film bursting phenomenon as a whole, which is constructed of a series of complex dynamics, such as drainage, puncture, film retraction, and film disintegration into film drops. The healing threshold of a hole on a film is a critical parameter that could impact the film bursting dynamics, particularly the film thickness at bursting and, thus, the liquid budget for the film drop production. The present work could be a foundation for future studies on the film bursting phenomenon, particularly in the oceanic context, and in integration with previous works on the subject.

References

Abbena, E., Salamon, S., and Gray, A. (2017). *Modern Differential Geometry of Curves and Surfaces with Mathematica*. CRC Press. Google-Books-ID: NDoPEAAAQBAJ.

Agbaglah, G. G. (2021). Breakup of thin liquid sheets through hole–hole and hole–rim merging. *Journal of Fluid Mechanics*, 911:A23. Publisher: Cambridge University Press.

Asher, W. E. and Wanninkhof, R. (1998). The effect of bubble-mediated gas transfer on purposeful dual-gaseous tracer experiments. *Journal of Geophysical Research: Oceans*, 103(C5):10555–10560.

Behroozi, F. (2022). A Fresh Look at the Young-Laplace Equation and Its Many Applications in Hydrostatics. *The Physics Teacher*, 60(5):358–361.

Berny, A., Popinet, S., Séon, T., and Deike, L. (2021). Statistics of jet drop production. *Geophysical Research Letters*, 48(10):e2021GL092919. e2021GL092919 2021GL092919.

Bird, J. C., de Ruiter, R., Courbin, L., and Stone, H. A. (2010). Daughter bubble cascades produced by folding of ruptured thin films. *Nature*, 465(7299):759–762. Number: 7299 Publisher: Nature Publishing Group.

Blanchard, D. C. (1989). The ejection of drops from the sea and their enrichment with bacteria and other materials: A review. *Estuaries*, 12(3):127–137.

Culick, F. E. C. (1960). Comments on a Ruptured Soap Film. *Journal of Applied Physics*, 31(6):1128–1129.

de Gennes, P.-G., Brochard-Wyart, F., and Quéré, D. (2004). *Capillarity and Wetting Phenomena*. Springer, New York, NY.

Deane, G. B. and Stokes, M. D. (2002). Scale dependence of bubble creation mechanisms in breaking waves. *Nature*, 418(6900):839–844.

Debrégeas, G., de Gennes, P.-G., and Brochard-Wyart, F. (1998). The Life and Death of "Bare" Viscous Bubbles. *Science*, 279(5357):1704–1707. Publisher: American Association for the Advancement of Science.

Dombrowski, N., Fraser, R. P., and Newitt, D. M. (1954). A photographic investigation into the disintegration of liquid sheets. *Philosophical Transactions of the Royal Society of London. Series A, Mathematical and Physical Sciences*, 247(924):101–130. Publisher: Royal Society.

Ernie R. Lewis, S. S. (2004). *Sea Salt Aerosol Production: Mechanisms, Methods, Measurements, and Models | Wiley*.

Gilet, T., Mulleners, K., Lecomte, J. P., Vandewalle, N., and Dorbolo, S. (2007). Critical parameters for the partial coalescence of a droplet. *Phys. Rev. E*, 75:036303.

Gonzalez Viejo, C., Torrico, D. D., Dunshea, F. R., and Fuentes, S. (2019). Bubbles, Foam Formation, Stability and Consumer Perception of Carbonated Drinks: A Review of Current, New and Emerging Technologies for Rapid Assessment and Control. *Foods*, 8(12):596. Number: 12 Publisher: Multidisciplinary Digital Publishing Institute.

Guémas, M., Sellier, A., and Pigeonneau, F. (2015). Slow viscous gravity-driven interaction between a bubble and a free surface with unequal surface tensions. *Physics of Fluids*, 27:043102.

Karthik Ms, V Seshadri, and MAHARAJA INSTITUTE OF ENGINEERING (2015). Prediction of Viscous Coefficient of Venturi Meter under Non ISO Standard Conditions. *International Journal of Engineering Research and*, V4(05):IJERTV4IS051264.

Koch, M. K., Voßnacke, A., Starflinger, J., Schütz, W., and Unger, H. (2000). Radionuclide reentrainment at bubbling water pool surfaces. *Journal of Aerosol Science*, 31(9):1015–1028.

Lamb, H. (1916). *Hydrodynamics*. University Press.

Laporte, M., Montillet, A., Della Valle, D., Loisel, C., and Riaublanc, A. (2016). Characteristics of foams produced with viscous shear thinning fluids using microchannels at high throughput. *Journal of Food Engineering*, 173:25–33.

Lehmann, M. (2023). *Computational study of microplastic transport at the water-air interface with a memory-optimized lattice Boltzmann method*. PhD thesis, Bayreuth. Forschungsdaten Simulationsergebnisse zu "Ejection of marine microplastics by raindrops" https://zenodo.org/record/5683801 Simulationsergebnisse zu "Modeling of vertical microplastic transport by rising bubbles" https://zenodo.org/record/76551.

Lewis, E. and Schwartz, S. (2004). Sea salt aerosol production: Mechanisms, methods, measurements and models—a critical review. *Washington DC American Geophysical Union Geophysical Monograph Series*, 152:3719–.

Lhuissier, H. and Villermaux, E. (2012). Bursting bubble aerosols. *Journal of Fluid Mechanics*, 696:5–44. Publisher: Cambridge University Press.

Lu, J., Campana, D. M., and Corvalan, C. M. (2018). Contraction of Surfactant-Laden Pores. *Langmuir*, 34(15):4701–4706. Publisher: American Chemical Society.

Lu, J. and Corvalan, C. M. (2015). Free-surface dynamics of small pores. *Chemical Engineering Science*, 132:93–98.

Lu, J. and Corvalan, C. M. (2019). Dynamical transitions during the collapse of inertial holes. *Scientific Reports*, 9(1):14649. Number: 1 Publisher: Nature Publishing Group.

Lu, J., Ferri, M., Ubal, S., Campanella, O., and Corvalan, C. M. (2019). Contraction of a shear-thinning axisymmetric cavity. *Physics of Fluids*, 31(12):123103.

Lu, J., Yu, J., and Corvalan, C. M. (2015). Universal Scaling Law for the Collapse of Viscous Nanopores. *Langmuir*, 31(31):8618–8622. Publisher: American Chemical Society.

Ma, Q., Zhou, Y., Gu, H., Sun, Z., Li, L., and Cui, X. (2022). Experimental research on aerosol deposition phenomenon in single-sized rising bubble. *Progress in Nuclear Energy*, 154:104456.

Miyamoto, K. and Katagiri, Y. (1997). *Curtain Coating*, pages 463–494. Springer Netherlands, Dordrecht.

Mondal, A. and Niranjan, K. (2019). The Role of Bubbles in the Development of Food Structure.

Moriarty, J. A. and Schwartz, L. W. (1993). Dynamic Considerations in the Closing and Opening of Holes in Thin Liquid Films. *Journal of Colloid and Interface Science*, 161(2):335–342.

Nayar, K. G., Sharqawy, M. H., Banchik, L. D., and Lienhard V, J. H. (2016). Thermophysical properties of seawater: A review and new correlations that include pressure dependence. *Desalination*, 390:1–24.

Peixoto, J. P. and Oort, A. H. (1992). Physics of climate.

Pigeonneau, F. and Sellier, A. (2011). Low-Reynolds-number gravity-driven migration and deformation of bubbles near a free surface. *Physics of Fluids*, 23(9):092102.

Popinet, S. (2003). Gerris: a tree-based adaptive solver for the incompressible Euler equations in complex geometries. *Journal of Computational Physics*, 190(2):572–600.

Popinet, S. (2009). An accurate adaptive solver for surface-tension-driven interfacial flows. *Journal of Computational Physics*, 228:5838 – 5866.

Popinet, S. (2018). Numerical models of surface tension. *Annual Review of Fluid Mechanics*, 50(1):49–75.

Quan, S. and Schmidt, D. P. (2007). A moving mesh interface tracking method for 3D incompressible two-phase flows. *Journal of Computational Physics*, 221(2):761–780.

Richter, D. H. and Veron, F. (2016). Ocean spray: An outsized influence on weather and climate. *Physics Today*, 69:34–39.

Rohatgi, A. (2022). Webplotdigitizer: Version 4.6.

Scardovelli, R. and Zaleski, S. (1999). Direct Numerical Simulation of Free-Surface and Interfacial Flow. *Annual Review of Fluid Mechanics*, 31(1):567–603. _eprint: https://doi.org/10.1146/annurev.fluid.31.1.567.

Sharma, A. and Ruckenstein, E. (1990). Energetic criteria for the breakup of liquid films on nonwetting solid surfaces. *Journal of Colloid and Interface Science*, 137(2):433–445.

Slotnick, J. P., Khodadoust, A., Alonso, J., Darmofal, D., Gropp, W., Lurie, E., and Mavriplis, D. J. (2014). CFD Vision 2030 Study: A Path to Revolutionary Computational Aerosciences. Technical Report NF1676L-18332. NTRS Author Affiliations: Boeing (United States), Stanford University, Massachusetts Institute of Technology, National Center for Supercomputing Applications, Pratt & Whitney United Technologies Corp., University of Wyoming NTRS Document ID: 20140003093 NTRS Research Center: Langley Research Center (LaRC).

Smith, C. J., Kramer, R. J., Myhre, G., Alterskjær, K., Collins, W., Sima, A., Boucher, O., Dufresne, J.-L., Nabat, P., Michou, M., Yukimoto, S., Cole, J., Paynter, D., Shiogama, H., O'Connor, F. M., Robertson, E., Wiltshire, A., Andrews, T., Hannay, C., Miller, R., Nazarenko, L., Kirkevåg, A., Olivié, D., Fiedler, S., Lewinschal, A., Mackallah, C., Dix, M., Pincus, R., and Forster, P. M. (2020). Effective radiative forcing and adjustments in cmip6 models. *Atmospheric Chemistry and Physics*, 20(16):9591–9618.

Spiel, D. E. (1998). On the births of film drops from bubbles bursting on seawater surfaces. *Journal of Geophysical Research: Oceans*, 103(C11):24907–24918. _eprint: https://onlinelibrary.wiley.com/doi/pdf/10.1029/98JC02233.

Storm, A. J., Chen, J. H., Ling, X. S., Zandbergen, H. W., and Dekker, C. (2005). Electron-beam-induced deformations of SiO2 nanostructures. *Journal of Applied Physics*, 98(1):014307.

Stumpf, B., Roisman, I. V., Yarin, A. L., and Tropea, C. (2023). Drop impact onto a substrate wetted by another liquid: corona detachment from the wall film. *Journal of Fluid Mechanics*, 956:A10.

Taylor, G. and Michael, D. (1973). On making holes in a sheet of fluid. *Journal of fluid mechanics*, 58(4):625–639.

Taylor, G. I. (1959). The dynamics of thin sheets of fluid. III. Disintegration of fluid sheets. *Proceedings of the Royal Society of London. Series A. Mathematical and Physical Sciences*, 253(1274):313–321. Publisher: Royal Society.

Thoroddsen, S. T., Etoh, T. G., and Takehara, K. (2007). Experiments on bubble pinch-off. *Physics of Fluids*, 19(4):042101.

Tryggvason, G., Bunner, B., Ebrat, O., and Tauber, W. (1998). Computations of multiphase flows by a finite difference/front tracking method. i. multi-fluid flows. *Lecture Series-von Karman Institute For Fluid Dynamics*, pages 7–7.

van Hooft, J. A., Popinet, S., van Heerwaarden, C. C., van der Linden, S. J. A., de Roode, S. R., and van de Wiel, B. J. H. (2018). Towards Adaptive Grids for Atmospheric Boundary-Layer Simulations. *Boundary-Layer Meteorology*, 167(3):421–443.

Veron, F. (2015). Ocean spray. *Annual Review of Fluid Mechanics*, 47(1):507–538.

Villermaux, E. (2007). Fragmentation. *Annual Review of Fluid Mechanics*, 39(1):419–446. _eprint: https://doi.org/10.1146/annurev.fluid.39.050905.110214.

Witelski, T. P. and Bernoff, A. J. (2000). Dynamics of three-dimensional thin film rupture. *Physica D: Nonlinear Phenomena*, 147(1):155–176.

Xu, X., Dey, M., Qiu, M., and Feng, J. J. (2020). Modeling of van der Waals force with smoothed particle hydrodynamics: Application to the rupture of thin liquid films. *Applied Mathematical Modelling*, 83:719–735.

Yu, X., Gu, H., Gupta, S., Ma, Q., Cheng, L., Zhou, Y., and Liang, H. (2023). Bubble floatation, burst, drainage, and droplet release characteristics on a free surface: A review. *Physics of Fluids*, 35(4):041302.

Zhang, H. and Liu, Q. (2020). Numerical investigation on performance of moisture separator by lagrangian-eulerian strategy: Physical mechanisms, theoretical models, and advanced algorithms. *Annals of Nuclear Energy*, 137:107081.

Appendix A

Mesh Convergence

One of the most important aspects of the numerical simulations is the convergence of the results concerning the numerical parameters. Among the numerical parameters, the maximum mesh refinement level is a crucial parameter in this regard. Basilisk solver uses a quadtree adaptive mesh grid, which restricts the resolution to powers of two. The size of the smallest cell in the domain is

$$\Delta_{\min} = \frac{L}{2^{\mathrm{GML}}} \tag{2.37}$$

where GML is the global maximum level for mesh refinement in the quadtree grid or the maximum number of divisions that the solver is allowed to make on the domain of size L. Since $\Delta_{\min}$ also depends on the size of the domain, the effect of the mesh resolution is instead quantified here by the maximum number of cell divisions allowed across the initial film thickness of the film, here is referred to as "*level*", or FML.

As one can expect, the accuracy of the results increases by increasing the mesh resolution. However, this comes at the computational time cost, as discussed in section 2.3.4. Therefore, it is necessary to balance the accuracy and the computational cost.

On the other hand, the results should be independent of the mesh resolution within a specific range. This means that in an ideal case, the specific outcome of the simulation should asymptotically converge to a particular value as the mesh resolution increases. To find the minimum mesh resolution that satisfies this condition, we perform a convergence study by varying the mesh resolution and comparing the results for a hole on a film with parameters according to table 2.1 for a standard oceanic case.

In this examination, the mesh maximum mesh refinement level within the film thickness, FML, varies from three to eight. At the same time, the dichotomy process finds the hole heating threshold d^{*c} for each case. On the other hand, the dichotomy accuracy is limited by the mesh

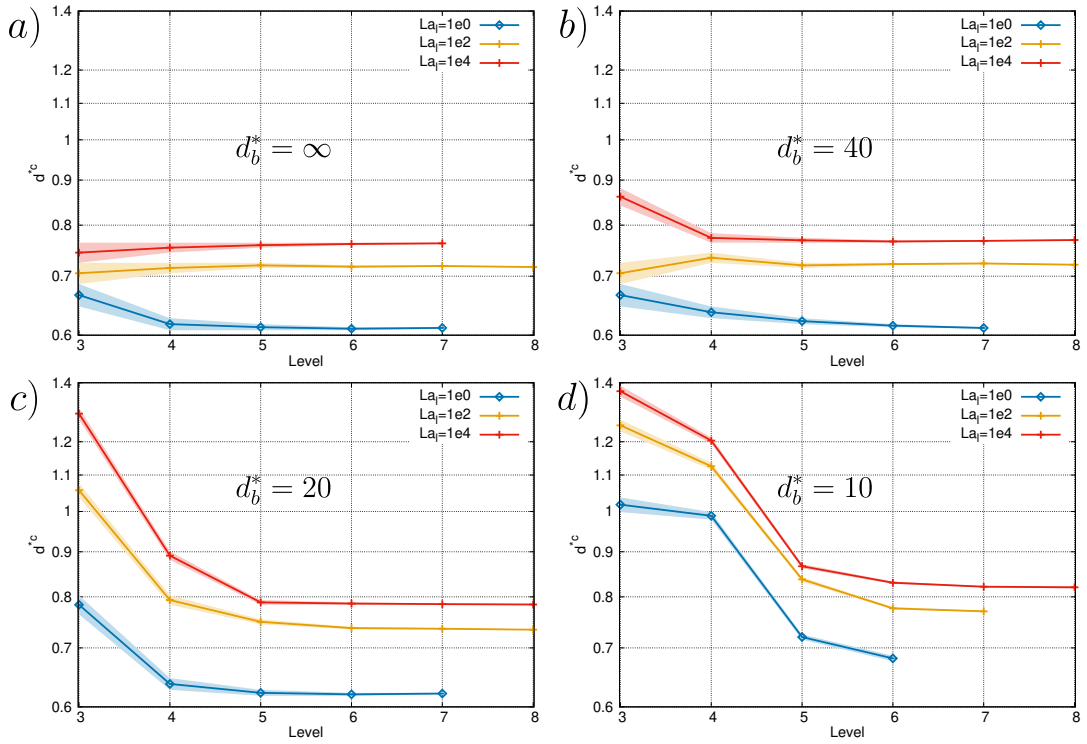

Fig. A.1 Convergence study showcasing the effect of mesh resolution on the hole heating threshold d^{*c}. Subplots (a) to (d) represent the convergence study as a function of mesh maximum refinement level within the film thickness, corresponding to bubble sizes $d_b^* = \infty, 40, 20,$ and 10, respectively. Each subplot varies the film Laplace number La_l over several orders of magnitude, illustrating the sensitivity of the dichotomy results to mesh resolution under different film curvatures and gas Laplace numbers. Smaller bubble sizes and higher Laplace numbers render the results more sensitive to the mesh resolution.

resolution and $\Delta_{\min}$. This means that the dichotomy process has a broader error margin for coarser meshes, as illustrated in figure A.1.

Additionally, the film curvature is varied by studying four cases with bubble sizes $d_b^* = \infty, 40, 20,$ and 10 where $d_b^* = \infty$ corresponds to a flat film. These results are shown in figure A.1 in four subplots corresponding to the four different film curvatures. Within each subplots, the film Laplace number La_l is varied from 1 to 10^4. In this manner, one can examine the effect of d_b^* and La_l on the sensitivity of the results to the mesh resolution while keeping constant $\rho_{l/g} = 833$ and $La_g = 3446$ for all cases.

Figure A.1 shows the results of this study. As one can see, the dichotomy results demonstrate different sensitivity levels to the mesh resolution for different film curvatures and gas Laplace numbers. Comparing the four subplots, one can see that the results are more sensitive to the mesh resolution for smaller bubble sizes, which create a higher initial pressure difference and a more intense gas outflow. On the other hand, the results are more sensitive to the mesh resolution for more significant film Laplace numbers.

As a result of this examination, $level = 6$ was considered the minimum mesh resolution that satisfies the convergence condition for all cases within a proper error margin (i.e., $\pm 5\%$ difference in results with $level = 7$). However, to ensure higher accuracy, $level = 7$ was chosen as the standard mesh resolution for all simulations in this study, except for a few cases where $level = 6$ was used.

Appendix B

Film Confinement and Gas Backflow Effects

The domain size could be a parameter that affects the numerical results by creating a confinement effect if chosen too small. This parameter is investigated for both the flat film and bubble cap problem. In both cases, the domain is a square of size L.

In the case of the flat film, as shown in figure 2.8, the size of the domain L is made of the hole area $d_1/2$ in addition to the flat part of the film that connects to the rim and ends with the symmetrical boundary condition. In the case of a circular shape for the hole, the hole area is already determined by $d/2$ and $\delta/2$ since $d_1 = d + \delta$. Therefore, when changing the domain size, the parameter to vary is the length of the flat part of the film $L - d_1/2$.

One can find the minimum length for $L - d_1/2$ so that there would be minimal effects of reflection from the boundaries (i.e., confinement effects). For this purpose, the dichotomy process is used to find the variation of the hole healing threshold d^{*c} when varying $L - d_1/2$. Since the reflection from the boundaries is related to the speed of the capillary waves and the rate at which they are damped, this examination has been carried out for different Laplace numbers of the liquid La_l while keeping constant $\rho_{l/g} = 833$ and $La_g = 3446$ for all cases.

The results are shown in figure B.1, where it is observed that for $L^* - d_1^*/2 > 6$ there is no confinement effect. Therefore, this value has been chosen for all the simulations of the flat film to ensure a minimal confinement effect while avoiding unnecessary large domains. However, it is worth noting that since Basilisk uses an effective mesh adaptation technique, the increase in domain size does not necessarily result in a substantially larger number of mesh cells. Nevertheless, the confinement effect was investigated for different Laplace numbers to ensure that the results were not affected by the domain size. Figure B.1 also shows that for lower film Laplace numbers (i.e., more viscous films), the confinement effect is more pronounced than those dominated by capillary forces.

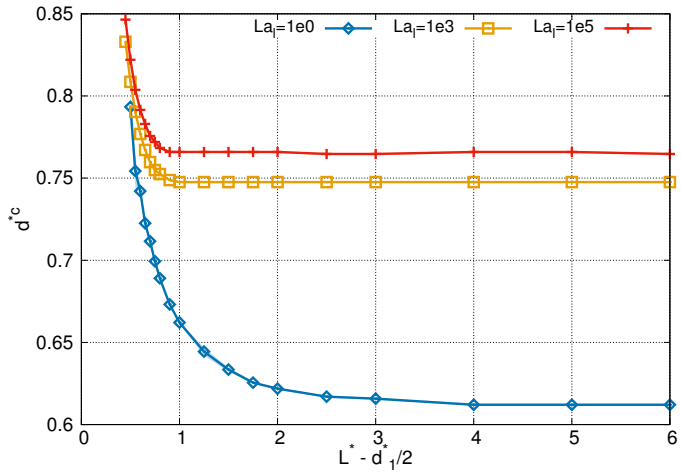

Fig. B.1 Variation of the hole healing threshold d^{*c} with respect to the domain effective size $L^* - d_1^*/2$ in the case of a flat film for different liquid Laplace numbers La_l. The graph indicates the absence of confinement effects for $L^* - d_1^*/2 > 6$. The inset highlights the increased sensitivity to confinement for films with lower La_l.

In the case of a bubble cap, and in the specific configuration that is used in this study as illustrated in figure 2.11, the length of the curved film that connects to the rim of the hole is always large enough to prevent any notable confinement effects from happening within the film, even for smallest bubble sizes studied in the present work with $d_b^* = 8$. However, the size of the domain can affect the dynamics of the hole by reflecting the gas outflow from the boundaries if placed too close to the hole. It is plausible that the reflected gas flow from the boundaries could create a backflow that alters the Venturi effect and, thus, the hole healing threshold d^{*c}. Therefore, this effect is investigated here by examining d^{*c} variations when varying $L - d_b/2$ for different gas and liquid Laplace numbers, both of which affect the intensity of the gas outflow and the hole dynamics. In these simulations, $\rho_{l/g} = 833$ and $d_b^* = 20$ is kept constant.

Figure B.2 shows the results of this investigation, where it is observed that for $L^* - d_b^*/2 > 4$, there is no gas backflow effect regardless of the Laplace numbers. Hence, this value has been set as a lower limit for all the simulations of the bubble. To avoid complex divisions in the quadtree grid, the size of the domain is set to the closest power of two, resulting in a domain twice the size of the bubble with

$$L^* = ceil(\log_2^{d_b^*}) \tag{B.1}$$

for all the simulations of the bubble cap configuration. It is also worth noting that the gas backflow effect is more pronounced for Laplace numbers.

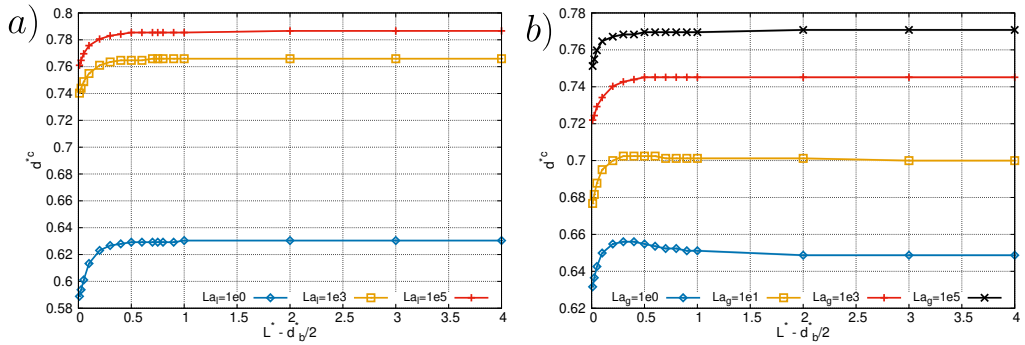

Fig. B.2 Variation of the hole healing threshold d^{*c} with respect to the effective domain size $L^* - d_b^*/2$ for different gas and liquid Laplace numbers, in panels (a) and (b), respectively. The result indicates no gas backflow effect for $L^* - d_b^*/2 > 4$. The impact of Laplace numbers on the gas backflow effect is also depicted.

Appendix C

Potential Energy and Film Interface Area

As discussed in section 5.1.2, the total potential energy of the system is calculated by

$$E_p^* = A\gamma \tag{5.6}$$

where A is the surface area of the film interface, and γ is the capillary coefficient. To measure A in the numerical simulations, different methods could be used. The default function within the Basilisk code suited for this task is `interface_area`. However, this function is not adapted to the case of the axisymmetric geometries. To adapt this function to the axisymmetric condition, three different methods are examined here, which are discussed in the order of accuracy. Starting with the simplest method, method one calculates the interface area by

$$A_1 = \sum_{i=1,j=1}^{i=\infty,j=\infty} 2\pi l(i,j)y(j) \tag{C.1}$$

where $l(i,j)$ is the length of the interface in the cell (i,j), $y(j)$ is the position of the cell j in the global x-y coordinate. Point P marks the center of the interface in the cell (i,j) and has the local coordinates $(X_P(i,j),Y_P(i,j))$. Figure C.1 illustrates these definitions. The length of the interface in the cell (i,j) is calculated by a separate function called `plane_area_center`, which is also a part of the Basilisk code but not discussed here.

Equation C.1 calculates the surface area of a cylinder with the radius of $y(j)$ and the height of $l(i,j)$. The second method modifies this expression by taking into account the fact that the radius of this cylinder could be better represented by $Y_P(i,j)$, such that

$$A_2 = \sum_{i=1,j=1}^{i=\infty,j=\infty} 2\pi l(i,j)Y_P(i,j) \tag{C.2}$$

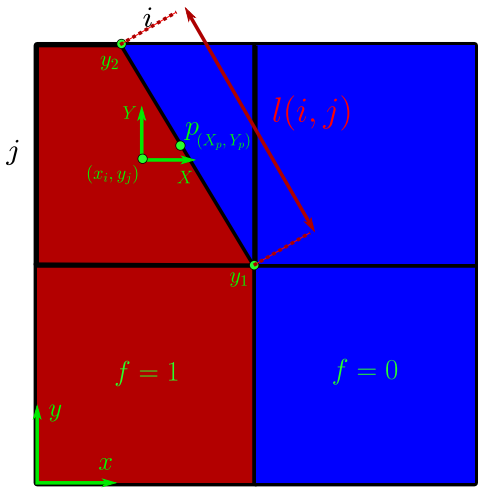

Fig. C.1 Schematic representation of the interface area calculation with the axisymmetric condition. The center point P with local coordinates (X_P, Y_P) is defined in the local X-Y coordinate system and denotes the center of the interface segment within the cell (i, j). The segment length is $l(i, j)$. On the other hand, (x_i, y_j) are defined in the global x-y coordinate system for the center of the cell.

The third method increases the accuracy of the calculation by taking into account the fact that the interface element in the cell (i, j) is not a cylinder but a truncated cone or conical frustum with a lateral surface area of

$$A_{\text{frustum lateral}} = 2\pi\left(\frac{r_1 + r_2}{2}\right)s \tag{C.3}$$

where r_1 is the radius of the bottom base of the frustum, r_2 is the radius of the top base of the frustum, and s is the slant height of the frustum. Accordingly, the surface area using this method is calculated by

$$A_3 = \sum_{i=1,j=1}^{i=\infty,j=\infty} \pi l(i,j)\left(y_1(i,j) + y_2(i,j)\right) \tag{C.4}$$

In order to compare these three methods, the surface area of a sphere with a radius of 1 is calculated and compared with the analytical value of 4π. Figure C.2 shows the results of this comparison, where the error of each method in calculating A is plotted against the maximum mesh refinement level. As expected, the error in all three methods decreases with increasing the mesh resolution. However, the error in the first method is significantly higher than the other two methods. Method two and three have almost the same accuracy, but method three is slightly more accurate for low mesh resolutions.

Despite the attempt made above to calculate the interface area accurately enough so that the total energy of the system E does not violate the energy conservation law, the results of the

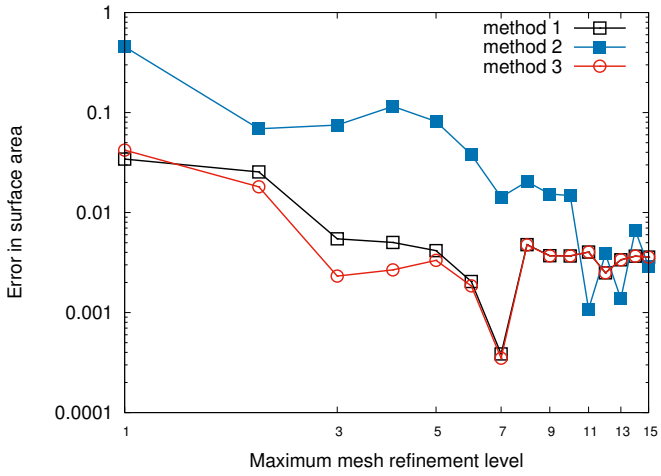

Fig. C.2 Comparison of the three interface area calculation methods for a sphere shape simulated using the axisymmetric condition against maximum mesh refinement level. The error associated with each method is shown relative to the analytical surface area of a sphere with radius 1. Method one displays a significantly higher error, while methods two and three are nearly equivalent in accuracy, with method three being marginally more precise at lower mesh resolutions. Nevertheless, neither method converges to zero error value; rather, it reaches a plateau.

simulations for holes on a flat film show that E is initially increased, even when the interface area is calculated using method three. This effect was illustrated in figure 5.5. Since the resolution of this issue was not crucial to the main objectives of this study, it was not pursued further.

Appendix D

Additional Results for d^{c*} Variations

This appendix contains additional results for the variation of the healing threshold d^{c*} with the parameters involved in the problem of a hole on a bubble cap. Figure D.1 shows the variation of d^{c*} with the gas Laplace number La_g for a broad range of values where the data points with unfinished dichotomy are included as opposed to the modified figure 7.3. Figure D.2 provides further results on the hole healing threshold variation with $\rho_{l/g}$ with varying La_l and La_g, while keeping $d_b^* = 50$ for all cases. The three panels of this figure correspond to three different values for La_g, within each of which La_l is varied.

In the dichotomy process for the results given in figure 7.3, some data points were not included in the presented figure as the dichotomy process for these points was not completed to reach the maximum accuracy allowed by the mesh refinement level. The complete results of the dichotomy process for the case of $d_b^* = 20$ are provided in the appendix in figure D.1. Considering the full plot with incomplete dichotomies, the trend of the results is clear, and the missing data points do not appear to affect the overall conclusion. Thus, they were removed from figure 7.3 for clarity. However, it is worth noting that Λ_i for the cases with $d_b^* = 20$ and 80 were estimated from figure D.1.

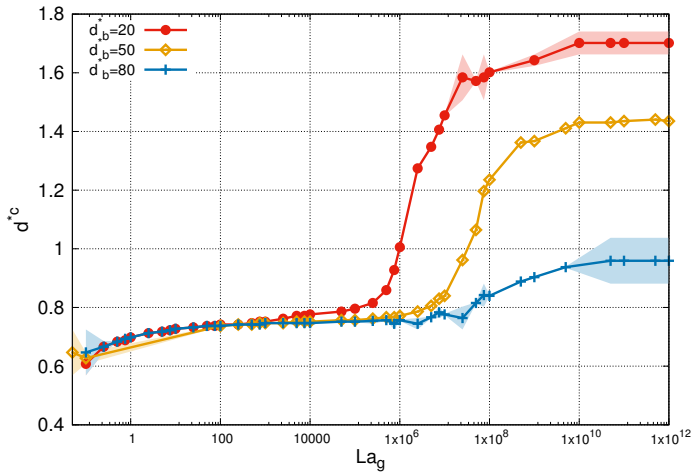

Fig. D.1 Variation of d^{c*} as a function of the gas Laplace number La_g for different bubble sizes. This plot includes the full range of investigated values and represents all dichotomy data points, including those with unfinished dichotomy, particularly for $d_b^* = 20$ and 80. The trend is indicative of the general behavior despite the inclusion of incomplete data, providing a comprehensive overview that supports the estimates of Λ_i for the cases with $d_b^* = 20$ and 80 as discussed in section 7.2.1.2.

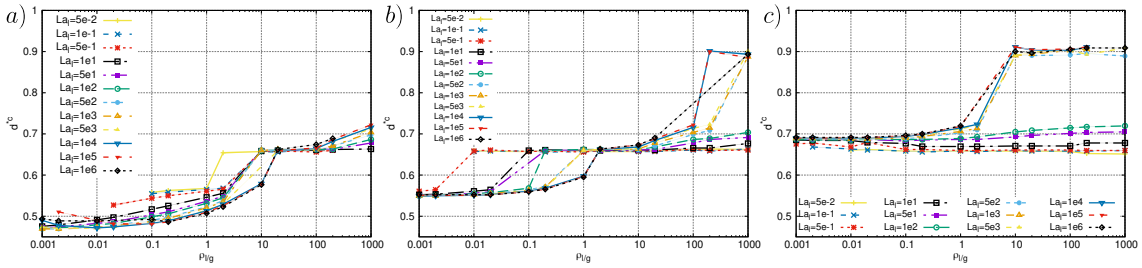

Fig. D.2 Variation of d^{c*} with $\rho_{l/g}$ when varying La_l, while keeping $d_b^* = 50$ for all cases. The three panels of this figure correspond to three different values for La_g.

Appendix E

Rim Retraction and Contraction

Here are presented extensive measurements of the tip minimum radius, its velocity, and its acceleration for the bubble cap case while varying for each parameter of the problem individually. As discussed in chapter 2, the bubble cap problem is governed by the following parameters:

$$d^{*c} = f(\mathrm{La}_l, \mathrm{La}_g, \rho_{l/g}, d_b/\delta).. \tag{2.30}$$

However, here, the examination is not focused on the variations of the hole healing threshold d^{*c} with other parameters. Instead, the focus is on the rim retraction and contraction and how they are affected by the parameters of the problem: La_l, La_g, $\rho_{l/g}$, and d_b/δ, while keeping the initial hole size d^* constant in each of the following examinations. The maximum mesh refinement within the film thickness was set to 6 levels (instead of 7) to facilitate the completion of these numerous simulations.

The following results are presented without any discussion or analysis. They are presented as a reference for future studies since they are not directly related to the main focus of this thesis. However, they are still essential to be presented, given their extensiveness and the fact that they are not analyzed to this extent in the literature.

Figure E.1 shows the effect of film curvature on the hole tip movement while keeping $\mathrm{La}_l = 1725$, $\mathrm{La}_g = 1000$, $\rho_{l/g} = 10$. These values are not set according to the standard oceanic case in table 2.1, especially for the density ratio, which was set to 10 instead of 833 to speed up these simulations. Figure E.2 shows the effect of La_l on the hole tip movement while keeping $\mathrm{La}_g = 1000$, $\rho_{l/g} = 10$, and $d_b^* = 50$ constant across simulations and using only 4 mesh level refinement within the film thickness. Figure E.3 shows the effect of La_g on the hole tip movement while keeping $\mathrm{La}_l = 1725$, $\rho_{l/g} = 10$, and $d_b^* = 50$ constant across simulations and utilizing 6 mesh level refinement within the film thickness. Figure E.4 shows the effect of $\rho_{l/g}$

on the hole tip movement while keeping $\mathrm{La}_l = 1725$, $\mathrm{La}_g = 1000$, and $d_b^* = 50$ constant across simulations and employing 6 mesh level refinement within the film thickness.

In each figure, there are 6 subplots. Subplots (a) and (b) show the tip minimum radius versus time, using the log scale only on the x-axis and the log scale on both the y-axis and the x-axis, respectively. Similarly, subplots (c) and (d) show the tip velocity versus time, using the log scale only on the x-axis and the log scale on both the y-axis and x-axis, respectively. Finally, subplots (e) and (f) show the tip acceleration versus time, using the log scale only on the x-axis and the log scale on both the y-axis and x-axis, respectively. The results are presented in this format to facilitate the examination of the data. It is important to note that smoothing functions have been applied to the data for tip velocity and acceleration to reduce the noise, which in most cases is considerable. Moreover, it is worth reminding that the presented data is only on the tip movement in the y-direction, while the tip moves in the x-direction. However, the movement in the x-direction is often not significant for $t^* \lessapprox 10$.

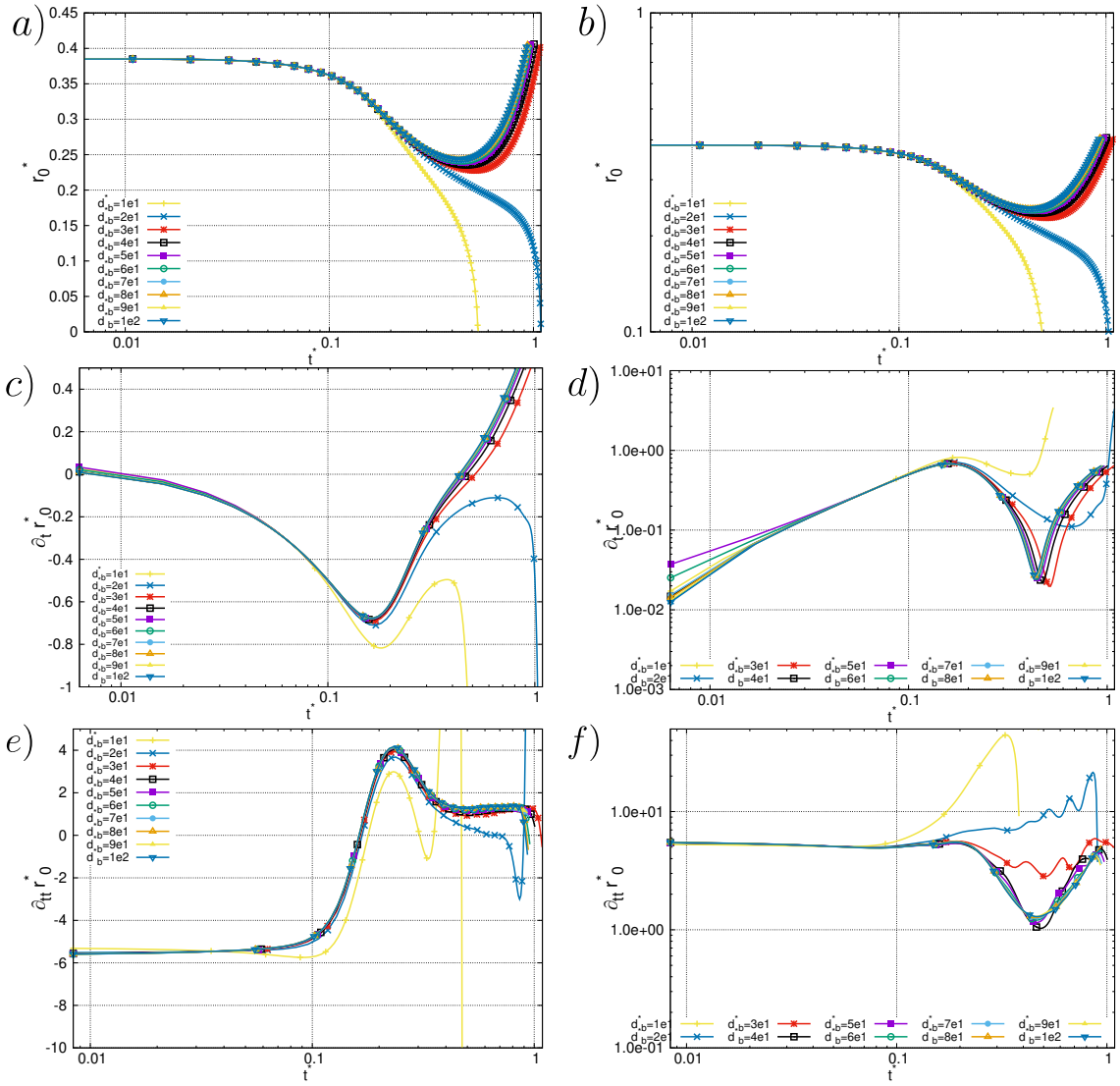

Fig. E.1 Effects of film curvature on hole tip movement. Subplots (a) and (b) depict the evolution of the tip minimum radius over time on semi-log and log-log scales, respectively. Subplots (c) and (d) represent the tip velocity over time, and subplots (e) and (f) present the tip acceleration over time, each with similar scaling as in (a) and (b). Smoothing functions were applied to velocity and acceleration data.

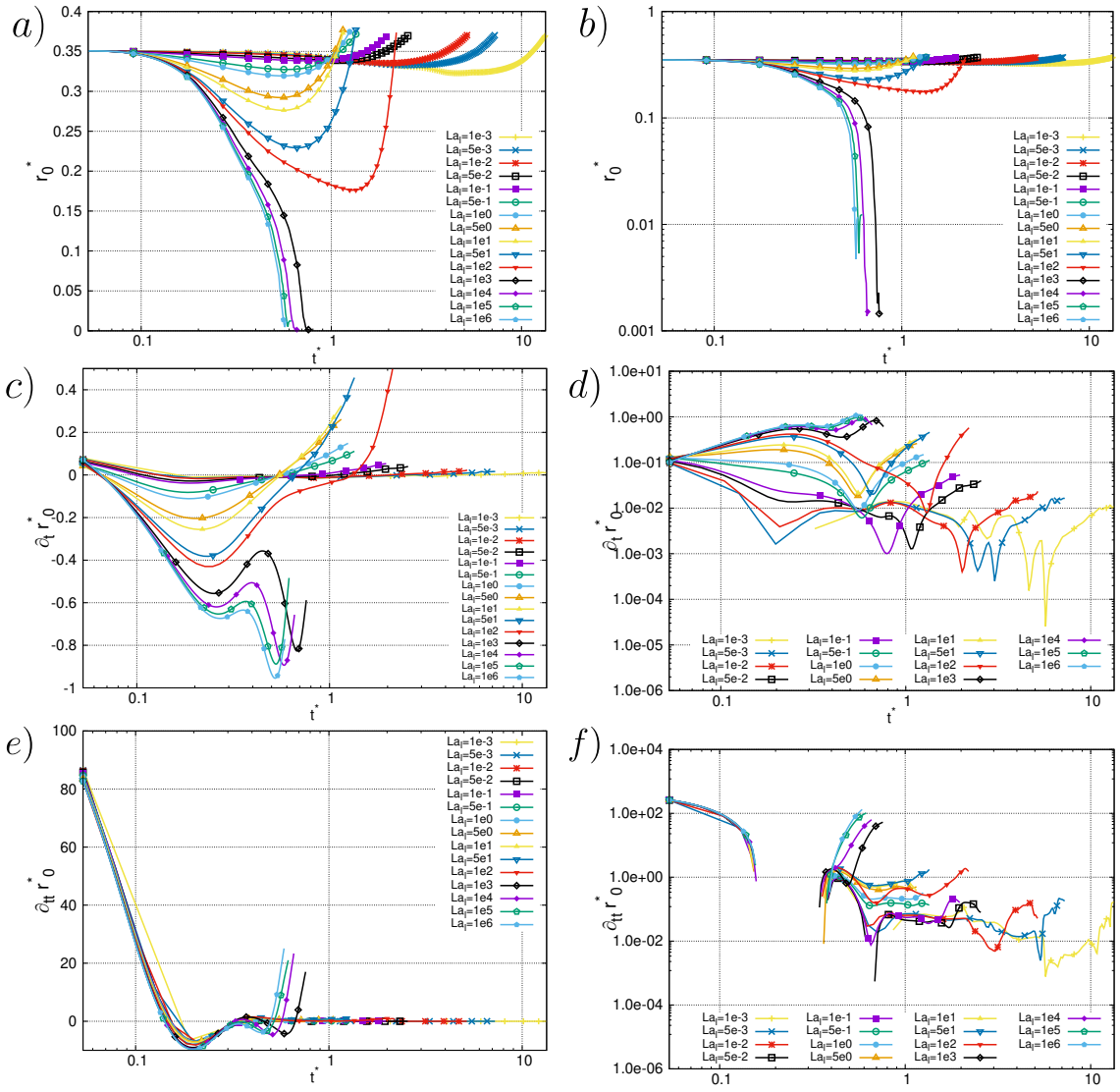

Fig. E.2 Impact of liquid Laplace number on hole tip movement. Subplots (a) and (b) depict the evolution of the tip minimum radius over time on semi-log and log-log scales, respectively. Subplots (c) and (d) represent the tip velocity over time, and subplots (e) and (f) present the tip acceleration over time, each with similar scaling as in (a) and (b). Smoothing functions were applied to velocity and acceleration data.

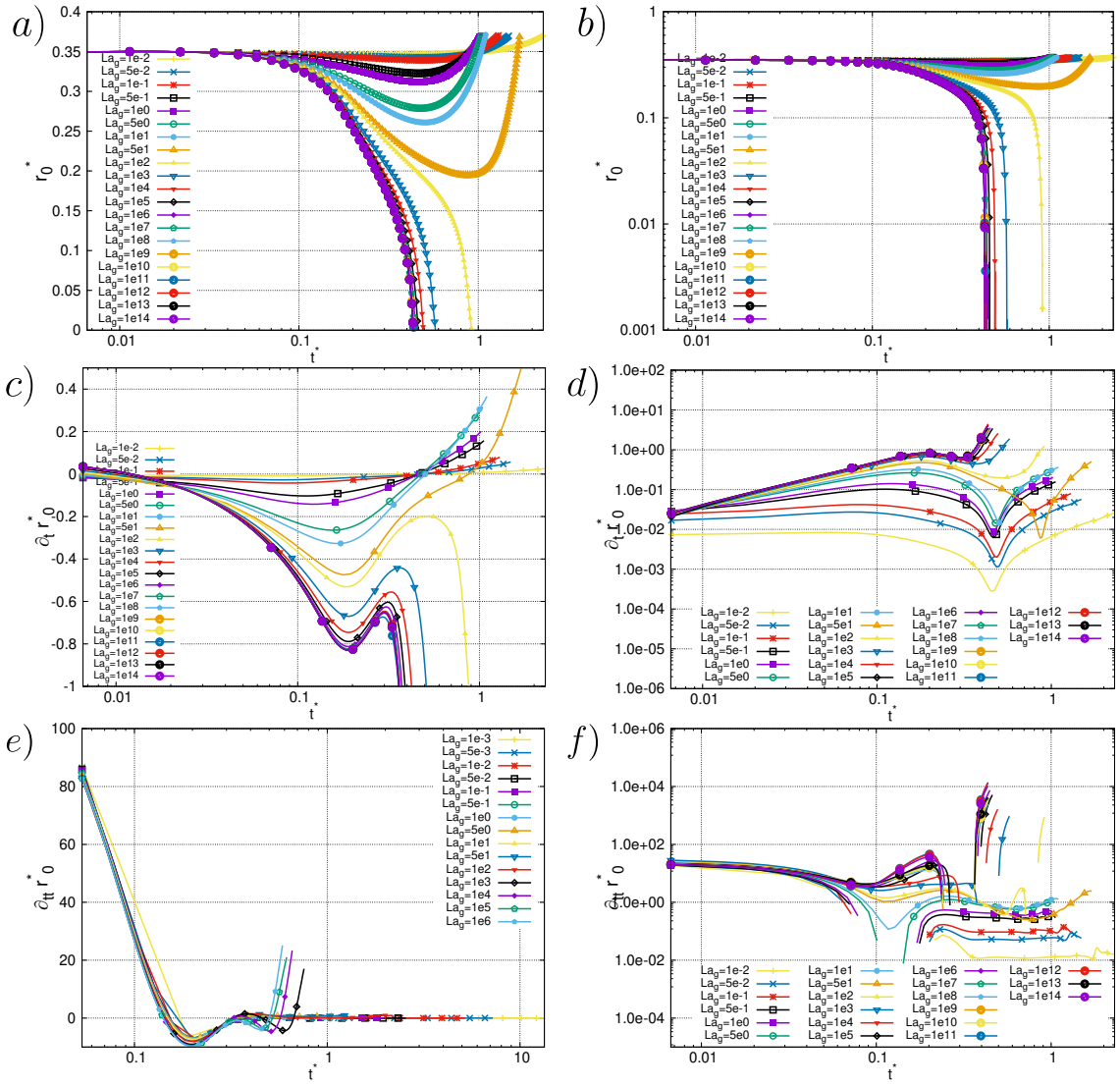

Fig. E.3 Impact of gas Laplace number on hole tip movement. Subplots (a) and (b) depict the evolution of the tip minimum radius over time on semi-log and log-log scales, respectively. Subplots (c) and (d) represent the tip velocity over time, and subplots (e) and (f) present the tip acceleration over time, each with similar scaling as in (a) and (b). Smoothing functions were applied to velocity and acceleration data.

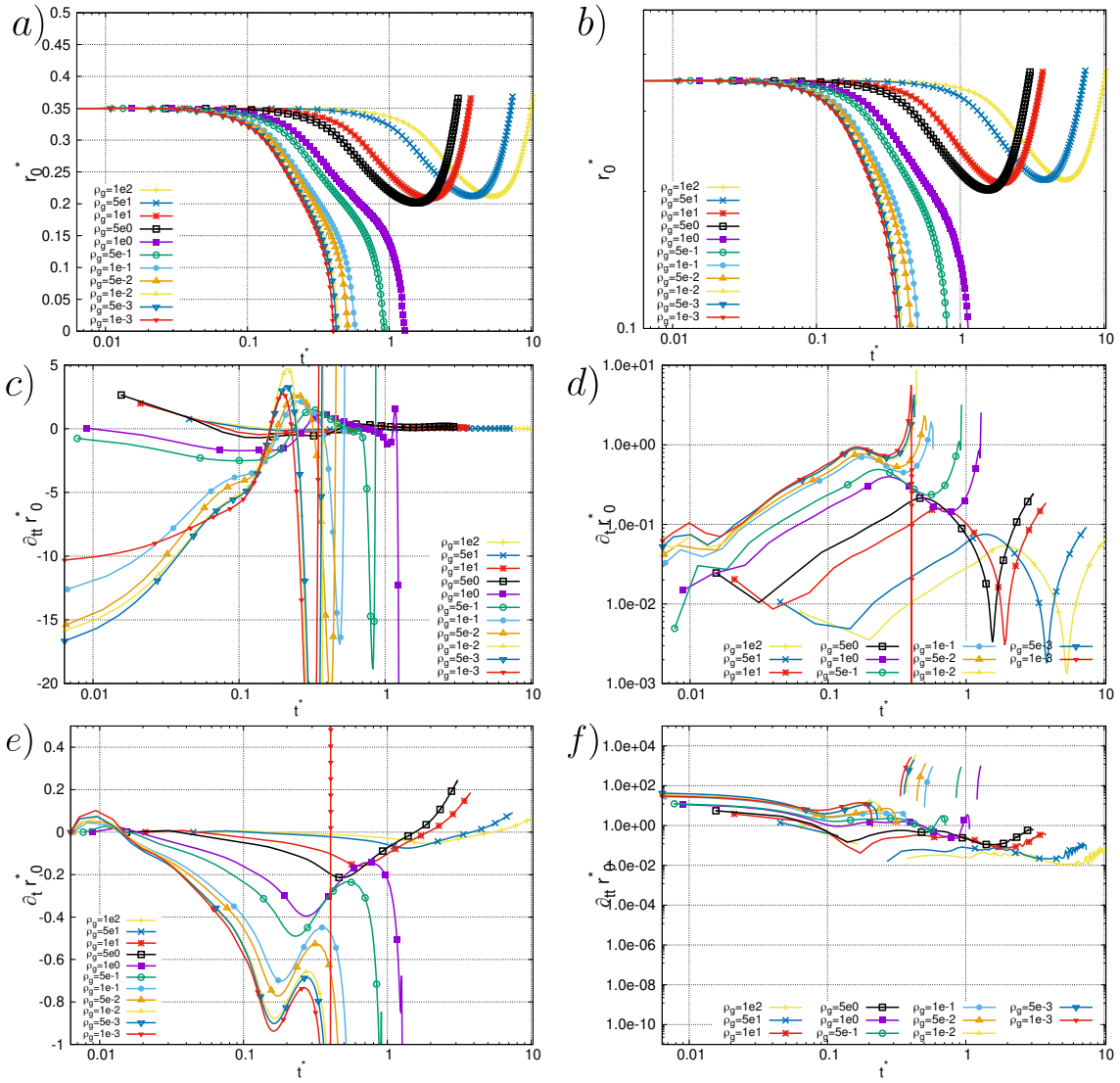

Fig. E.4 Effects of density ratio on hole tip movement. Subplots (a) and (b) depict the evolution of the tip minimum radius over time on semi-log and log-log scales, respectively. Subplots (c) and (d) represent the tip velocity over time, and subplots (e) and (f) present the tip acceleration over time, each with similar scaling as in (a) and (b). Smoothing functions were applied to velocity and acceleration data.

Appendix F

Other Numerical Configurations

Besides the main numerical configuration studied in the present work and discussed in chapter 2, other configurations have been developed to study different dynamics of the film and bubble in different scenarios, even though they were not studied extensively and were not the main focus of this work. For example, the numerical configuration for straight and toroidal rim retraction of a flat film detailed in section F.1 was employed as an initial attempt to numerically study the film dynamics using the Basilisk solver and verify the accuracy of the numerical model and the implementation against the extensive results in the literature on the Taylor-Culick velocity, including the recent work of Agbaglah (2021), which employed the Basilisk solver.

In addition, the hemispherical bubble configuration was developed for qualitative demonstrations of bubble bursting with a hemispherical cap with the production of jet drops and the drainage of the bubble cap. This configuration is discussed in section F.2.

Finally, the bubble-rising configuration was developed for qualitative demonstrations of bubble raising and the drainage of the bubble cap when at the surface, which illustrates the formation of the pinching area at the foot of the bubble. This configuration is discussed in section F.3.

F.1 Retracting Flat Film with a Straight Rim

To simulate the retraction of an infinitely long sheet with a straight rim, the numerical domain of a square size of L is configured as shown in figure F.1. The retracting film is constructed by joining part A, a rectangle, and B, a quarter circle, with the former representing the flat part of the film and the latter the initial shape of the retracting rim, which is set as a circular profile. This 2D numerical configuration in the Cartesian coordinate system models what is shown in figure F.1(b) in 3D. The boundary condition on both axes is the symmetry condition. The simulation is initiated with the pressure and velocity fields uniformly set to zero values. The

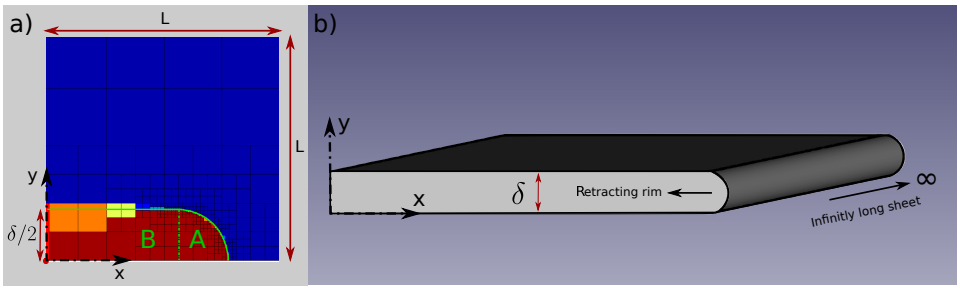

Fig. F.1 Schematic representation of the numerical domain configured to simulate the retraction of an infinitely long sheet with a straight rim. The figure delineates the combination of a rectangle (Part A) representing the flat part of the film and a quarter circle (Part B) representing the initial shape of the retracting rim, showcasing the 2D Cartesian coordinate system modeling of the 3D configuration in sub-figure b.

initial pressure values, even though not representative of the film dynamics at $i = 0$ (since the interface mean curvature is not zero), are quickly adjusted to accurate values by the Basilisk Poisson solver.

This configuration will be deployed to study the velocity of rim retraction and juxtapose the outcomes with the theoretical prediction, known as the Taylor-Culick velocity, derived from the research conducted by Taylor (1959) and Culick (1960) and reviewed by many subsequent works.

F.2 Hemispherical Bubble

In this part, a simple numerical configuration is introduced to simulate a bubble with a hemispherical shape and Bo $\to \infty$ by attaching a bulk of liquid to the bottom of the bubble cap described in figure 2.11a. Applying the same axisymmetry and boundary condition as in for the bubble cap in the previous section, the result is a bubble of diameter d_b with a cap of thickness δ illustrated in figure F.2. This configuration examines not only the hole opening or closing dynamic, similar to the bubble cap configuration, but also the bubble collapse and production of jet drop. Furthermore, due to the existence of liquid bulk, this configuration with the symmetry condition applied to its r axis no longer creates a full spherical bubble with two exit holes but rather two separate half-sphere bubbles, both with pressure $p = \Delta p_\gamma$ inside the bubble and one exit.

In addition, the numerical configuration given in figure F.2, even though not a realistic shape for a typical surface bubble, simulates the pinching of the film at the bubble foot and the drainage of the liquid from the bubble cap to the liquid bulk containing the bubble. As depicted in F.2, the initial shape of the bubble foot, where the cap meets the liquid bulk, is arbitrarily set

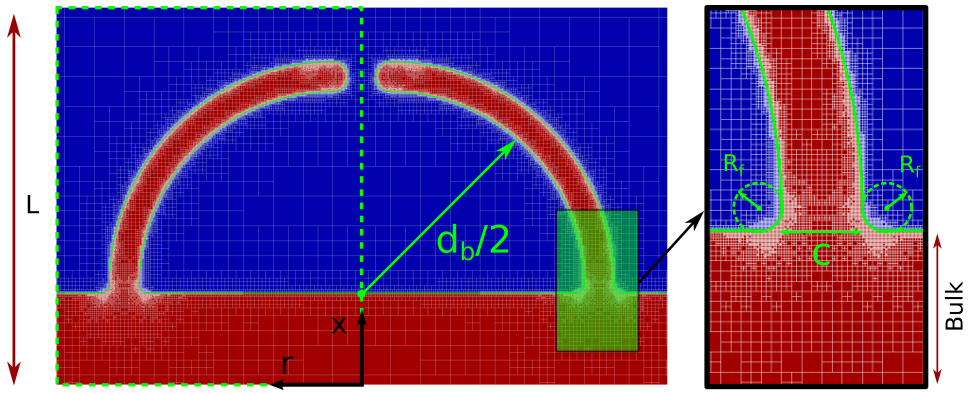

Fig. F.2 Depicting a numerical configuration simulating a hemispherical bubble, showcasing potential dynamics like hole opening or closing, bubble collapse, and jet drop production. The initial interface where the cap meets the liquid bulk is simplified to a circular shape of radius $R_f = 0.25\delta$.

to a circular shape of radius $R_f = 0.25c$ for simplicity. In this case, the initialization is done similarly to the bubble cap problem.

The numerical configuration discussed in this section has been mainly used for visualization purposes, for instance, qualitative results on jet drop formation and cap retraction and deformation, rather than for specific measurements. An example of such a result is shown in figure F.3 with six subplots corresponding to six different times in the simulation, capturing the color map of the fraction field. The figure shows the initial hole retraction and rim formation while the cap liquid is drained and pinched at the foot of the bubble cap. The figure also shows the collapse of the bubble and the production of jet drops.

F.3 Bubble Rising and Drainage

In this section, an axisymmetric bubble rising is simulated where an initially spherical bubble of size d_b starts rising due to gravity from a starting position well below the surface of the liquid bulk until it reaches the surface and forms a quasi-steady-state surface bubble with ongoing drainage. Figure F.4a shows the initial numerical configuration of this problem. The initial pressure field inside the bubble is set to the capillary pressure $\Delta p_\gamma \approx 4\gamma/(d_b)$, and similar axisymmetric boundary conditions as in section 2.4.2 are employed. The maximum mesh level in this example is 11, where the smallest cell at level 4 is the size of the initial bubble. Therefore, the film thickness could not exceed $d_b/2^7$. That corresponds to a bubble with a cap of thickness around only 100 times smaller than the bubble size.

Beyond the minimum thickness represented by the smallest mesh cell, the film ruptures only due to the lack of numerical resolution and not a physical requirement since film rupture is not an inherent feature of the Navier-Stokes equations. This also explains why the hole had

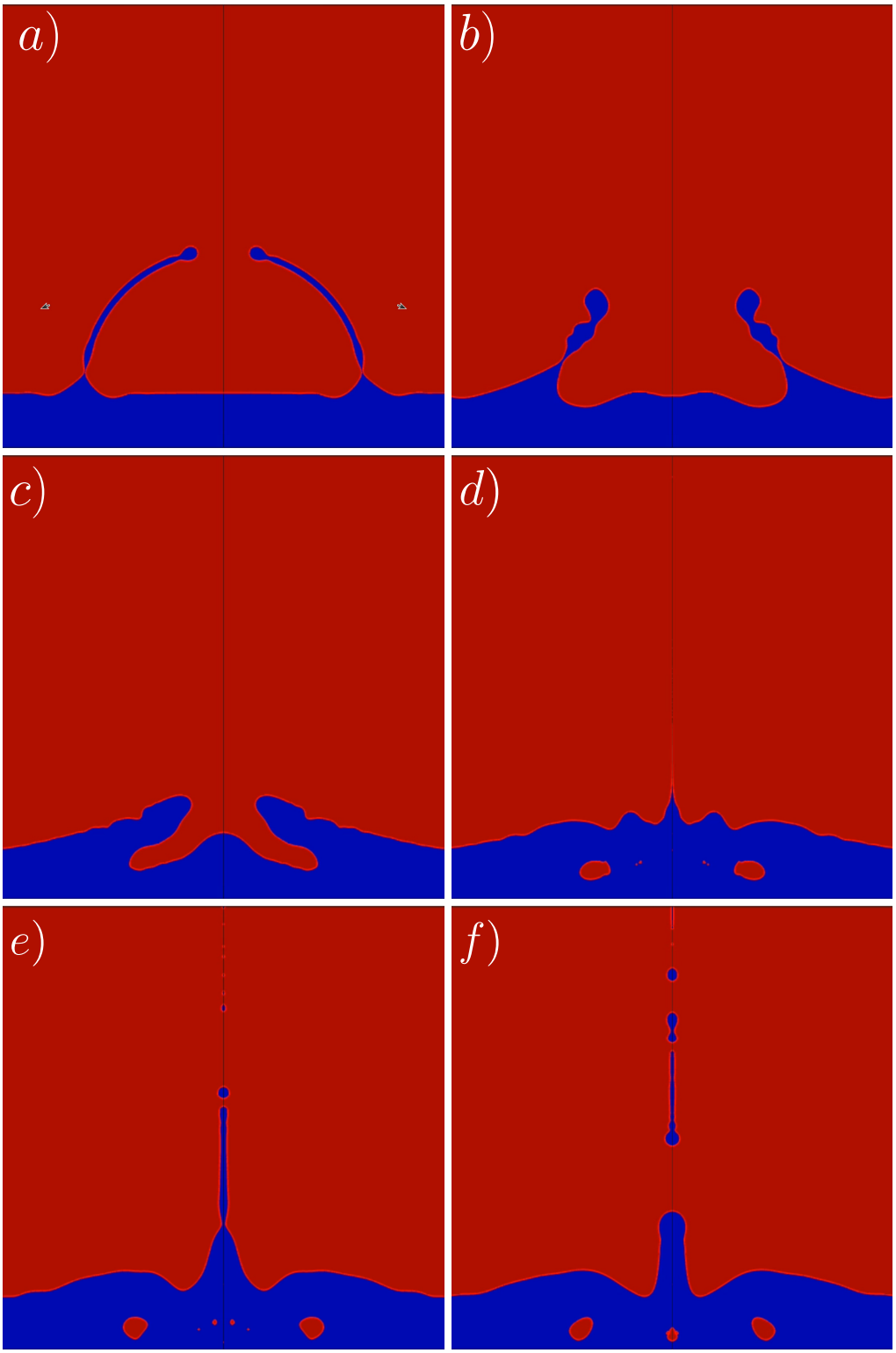

Fig. F.3 Temporal evolution of the dynamics of a bursting hole in a thin curved liquid film as the cap of a hemispherical bubble captured at six sequential time frames. The color map represents the fraction field. The liquid Laplace number is set to La $= 10^4$, density ratio $\rho_l/\rho_g = 833$, viscosity ratio $\mu_l/\mu_g = 7.7$, and bubble size $d_b = 40\delta$. Accordingly, the dimensionless time is $t^* = 476\ ns$ with Taylor-culick velocity $U_{tc} = 7.43\ m/s$ for a film thickness of $\delta = 2.5\mu m$ and an initial hole size of $d = 0.9\delta$. The time stamps of the captured fraction fields are a) $t^* = 3.75$, b) $t^* = 11.25$, c) $t^* = 18.75$, d) $t^* = 22.5$, e) $t^* = 26.25$, and f) $t^* = 30$.

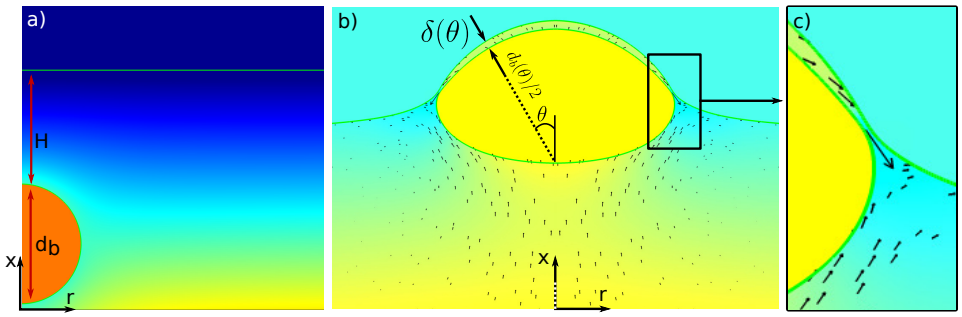

Fig. F.4 Sub-figure a) depicts the initial setup for simulating the ascent of an axisymmetric bubble of size d_b positioned below the liquid surface by distance H. Boundary conditions are aligned with those in section 2.4.2. Sub-figure b) shows the quasi-steady-state pressure color map with a coarsened velocity vector field of the liquid phase, showing the varying thickness δ_θ and radius $d_b(\theta)$ of the bubble cap. Sub-figure c) highlights the drainage flow at the pinching area.

to be artificially created in the numerical configurations presented previously to study the hole dynamics.

It is essential to note that even though gravity was not included in other configurations, it has not been omitted from the governing equation 2.24 in the present case. That is because, in this problem, the Bond number is defined by the characteristic length scale of the bubble d_b and not the size of the hole, which does not exist in this case, resulting in ineligible $Bo_b \gg 1$ values. In this particular case given in figure F.4, the Bond number and Galilei number are $\mathrm{Bo}_b = 1$ and $\mathrm{Ga} = 1$.

Figure F.4b shows a qualitative outcome of such a simulation where the color map of the pressure field superimposed by the liquid phase velocity vectors is given. One could note the bubble cap formation with an uneven thickness δ_θ, varying with the angle θ from the vertical line dividing the bubble in half. In this case, the inhomogeneity of the bubble thickness is attributed to the gravity-driven drainage of the liquid in the bubble cap.

Moreover, one could spot the formation of the pinching area, observable in figure F.4c at the foot of the bubble as a consequence of the cap drainage, discussed in detail by Lhuissier and Villermaux (2012). In this area, the higher values in the velocity of the draining liquid result in the local decrease of pressure, further decreasing the cross-section area and increasing the velocities, yet counteracted by the surface tension forces due to the deformation of the two interfaces.

Apart from the possibility of studying the drainage of the bubble cap, bubble foot pinching, and bubble rising, the quasi-steady-state shape of the bubble given in figure F.4b is also a direct numerical solution for the bubble shape, which itself is studied extensively using various numerical models (see Guémas et al., 2015; Pigeonneau and Sellier, 2011).